Spring 2018

High-fidelity multidisciplinary design optimization of a 3D composite material hydrofoil

Silvia Volpi
University of Iowa

HIGH-FIDELITY MULTIDISCIPLINARY DESIGN OPTIMIZATION OF A 3D COMPOSITE MATERIAL HYDROFOIL

by

Silvia Volpi

A thesis submitted in partial fulfillment
of the requirements for the Doctor of Philosophy
degree in Mechanical Engineering in the
Graduate College of
The University of Iowa

May 2018

Thesis Supervisor: Professor Frederick Stern

Graduate College
The University of Iowa
Iowa City, Iowa

CERTIFICATE OF APPROVAL

_____

PH.D. THESIS

_____

This is to certify that the Ph.D. thesis of

Silvia Volpi

has been approved by the Examining Committee for
the thesis requirement for the Doctor of Philosophy degree
in Mechanical Engineering at the May 2018 graduation.

Thesis Committee: _____
Frederick Stern, Thesis Supervisor

_____
Jasbir S. Arora

_____
Kyung K. Choi

_____
Ching-Long Lin

_____
H.S. Udaykumar

ACKNOWLEDGEMENTS

The accomplishment of this research was made possible thanks to the compelling and stimulating environment of the IIHR-Hydroscience & Engineering Laboratory, especially in the ship hydrodynamics research group. Prof. Frederick Stern has been an exceptional mentor teaching me what performing research means and how to create a rigorous base on which building and developing ideas. Dr. Matteo Diez of CNR-INSEAN, the National Research Council-Marine Technology Research Institute of Rome (Italy), as a visiting scholar at IIHR contributed to the development and completion of this research providing invaluable help and support along the entire process. Drs. Hamid Sadat-Hosseini and Maysam Mousaviraad, with their expertise in computational ship hydrodynamics, helped me overcoming many practical issues I had to face as a student learning something new every day.

I am truly thankful to the Office of Naval Research (ONR) that sponsored this research through grants No. N00014-13-1-0616 and No. N00014-13-1-0617, administered by Dr. Roshdy Barsoum, and through grant No. N00014-14-1-0195, administered by Dr. Ki-Han Kim.

Finally, I want to thank Prof. Paul Brandner from University of Tasmania-AMC for providing the hydrofoil design and the associated experimental data.

ABSTRACT

Multidisciplinary design optimization (MDO) refers to the process of designing systems characterized by the interaction of multiple interconnected disciplines. High-fidelity MDO usually requires large computational resources due to the computational cost of achieving multidisciplinary consistent solutions by coupling high-fidelity physics-based solvers. Gradient-based minimization algorithms are generally applied to find local minima, due to their efficiency in solving problems with a large number of design variables. This represents a limitation to performing global MDO and integrating black-box type analysis tools, usually not providing gradient information. The latter issues generally inhibit a wide use of MDO in complex industrial applications.

An architecture named multi-criterion adaptive sampling MDO (MCAS-MDO) is presented in the current research for complex simulation-based applications. This research aims at building a global derivative-free optimization tool able to employ high-fidelity/expensive black-box solvers for the analysis of the disciplines. MCAS-MDO is a surrogate-based architecture featuring a variable level of coupling among the disciplines and is driven by a multi-criterion adaptive sampling (MCAS) assessing coupling and sampling uncertainties. MCAS uses the dynamic radial basis function surrogate model to identify the optimal solution and explore the design space through parallel infill of new solutions.

The MCAS-MDO is tested versus a global derivative-free multidisciplinary feasible (MDF) approach, which solves fully-coupled multidisciplinary analyses, for two analytical test problems. Evaluation metrics include number of function evaluations required to achieve the optimal solution and sample distribution. The MCAS-MDO

outperforms the MDF showing a faster convergence by clustering refined function evaluations in the optimum region.

The architecture is applied to a steady fluid-structure interaction (FSI) problem, namely the design of a tapered three-dimensional carbon fiber-reinforced plastic hydrofoil for minimum drag. The objective is the design of shape and composite material layout subject to hydrodynamic, structural, and geometrical constraints. Experimental data are available for the original configuration of the hydrofoil and allow validating the FSI analysis, which is performed coupling computational fluid dynamics, solving the Reynolds averaged Navier-Stokes equations, and finite elements, solving the structural equation of elastic motion. Hydrofoil forces, tip displacement, and tip twist are evaluated for several materials providing qualitative agreement with the experiments and confirming the need for the two-way versus one-way coupling approach in case of significantly compliant structures.

The free-form deformation method is applied to generate shape modifications of the hydrofoil geometry. To reduce the global computational expense of the optimization, a design space assessment and dimensionality reduction based on the Karhunen–Loève expansion (KLE) is performed off-line, i.e. without the need for high-fidelity simulations. It provides with a selection of design variables for the problem at hand through basis rotation and re-parametrization. By using the KLE, an efficient design space is identified for the current problem and the number of design variables is reduced by 92%.

A sensitivity analysis is performed prior to the optimization to assess the variability associated with the shape design variables and the composite material design variable, i.e. the fiber orientation. These simulations are used to initialize the surrogate model for the

optimization, which is carried out for two models: one in aluminum and one in composite material. The optimized designs are assessed by comparison with the original models through evaluation of the flow field, pressure distribution on the body, and deformation under the hydrodynamic load. The drag of the aluminum and composite material hydrofoils is reduced by 4 and 11%, respectively, increasing the hydrodynamic efficiency by 4 and 7%. The optimized designs are obtained by evaluating approximately 100 designs. The quality of the results indicates that global derivative-free MDO of complex engineering applications using expensive black-box solvers can be achieved at a feasible computational cost by minimizing the design space dimensionality and performing an intelligent sampling to train the surrogate-based optimization.

PUBLIC ABSTRACT

The goal of this research is developing a numerical tool for designing systems subject to the interaction of various physical processes (disciplines), each one governed by its particular laws. This tool, which has been named multi-criterion adaptive sampling multidisciplinary design optimization (MCAS-MDO), performs design optimization combining: an optimizer, a design modification tool, and a multidisciplinary analysis tool able to couple and solve the equations of the disciplines involved. With the constantly advancing research in each field, it is of interest to build a modular MDO framework which allows using state-of-the-art discipline solvers often already available to the designer. Such solvers are called black-boxes since, when provided with the input, they produce the output without track of the state variables involved in the computation. This greatly increases the computational effort of the optimizer due to the lack of gradient information, i.e. the behavior of the output of interest around the design under investigation. In this research, instead of building an approximation of the gradient, a gradient-free (derivative-free) approach is employed and its large computational cost is mitigated by: reducing the number of design variables ahead of the optimization, using surrogate models, and using a variable level of coupling among the disciplines. The optimization is then driven by a multi-criterion adaptive sampling, an algorithm that identifies promising regions of the design space where more expensive simulations are worth the investigation. Herein, MCAS-MDO is applied to fluid-structure interaction, a challenging mechanical engineering problem involving flexible structures deforming under the load exerted by a fluid. The structure at hand is a hydrofoil in carbon fiber reinforced plastic, which is a prototypical problem for marine vessel appendages such as rudders, fins, and propeller blades.

TABLE OF CONTENTS

LIST OF TABLES

LIST OF FIGURES

LIST OF ABBREVIATIONS

AAO	All-at-once formulation
AL	Aluminum
ACO	Ant colony optimization
ASO	Asymmetric subspace optimization
ARS	Algebraic Reynolds stress
RAS-DES	Algebraic Reynolds stress detached eddy simulation
BA	Bat algorithm
BLISS	Bi-level integrated system synthesis
CFD	Computational fluid dynamics
CFRP	Carbon fiber-reinforced plastic
CO	Collaborative optimization
CS	Cuckoo search
CSD	Computational structural dynamics
CSSO	Concurrent subspace optimization
DES	Detached eddy simulation
DoE	Design of experiments
DPSO	Deterministic particle swarm optimization
DRBF	Dynamic radial basis functions
EFD	Experimental fluid dynamics
EGO	Efficient global optimization
ESD	Experimental structural dynamics
FA	Firefly algorithm
FE	Finite elements
FFD	Free-form deformation

FSI	Fluid-structure interaction
G-DF	Global derivative-free
HSS	Hammersley sequence sampling
IDF	Individual discipline feasible
KKT	Karush-Kuhn-Tucker
KL	Karhunen-Loève
KLE	Karhunen-Loève expansion
LES	Large eddy simulation
MCAS	Multi-criterion adaptive sampling
MCAS-MDO	Multi-criterion adaptive sampling multidisciplinary design optimization
MDA	Multidisciplinary analysis
MDF	Multidisciplinary feasible
MDO	Multidisciplinary design optimization
NACA	National advisory committee for aeronautics
PSO	Particle swarm optimization
RANS	Reynolds averaged Navier-Stokes
RBF	Radial basis function
RE	Richardson extrapolation
SAND	Simultaneous analysis and design
SBDO	Simulation-based design optimization
SS	Stainless steel
URANS	Unsteady Reynolds averaged Navier-Stokes
UQ	Uncertainty quantification

CHAPTER 1: INTRODUCTION

Background

Multidisciplinary design optimization (MDO) is a powerful numerical tool for the design of engineering systems subject to the interaction of two or more physical processes. It belongs to simulation-based design optimization (SBDO) methodologies. SBDO partially replaced the classic build-and-test paradigm due to, on one hand, the high cost of prototypes and experiments and, on the other hand, the increasing availability of computational resources. It uses numerical optimization for improving conceptual and detailed designs relying on the accuracy of specialized analysis/simulation tools. SBDO integrates three main components: the analysis tool, the optimizer, and the design modification tool. The analysis tool is used to assess the performance of a design by means of numerical simulations. The optimizer iteratively generates improved designs, aiming at a specified performance target. The design modification tool, according to the specifications given by the optimizer, generates design variants and the associated computational domain in a form that can be processed by the analysis tool. SBDO is an iterative process whose completion is based upon satisfaction of user-defined convergence criteria. Figure 1 shows a diagram of the SBDO loop and the flow of information among its components.

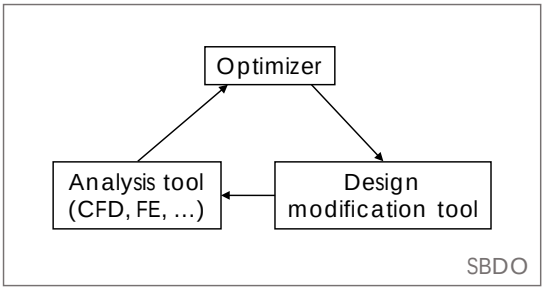

Figure 1: Simulation-based design optimization diagram

When performing SBDO of complex engineering systems, multiple physical processes (disciplines) are often involved and design goals and requirements are often multidisciplinary. The analysis tool of SBDO, specific to a single discipline, is thus substituted by a multidisciplinary analysis (MDA) which solves the interaction among the disciplines and provides the multidisciplinary solution of the system by coupling multiple

analysis tools. A diagram of the MDA is depicted in Figure 2 showing the mutual dependency of the discipline outputs in case of four processes. The accuracy of the MDA relies upon the multidisciplinary consistency achieved. The complexity of the MDA depends on the specific complexity of the single-discipline simulation and the number of disciplines involved. For instance, fluid-structure interaction (FSI) analyses involve two disciplines, fluid and structural mechanics; however, its complexity is large, due to the difficulty in the physical and numerical modeling of fluid, solid, and their interaction.

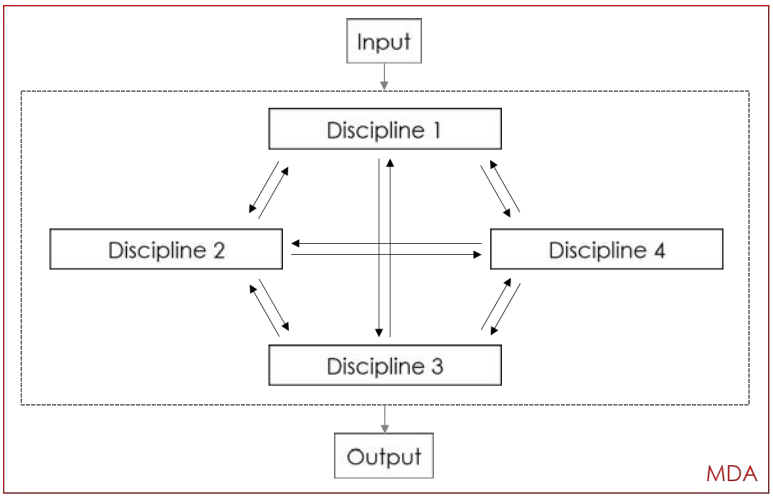

Figure 2: Multidisciplinary analysis diagram

MDO aims at the optimization of a design accounting for the discipline interaction. The formulation and implementation of MDO needs considering how the disciplines interact and how the optimizer and the MDA handle the interaction. Figure 3 presents a diagram of the MDO procedure showing how optimizer and MDA manage the calls to the discipline solvers. The organizational strategy adopted defines the MDO architecture which regulates how the multidisciplinary equilibrium is solved and how the optimal design is achieved. The computational cost of achieving accurate MDA solutions through coupling of multiple high-fidelity physics-based solvers, along with the algorithmic and technological difficulty of exploring large high-dimensional design spaces aiming at global optima, represent critical limitations of current state-of-the art MDO methods and applications.

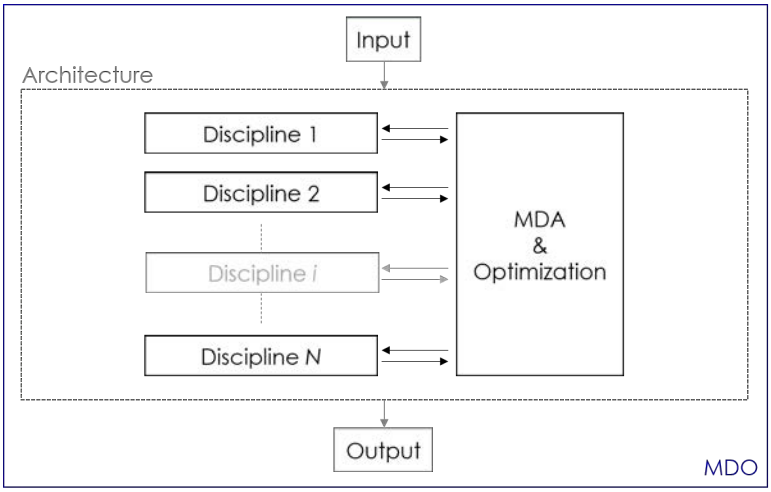

Figure 3: Multidisciplinary optimization diagram

In the present work, MDO is applied to FSI. In this challenging mechanical engineering application, the MDA aims at the dynamic equilibrium of a flexible structure deforming under the load exerted by a fluid. Depending on the physical model of choice, fluid and structural simulations can range from computationally inexpensive, for instance in the case of potential flow and beam theory for a simple structure, to very expensive, when viscosity and compressibility are included in the fluid model and no approximation of geometry and material properties is used for the structure. Generally, inexpensive models offer fast but low-fidelity solutions, while expensive solvers can achieve more accurate results (high-fidelity) at the expense of a long computational time. In FSI, typical expensive tools are computational fluid and structural dynamics (CFD and CSD) simulations based on Reynolds Averaged Navier-Stokes (RANS) equations and finite elements (FE). In complex industrial applications, high-fidelity numerical solvers are usually developed by specialists of the field and may be available to the designer in the form of black-box tools whose source code and state variables are not easily accessible. Additionally, the residuals associated to the numerical solution of systems of partial differential equations introduce noise in the black-box outputs. In the context of optimization, the lack of accurate gradient information is of paramount significance making efficient gradient-based algorithms difficult to use. Furthermore, in most applications the existence of multiple local optima cannot be excluded *a priori* motivating the use of global approaches. Performing global derivative-free MDO for complex

engineering applications, such as high-fidelity FSI, requires large computational resources and represents a technological challenge.

A common approach for reducing the computational cost of optimization is using surrogate models, also called metamodels. These are approximations of the objective function based on interpolation or regression. Surrogate models are trained by a set of function evaluations whose distribution in the design space is arbitrarily chosen. The optimization is performed on the surrogate model and can be sequentially repeated evaluating the predicted optimum with the analysis tool and including its performance in the training set. To improve the accuracy of the surrogate and the efficiency of the surrogate-based optimization, extensive research has been done in sampling methodologies moving from standard *a priori* designs of experiments (DoE) to function-adaptive techniques that exploit information becoming available during the optimization process.

The computational efficiency of performing MDO (or optimization in general) also benefits from the use of dimensionality reduction methodologies. These aim at reducing the number of design variables handled by the optimizer while retaining only the most significant and establishing proper domain dimension. The dimensionality reduction is traditionally carried out through sensitivity analysis, thus requiring high-fidelity function evaluations. For shape optimization, off-line techniques based on purely geometrical considerations have been recently developed, which do not need high-fidelity simulations and allow assessing the global variability of the design space.

An overview of methodologies and relevant references can be found in the following paragraphs for MDO, FSI, surrogate-based optimization, derivative-free global optimization, and design space dimensionality reduction. Furthermore, an overview of recent developments of hydro-structural analysis and optimization in naval engineering is provided.

Multidisciplinary design optimization

MDO has been widely applied in mechanical engineering, especially for aerospace and automotive design. For instance, Grossman et al. (1990), Haftka et al. (1992), and Diez and Iemma (2012) present MDO of wings considering disciplines such as aerodynamics, structures, flight mechanics, aeroelasticity and control. With a smaller extent, MDO has been applied also to marine vehicles, for example in Peri and Campana (2003) and

Campana et al. (2006), and marine structures in Leotardi et al. (2016) and Garg et al. (2017).

MDO methods are fundamentally different from standard optimization algorithms since their architecture is integrated in the formulation of the problem (Perez et al. 2004). When a single optimization problem is solved, the MDO architecture is called monolithic. Monolithic architectures generally maintain a strong dependency among disciplines and suit applications where individual sub-problems cannot be identified. They may or may not achieve multidisciplinary consistency at each optimization iteration (Martins and Lambe, 2013). For instance, in the multidisciplinary feasible (MDF, Cramer et al. 1994) architecture a full MDA is solved for each function call, ensuring multidisciplinary accuracy during the entire procedure. A different approach is adopted in the all-at-once (AAO, Cramer et al. 1994) formulation, simultaneous analysis and design (SAND, Haftka 1985), and individual discipline feasible (IDF, Cramer et al. 1994), where complete system feasibility is achieved only at optimization convergence. A detailed overview of these monolithic architectures is given in the Appendix.

When the optimization problem is divided into smaller tasks, the architecture is called distributed. Each sub-problem includes only the disciplines, variables, and functions that are involved. The use of distributed MDO allows a level of independency between tasks which fits well engineering environments where knowledge and resources are logistically scattered. Distributed architectures are more problem-specific than monolithic and include, among others, concurrent subspace optimization (CSSO, Sellar et al. 1996), collaborative optimization (CO, Braun et al. 1996), bi-level integrated system synthesis (BLISS, Sobieszczanski-Sobieski et al. 2000), and asymmetric subspace optimization (ASO, Chittick and Martins 2009). Reviews of monolithic and distributed architectures can be found in Haftka et al. (1992), Kroo (1997), Hulme and Bloebaum (1998), Tedford and Martins (2010), and Martins and Lambe (2013), among others. These include formulations, advantages/drawbacks, and comparisons aimed at evaluating accuracy and efficiency.

Managing the convergence of multidisciplinary consistency and design optimization within the MDO architecture remains an open issue that affects significantly the affordability of MDO for complex industrial applications.

Most of well assessed MDO architectures use in-house implementations of the discipline solvers which either provide gradient information or are suitable for the application of adjoint methodologies. This allows employing gradient-based optimization algorithms, generally more efficient than derivative-free methods since less affected by the curse of dimensionality. If specialized high-fidelity black-box software is to be used, the gradient information is generally not available and its approximation may be expensive and lack sufficient accuracy, as for finite differences and complex-step methods. This represents one of the major limitation for the extensive application of MDO procedure in the system-level design of complex industrial applications.

Surrogate models played an important role in the development of MDO positively contributing to the integration of specific discipline solvers, the reduction of the computational cost, and the handling of data noise (Hosder at al. 2001, Viana et al. 2014). Some applications can be found, for example, in Sellar et al. (1996) and Sobieszczanski-Sobieski and Haftka (1997). The interest in surrogate modeling stimulated an extensive literature in the last 25 years. Several review papers (e.g. Jin et al. 2001, Simpson et al. 2001b, Simpson et al. 2004, Queipo et al. 2005, Forrester and Keane 2009, Shan and Wang 2010) discussed the advantages and limitations of surrogate models. Viana et al. 2014, overviewing the history and developments in the field, summarize some of the still open issues as follows: "[…] the definition of the metamodel (either by selecting the metamodeling technique or its parameters) is a theme that constantly attracts interest from the community. Another never-ending problem is the curse of dimensionality. Surprisingly, global optimization […] is still one of the topics that will benefit from future research in design and analysis of computer experiments."

Fluid-structure interaction

Along with the choice of proper solution methods for fluid and structure, the coupling method plays a key role in a successful application of numerical FSI. A one-way type of coupling is realized by applying the hydrodynamic load, determined for the rigid body, on the flexible structure. In the two-way coupling, the structural deformation is fed back into the fluid solver. The use of a one- versus two-way coupling technique depends on the hydro-elastic effects due to the mutual coupling of fluid and structural dynamics. The two-way coupling can be loose or tight (Matthies and Steindorf 2003). In a loose

coupling, also referred to as weak, staggered, or explicit, the structural deformation is fed back into the fluid solver only at the beginning of the time step. In a tight coupling, also referred to as strong or implicit, fluid and structure solvers exchange load and deformation in an iterative manner using non-linear inner iterations (such as predictor/corrector steps or Gauss-Seidel sub-iterations) until convergence within each time step. The loose coupling is usually performed in a partitioned framework, i.e. using different solvers for fluid and structure, each one with its own discretization and numerical parameters. The tight coupling can be performed in either a partitioned or a monolithic fashion, where a monolithic framework regards fluid and structure as a single system of equations and employs a unique solution strategy. Tightly coupled solutions by partitioned solvers are usually computationally expensive to achieve, especially if high-fidelity solvers are used. This represents a limitation for their use within MDO.

Monolithic approaches potentially achieve full fluid-structure coupling, since the latter occurs at the governing equations level (Michler at al. 2004). For this reason, they are often referred to as full coupling methods. However, the accuracy of the single discipline analysis is limited by the use of a unique numerical method for both fluid and solid, often implemented by FE). Moreover, ill-conditioning of the system of equations and difficulty in integrating state-of-the-art fluid/structure solvers in a single framework remain open issues. In hydrodynamics, Reynolds number and free-surface effects limit significantly the use of monolithic FSI.

In partitioned methods, the solution of the coupled problem is advanced over the separate fluid, structure, and dynamic mesh partitions, in a sequential or parallel fashion. Although generally this approach conserves momentum and energy only in an asymptotic sense (as grid element and time step tend to zero), it offers several appealing features, including the ability to use available high-fidelity tools specifically designed for complex industrial problems, with well-established discretization and solution methods within each discipline, and preservation of software modularity (Farhat et al. 1998). As a result, a successful partitioned method can solve FSI problems with sophisticated fluid and structural physics models (Hou et al. 2012). Accuracy and robustness of partitioned methods depends on both the conservation properties at the interface and the convergence properties of the non-linear iterations. The issue of convergence occurs in monolithic

methods as well but within partitioned framework a formal proof of convergence is often unattainable.

Surrogate-based optimization

Metamodelling techniques have been developed and widely applied in several engineering fields. Among others, radial basis functions (RBF, Hardy 1971) and Kriging (Matheron 1963) have proved their efficacy in many design applications. RBF studies are shown, for instance, in Jin et al. (2001), Jin et al. (2003), Mullur and Messac (2006), Regis (2011), and Glaz et al. (2009). Developments and comparative studies on the Kriging model are presented in Jones et al. (1998), Jin et al. (2001), and Kleijnen and Van Beers (2004) among others. A dynamic RBF (DRBF) metamodel for uncertainty quantification (UQ) in ship hydrodynamics has been presented in Volpi et al. (2015); DRBF was compared to the dynamic Kriging of Zhao et al. (2011) focusing on the performance of sequential surrogate-based analyses versus standard metamodel applications. DRBF has then been extended to optimization in Diez et al. (2015b) and applied in a multi-fidelity framework in Pellegrini at al. (2018).

The accuracy and efficiency of metamodels depend on several concurrent issues, such as the dimensionality of the problem, the noisy or smooth nature of the function, and the sampling method for its training (Matsumura et al. 2015). These should be carefully addressed in the optimization process. The sampling of the design space needs to be efficient and effective, possibly achieving two competitive goals: an adequate global accuracy of the surrogate model (especially when a global optimum is sought), and a fine investigation of promising design regions (Booker et al. 2009). Sampling defined *a priori* can hardly achieve these goals. For this reason, adaptive sampling techniques have been developed, which adjust to the specific function. The literature proposes a variety of adaptive sampling criteria. Some examples include: the Kushner's criterion (Kushner 1964), which maximizes the probability of improving the objective; the expected improvement criterion, used in the efficient global optimization (EGO) algorithm (Jones et al. 1998); the lower confidence bounding function (Cox 1997), which minimizes the linear combination of surrogate model prediction and surrogate model uncertainty; locating the threshold-bounded extreme, locating the regional extreme, and minimizing surprises presented by Watson and Barnes (1995). A multi-criterion adaptive sampling (MCAS)

method that recast the sampling problem as a multi-objective optimization problem has been presented in Diez et al. (2015b). The MCAS uses a surrogate model and its prediction uncertainty to identify promising regions of the design space balancing out search for the optimum and improvement of surrogate model accuracy. The method has been extended to multidisciplinary problems in Volpi et al. (2017) combining surrogate model prediction uncertainty and MDA coupling uncertainty. The method has been found promising allowing for an efficient global approach to MDO. Generally, the adaptive sampling approach significantly affects the optimization efficiency and plays a critical role, especially for complex industrial applications.

Derivative-free global optimization

Although surrogate models are often used in solving MDO and, in general, complex SBDO, gradient-based optimization algorithms are not always employed. Algorithms' developments often require benchmark solutions which need to be achieved through a direct connection between optimization algorithms and simulation tools. Additionally, depending of the metamodeling technique, derivatives may not be always available. Efficient derivative-free algorithms are especially required when fine search regions are not known *a priori* and a global approach is used.

In the last decade, global derivative-free optimization research focused on metaheuristics. Methods as particle swarm optimization (PSO, Kennedy and Eberhart 1995) and ant colony optimization (ACO, Dorigo et al. 1996) have been extensively applied along with more recent algorithms such as firefly algorithm (FA, Yang 2010a), cuckoo search (CS, Yang and Deb 2009), and bat algorithm (BA, Yang 2010b). Given the stochastic nature of typical metaheuristics implementations, extensive numerical campaigns are needed to achieve statistically significant results. Since this approach is generally computationally unaffordable when using expensive solvers, deterministic versions of global derivative-free algorithms, such as deterministic PSO (DPSO, Serani et al. 2014), have been developed and applied in SBDO.

Efficient converge to the global optimum, possibly balancing global and local search, is highly problem dependent and still remains an open issue for all algorithms especially when solving new problems for which previous experience cannot be used.

Design space dimensionality reduction

Theory and mathematical derivation of dimensionality-reduction techniques is very limited, especially for continuous shape-design representation based on design variability analysis. Very few applications to simulation-based shape optimization of complex industrial problems by design-space dimensionality reduction are available from the literature. Generally, dimensionality reduction techniques can be classified as either on-line or off-line. On-line techniques requires the evaluation of the objective function or its gradient. They improve the optimization efficiency but do not give an assessment of the design space before the evaluation of the objective function. On the contrary, off-line methods provide the shape modification variability beforehand and assist the designer in the definition of design space and reduce dimensionality model.

Some recent research focused on design space variability and dimensionality reduction using the Karhunen–Loève expansion (KLE, also known as proper orthogonal decomposition). KLE has been used for representing distributed geometrical uncertainties and building a reduced-order spatial model for uncertainty quantification (Borzì et al. 2010, Schillings et al. 2011). An off-line quantitative approach based on KLE to assess the shape modification variability and build a reduced dimensionality global model of the design space is given in Diez et al. (2014), and used for metamodel-based high-fidelity optimization of a high-speed catamaran in Chen et al. (2015). The formulation is given in discrete form and relies on confidence levels for the geometric variance. A continuum description of the method is given in Diez et al. (2015a). Diez et al. (2016b) extended the method including physics-based information in the dimensionality reduction process; distributed shape modification and distributed/concentrated physical parameters obtained with a low-fidelity solver are combined into the formulation, which is still off-line with respect to the higher-fidelity function evaluations used in the optimization. Recently, nonlinear methods have been applied to design space dimensionality reduction in the SBDO context. For instance, D'Agostino et al. (2018a, 2018b) and Serani et al. (2018) propose kernel and local principal component analysis and deep autoencoders (DAE) as nonlinear extension of KLE.

The tradeoff between using shape-based methods (computationally very efficient, but possibly not accurate) and combined shape- and physics-based methods (more

accurate, but computationally expensive) is still an open issue that need to be addressed carefully, depending on the application, the design space, and the physical phenomena involved.

Hydro-structural analysis and optimization in naval engineering

Naval engineering research on hydro-structural dynamics has been moving from employing semi-analytical and low-fidelity methodologies to using high-fidelity numerical solvers such as RANS-based CFD and FE.

Numerical investigations of FSI mainly focuses on appendages and propeller blades (for instance, Ducoin and Young 2013, Kumar and Wurm 2015) and ship slamming (for instance, Oberhagemann et al. 2009, Paik et al. 2009, Stenius et al. 2011, Piro and Maki 2013). Volpi et al. (2015b, 2016, 2017b) show composite material bottom panel slamming of a fast planing hull. These studies use unsteady tightly coupled FSI simulations, based on CFD and FE, aiming at validation against full scale experimental data in real sea conditions, with associated large uncertainty, achieving reasonable agreement. The same FSI approach to fast craft slamming is used by Weil et al. (2018) that obtain error and uncertainty reduction with respect to earlier studies by validation using laboratory experiments in model scale.

Examples of CFD-based hydrodynamic optimization methodologies and results may be found for surface ships (Duvigneau and Visonneau 2004), appendages, energy saving devices, and propellers. Kandasamy et al. (2013), Chen et al. (2015), and Diez et al. (2015a) present shape optimization of a high-speed catamaran. The same application is studied by Diez et al. (2013) and Tahara et al. (2014) that perform stochastic optimization. The shape optimization of a tapered NACA 0009 hydrofoil is presented in Garg et al. (2015).

For naval hydro-structural optimization using high-fidelity solvers, a limited literature is available. Garg et al. (2017) extends the hydrofoil analysis to shape MDO comparing single- and multi-point optimizations in order to address off design conditions. Single- and multi-disciplinary optimization of industrial applications by high-fidelity solvers is still limited and represents a computational challenge.

Shortcomings of earlier research

Most MDO applications use gradient-based optimization which requires gradient approximations or adjoint solvers. For instance, Garg et al. (2017), in studying the same application considered in the current research, but limited to metal hydrofoils, use the adjoint method for both the CFD and the FE solvers, effectively supporting the use of gradient-based optimization. Although this approach is generally efficient, it can be applied only when source code and/or state variables from the discipline solvers are accessible. This leads to a significantly difficult integration of black-box solvers such as well-assessed high-fidelity software. When this type of comprehensive codes cannot be used, the application of MDO to complex industrial problems is limited by the capabilities of in-house analysis tools. Also, gradient-based optimization is usually applied in a local fashion, limiting the use of a global approach to optimization.

MDO efficiency, especially when using surrogate models, is strongly affected by the number of design variables, often referred to as the "curse of dimensionality," which is a practical constraint designers have to deal with that limits the exploration of original designs.

Objective

The objective of the present work is the development and assessment of a surrogate-based MDO architecture performing global derivative-free optimization and characterized by software modularity, allowing for the use of pre-existing specialized (high-fidelity) discipline solvers. In the present formulation, the multidisciplinary problem is FSI which is evaluated using expensive black-box solvers. The architecture is applied to the design of a composite material naval structure aiming at improving the hydrodynamic performance. The final design will feature optimized shape and optimized composite material layout.

Approach

The novel MDO architecture is called multi-criterion adaptive sampling MDO (MCAS-MDO). The identification of the optimal design is achieved by sequential surrogate-based optimizations. At the beginning of the process, the surrogate model is trained by MDA evaluations whose distribution in the design space is given by *a priori* sampling technique. Successive iterations are driven by the multidisciplinary MCAS which

balance out objective function value, surrogate model uncertainty, and MDA coupling uncertainty. As the optimization advances, MCAS yields refinements of the multidisciplinary consistency and further exploration of the design space. The full multidisciplinary consistency is achieved at the end of the optimization process; however, it is guaranteed at some extent at each iteration. The efficiency of the process is enhanced using an off-line design space dimensionality reduction by KLE based on purely geometrical considerations and combining distributed and concentrated parameters. The KLE uses a free-form deformation (FFD, Sederberg and Parry 1986) method to generate the shape modifications. MCAS-MDO performance is evaluated on analytical test problems by comparison with derivative-free MDF.

The application is the design of a NACA 0009 hydrofoil in composite material. The structure is made of a sandwich panel with layers of carbon fiber reinforced plastic (CFRP) and a foam core. For comparison purposes, the optimization is carried out also for a geometrically equivalent hydrofoil model made in aluminum. A steady partitioned two-way coupled FSI evaluates the hydro-structural behavior by Gauss-Seidl iterations. The associated coupling uncertainty is quantified by the difference between MDA iterations. The surrogate model is based on DRBF, which gives both the function prediction and its uncertainty. A multi-objective DPSO is embedded into the MCAS to handle the sampling by providing the optimum of the surrogate model and new infill points.

Preliminary hydrodynamic, structural, and FSI studies for the NACA 0009 hydrofoil in stainless steel, aluminum, and two CFRP models allow performing validation and verification of the computational grids and assessing the hydro-structural behavior of different materials.

CHAPTER 2: NUMERICAL METHODS

Hydrodynamics

The unsteady RANS (URANS) and the detached eddy simulation equations (DES) are used to model the hydrodynamics. The equations are solved numerically using the CFD code CFDShip-Iowa V4.5, developed at the University of Iowa (Huang et al. 2008). The set of governing equations for a fluid includes conservation of mass, i.e. continuity, and conservation of momentum (RANS equations).

$$\nabla \cdot \mathbf{u} = 0 \tag{1}$$

$$\frac{\partial \mathbf{u}}{\partial t} + \mathbf{u} \cdot \nabla \mathbf{u} = -\nabla p + \nabla \cdot \left[\frac{1}{\mathrm{Re}_{eff}} (\nabla \mathbf{u} + \nabla \mathbf{u}^{\mathrm{T}}) \right] + \mathbf{s} \tag{2}$$

u is the velocity vector, **s** is source term that accounts for the body force, p is the non-dimensional piezometric pressure defined as

$$p = \frac{p_{abs}}{\rho U_0^2} + \frac{z}{\mathrm{Fr}^2} + \frac{2k}{3} \tag{3}$$

The effective Reynolds number and Froude number are

$$\mathrm{Re}_{eff} = \frac{U_0 L}{\nu + \nu_t} \qquad \mathrm{Fr} = \frac{U_0}{\sqrt{gL}} \tag{4}$$

The turbulence is modeled by the isotropic Menter's blended *k-ω/k-ε* model or the anisotropic algebraic Reynolds stress (ARS). The ARS model is based on a modified version of the Menter's approach which is used as the scale determining model; an explicit algebraic Reynolds stress model is introduced as constitutive relation in place of the Boussinesq hypothesis. The ARS model is also extended to ARS-DES. The approach modifies the dissipative term of the transport equation of the turbulent kinetic energy *k* and determines where a large eddy simulation (LES) or URANS will be applied. Inside the boundary layer of a wall or inside a region where no separation occurs, the URANS is used. When the flow separates, vortices generate a significant increase of *k* and LES is used. *k* is computed using a blended *k-ω/k-ε* model as per

$$\frac{\partial k}{\partial t} + (\mathbf{u} - \sigma_k \nabla \nu_t) \cdot \nabla k - \frac{1}{P_k} \nabla^2 k + s_k = 0 \tag{5}$$

$$\frac{\partial \omega}{\partial t} + (\mathbf{u} - \sigma_\omega \nabla \nu_t) \cdot \nabla \omega - \frac{1}{P_\omega} \nabla^2 \omega + s_\omega = 0 \tag{6}$$

where ω is the specific dissipation rate, σ_k and σ_ω are constants, and $\nu_t = k/\omega$ is the turbulent viscosity. The source terms are defined as

$$s_k = R_k(-G + \beta^* \omega k) \tag{7}$$

$$s_\omega = R_\omega \left[-\gamma \frac{\omega}{k} G + \beta \omega^2 + 2(1 - F_1)\sigma_{\omega 2} \frac{1}{\omega} \frac{\partial k}{\partial x_j} \frac{\partial \omega}{\partial x_j} \right] \tag{8}$$

β, β^*, and $\sigma_{\omega 2}$ are constants and G is

$$\begin{aligned} G = \tau_{ij} \frac{\partial u_i}{\partial x_j} = \nu_t \left[(u_y + v_x)^2 + (u_z + w_x)^2 + (v_z + w_y)^2 \right] \\ + \nu_t \left[2u_x^2 + 2v_y^2 + 2w_z^2 \right] \end{aligned} \tag{9}$$

F_1 is a blending function designed to take advantage of the strength of either the *k*-ω or *k*-ε model in different positions of the space. To accomplish this, F_1 is equal to the unit in the sub-layer and logarithmic regions of boundary layers and gradually switches to zero in the wake region. Each model constant a_i is calculated from the standard *k*-ω and *k*-ε values using the blending function

$$a_i = F_1 a_{i,k-\omega} + (1 - F_1) a_{i,k-\varepsilon} \tag{10}$$

DES based on the *k*-ω/*k*-ε turbulence model is used to model regions of massively separated flows. The dissipative term of the *k*-transport equation is modified as

$$D_{RANS}^k = \rho \beta^* k \omega = \frac{\rho k^{\frac{3}{2}}}{l_{k-\omega}} \quad \text{and} \quad D_{DES}^k = \frac{\rho k^{\frac{3}{2}}}{\tilde{l}} \tag{11}$$

where the length scale is chosen from the length scale of the *k*-ω model and the characteristic grid size Δ as $\tilde{l} = \min(l_{k-\omega}, C_{DES}\Delta)$, with $l_{k-\omega} = k^{\frac{1}{2}}/(\beta^* \omega)$ and C_{DES} = 0.65.

The numerical solution strategy employed by CFDShip-Iowa V4.5 is depicted in the block diagram of Figure 4 including the fully implicit predictor-corrector methods used

for determining the motions in case of moving structure simulation (air/marine vehicles) and semi-coupled air/water method for free surface applications.

Finite difference schemes are used on body-fitted curvilinear grids to discretize the continuum equations with second order implicit Euler backward difference time integration. The convective velocities are linearized when solving the momentum equations, but are changed within the nonlinear iteration loop to account for nonlinearities from turbulence equations, nonlinear momentum transport, etc. The spatial discretization of the convection terms uses a second-order upwind scheme. The diffusion and pressure terms in the momentum equations are discretized using a second order central scheme. The temporal and spatial discretizations for the $k-\omega/k-\varepsilon$ equations are consistent with the momentum equations. Finally, the projection algorithm is used to couple the momentum and continuity equations. Details of numerical methods can be found in Huang et al. (2008).

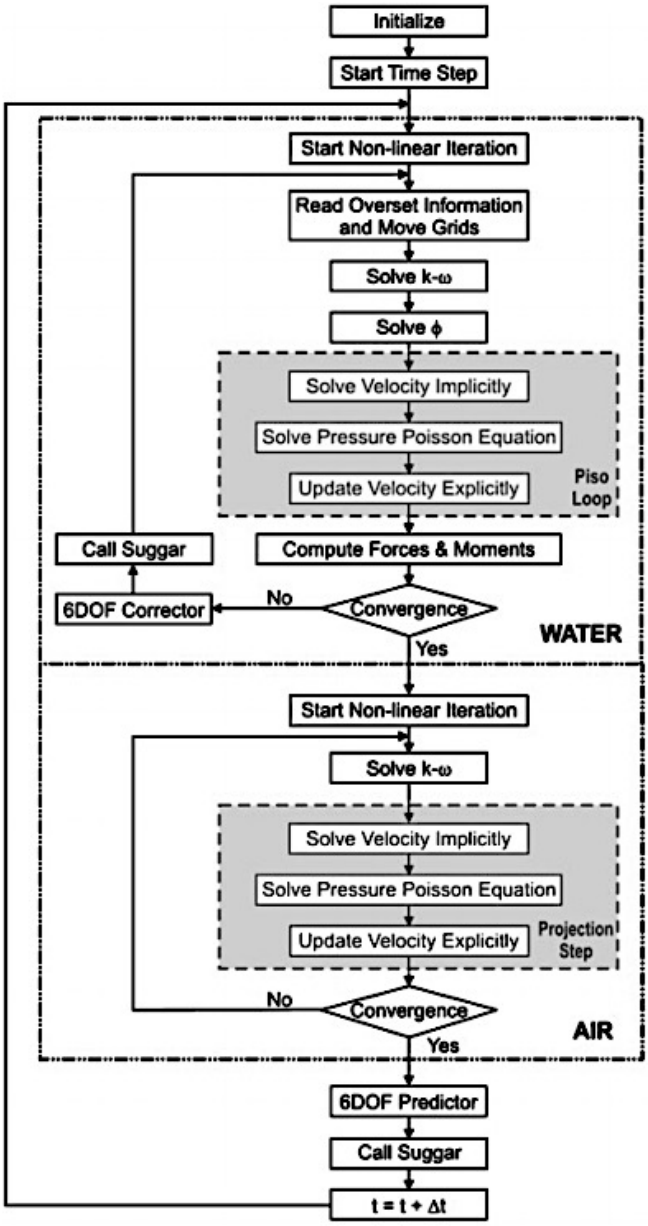

Figure 4: CFDShip-Iowa solution strategy diagram (Huang et al. 2008)

Structural dynamics

Modal analysis

The modal analysis aims at identifying the natural modes of vibration of the structure and the associated natural frequencies. A finite number of modes of interest may be determined numerically using FE. Herein, the commercial code ANSYS Mechanical APDL V14.5 is used.

The structure equation of motion is

$$\rho(\mathbf{x})\ddot{\boldsymbol{\delta}}(\mathbf{x},t) + C\dot{\boldsymbol{\delta}}(\mathbf{x},t) + \mathcal{L}\boldsymbol{\delta}(\mathbf{x},t) = \mathbf{f}(\mathbf{x},t) \tag{12}$$

where ρ is the density, $\boldsymbol{\delta}$ is the displacement vector, $\mathbf{x}$ is the position vector, t is time, C is the damping operator, $\mathcal{L}$ is the structural operator, and $\mathbf{f}$ is the load source term. Assume that there are no forces acting on the structure. If the structure vibrates with harmonic motion, the shape of vibrating structure is the natural mode of vibration and the corresponding frequency is the natural frequency. The natural modes $\boldsymbol{\varphi}_i$, or eigenfunctions of the operator $\mathcal{L}$, are solution of the eigenproblem

$$\mathcal{L}\boldsymbol{\varphi}_i = \lambda_i \boldsymbol{\varphi}_i \tag{13}$$

where λ_i are the eigenvalues and are associated with the natural frequencies ω_i.

By discretization using FE, Eq. 12 becomes

$$\mathbf{M}\ddot{\boldsymbol{\delta}} + \mathbf{C}\dot{\boldsymbol{\delta}} + \mathbf{K}\boldsymbol{\delta} = \mathbf{F} \tag{14}$$

where $\mathbf{M}$, $\mathbf{C}$, and $\mathbf{K}$ are mass, damping and stiffness matrices, respectively, whereas $\mathbf{F}$ is the load matrix. ANSYS is used to predict $\boldsymbol{\varphi}_i$ and ω_i by solving the un-damped homogeneous governing equations

$$\mathbf{M}\ddot{\boldsymbol{\delta}} + \mathbf{K}\boldsymbol{\delta} = \mathbf{0} \tag{15}$$

derived from Eq. 12. The solution is obtained using the discretized eigenvalue problem

$$(-\omega_i^2\mathbf{M} + \mathbf{K})\boldsymbol{\varphi}_i = \mathbf{0} \tag{16}$$

The results of the analysis are $\boldsymbol{\varphi}_i$ and ω_i of the structure in vacuum, which are called *dry* modes. The identification of the *wet* modes, which are the natural frequencies and mode shapes of the structure when immersed in a medium, can be performed in

ANSYS by embedding the body in a fluid domain modeled by acoustic elements. The presence of the fluid is represented using an additional damping term in Eq. 15. The acoustic domain accounts for the added mass effects due to the presence of a fluid.

Static analysis

A static analysis quantifies the effects of steady loading conditions on a structure without considering inertia and damping effects. The governing equation, derived from Eq. 12, is

$$\mathcal{L}\boldsymbol{\delta}(\mathbf{x}) = \mathbf{f}(\mathbf{x}) \tag{17}$$

According to Eq. 17, the discretized FE equation solved by ANSYS for a static analysis is

$$\mathbf{K}\boldsymbol{\delta} = \mathbf{F} \tag{18}$$

Fluid-structure interaction

In multidisciplinary environments, such as FSI problems that employ partitioned approaches, discipline solvers need to be coupled aiming at a proper representation of the multidisciplinary physics. The coupling can be performed using Gauss-Seidl iterations where the CFD analysis is carried out first until convergence and the CSD analysis uses the hydrodynamic load to compute the deformation.

Within a one-way FSI approach, structural displacements are not fed back into the fluid solver. Figure 5 depicts a diagram of the implementation of the one-way coupling using CFDShip-Iowa and ANSYS finite elements. Since fluid and structure grids are generally non-matching, an interpolation algorithm is required to transfer the hydrodynamic load to the structural model, i.e. calculating the term $\mathbf{f}$ in Eq. 12. Herein, Gaussian interpolation of the hydrodynamic load on the structural nodes is performed at each iteration. The method conserves energy and momentum only asymptotically, namely for time step and grid size tending to zero.

In a tightly coupled two-way approach, represented in Figure 6, fluid and structural solvers exchange hydrodynamic load $\mathbf{f}$ and structural displacement $\boldsymbol{\delta}$ and velocities $\dot{\boldsymbol{\delta}}$ until convergence, in an inner loop within each time step. Along with the interpolation of $\mathbf{f}$ onto the structure grid, the two-way approach requires also the deformation of the fluid grid

according to the structural displacement, within each time step. The grid deforms in a two-step process. The fluid volume grid is structured with indices *I*, *J*, and *K*, where $J = 1$ corresponds the fluid-solid interface. First, the $J = 1$ surface is deformed by interpolation from the structure grid. Then, the volume inner nodes are morphed by linear interpolation between interface ($J = 1$) and outer ($J = J_{MAX}$) boundary layer surface as

$$\mathbf{x} = \mathbf{x}_0 + \frac{l^* - l}{l^*}\boldsymbol{\delta}_{int} \tag{19}$$

where $\mathbf{x}_0$ is the original coordinate of the node, $\mathbf{x}$ is the modified position, $\boldsymbol{\delta}_{\text{int}}$ is the displacement at the interface, l is the distance between the volume node and the interface node, and l^* is the distance between outer and interface node; l and l^* are computed as girth length along the grid line with constant *I* and *K*.

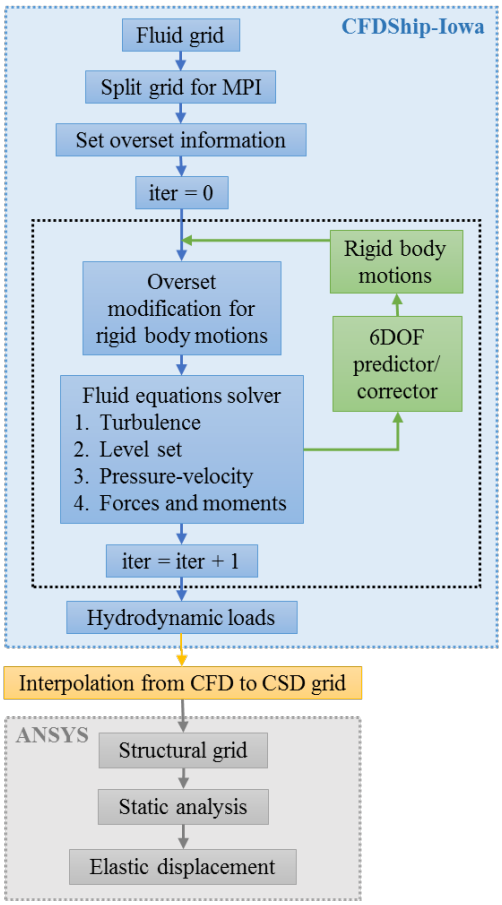

Figure 5: Diagram of the one-way FSI routine using CFDShip-Iowa and ANSYS

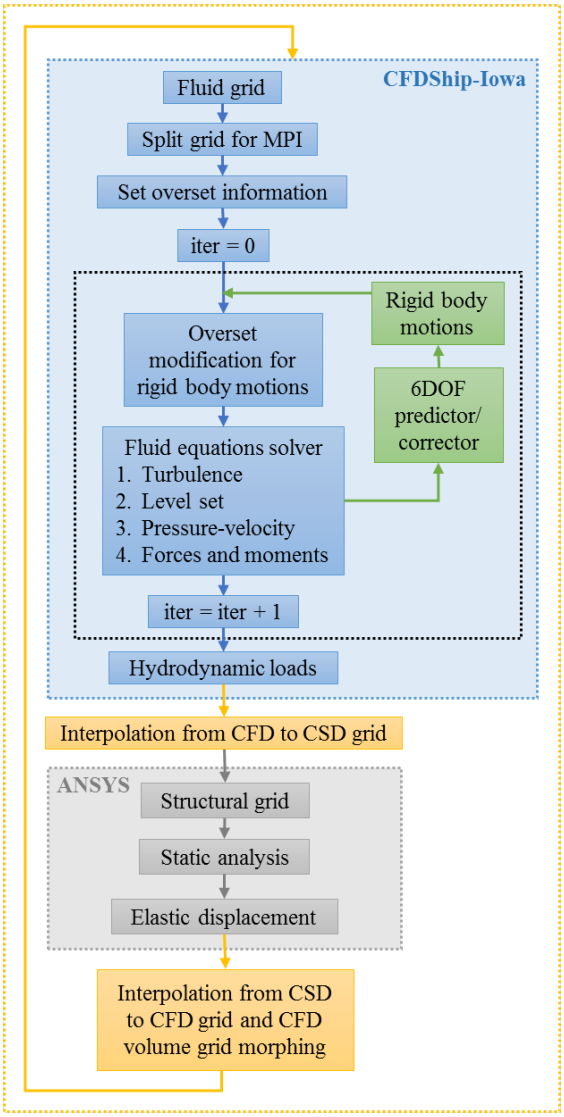

Figure 6: Diagram of the two-way FSI routine using CFDShip-Iowa and ANSYS

Multidisciplinary design optimization

This section provides detailed descriptions of the methods used in the MCAS-MDO framework starting from the problem formulation and including architecture, surrogate model, sampling approach, optimization algorithm, shape modification, and dimensionality reduction.

Formulation

The formulation of the multidisciplinary design optimization problem involving fluid dynamics and structural mechanics is

$$\min_{\mathbf{u}} f[\mathbf{u}, \mathbf{y}(\mathbf{u}, \mathbf{y})] \tag{20}$$

$$\text{subject to} \quad \mathbf{c}_0[\mathbf{u}, \mathbf{y}(\mathbf{u}, \mathbf{y})] \leq 0 \tag{21}$$

$$\mathbf{c}_F[\mathbf{u}_0, \mathbf{u}_F, \mathbf{y}_F(\mathbf{u}_0, \mathbf{u}_F, \mathbf{y}_S)] \leq 0 \tag{22}$$

$$\mathbf{c}_S[\mathbf{u}_0, \mathbf{u}_S, \mathbf{y}_S(\mathbf{u}_0, \mathbf{u}_S, \mathbf{y}_F)] \leq 0 \tag{23}$$

where f is the objective function, $\mathbf{c}$ are the constraint functions, $\mathbf{u}$ is the set of design variables, and $\mathbf{y}$ is the set of coupling variables, i.e. the responses of the discipline analyses to the specific design. The subscript $(\cdot)_0$ denotes a variable/function shared by the disciplines; the subscript $(\cdot)_F$ denotes that the variable/function pertains exclusively to the fluid analysis, while the subscript $(\cdot)_S$ refers to the structural analysis. The number of constraints is $N_c = N_{c0} + N_{cF} + N_{cS}$. This formulation resembles a general non-linear programming problem.

To employ a global derivative-free optimization algorithm, the constrained optimization problem in Eq. 20 to 23 is recast as unconstrained optimization. The inequality constraints $\mathbf{c}$ are integrated in a new penalized objective function f_p as linear penalty functions weighted by the coefficient γ:

$$\min_{\mathbf{u}} f_p[\mathbf{u}, \mathbf{y}(\mathbf{u}, \mathbf{y})] \tag{24}$$

$$f_p[\mathbf{u}, \mathbf{y}(\mathbf{u}, \mathbf{y})] = f[\mathbf{u}, \mathbf{y}(\mathbf{u}, \mathbf{y})] + \gamma \sum_{i=1}^{N_{c0}} \max\{\mathbf{c}_0[\mathbf{u}, \mathbf{y}(\mathbf{u}, \mathbf{y})], 0\} \tag{25}$$

$$+\gamma \sum_{i=1}^{N_{cF}} \max\{\mathbf{c}_F[\mathbf{u}_0, \mathbf{u}_F, \mathbf{y}_F(\mathbf{u}_0, \mathbf{u}_F, \mathbf{y}_S)], 0\}$$

$$+\gamma \sum_{i=1}^{N_{cS}} \max\{\mathbf{c}_S[\mathbf{u}_0, \mathbf{u}_S, \mathbf{y}_S(\mathbf{u}_0, \mathbf{u}_S, \mathbf{y}_F)], 0\}$$

Architecture

The framework of MCAS-MDO is monolithic, solving a single optimization problem at the system level. The surrogate model is built over the entire design space allowing for the use of a global optimization algorithm. The MCAS produces iteratively sets of new samples to enrich the surrogate model training set. The samples are evaluated by the MDA tool with a loose coupling approach. The design space is explored by infill of new samples. As the optimization advances, the accuracy of the surrogate is increased by tightening the coupling in the MDA at available training points located in promising regions of the design space. Figure 7 depicts a standard approach to MDO in the form of a MDF architecture. The optimizer handles the procedure by calling directly the MDA tool and using the objective/constraint function values to locate the optimum. Figure 8 depicts the MCAS-MDO, where the adaptive sampling calls the MDA tool and drives the sequential optimizations based on the surrogate model of the objective/constraint functions.

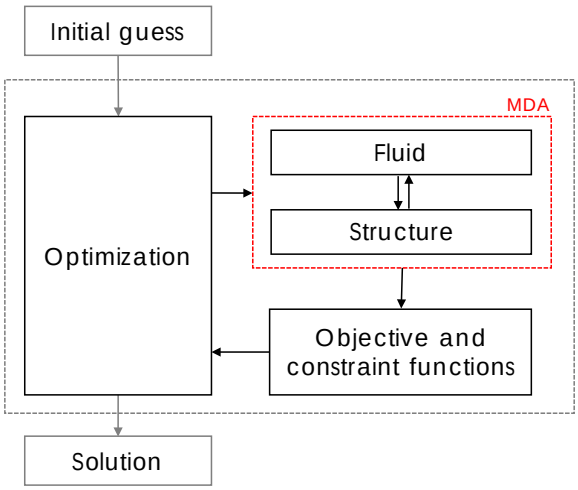

Figure 7: MDF architecture

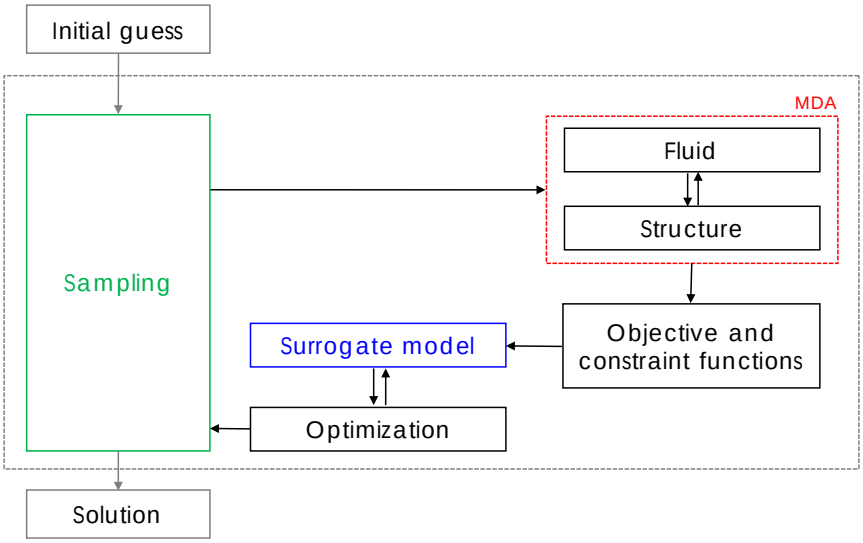

Figure 8: MCAS-MDO architecture

As follows, a general form of the algorithm, introducing the nomenclature adopted, is presented.

1. Apply a (non-adaptive) sampling technique over the design space. The training set obtained is indicated by $\{\mathbf{u}_i^{train}\}_{i=1}^{M}$.
2. Perform a loosely-coupled MDA at $\{\mathbf{u}_i^{train}\}_{i=1}^{M}$ to evaluate $\mathbf{y}$.
3. Compute f and $\mathbf{c}$ based on $\mathbf{y}$ and assess their coupling uncertainties $U_{c,f}$ and $U_{c,c}$.
4. Compute f_p and its coupling uncertainty $U_c = \sqrt{U_{c,f}^2 + \sum_{i=1}^{N_c} U_{c,c_i}^2}$.
5. Initialize the optimum as the best solution among available training points. $\mathbf{u}^* = \text{argmin}\,\{f_p(\mathbf{u}_i^{train})\}_{i=1}^{M}$ and $f_p{}^* = \min\{f_p(\mathbf{u}_i^{train})\}_{i=1}^{M}$.
6. Build surrogate models trained by $\{\mathbf{u}_i^{train}\}_{i=1}^{M}$ for f and $\mathbf{c}$ and assess the surrogate model uncertainties $U_{s,f}$ and $\mathbf{U}_{s,c}$.
7. Compute the prediction $\widehat{f_p}$ based on the surrogate models and its uncertainty, from now on referred to as sampling uncertainty, $U_s = \sqrt{U_{s,f}^2 + \sum_{i=1}^{N_c} U_{s,c_i}^2}$.
8. Using $f_p(\mathbf{u}_i^{train})$, $U_c(\mathbf{u}_i^{train})$, $\widehat{f_p}(\mathbf{u})$, and $U_s(\mathbf{u})$, apply the adaptive sampling technique to find:

- a set of new samples $\{\mathbf{u}_i^{infill}\}_{i=1}^{I}$,
- a subset $\{\mathbf{u}_i^{train}\}_{i=1}^{C}$ of the training set whose function value accuracy is to be improved,
- the optimum predicted by the metamodel $\hat{\mathbf{u}}^*$.

9. If $\hat{\mathbf{u}}^* \neq \mathbf{u}_i^{train}$ for all i, evaluate f_p and U_c at $\hat{\mathbf{u}}^*$ following points 2, 3, and 4.
10. Evaluate f_p and U_c at $\{\mathbf{u}_i^{infill}\}_{i=1}^{I}$ following points 2, 3, and 4.
11. Iterate the MDA at $\{\mathbf{u}_i^{train}\}_{i=1}^{C}$ for new $\mathbf{y}$ with improved multidisciplinary consistency.
12. Compute f_p and U_c at $\{\mathbf{u}_i^{train}\}_{i=1}^{C}$ following points 3 and 4.
13. Update the optimum $\mathbf{u}^*$ if any f_p at $\hat{\mathbf{u}}^*$, $\{\mathbf{u}_i^{infill}\}_{i=1}^{I}$, or $\{\mathbf{u}_i^{train}\}_{i=1}^{C}$ improves the current solution.
14. Update the training set:
    -
    - the I new infill points are added, therefore the training set size increases from the current M to $M + I$,
    - the function values and uncertainties at the C training points are updated.
15. Repeat step 6 to 14 until convergence of $\mathbf{u}^*$

As described, the methodology does not prescribe a fixed number of disciplines nor it imposes the use of specific MDA, surrogate, or sampling/optimization techniques. The choice of them depend on the application at hand and can be tailored to take advantage of software already available to the designer. Herein, the Hammersley Sequence Sampling (HSS) is used as non-adaptive sampling method, the DRBF is used as surrogate model, the MCAS is used as adaptive sampling technique, and DPSO is the optimization algorithm.

Dynamic radial basis functions

Given a set of M training points $\{\mathbf{u}_i^{train}\}_{i=1}^{M}$ with associated function evaluations $\mathbf{f}^{train} = \{f_i^{train}\}_{i=1}^{M}$, a linear combination of RBF provides the prediction of the objective function as

$$\hat{f}_{RBF}(\mathbf{u},\varepsilon)=\sum_{i=1}^{M} w_i \psi\left(\left\|\mathbf{u}-\mathbf{u}_i^{train}\right\|,\varepsilon\right) \tag{26}$$

where ψ is the RBF kernel, $\varepsilon \in \mathbb{R}$ is the tuning parameter of the specific kernel, and $\mathbf{w}=\{w_i\}_{i=1}^{M}$ is solution of the linear system that provides exact prediction at $\mathbf{u}=\mathbf{u}_i^{train}$

$$\mathbf{A}\mathbf{w}=\mathbf{f}^{train} \tag{27}$$

with $a_{ij}=\psi\left(\left\|\mathbf{u}_i^{train}-\mathbf{u}_j^{train}\right\|,\varepsilon\right)$.

The DRBF model provides the prediction of the function $\hat{f}(\mathbf{u})$ as the expected value of a sample of RBF predictions $\hat{f}_{RBF}(\mathbf{u},\varepsilon_k)$ over a stochastic distribution of ε_k as

$$\hat{f}(\mathbf{u})=\mathrm{EV}\left[\hat{f}_{RBF}(\mathbf{u},\varepsilon_k)\right] \tag{28}$$

with $\{\varepsilon_k\}_{k=1}^{N_\varepsilon}$ uniformly distributed between ε_{min} and ε_{max}.

Sampling and coupling uncertainty quantification

The sampling uncertainty $U_s(\mathbf{u})$, is quantified by the 95% confident band of $\hat{f}_{RBF}(\mathbf{u},\varepsilon_k)$. It is defined over the entire design space.

The coupling uncertainty $U_c(\mathbf{u})$ does not depend on the surrogate model but stems from not satisfying the multidisciplinary equilibrium. U_c decreases as the discipline interaction tightens, i.e. as the mutual exchange of structural and fluid solutions approaches convergence. The accuracy of a loose multidisciplinary solution generally depends on the specific design. Stiffer structures may show little difference in the MDA solution between a loose and a tight coupling. On the opposite, compliant structures may show significant coupling effects and difference between loose and tight coupling. Herein, U_c is quantified as the difference in objective function between two consecutive MDA iterations. U_c exists only at the training points where the MDA is solved.

Multi-criterion adaptive sampling

MCAS aims at balancing search for the global minimizer and surrogate model accuracy. In case of single-discipline optimization, this is pursued by solving the multi-objective optimization problem:

$$\min_{\mathbf{u}} \hat{f}_p(\mathbf{u}) \quad \text{and} \quad \min_{\mathbf{u}} U(\mathbf{u}) \tag{29}$$

where U is the surrogate model uncertainty U_s. The Pareto set $\wp$ with size $N_\wp$ obtained from solving Eq. 29 is down-sampled to identify I equally spaced points along the curvilinear coordinate. A one-dimensional example is given in Figure 9. On the left, the surrogate model prediction and its uncertainty band are depicted showing the zero-valued U_s at the training points. On the right, the solution of Eq. 29 is presented in the $\hat{f}$-U space showing the selection of infill points along the Pareto frontier.

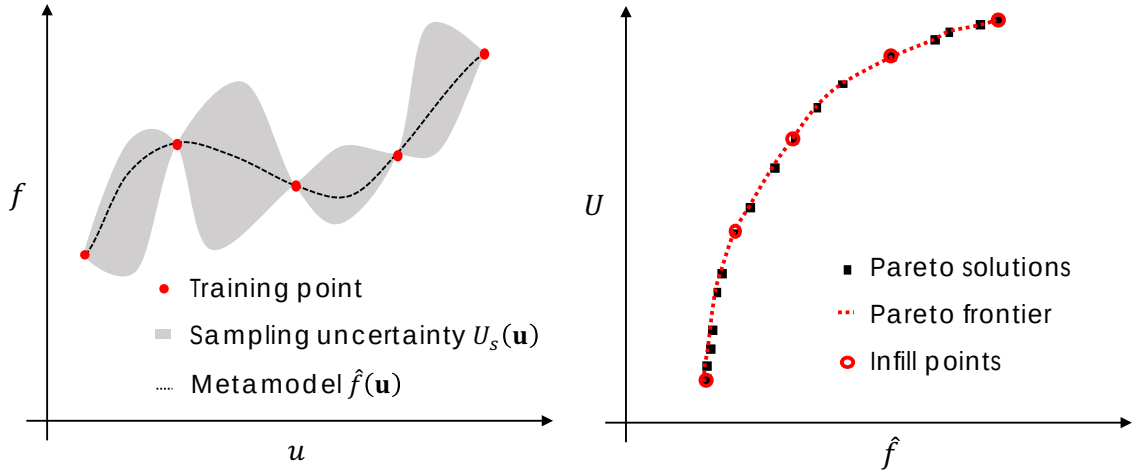

Figure 9: Single-discipline MCAS

In view of the fact that: (a) sampling too close to available training points does not add useful information to the analysis, (b) as the distance between training points decreases, Eq. 27 may result ill-conditioned, and (c) the uncertainty at the training points is zero, $\wp$ is reduced to eliminate points with U smaller than a user-defined $u_{\min}$ threshold.

Since $\wp$ may have a strongly irregular distribution, the down-sampling procedure requires careful application. To tackle this task, the following algorithm is proposed:

1. $\wp$ points are ordered with increasing $\hat{f}$.
2. The position $\{\xi_i\}_{i=1}^{N_\wp}$ of the $\wp$ points, defined initially by $\{(\hat{f}_i, U_i)\}_{i=1}^{N_\wp}$, along the curvilinear coordinate representing the Pareto frontier is computed. The total length $l_\wp$ of $\wp$ is also evaluated.

3. The position of I^* equally spaced samples χ_j is determined along ξ; the ideal distance between χ_j and χ_{j+1} is $d = l_{\wp}/(N_{\wp} - 1)$. I^* is set equal to I at the beginning of the procedure.
4. The distance $D_{i,j}$ between each ξ_i and each χ_j is computed
5. The I^* $\wp$ points $\widetilde{\xi}_\iota$ closest to the χ_j ideal sample locations (i.e. the locations with minimum $D_{i,j}$) are identified.
6. If $D_{i,j} \geq d/2$ at any $\widetilde{\xi}_\iota$, I^* is increased by 1 and the process is repeated from step 3.
7. If $D_{i,j} < d/2$ at all $\widetilde{\xi}_\iota$, then $\widetilde{\xi}_\iota$ are ordered with increasing $D_{i,j}$.
8. The first I $\widetilde{\xi}_\iota$ with minimum $D_{i,j}$ are selected as new infill points.

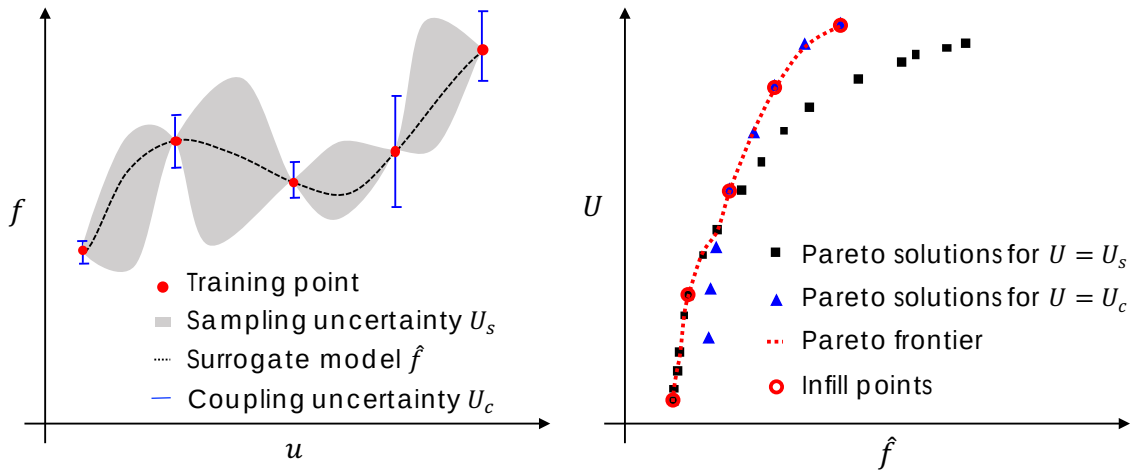

Figure 10: Multidisciplinary MCAS

In case of multidisciplinary problems, the adaptive sampling technique accounts for both U_s and U_c. Two independent Pareto fronts, $\wp_s$ and $\wp_c$, are built, according to Eq. 29, using $U = U_s$ and $U = U_c$. An illustrative example for a one-dimensional problem is depicted in Figure 10. The two sets (black squares for $\wp_s$, blue triangles for $\wp_c$) are superposed in the objective function space and a new Pareto set $\wp$ is defined taking the non-dominated solutions in the sample $\wp_s \cup \wp_c$. $\wp$ is then treated as described above for the single-discipline MCAS keeping track of the original Pareto set of each point. If a sample originally belonged to $\wp_s$, it contributes to the set of new infill points $\left\{\mathbf{u}_i^{infill}\right\}_{i=1}^{I}$.

Otherwise, if it belonged to $\wp_c$, it contributes to $\{\mathbf{u}_i^{train}\}_{i=1}^{C}$, where the MDA is to be iterated.

In order to improve the numerical stability in solving Eq. 27 and the efficiency in the search of the optimum, two additional sampling criteria are applied to $\wp$ before down-sampling: a threshold for the minimum distance among potential infill samples Δ_{min} to prevents oversampling, and a threshold for the maximum function value $\hat{f} < \hat{f}^* + \sqrt{U_s^2 + U_s^{*2}}$, where $(\cdot)^*$ indicates the current optimum predicted, to prevent sampling in regions with large objective function values.

Deterministic particle swarm optimization

In order to make PSO more efficient for its use within SBDO, a deterministic version of the algorithm (DPSO) was formulated by Campana et al. (2009) as follows

$$\begin{cases} \mathbf{v}_i^{k+1} = c_0\left[\mathbf{v}_i^k + c_1\left(\mathbf{u}_{i,pb} - \mathbf{u}_i^k\right) + c_2\left(\mathbf{u}_{gb} - \mathbf{u}_i^k\right)\right] \\ \mathbf{u}_i^{k+1} = \mathbf{u}_i^k + \mathbf{v}_i^{k+1} \end{cases} \tag{30}$$

The system gives velocity $\mathbf{v}$ and position $\mathbf{u}$ of the i^{th} particle at the k^{th} iteration. Particles are attracted by the personal best position $\mathbf{u}_{i,pb}$ ever found by the i^{th} particle, and by the global best position $\mathbf{u}_{gb}$ ever found by all particles. The effectiveness of DPSO depends on the constriction factor c_0, the social and cognitive learning rate c_1 and c_2, along with the number of individuals N_p and their initial distribution and velocity. Serani et al. (2014) investigate the effect of such parameters and propose guidelines for an efficient use of the algorithm, in the context of ship hydrodynamic optimization. The extension of DPSO to multi-objective problems can be found for instance in Pellegrini et al. (2014). This is based on extending the definition of the personal and global best in the Pareto-optimality sense. Specifically, the personal attractor $\mathbf{u}_{i,pb}$ is the closest point to $\mathbf{u}_i$ of the personal Pareto front. The global attractor $\mathbf{u}_{i,gb}$ is different for each particle and defined as the closest point to $\mathbf{u}_i$ of the global Pareto front.

Shape modification: free-form deformation

The FFD is selected as shape modification technique similarly to Garg et al. (2015, 2017). FFD refers to the deformation of the space containing the body under investigation.

A trapezoidal prism that embeds the body defines the space. A coordinate system is assumed, with origin $\mathbf{x}_0$ at one of the prism vertices. Any point within the prism has s, t, and u coordinates such that

$$\mathbf{x} = \mathbf{x}_0 + s\hat{\mathbf{s}} + t\hat{\mathbf{t}} + u\hat{\mathbf{u}} \tag{31}$$

with s, t, and u bounded by [0,1] and given by

$$s = \frac{\hat{\mathbf{t}}\times\hat{\mathbf{u}}\cdot(\mathbf{x}-\mathbf{x}_0)}{\hat{\mathbf{t}}\times\hat{\mathbf{u}}\cdot\hat{\mathbf{s}}} \qquad t = \frac{\hat{\mathbf{s}}\times\hat{\mathbf{u}}\cdot(\mathbf{x}-\mathbf{x}_0)}{\hat{\mathbf{s}}\times\hat{\mathbf{u}}\cdot\hat{\mathbf{t}}} \qquad u = \frac{\hat{\mathbf{s}}\times\hat{\mathbf{t}}\cdot(\mathbf{x}-\mathbf{x}_0)}{\hat{\mathbf{s}}\times\hat{\mathbf{t}}\cdot\hat{\mathbf{u}}} \tag{32}$$

Control points are distributed over a grid, compliant with the trapezoidal space. The number of points assigned in the $\hat{\mathbf{s}}$, $\hat{\mathbf{t}}$, and $\hat{\mathbf{u}}$ directions are $l+1$, $m+1$, and $n+1$, respectively. The location of the ijk control point is given by

$$\mathbf{P}_{ijk} = \mathbf{x}_0 + \frac{i}{l}\hat{\mathbf{s}} + \frac{j}{m}\hat{\mathbf{t}} + \frac{k}{n}\hat{\mathbf{u}} \tag{33}$$

The shape modification is performed by moving the control points and interpolating the modification over the embedding space. The interpolation can be performed using different polynomial bases. Herein, a tensor product of trivariate Bernstein polynomial is used, following Sederberg and Parry (1986):

$$\mathbf{x}_{FFD} = \sum_{i=0}^{l}\binom{l}{i}(1-s)^{l-i}s^i\left[\sum_{i=0}^{m}\binom{m}{j}(1-t)^{m-j}t^j\left[\sum_{i=0}^{n}\binom{n}{k}(1-u)^{n-k}u^k\right]\right] \tag{34}$$

Design space analysis

In the shape optimization of a simple structure such as a three-dimensional hydrofoil, the choice of the design variables plays a key role. Potential design improvements significantly depend on dimension and extension of the design space: high dimension and variability spaces are more difficult and expensive to explore but, at the same time, potentially allow for larger improvements. A set of design variables that can be used is the one that includes standard modifications of a wing-type structure. An example may be span length, chord length, thickness to chord ratio, twist angle at multiple stations along the span, and swept angle. The resulting number of design variables is potentially low allowing for computationally efficient optimization. Shortcomings arise from the

stiffness of the method, which does not allow for truly original design. Another possible choice of design variables comes from continuous parametrizations of the domain. This allows for a much larger design variability but often requires a large number of design variables, even prohibitive when expensive black-box functions are used for the MDA and global derivative-free optimization is performed.

A dimensionality reduction technique is therefore applied in order to reduce the design space dimensionality for the shape optimization. The dimensionality reduction technique is based on the KLE and it is an off-line methodology. Once the tool for the geometry modification is chosen, with its associated design variables, the technique can be applied ahead of the optimization process based purely on geometrical considerations with no evaluation of objective function and sensitivities. The technique can be coupled with any geometry modification method. The dimensionality reduction is herein performed by application of the KLE on the geometry modifications given by FFD. A brief description of the KLE-based dimensionality reduction follows. A detailed analysis can be found in Diez et al. (2015a).

Consider a geometric domain G, which identifies the initial shape, and a set of coordinates $\mathbf{x} \in G$. Generally, $\mathbf{x} \in \mathbb{R}^n$ with n = 1, 2, 3. Assume that the design variable vector is $\mathbf{u} \in U$. $\mathbf{u} \in \mathbb{R}^M$ where M is the number of design variables. Let U be a stochastic space with associated probability density function $f(\mathbf{u})$.

Let $\boldsymbol{\delta}$ be the shape modification vector, i.e. a modification of the shape with respect to the initial one, corresponding to the design variable vector $\mathbf{u}$. $\boldsymbol{\delta} \in \mathbb{R}^m$ with m = 1, 2, 3 but not necessarily equal to n. $\boldsymbol{\delta}$ belongs to the vector space of all possible square-integrable modifications of the initial space. Since $\mathbf{u}$ belongs to a stochastic space, a mean shape modification can be defined by a generalized inner product

$$\langle \boldsymbol{\delta} \rangle = \int_U \rho(\mathbf{x}) \boldsymbol{\delta}(\mathbf{x}, \mathbf{u}) f(\mathbf{u}) \, d\mathbf{u} \tag{35}$$

where $\rho(\mathbf{x})$ is a weight function. $\langle \cdot \rangle$ represents an ensemble average over $\mathbf{u} \in U$. Accordingly, the variance of the shape modification vector, which will be referred to as geometric variance, is defined as

$$\sigma^2 = \langle \|\boldsymbol{\delta}\|^2 \rangle = \int_U \int_G \rho(\mathbf{x}) \hat{\boldsymbol{\delta}}(\mathbf{x},\mathbf{u}) \cdot \hat{\boldsymbol{\delta}}(\mathbf{x},\mathbf{u}) f(\mathbf{u})\, d\mathbf{x}\, d\mathbf{u} \tag{36}$$

where $\hat{\boldsymbol{\delta}} = \boldsymbol{\delta} - \langle \boldsymbol{\delta} \rangle$ is the deviation from the mean shape modification vector.

The application of the KLE to the geometry modification aims at identifying an optimal basis of orthonormal functions $\boldsymbol{\varphi}_k$ for a linear representation of $\hat{\boldsymbol{\delta}}$

$$\hat{\boldsymbol{\delta}}(\mathbf{x},\mathbf{u}) = \sum_{k=1}^{\infty} \alpha_k(\mathbf{u}) \boldsymbol{\varphi}_k(\mathbf{x}) \tag{37}$$

The original design variables $\mathbf{u}$ can therefore be substituted by the basis-function components α_k, which are given by

$$\alpha_k(\mathbf{x}) = \left(\hat{\boldsymbol{\delta}}, \boldsymbol{\varphi}_k\right)_\rho = \int_G \rho(\mathbf{x}) \hat{\boldsymbol{\delta}}(\mathbf{x},\mathbf{u}) \cdot \boldsymbol{\varphi}_k(\mathbf{x})\, d\mathbf{x} \tag{38}$$

The geometric variance of the KLE vector space of the modifications is obtained by substituting Eq. 37 and 38 in Eq. 36

$$\sigma^2 = \sum_{k=1}^{\infty} \sum_{j=1}^{\infty} \langle \alpha_k \alpha_j \rangle \left(\boldsymbol{\varphi}_k, \boldsymbol{\varphi}_j\right)_\rho = \sum_{j=1}^{\infty} \langle \alpha_j^2 \rangle = \sum_{j=1}^{\infty} \langle \left(\hat{\boldsymbol{\delta}}, \boldsymbol{\varphi}_j\right)_\rho^2 \rangle \tag{39}$$

The basis retaining the maximum variance is formed by those $\boldsymbol{\varphi}$ solutions of the variational problem

$$\begin{aligned} &\max \; J(\boldsymbol{\varphi}) = \langle \left(\hat{\boldsymbol{\delta}}, \boldsymbol{\varphi}\right)_\rho^2 \rangle \\ &\text{subject to} \qquad (\boldsymbol{\varphi}, \boldsymbol{\varphi})^2 = 1 \end{aligned} \tag{40}$$

which yields to

$$\int_G \rho(\mathbf{y}) \langle \hat{\boldsymbol{\delta}}(\mathbf{x},\mathbf{u}) \otimes \hat{\boldsymbol{\delta}}(\mathbf{y},\mathbf{u}) \rangle \boldsymbol{\varphi}(\mathbf{y})\, d\mathbf{y} = \lambda \boldsymbol{\varphi}(\mathbf{x}) \tag{41}$$

Eq. 41 is an eigenproblem. The eigenfunctions $\{\boldsymbol{\varphi}_k\}_{k=1}^{\infty}$, also referred to as KL modes, are orthogonal and form a complete basis. The eigenvalues λ_k, also referred to as KL values, represent the variance retained by the associated basis function $\boldsymbol{\varphi}_k$ through its component α_k. It may be proven that

$$\sigma^2 = \sum_{k=1}^{\infty} \lambda_k \tag{42}$$

The reduced dimensionality space is built on the KL modes and values by truncating the combination to the N^{th} order, provided that

$$\sum_{k=1}^{N} \lambda_k \geq l \sum_{k=1}^{\infty} \lambda_k = l\sigma^2 \tag{43}$$

with $0 < l \leq 1$ and $\lambda_k \geq \lambda_{k+1}$.

To determine numerically the KL modes and values, Eq. 41 needs to be discretized. $\widehat{\boldsymbol{\delta}}$ and $\boldsymbol{\varphi}$ are expressed in terms of components on a basis of orthogonal unit vectors $\{\mathbf{e}_q\}_{q=1}^{m}$ as

$$\widehat{\boldsymbol{\delta}}(\mathbf{x}, \mathbf{u}) = \sum_{q=1}^{m} \delta_q(\mathbf{x}, \mathbf{u})\mathbf{e}_q \qquad \boldsymbol{\varphi}(\mathbf{x}, \mathbf{u}) = \sum_{q=1}^{m} \varphi_q(\mathbf{x})\mathbf{e}_q \tag{44}$$

The variable of integration $\mathbf{y}$ is discretized using L elements of measure Δ_j and centroid at $\mathbf{x}_j$ with $j = 1, \ldots, L$. The solution $\varphi_p(\mathbf{x})$ is evaluated at the same element centroids. Define the following variables

$$\mathbf{d}_p(\mathbf{u}) = \{\delta_p(\mathbf{x}_i, \mathbf{u})\} \tag{45}$$

$$\mathbf{z}_p = \{\varphi_p(\mathbf{x}_i)\} \tag{46}$$

$$\mathbf{R}_{pq} = \langle \mathbf{d}_p(\mathbf{u}) \left[\mathbf{d}_q(\mathbf{u})\right]^{\mathrm{T}} \rangle \tag{47}$$

$$\mathbf{W} = \left[\rho(\mathbf{x}_i)\Delta_j \, \delta_{ij}\right] \tag{48}$$

where δ_{ij} is the Kronecker delta. The discretized form of Eq. 41 is

$$\sum_{q=1}^{m} \sum_{j=1}^{L} \left[\mathbf{R}_{pq}\mathbf{W}\right]_{ij} \{\mathbf{z}_p\}_j = \lambda_i \{\mathbf{z}_p\}_j \tag{49}$$

The problem can be written as $\mathbf{Az} = \lambda\mathbf{z}$. This form can be solved numerically for the KL modes $\mathbf{z}$ and the KL values λ. The eigenvectors $\mathbf{z}_k$ are used to build the reduced-dimensionality discrete representation of $\boldsymbol{\delta}$ as

$$\mathbf{d} = \begin{Bmatrix} \delta_1(\mathbf{x}_1) \\ \vdots \\ \delta_1(\mathbf{x}_L) \\ \vdots \\ \delta_m(\mathbf{x}_1) \\ \vdots \\ \delta_m(\mathbf{x}_L) \end{Bmatrix} \approx \sum_{k=1}^{N} \alpha_k \mathbf{z}_k \tag{50}$$

The ensemble average can be evaluated numerically by Monte Carlo sampling using a statistically converged number of random realizations S of the design variables, $\{\mathbf{u}_r\}_{r=1}^{S}$. The r^{th} sample provides the shape modification

$$\boldsymbol{\gamma} = \begin{Bmatrix} \gamma_1(\mathbf{x}_1, \mathbf{u}_r) \\ \vdots \\ \gamma_1(\mathbf{x}_L, \mathbf{u}_r) \\ \vdots \\ \gamma_m(\mathbf{x}_1, \mathbf{u}_r) \\ \vdots \\ \gamma_m(\mathbf{x}_L, \mathbf{u}_r) \end{Bmatrix} \tag{51}$$

The p^{th} component of the discretized deviation from the mean of the shape modification vector is then evaluated as per

$$\mathbf{d}_p(\mathbf{u}_r) = \begin{Bmatrix} \gamma_p(\mathbf{x}_1, \mathbf{u}_r) \\ \vdots \\ \gamma_p(\mathbf{x}_L, \mathbf{u}_r) \end{Bmatrix} - \frac{1}{S} \sum_{r=1}^{S} \begin{Bmatrix} \gamma_p(\mathbf{x}_1, \mathbf{u}_r) \\ \vdots \\ \gamma_p(\mathbf{x}_L, \mathbf{u}_r) \end{Bmatrix} \tag{52}$$

Accordingly, the submatrix $\mathbf{R}_{pq}$ can be computed directly as $\mathbf{R}_{pq} = \frac{1}{S}\mathbf{D}_p\mathbf{D}_q^{\mathrm{T}}$, where $\mathbf{D}_p$ is defined as

$$\mathbf{D}_p = \left[\mathbf{d}_p(\mathbf{u}_1) \,|\ldots|\, \mathbf{d}_p(\mathbf{u}_S)\right] \tag{53}$$

The combined distributed/concentrated parameters approach to KLE presented in Diez et al. (2016b), which aims at including physical quantities in the dimensionality reduction, is here extended to combined distributed/concentrated geometrical parameters. In Diez et al. (2016b), the shape modification is the geometrical distributed quantity while physical quantities include distributed, such as the hull pressure in ship hydrodynamics applications, and concentrated parameters, such as ship total resistance. The goal of steering the dimensionality reduction towards physically meaningful design variables is pursued by objective function evaluations using low fidelity simulations. To keep the

method exclusively off-line, the distributed shape modification is here combined with concentrated geometrical parameters which are known to the designer to be physically meaningful. In the hydrofoil example, this means integrating classic approach to wing-type structure modifications with continuous shape parametrization.

The linear representation of the shape modification uses the optimal basis of orthonormal functions $\boldsymbol{\psi}_k(\mathbf{x})$ as per

$$\widehat{\boldsymbol{\gamma}}(\mathbf{x},\mathbf{u}) = \sum_{k=1}^{\infty} \alpha_k(\mathbf{u})\boldsymbol{\psi}_k(\mathbf{x}) \tag{54}$$

where

$$\widehat{\boldsymbol{\gamma}}(\mathbf{x},\mathbf{u}) = \begin{cases} \widehat{\boldsymbol{\delta}}(\mathbf{x},\mathbf{u}), \mathbf{x} \in D \\ \widehat{\boldsymbol{\theta}}(\mathbf{x},\mathbf{u}), \mathbf{x} \in C \end{cases} \tag{55}$$

and

$$\boldsymbol{\psi}_k(\mathbf{x}) = \begin{cases} \boldsymbol{\varphi}_k(\mathbf{x}), \mathbf{x} \in D \\ \boldsymbol{\upsilon}_k(\mathbf{x}), \mathbf{x} \in C \end{cases} \tag{56}$$

with D and C being the domains of the distributed and concentrated modifications $\widehat{\boldsymbol{\delta}}$ and $\widehat{\boldsymbol{\theta}}$, respectively. For instance, in the hydrofoil application, $\widehat{\boldsymbol{\delta}}$ is the distributed shape modification vector (displacement) and $\widehat{\boldsymbol{\theta}}$ includes twist and camber at specified sections along the span.

CHAPTER 3: TEST CASES

Analytical test problems

Two analytical test problems are used to evaluate the architecture. A solution by global derivative-free MDF provides a benchmark for the assessment of the performance of MCAS-MDO.

The first multidisciplinary test is a two-dimensional unconstrained problem involving two disciplines:

$$\min_{\mathbf{u}} \quad f(\mathbf{u}) = u_1^2 + u_2 + y_1 + e^{-y_2} \tag{57}$$

$$\text{with} \quad y_1(\mathbf{u}, y_2) = 100 + u_1 + u_2 - 0.2y_2$$

$$y_2(\mathbf{u}, y_1) = \sqrt{|y_1|} + 10 + u_2$$

Box-constraints are $-10 \leq u_1 \leq 25$ and $-25 \leq u_2 \leq 10$. A stochastic extension of this problem is used, for instance, in Leotardi et al. (2016).

The second test is the three-dimensional constrained version of the first problem. Two disciplines and two constraints are used:

$$\min_{\mathbf{u}} \quad f(\mathbf{u}) = u_1^2 + u_2 + y_1 + e^{-y_2} \tag{58}$$

$$\text{with} \quad y_1(\mathbf{u}, y_2) = u_1 + u_2 + u_3^2 - 0.2y_2$$

$$y_2(\mathbf{u}, y_1) = \sqrt{|y_1|} + u_2 + u_3$$

$$\text{Subject to} \quad 1 - \frac{y_1}{3.16} \leq 0$$

$$\frac{y_2}{24} - 1 \leq 0$$

Box-constraints are $0 \leq u_1 \leq 10$, $0 \leq u_2 \leq 10$, and $-10 \leq u_3 \leq 10$. The solution of this problem is given in Tedford and Martins (2010) that also provide a comparison of several gradient-based architectures.

NACA 0009 three-dimensional hydrofoil

Experimental data

An experimental study has been carried out at the University of Tasmania—AMC to investigate the hydro-elastic behavior of a series of three-dimensional hydrofoils with nominally identical geometry but manufactured using different materials (Zarruk et al. 2014). The hydrofoil has un-swept trapezoidal plan-form and is tapered with streamlined section as per NACA 0009 section. The models have been manufactured using Stainless Steel (SS), Aluminum (AL), and Carbon Fiber Reinforced Plastic (CFRP). Two types of CFRP models have been used; they have common layups but differ in fiber orientation. The tests have been conducted inside a pressurized water tunnel for several Reynolds numbers (Re) and angles of attack (α) including pre- and post-stall conditions. The models are constrained at the root section and free at the opposite end (tip section). Measured outputs include forces and deformation. The experimental FSI analysis, integrating experimental fluid and structural dynamics (EFD and ESD), focuses on steady conditions (pre-stall α) and assesses the Reynolds number dependency of the hydrofoil forces and deformation.

The geometrical parameters of the hydrofoil are given in Table 1.

Table 1: Hydrofoil geometry details

Parameter	Symbol	Unit	Value
Span	s	m	0.3
Chord at root	c_r	m	0.12
Chord at tip	c_t	m	0.06
Mean chord	c	m	0.09
Thickness to mean chord ratio	t	-	0.09
Aspect ratio	AR	-	3.33

To accommodate the composite material structure, the NACA 0009 section, expressed by Eq. 59, is modified by thickening of the trailing edge as per Eq. 60.

$$y_{\text{standard}} = 5t(0.2969x^{0.5} - 0.126x - 0.3516x^2 + 0.2843x^3 - 0.1015x^4) \quad (59)$$

$$y_{\text{modified}} = 5t(0.2969x^{0.5} - 0.126x - 0.3516x^2 + 0.2843x^3 - 0.0889x^4) \quad (60)$$

The hydrofoils with standard NACA 0009 section are referred to as type I while the hydrofoils with modified section are regarded as type II. The difference between type I and II is displayed in Figure 11 highlighting the trailing edge thicknesses τ_{TE} which are approximately 0.3% and 1.3% of the chord.

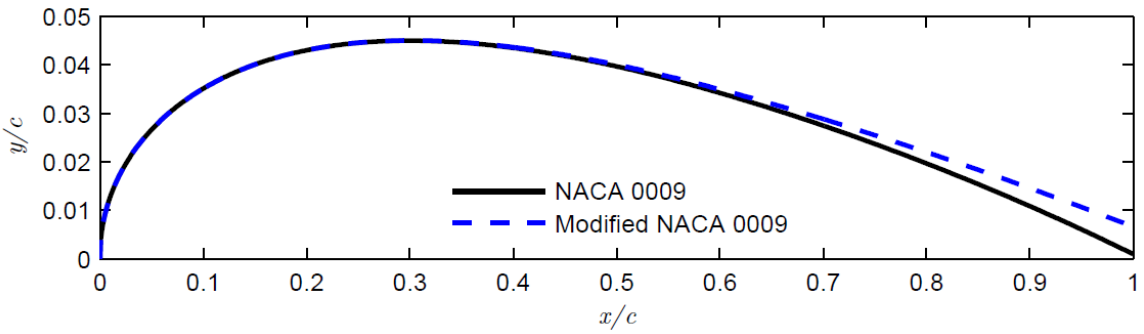

Figure 11: Standard and modified NACA 0009 sections (Zarruk et al. 2014)

The material properties of the hydrofoils are summarized in Table 2. *K* is the bending stiffness, *E* is the elastic modulus, *I* is the base section second moment of area, *J* is the torsional constants, ρ_H is the material density, f_n is the natural frequency, and ρ_H/ρ is the ratio of hydrofoil material to water densities. For composite hydrofoil, whose structure is not isotropic, properties are given as average. Detailed material properties of the composite materials hydrofoils are given Table 3. They are also depicted in Figure 12 showing the layout of the different materials and the orientation of the fibers. Specifically, the CFRP00 has fibers aligned with the local *x* (ζ = 0°) while CFRP30 has ζ = 30° towards the leading edge.

Table 2: Material properties (Zarruk et al. 2014)

Parameter	Unit	SS		AL		CFRP00	CFRP30
Type	-	I	II	I	II	II	II
K	N/mm	61.7	60.2	23.0	22.1	20.0	8.2
E	GPa	193	193	71	71	65	26
I	mm^4	5956	6148	5956	6350	6148	6148
J	mm^4 $x10^3$	860.4	854.5	860.4	854.7	854.5	854.5
ρ_H	kg/m^3	7900	7900	2700	2700	1600	1600
f_n in air	Hz	100	96	100	96	112	72
f_n in water	Hz	62	61	42	41	41	26
ρ_H/ρ	-	7.9	7.9	2.7	2.7	1.6	1.6

Table 3: composite material properties and layout (Zarruk et al. 2014)

Layer	Material	Type	Weight [g/m^3]	Thickness [mm]
Carbon	12k T-700	Unidirectional (0°)	300	0.25
Glass	E-glass	Bi-axial (0°/90°)	600	0.6
Glass	E-glass	Basket (0°/90°)	130	0.15
Glass	E-glass/polyolefin	Continuous filament skins/polyolefin scaffold core	780	≈2.0

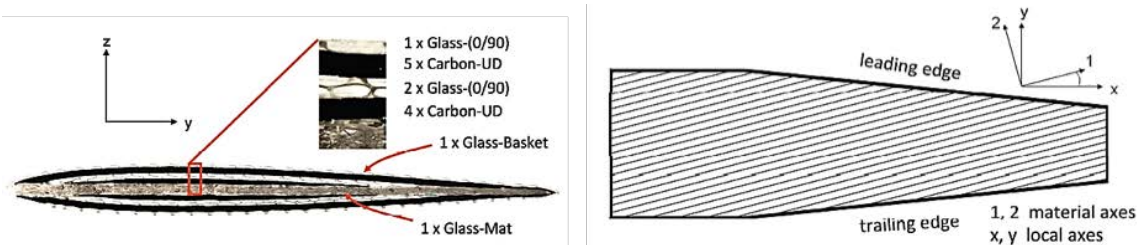

Figure 12: Composite material layout (Zarruk et al. 2014)

The experiments are performed in a variable pressure water tunnel at the Cavitation Research Laboratory at the University of Tasmania. The tunnel test section is 0.6 m^2 and 2.6 m long; the velocity is spatially uniform within a 0.5% uncertainty, and the temporal variations are less than 0.2%. The tunnel was pressurized up to 200 kPa to prevent

cavitation. The models are mounted on a six-component force balance extending vertically into the flow (Figure 13 and Figure 14). Measurements of forces and moments are performed at several mean chord-based Re in the range $0.2x10^6/1.0x10^6$ and several α values in the range -15/+15 degrees. The balance measures forces with less than 0.5% precision; the unsteady component is sampled at 1kHz. Deformations are measured using an image registration algorithm providing 3.6% average uncertainty. Experimental outputs are lift and drag forces, pitching moment, tip section displacement, and tip section twist.

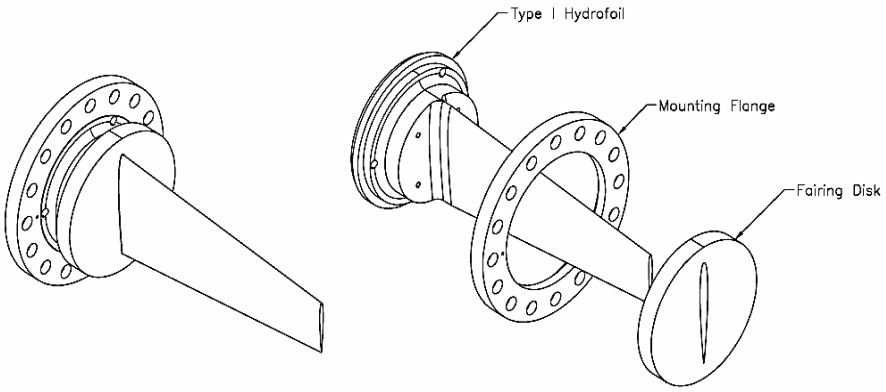

Figure 13: Type I hydrofoil mount (Zarruk et al. 2014)

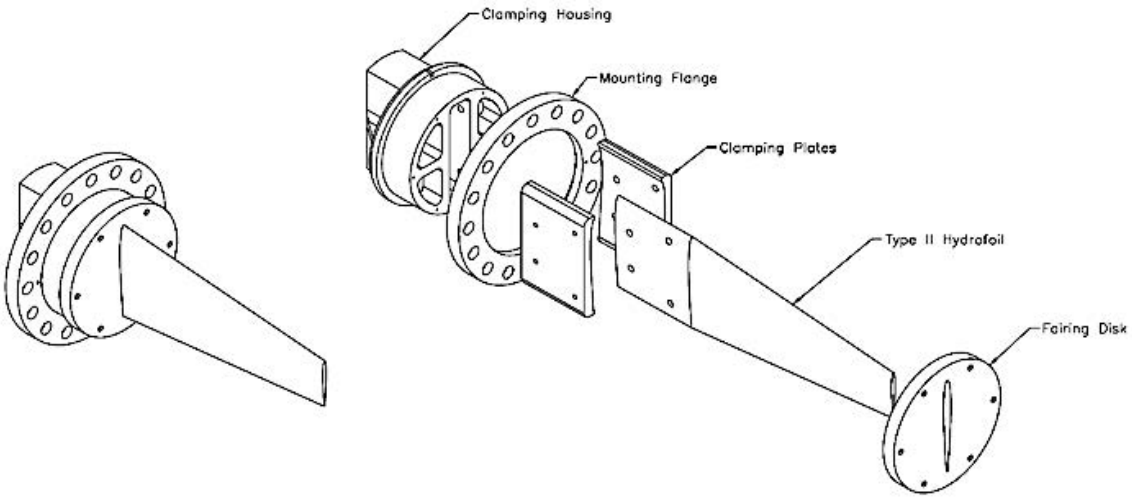

Figure 14: Type II hydrofoil mount (Zarruk et al. 2014)

Forces and moments are analyzed in non-dimensional form. The lift coefficient C_L, the drag coefficient C_D, and the pitching moment coefficient C_M are defined as

$$C_L = \frac{2L}{\rho U_\infty^2 sc} \qquad C_D = \frac{2D}{\rho U_\infty^2 sc} \qquad C_M = \frac{2M}{\rho U_\infty^2 sc^2} \tag{61}$$

Figure 15 to Figure 17 show C_L, C_D, and C_M versus α. Forces and moment curves compare closely for all Re and α values. Stall occurs at approximately 10.5°. The trend indicates that tip deflection has little effect for metal and CFRP00 hydrofoils whereas it has a more significant effect for the CFRP30 whose deformation leads to a delay in the stall.

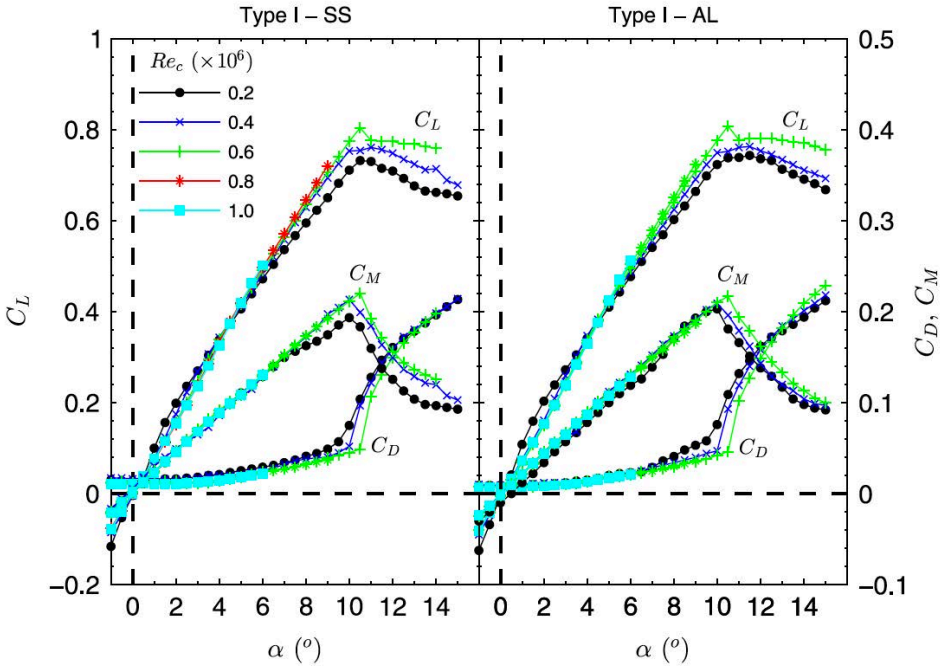

Figure 15: EFD lift, drag, and pitching moment coefficients for metal type I hydrofoils (Zarruk et al. 2014)

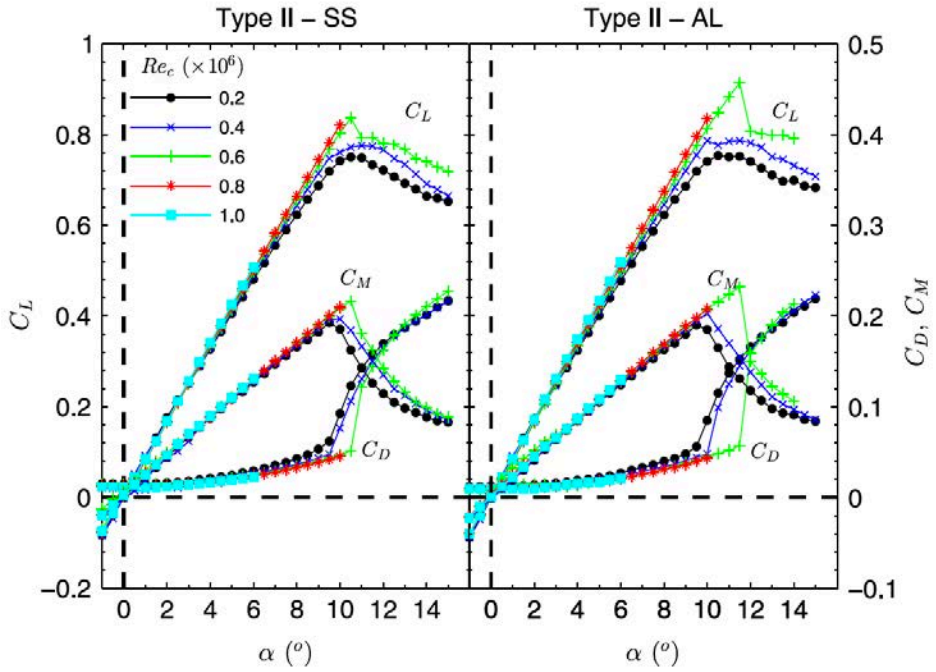

Figure 16: EFD lift, drag, and pitching moment coefficients for metal type II hydrofoils (Zarruk et al. 2014)

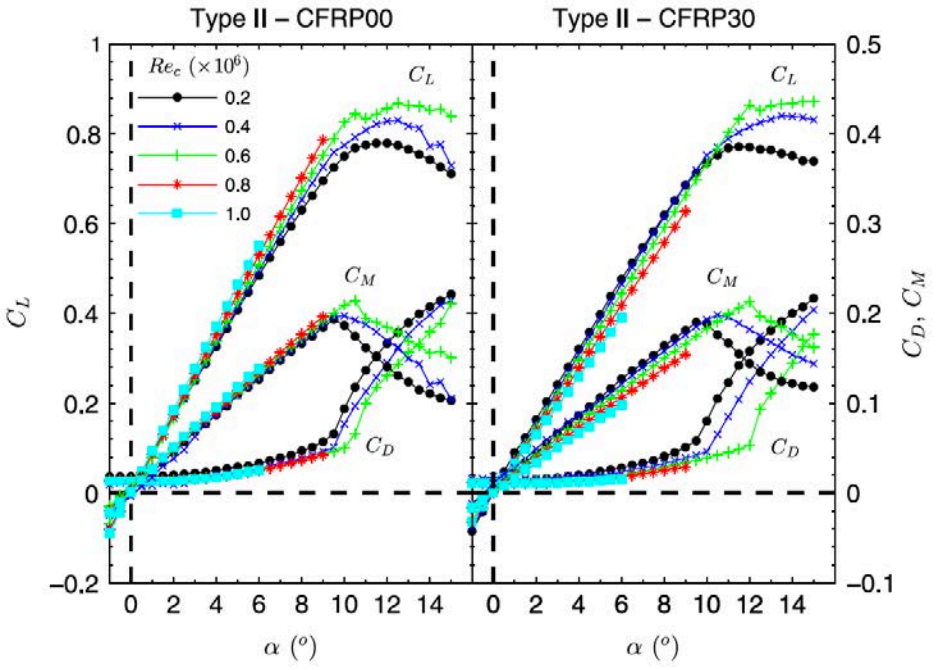

Figure 17: EFD lift, drag, and pitching moment coefficients for composite type II hydrofoils (Zarruk et al. 2014)

Figure 18 to Figure 21 show the spectra of the normal force fluctuations for type II hydrofoils. At post-stall incidence, peaks appear in the spectrum due to the excitation of the hydrofoil first mode with the onset of unsteady flow with stall.

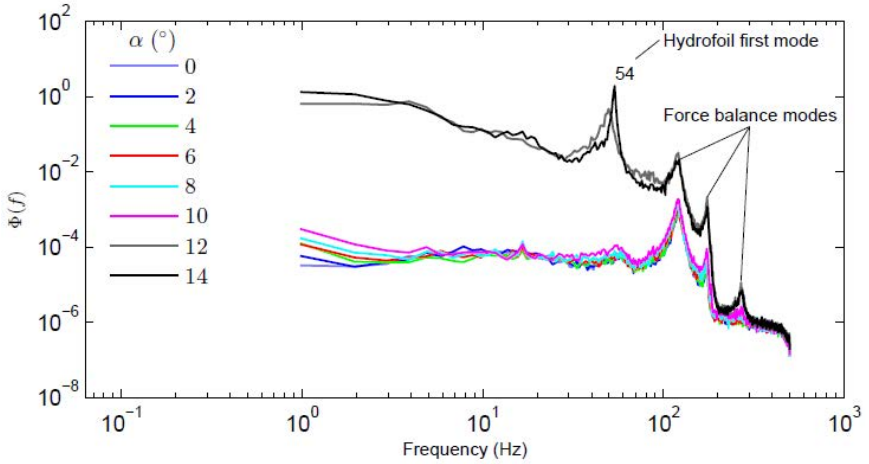

Figure 18: EFD power spectral densities of unsteady normal forces for the SS type II hydrofoil (Zarruk et al. 2014)

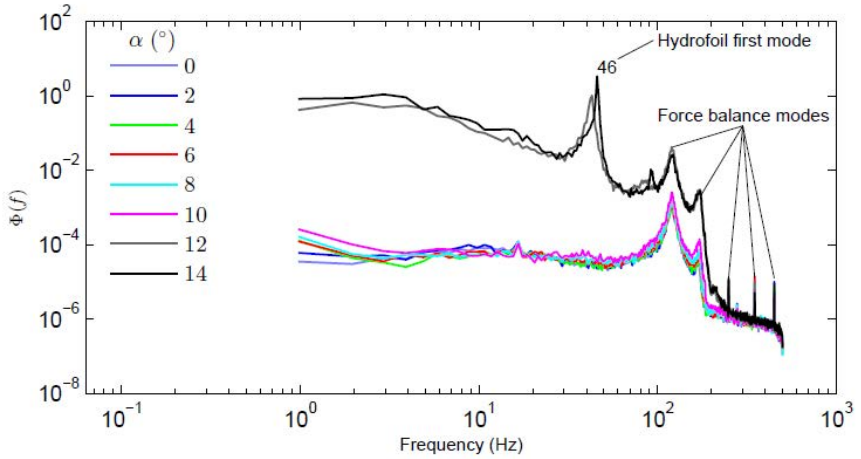

Figure 19: EFD power spectral densities of unsteady normal forces for the AL type II hydrofoil (Zarruk et al. 2014)

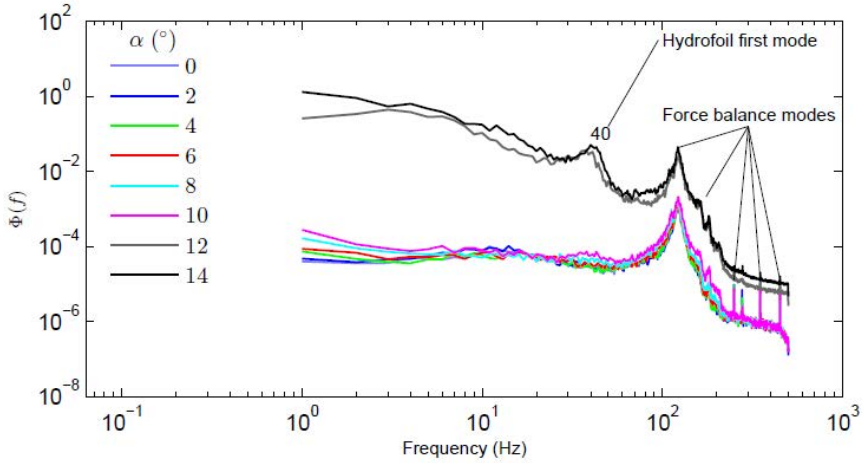

Figure 20: EFD power spectral densities of unsteady normal forces for the CFRP00 type II hydrofoil (Zarruk et al. 2014)

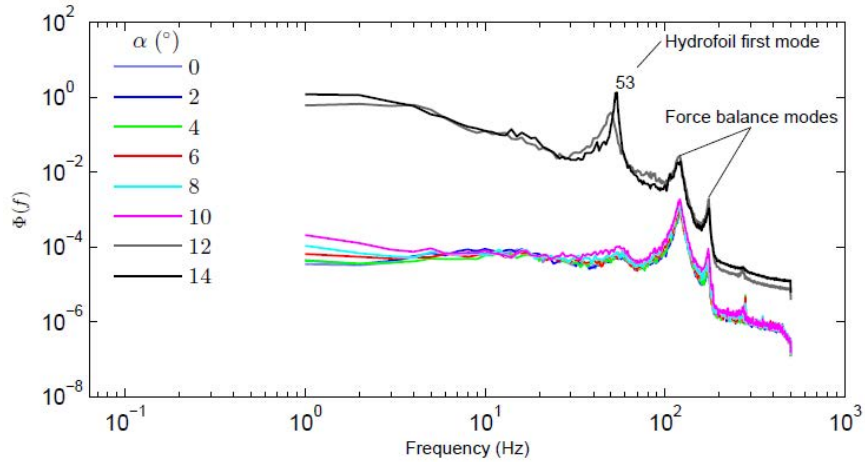

Figure 21: EFD power spectral densities of unsteady normal forces for the CFRP30 type II hydrofoil (Zarruk et al. 2014)

Figure 22 to Figure 25 show the non-dimensional displacement of the hydrofoil tip. For metal hydrofoils, the displacement is reported of the tip mid-point. For the composite material hydrofoils, the displacement is reported of leading and trailing edges of the tip since a significant twist of the section is found. Displacements are given in non-dimensional form according to

$$\delta' = \delta \frac{EI}{F_N s^3} \tag{62}$$

where F_N is the normal force, i.e. the component of the hydrodynamic force that is orthogonal to the hydrofoil chord.

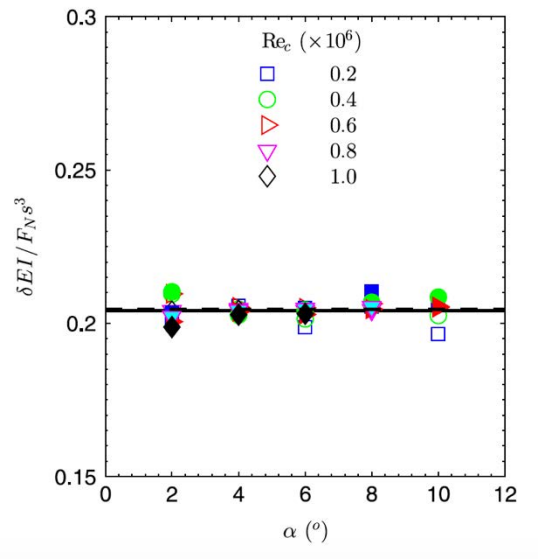

Figure 22: ESD tip displacement for SS (open symbols) and AL (close symbols) type I hydrofoils (Zarruk et al. 2014)

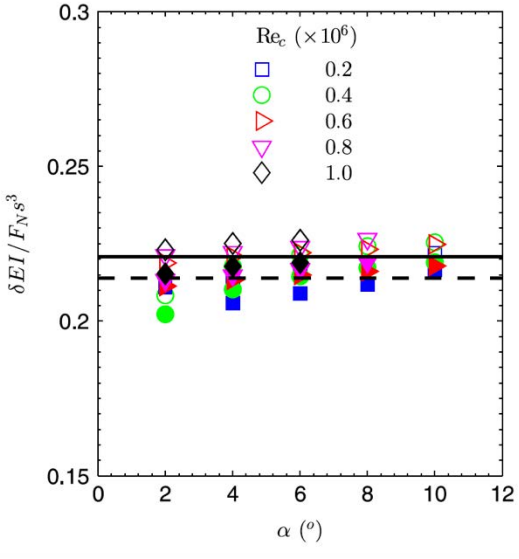

Figure 23: ESD tip displacement for SS (open symbols) and AL (close symbols) type II hydrofoils (Zarruk et al. 2014)

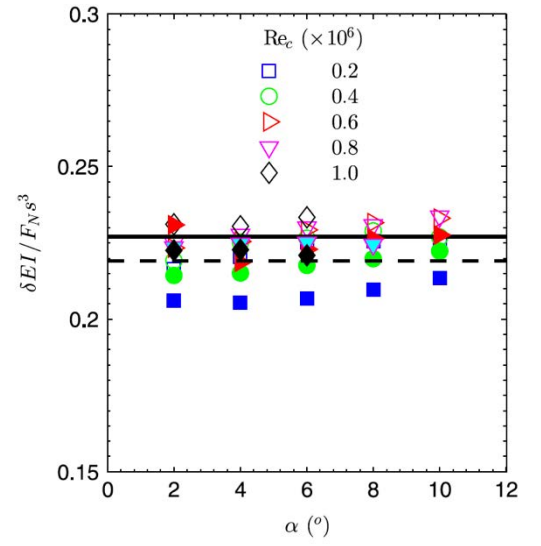

Figure 24: ESD tip displacement at leading (open symbols) and trailing edges (close symbols) for the type II CFRP00 hydrofoil (Zarruk et al. 2014)

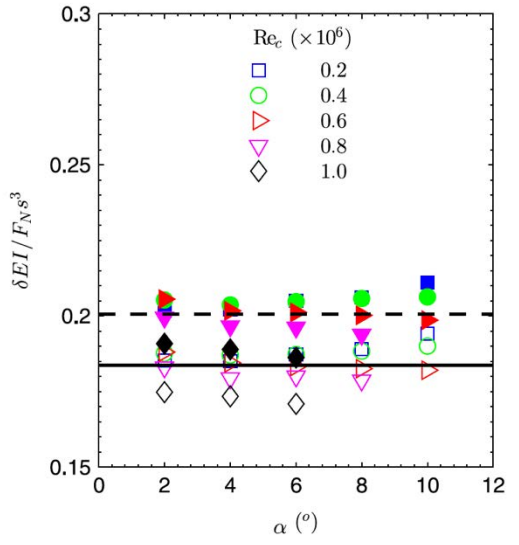

Figure 25: ESD tip displacement at leading (open symbols) and trailing edges (close symbols) for the type II CFRP30 hydrofoil (Zarruk et al. 2014)

Figure 26 show the composite hydrofoil tip twist. The CFRP00 hydrofoil shows positive twist whereas the CFRP30 model shows a negative twist. The latter has the effect of

reducing the effective angle of attack and therefore the acting normal force, which correlates well with the corresponding delay in stall.

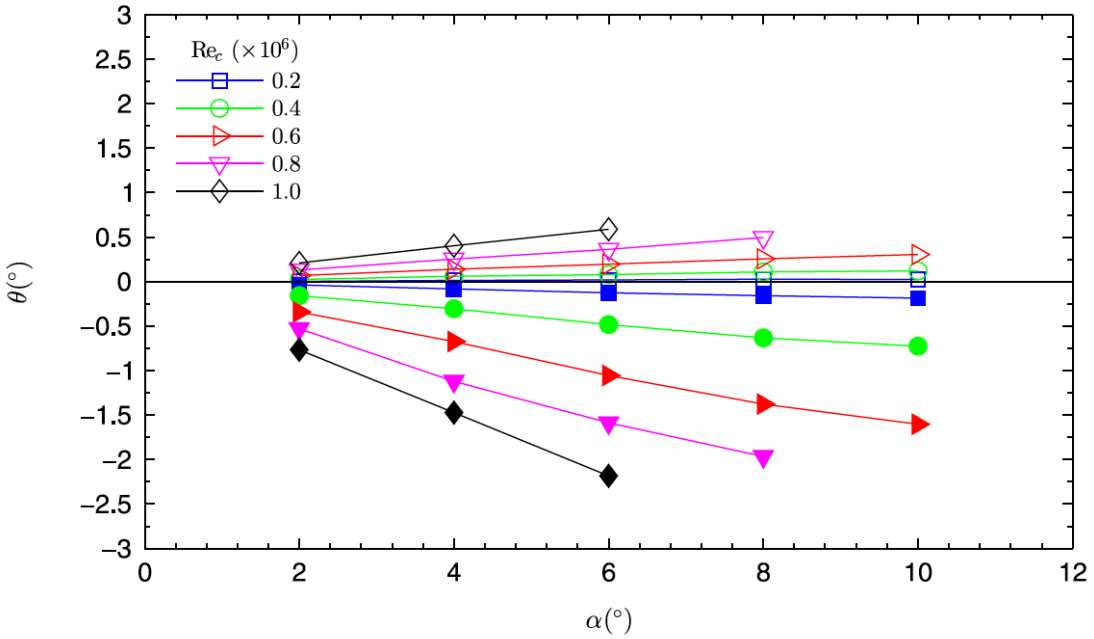

Figure 26: ESD tip twist for CFRP00 (open symbols) and CFRP30 (close symbols) hydrofoils (Zarruk et al. 2014)

Multidisciplinary design optimization formulation

The design optimization of the fully submerged NACA 0009 three-dimensional hydrofoil is aimed at minimizing the drag. The design conditions are defined by α = 8 degrees and Re = 0.6x10^6 and belong to pre-stall range. Two hydrofoils with equivalent shape but made of different material, namely AL and CFRP, are optimized.

The hydrofoil is subject to several constraints, including geometrical, structural, and hydrodynamic.

1. Geometrical constraints:
    - The span is assumed fixed. This constraint is automatically satisfied when enforced directly by the geometry modification tool.
    - The hydrofoil thickness needs to allow the allocation of the composite material. Therefore, a minimum thickness requirement is enforced over the plan-form equal to the minimum thickness of the original geometry.

2. Structural constraints:
    - Structural integrity is required and ensured by limiting a stress-based material failure index. For the metal, the failure index is defined as ratio between the Von Mises stress

$$\sigma_v = \sqrt{\frac{1}{2}[(\sigma_1 - \sigma_2)^2 + (\sigma_2 - \sigma_3)^2 + (\sigma_3 - \sigma_1)^2]} \tag{63}$$

where σ_i are the principal stresses, and the aluminum failure strength σ_f as

$$\phi = \frac{\sigma_v}{\sigma_f} \tag{64}$$

For the composite material, the Tsai-Wu criteria (see the ANSYS Mechanical APDL Theory Reference for implementation details) is used. In the form of the inverse of the strength ratio, it is given by

$$\phi = \frac{1}{-\frac{B}{2A} + \sqrt{\left(\frac{B}{2A}\right)^2 + \frac{1}{A}}} \tag{65}$$

$$A = -\frac{\sigma_{11}^2}{\sigma_{1t}^f \sigma_{1c}^f} - \frac{\sigma_2^2}{\sigma_{2t}^f \sigma_{2c}^f} - \frac{\sigma_3^2}{\sigma_{3t}^f \sigma_{3c}^f} - \frac{\sigma_{12}^2}{{\sigma_{12}^f}^2} - \frac{\sigma_{23}^2}{{\sigma_{23}^f}^2} - \frac{\sigma_{13}^2}{{\sigma_{13}^f}^2} + \frac{C_{12}\sigma_{11}\sigma_{22}}{\sqrt{\sigma_{1t}^f \sigma_{1c}^f \sigma_{2t}^f \sigma_{2c}^f}} + \frac{C_{23}\sigma_{22}\sigma_{33}}{\sqrt{\sigma_{2t}^f \sigma_{2c}^f \sigma_{3t}^f \sigma_{3c}^f}} + \frac{C_{13}\sigma_{11}\sigma_{33}}{\sqrt{\sigma_{1t}^f \sigma_{1c}^f \sigma_{3t}^f \sigma_{3c}^f}} \tag{66}$$

$$B = \left(\frac{1}{\sigma_{1t}^f} + \frac{1}{\sigma_{1c}^f}\right)\sigma_{11} + \left(\frac{1}{\sigma_{2t}^f} + \frac{1}{\sigma_{2c}^f}\right)\sigma_{22} + \left(\frac{1}{\sigma_{3t}^f} + \frac{1}{\sigma_{3c}^f}\right)\sigma_{33} \tag{67}$$

σ_{Xt}^f and σ_{Xc}^f are the failure stress values in the layer X-direction for tension and compression, respectively. C_{12}, C_{23}, and C_{13} are equal to $x - y$, $y - z$, and $x - z$, respectively. Failure is indicated by $\phi > 1$.

3. Hydrodynamic constraints:
    - The hydrofoil must deliver a minimum amount of lift.
4. Numerical constraints:
    - Bound-constraints for the design variables are directly handled by the optimization algorithm and do not require explicit treatment.

From a hydrodynamic viewpoint, lift and drag depend on the shape of the hydrofoil and on the flow conditions. Since the structure is flexible and its dynamics couples with the hydrodynamics, the forces depend also on the deformation. The structural deformation depends on the material properties and on the hydrodynamic load. The hydrofoil shape parameters are the independent variables, also referred to as design variables $\mathbf{u}$; load and deformations are the coupling variables $\mathbf{y}$. The objective function is $C_D(\mathbf{u})$.

The set of design variables includes the parameters defining the shape of the hydrofoil $\mathbf{u}_{shape}$ and the variables identifying the composite material layup. In the present, the overall structure of the sandwich material made of CFRP and foam core is assumed similar to the experiments of Zarruk et al. (2014). The material layout is modified only by the fiber orientation $u_{fiber} = \zeta$ of the carbon fiber reinforced layers. The global set of design variables is therefore $\mathbf{u}^{\mathrm{T}} = \mathbf{u}_{shape}^{\mathrm{T}}$ for the AL hydrofoil and $\mathbf{u}^{\mathrm{T}} = \left[\mathbf{u}_{shape}^{\mathrm{T}}, u_{fiber}\right]$ for the CFRP hydrofoil.

The optimization problem is formulated according to Eq. 20 to 23 as

$$\min_{\mathbf{u}\in U} \quad C_D(\mathbf{u}) \tag{68}$$

$$\text{subject to } 1 - \frac{C_L(\mathbf{u})}{C_L^*} \leq 0 \tag{69}$$

$$1 - \frac{\tau(\mathbf{u})}{{\tau_{TE}}^*} \leq 0 \tag{70}$$

$$\frac{\phi(\mathbf{u})}{\phi^*} - 1 \leq 0 \tag{71}$$

where C_L^* =0.645, based on the C_L of the rigid original geometry, ${\tau_{TE}}^* = 0.000783$, based of the minimum thickness of the original geometry (at the trailing edge), and $\phi^* = 0.65$, which is the maximum value among SS, AL, CFRP00, and CFRP30 simulations of the

original geometry. In the following chapters C_D will be referred to as the objective function f; Eq. 69 to 71 will be referred to as constraints $c_1 \leq 0$, $c_2 \leq 0$, and $c_3 \leq 0$.

CHAPTER 4: COMPUTATIONAL SETUP

Hydrodynamics via Reynolds averaged Navier-Stokes simulation

CFD simulations are performed at Re equal to 0.2, 0.6, and 1.0×10^6 and α equal to 0, 2, 4, 6, 8, 10, 12, and 14. Table 4 summarizes the conditions. Both type I and type II hydrofoil geometries are studied. The analysis is aimed at the identification of lift and drag force coefficients and pitching moment coefficient.

Table 4: CFD test cases

Parameter	Symbol/definition	Case 1	Case 2	Case 3
Reynolds number	Re	0.2×10^6	0.6×10^6	1.0×10^6
Froude number	Fr	2.7	8.2	13.7
Speed [m/s]	U_∞	2.57	7.70	12.8
Angle of attack [deg]	α	0,2,4,6,8,10,12,14		
Flow time [s]	$T = c/U_\infty$	0.035	0.012	0.007
Time step [s]	Δt	$T/180$		

The grid used for the CFD simulation is made of 11 million nodes, which are clustered around the body to catch the boundary layer, as shown in Figure 27 including the resolution of the sharp corners of the trailing edge. The maximum y^+ value is 0.84 occurring for Re equal to 1.0×10^6. The hydrofoil lays span-wise along z, while x and y are cross-section coordinates. The hydrodynamic force acting on the body has drag and lift aligned with the x and y axis, respectively. The x axis is aligned with the incoming flow, and α is defined positive when produces a positive lift (positive y direction). The hydrofoil grid includes 100 points along the span (z) and 353 points along the chord (x), as shown in Figure 28. The difference in the trailing edge thickness between type I and type II hydrofoil grids is displayed in Figure 29. Topology and grid size for the two types are analogous.

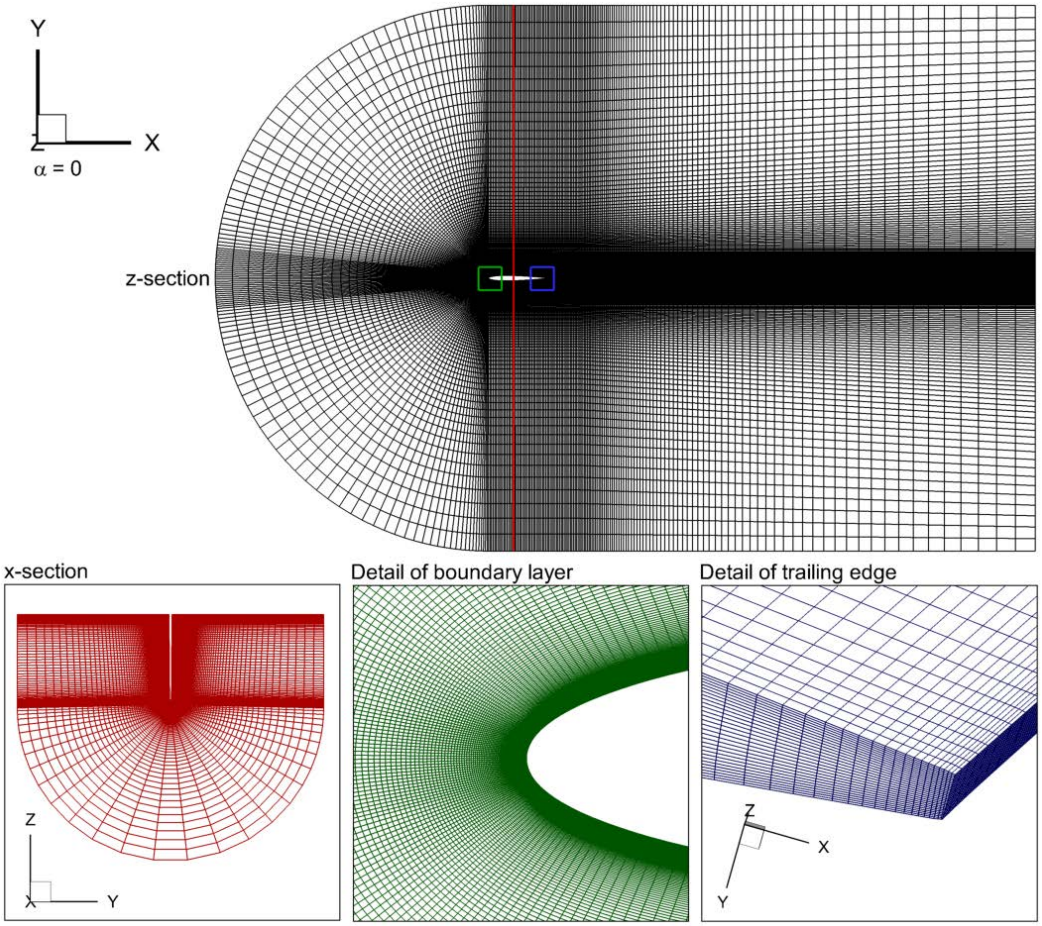

Figure 27: CFD mesh

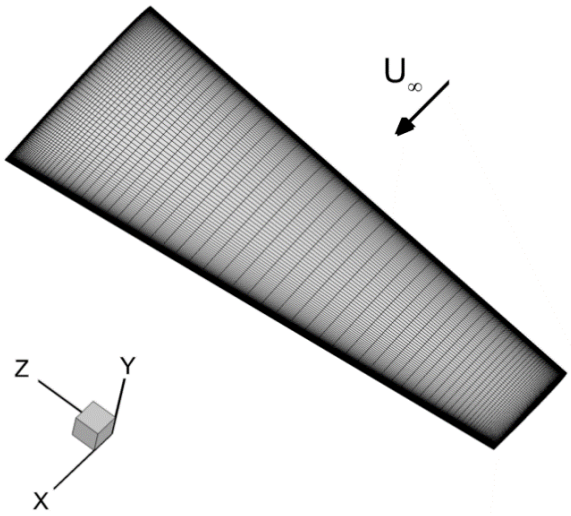

Figure 28: CFD wall mesh

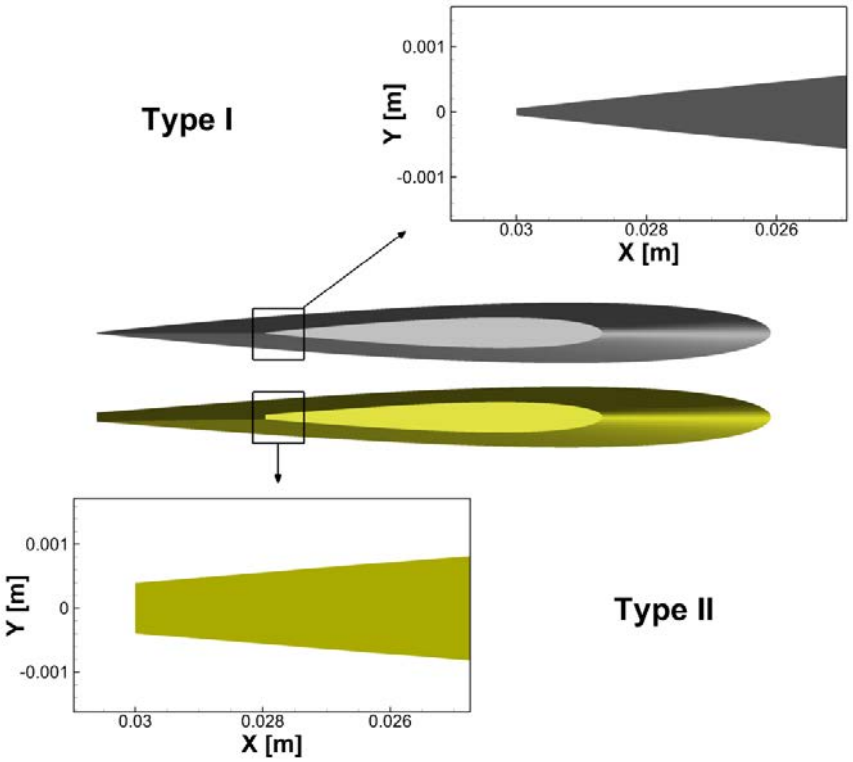

Figure 29: CFD mesh detail of the trailing edge for type I and II hydrofoils

The independence of the results from the mesh size is assessed by grid verification. G1, G2, and G3 refer to fine, medium, and coarse meshes having refinement ratio equal to $\sqrt{2}$ and, respectively, 11M, 3.3M, and 1.5M of nodes.

Structural dynamics via finite element analysis

CSD simulations for the modal analysis are performed for all hydrofoil models; it is aimed at the identification of the first five natural frequencies and mode shapes. The study is carried out using the FE analysis of ANSYS.

The hydrofoils are modeled by two-dimensional shell elements SHELL281 centered on the hydrofoil mid-plane in a structured-type arrangement. These elements have eight nodes, six degrees of freedom at each node, namely three translations and three rotations, and are suitable for analyzing thin to moderate thick shell structures. Figure 30 shows the hydrofoil structural grid, while Figure 31 provides a detailed view of the element. The SHELL281 elements are layered in order to model the composite sandwich; a variable total thickness is included and single layer thicknesses are scaled accordingly. Metal hydrofoil models, SS and AL, are built using both type I and type II geometries;

CFRP models are only type II. For the metal hydrofoil models, the section where the clamped boundary condition is applied extends 20 mm beyond the root section (Garg et al. 2017) to represent the fairing disk used in the experimental mount.

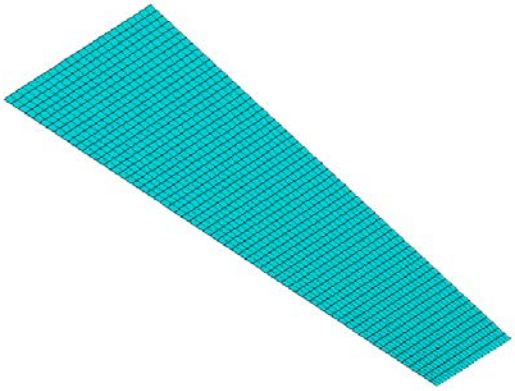

Figure 30: CSD mesh

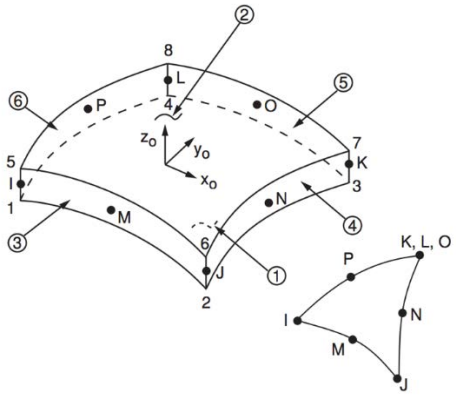

Figure 31: SHELL281 element (ANSYS Mechanical APDL Theory Reference)

In order to evaluate the wet modes of the hydrofoil, the mesh is embedded in a fluid domain modeled by acoustic elements as shown in Figure 32. Three-dimensional FLUID30 elements (Figure 33) fill the acoustic domain whose boundary is delimited by two-dimensional FLUID130 elements (Figure 34).

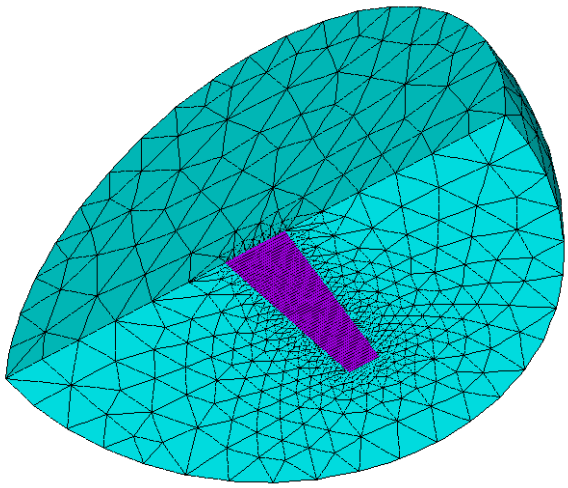

Figure 32: CSD acoustic domain mesh

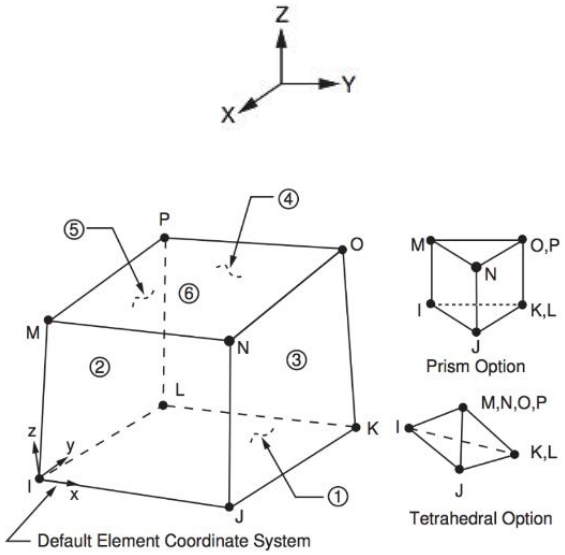

Figure 33: FLUID30 element (ANSYS Mechanical APDL Theory Reference)

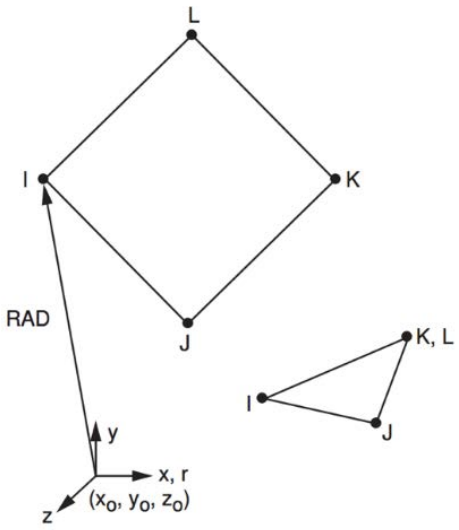

Figure 34: FLUID130 element (ANSYS Mechanical APDL Theory Reference)

Grid verification of hydrofoil model and acoustic domain is performed. The natural frequencies predicted by three levels of body grid refinement and three acoustic domain radii are compared. Maximum element size and radius of acoustic domain are used to define the grid and employ a refinement ratio equal to $\sqrt{2}$. G1, G2, and G3 refer to fine, medium, and coarse meshes having, respectively, 0.005 m, 0.071 m, and 0.010 of maximum element size. The associated number of elements is 1.5k, 0.7k, and 0.4k. D1, D2, and D3 refer to large, medium, and small acoustic domain, respectively, which have radius equal to 0.7, 0.5, and 0.35 m.

Fluid-structure interaction

The FSI is aimed at the identification of the hydrofoil deformation, specifically, tip displacement and twist. Steady one-way coupling FSI is performed for all hydrofoil models and four α values in the pre-stall range and all Re numbers. Steady two-way coupling FSI is performed for all type II hydrofoil at 8 degrees α and Re equal to 0.6×10^6 (Table 5).

Table 5: FSI test cases

Test case	α	Re	Condition	Coupling
1	2,4,6,8	$0.2x10^6$, $0.6x10^6$, $1.0x10^6$	Steady	One-way
2	8	$0.6x10^6$	Steady	Two-way

Shape modification via free-form deformation

The directions $\hat{\mathbf{s}}$, $\hat{\mathbf{t}}$, and $\hat{\mathbf{u}}$ lay on the chord-wise, thickness-wise, and span-wise directions, respectively. Displacements are allowed in the $\hat{\mathbf{s}}$ and $\hat{\mathbf{t}}$ directions only, giving 2 degrees of freedom to each control point and keeping the span fixed. Five design spaces are analyzed and compared having different number of control points and degrees of freedom.

Design space 1 to 4, present, in addition to the displacements in the $\hat{\mathbf{s}}$ and $\hat{\mathbf{t}}$ directions, a rotation imposed at the tip section of the hydrofoil and linearly interpolated along the span to reach a zero value at the root section. Design space 5 features rigid displacements and rotations at all the cross-sections, whose number and position is defined by the distribution of control points in the $\hat{\mathbf{u}}$ direction. Displacements are allowed in the range $\pm$20% of the mid chord; the range for rotations is $\pm$5 degrees.

Table 6 provides the number of control points N_{CP} and the associated number of design variables M for each design space. Control point locations are shown in Figure 35 to Figure 38.

Table 6: Design space definition based on FFD parameters

Design space	$l+1$	$m+1$	$n+1$	N_{CP}	M
1	2	2	2	8	17
2	5	2	5	50	101
3	10	2	10	200	401
4	20	2	20	800	1601
5	5	2	5	50	112

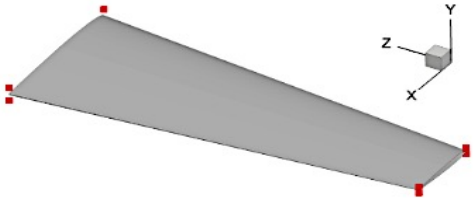

Figure 35: Design space 1 control points distribution

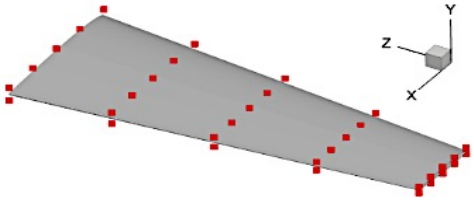

Figure 36: Design space 2 and 5 control points distribution

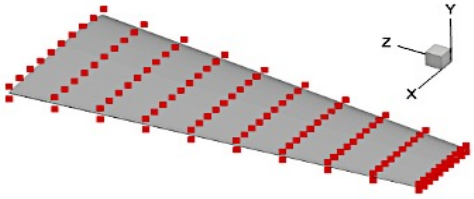

Figure 37: Design space 3 control points distribution

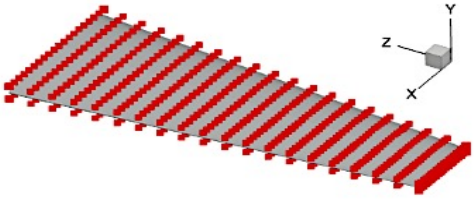

Figure 38: Design space 4 control points distribution

In the application of the KLE-based dimensionality reduction, the weight function is assumed constant and equal to one. The design spaces defined by FFD are sampled using a random distribution of $S = 100$, 1000, and 10000 items.

When performing combined distributed/concentrated parameter KLE, the distributed quantity is the displacement and the concentrated quantities are twist and camber. The twist is quantified on the modified shape using the positions of leading and trailing edges. The camber (curvature) is evaluated as second order finite difference using the positions of leading edge, mid-chord point, and trailing edge. When performing the KLE, a weight is assigned to distributed and concentrated modification variances in order to obtain global $\sigma^2 = 1$. The combined distributed/concentrated parameter KLE is applied to the design space with the largest geometrical variability and compares six sets of relative weights.

Analytical test problems

The non-adaptive sampling technique used to initialize the method is an Hammersley sequence of $4M$ size, i.e. 8 samples in the two-dimensional problem and 12 samples in the three-dimensional problem. The same number of samples is identified at

each iteration; the ratio between infill (I) and coupling (C) points is variable and depends on the Pareto solutions obtained. The sampling parameters adopted by the MCAS are $U_{min} = 10^{-2}\%$ and $\Delta_{min} = 10^{-4}\%$ of the function and design variable ranges, respectively. The DRBF surrogate model uses a power-law kernel with stochastic exponent $1 < \varepsilon < 3$. The multi-objective DPSO applied to the surrogate model employs 64 particles and 100 iterations and uses the coefficients $c_0 = 0.721$, $c_1 = 1.655$, and $c_2 = 1.655$. The MDO is considered converged when U_c in the neighborhood of the optimum reaches the tolerance $U_c^{(tol)} = 10^{-4}\%$ of the function range or the difference in objective function value between consecutive iterations at the optimum is lower than $U_c^{(tol)}$ for 15 iterations. Each infill point is initially evaluated by a two-iteration (loose) MDA corresponding to two function evaluations for each discipline.

The global derivative-free implementation of the MDF uses directly DPSO with the MDA. Initial sampling, number of particles, and DPSO coefficients are the same used for the MCAS-MDO. At each iteration, the MDA is considered converged when U_c reaches the tolerance $U_c^{(tol)} = 10^{-4}\%$. The MDO is considered converged when the difference in objective function value between consecutive iterations at the optimum is lower than $U_c^{(tol)}$ for 15 iterations.

Sensitivity analysis and multidisciplinary design optimization

The sensitivity analysis is performed exploring the response of the outputs of interest to the change in one design variable at the time around the original geometry and fiber orientation (in the case of the CFRP hydrofoil). Six MDA via FSI simulation are computed for each design variable. If $\mathbf{u} = 0$ corresponds to the original geometry and all the design variables have the lower bound at -1 and the upper bound at 1, the six sensitivity points have $u_i =$ -1, -0.667, -0.333, 0.333, 0.667, and 1 and $u_{j \neq i} = 0$. The FSI simulations are iterated till convergence, i.e. till the coupling uncertainty reaches the threshold value $U_c^{(tol)} = 1\%$ of the original geometry output of interest. A maximum iteration number equal to 40 is also enforced corresponding to 80 total function evaluations.

The MDO uses the available sensitivity points as initial DoE. At every iteration, MCAS aims at identifying 5 new samples that can be infill points, coupling points, or a

combination of the two. The sampling parameters adopted by the MCAS are $U_{min} = 10^{-2}\%$ and $\Delta_{min} = 10^{-4}\%$ of the approximated function and design variable ranges, respectively. Each infill point is initially evaluated by a single-iteration (loose) MDA corresponding to two function evaluations in total, one for the CFD and one for the FE analyses. Such loose MDA coincides with a one-way coupling approach. The DRBF surrogate model uses a power-law kernel with stochastic exponent $1 < \varepsilon < 3$. The multi-objective DPSO applied to the surrogate model employs 100 particles and 200 iterations and uses the coefficients $c_0 = 0.721$, $c_1 = 1.655$, and $c_2 = 1.655$. Given the large expense of the objective function evaluations, a simulation budget is imposed in place of convergence criteria to determine the completion of the MDO. After the sensitivity analysis, additional 200 function evaluations driven by the MDO are allowed, corresponding to 100 CFD and 100 CSD simulations.

CHAPTER 5: HYDRODYNAMIC AND STRUCTURAL ANALYSIS RESULTS

Hydrodynamics

Type I geometry

C_L, C_D, and C_M from type I CFD simulation are shown in Figure 39 including EFD data from SS type I. The latter is the hydrofoil model most closely comparable to a rigid body. The figure includes results from RANS simulation and DES simulatio1n for α = 14 degrees and Re = 0.6x10^6. For pre-stall conditions, the agreement is very good for all Re. For post-stall conditions, CFD results at Re = 0.2x10^6 indicate a larger reduction in C_L than shown by EFD data; the stall angle is under-estimate whereas it is accurately estimated for Re = 0.6x10^6. At Re = 1.0x10^6, EFD data is limited to a maximum α equal to 6 degrees.

Errors between CFD and EFD for forces and moment coefficients are reported in Table 7 as percentage of the dynamic range. The average error for pre-stall conditions is 1.11% whereas for post-stall is 12.1%. The DES simulation improves the prediction of C_D while worsening the prediction of C_L and C_M. The hydrodynamic efficiency $Eff = C_L/C_D$ is reported in Table 8 for all Re and α values. The maximum value given by EFD is reached at α = 4 degrees for all Re numbers. The maximum value is predicted by CFD at α equal to 6 degrees.

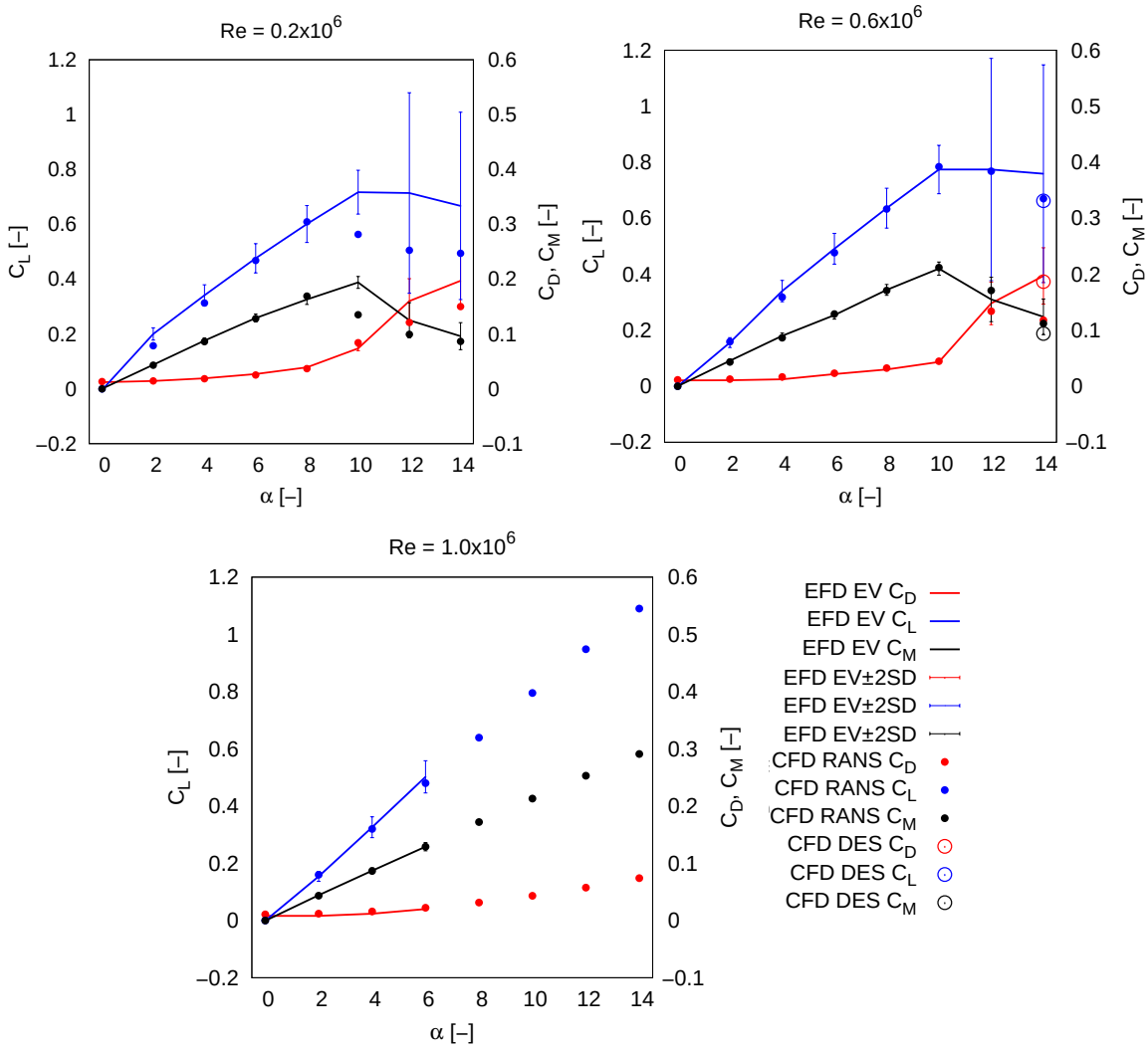

Figure 39: CFD lift, drag, and pitching moment coefficients (type I)

Table 7: CFD lift, drag, and pitching moment coefficient errors with respect to EFD (type I)

α	C_L E%$_{range}$ *			C_D E%$_{range}$ **			C_M E%$_{range}$ ***		
	Re = 0.2x10^6	Re = 0.6x10^6	Re = 1.0x10^6	Re = 0.2x10^6	Re = 0.6x10^6	Re = 1.0x10^6	Re = 0.2x10^6	Re = 0.6x10^6	Re = 1.0x10^6
0	0.49	0.04	0.08	0.61	0.58	1.39	-0.09	-0.04	0.20
2	-5.38	0.44	0.77	0.06	1.11	2.04	-0.30	-0.99	-0.36
4	-3.45	-2.75	-0.77	-0.35	2.27	2.08	-0.83	-1.62	-0.16
6	-0.95	-1.72	-2.72	-0.87	0.79	1.20	-0.16	0.98	0.24
8	1.09	-0.34	-	-1.23	1.33	-	2.73	-0.57	-
10	-19.22	1.29	-	5.49	0.72	-	-26.70	0.85	-
12	-26.01	-0.83	-	-20.42	-7.73	-	-11.88	7.34	-
14$_{RANS}$	-21.51	-11.07	-	-24.78	-10.23	-	-4.41	-4.29	-
14$_{DES}$	-	-12.01	-	-	-5.60	-	-	-13.92	-

*C_L dynamic range = 0.80

**C_D dynamic range = 0.19

***C_M dynamic range = 0.22

Table 8: CFD hydrodynamic efficiency including errors with respect to EFD (type I)

α	Re = 0.2x10^6			Re = 0.6x10^6			Re = 1.0x10^6		
	CFD	EFD	E%D	CFD	EFD	E%D	CFD	EFD	E%D
2	10.86	13.96	-22.24	12.43	14.52	-14.43	13.39	18.95	-29.32
4	17.01	17.87	-4.84	19.08	27.43	-30.44	20.25	27.40	-26.12
6	18.56	17.72	4.76	20.55	22.59	-9.04	21.54	25.05	-14.03
8	16.54	15.34	7.84	19.48	21.20	-8.13	-	-	-
10	6.70	9.73	-31.20	17.52	17.83	-1.74	-	-	-
12	4.16	4.47	-6.94	5.73	5.22	9.91	-	-	-
14$_{RANS}$	3.29	3.39	-2.95	3.76	3.85	-2.20	-	-	-
14$_{DES}$	-	-	-	3.55		-7.81	-	-	-

The steady behavior of the flow predicted by the CFD for pre-stall conditions is shown in Figure 40 and Figure 41 at Re equal to $0.6\text{x}10^6$ and α equal to 8 degrees. Specifically, the first figure depicts a rake of streamlines starting upstream of the body at y = 0 and colored by non-dimensional x-velocity $u^* = \frac{u}{U_\infty}$. The streamlines indicate that the flow stays attached to the body and a vortex is generated at the tip of the hydrofoil, responsible for the generation of lift at non-zero α. The second figure shows the u^* contours over a y-section at 50% of the span. The flow accelerates on the upper part of the body, while it decelerates on the lower forming the wake at the trailing edge with no separation.

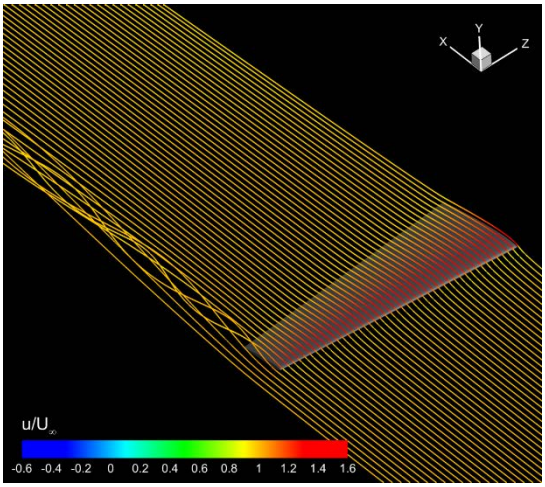

Figure 40: CFD streamlines for Re = $0.6\text{x}10^6$ and α = 8 (type I)

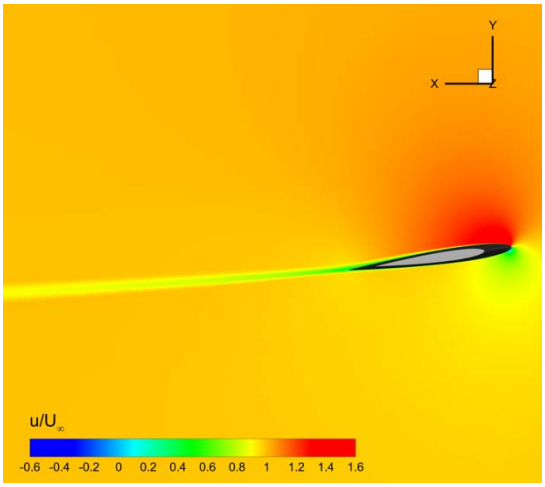

Figure 41: CFD x-velocity contour for Re = $0.6\text{x}10^6$ and α = 8 at 50% of the span (type I)

At post-stall conditions, the flow is unsteady. Streamlines and velocity contour are shown in Figure 42 and Figure 43. The flow separates close to the leading edge becoming strongly turbulent Figure 44 and Figure 45 show the iso-surfaces and contour of Q, the second invariant of the rate of strain tensor.

Since the flow shows strong turbulence in post-stall, DES simulation is additionally performed for Re equal to $0.6\text{x}10^6$ and α equal to 14 degrees to capture a higher frequency content than the RANS simulation. Streamlines and velocity contour are shown in Figure 46 and Figure 47. The Q criterion is shown in Figure 48 and Figure 49. Overall, the DES simulation allows for a higher resolution of the post-stall turbulence. This effect is shown by the spectral density, displayed in Figure 50, and time histories of the signals, shown in

Figure 51 to Figure 53 for RANS and DES, respectively. The DES simulation can capture the vortex shedding frequency, which is about 50 Hz and correlates well with the frequencies emerging from the spectral analysis of the experimental data (Zarruk et al. 2014).

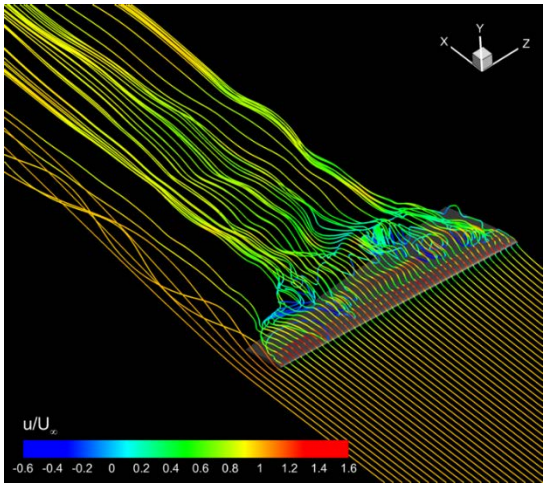

Figure 42: CFD streamlines for Re = 0.6×10^6 and α = 14 (type I, RANS)

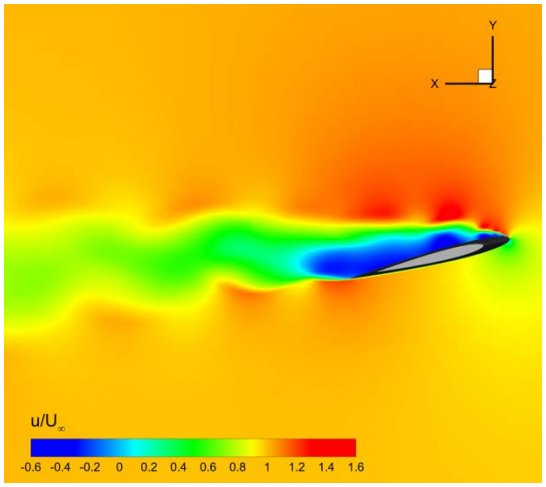

Figure 43: CFD *x*-velocity contour for Re = 0.6×10^6 and α = 14 at 50% of the span (type I, RANS)

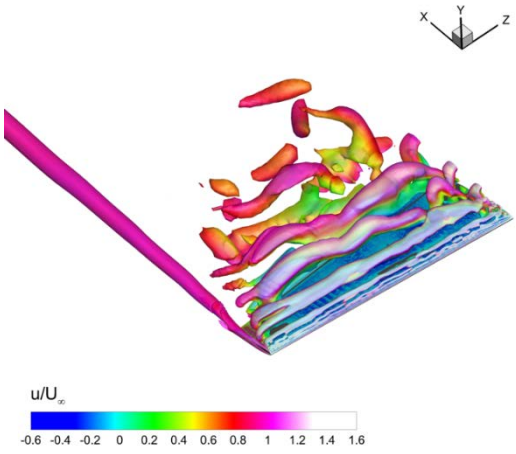

Figure 44: CFD iso-surface at Q = 150 for Re = 0.6×10^6 and α = 14 (type I, RANS)

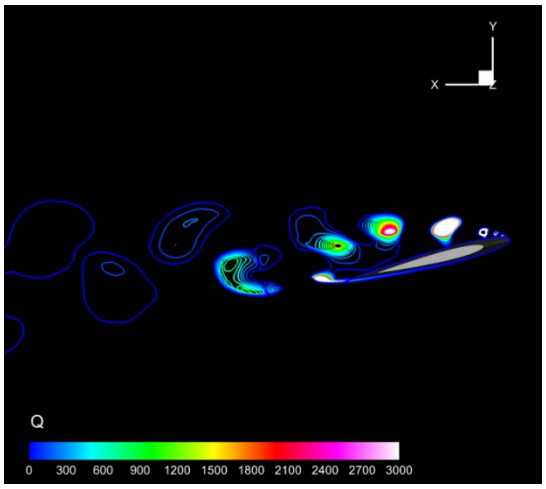

Figure 45: CFD Q contour for Re = 0.6×10^6 and α = 14 at 50% of the span (type I, RANS)

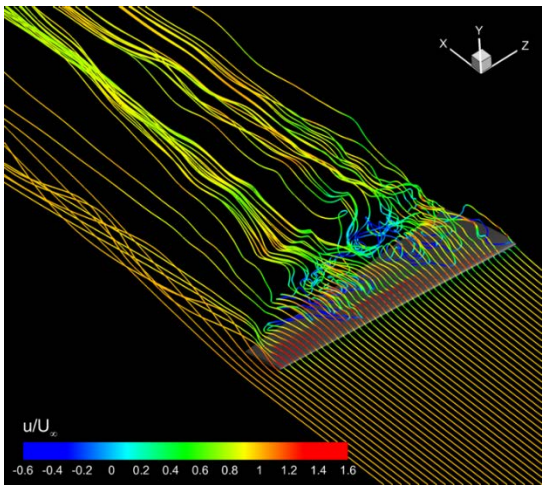

Figure 46: CFD streamlines for Re = 0.6×10^6 and $\alpha = 14$ (type I, DES)

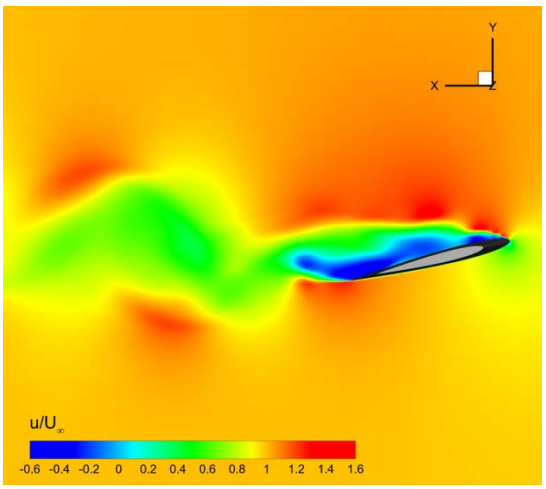

Figure 47: CFD *x*-velocity contour for Re = 0.6×10^6 and $\alpha = 14$ at 50% of the span (type I, DES)

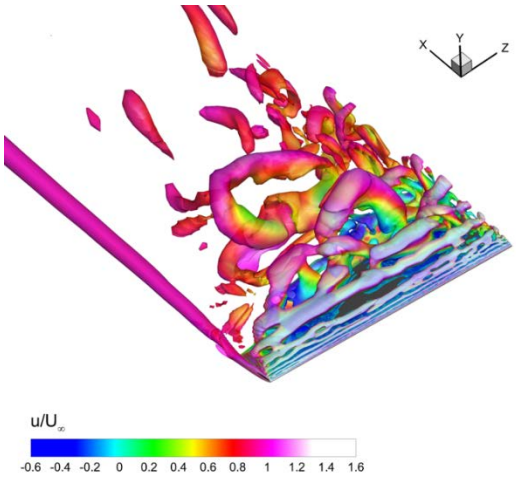

Figure 48: CFD iso-surface at $Q = 150$ for Re = 0.6×10^6 and $\alpha = 14$ (type I, DES)

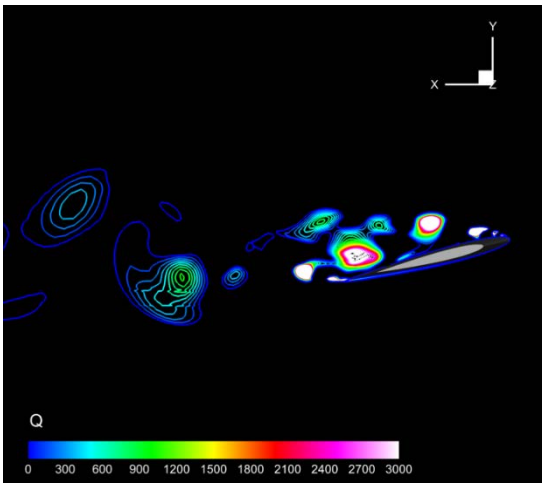

Figure 49: CFD Q contour for Re = 0.6×10^6 and $\alpha = 14$ at 50% of the span (type I, DES)

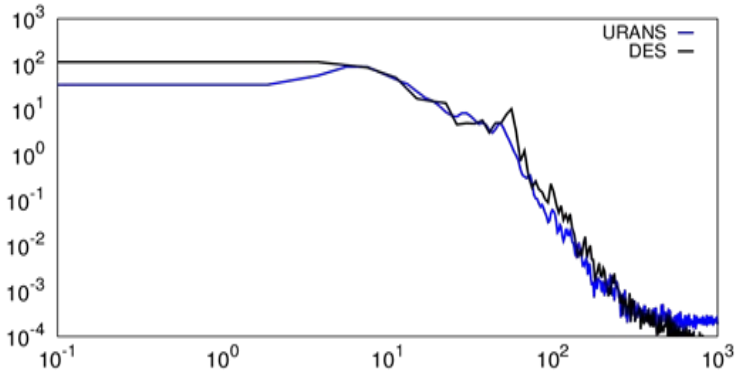

Figure 50: CFD FFT of normal force

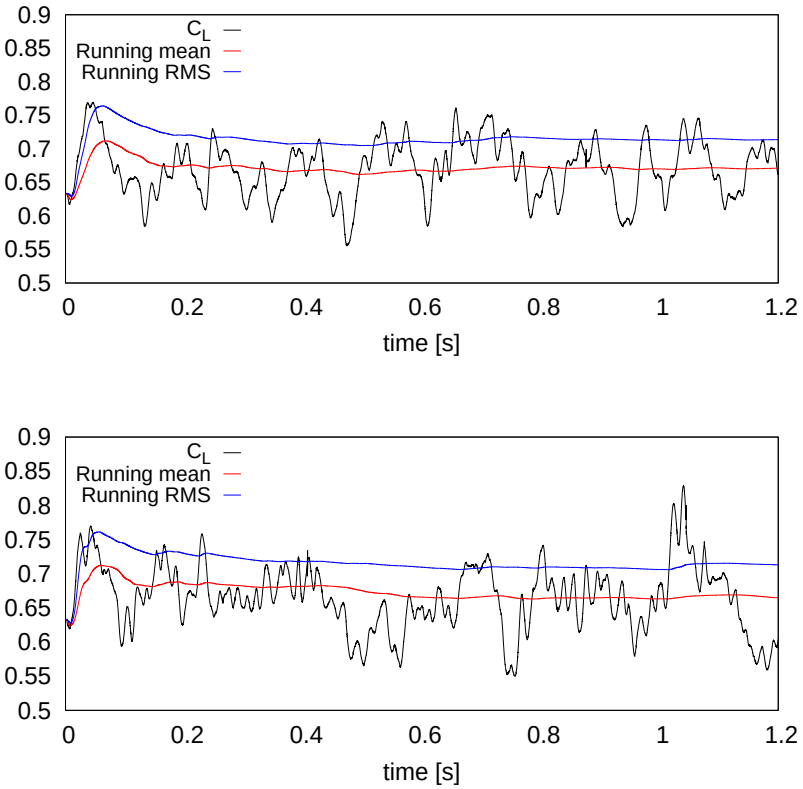

Figure 51: CFD time history of the lift coefficient using RANS (top) and DES (bottom)

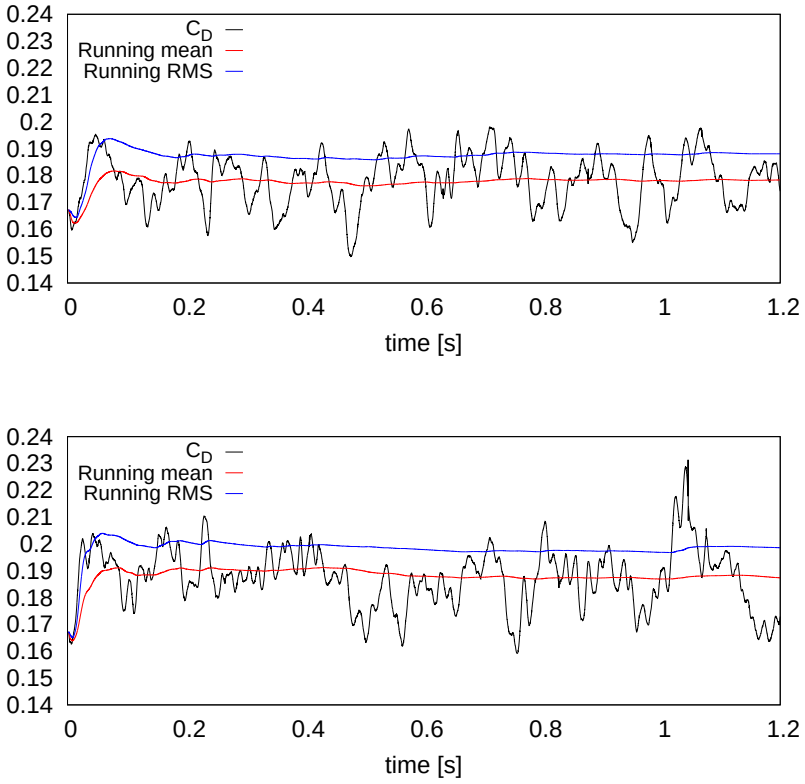

Figure 52: CFD time history of the drag coefficient using RANS (top) and DES (bottom)

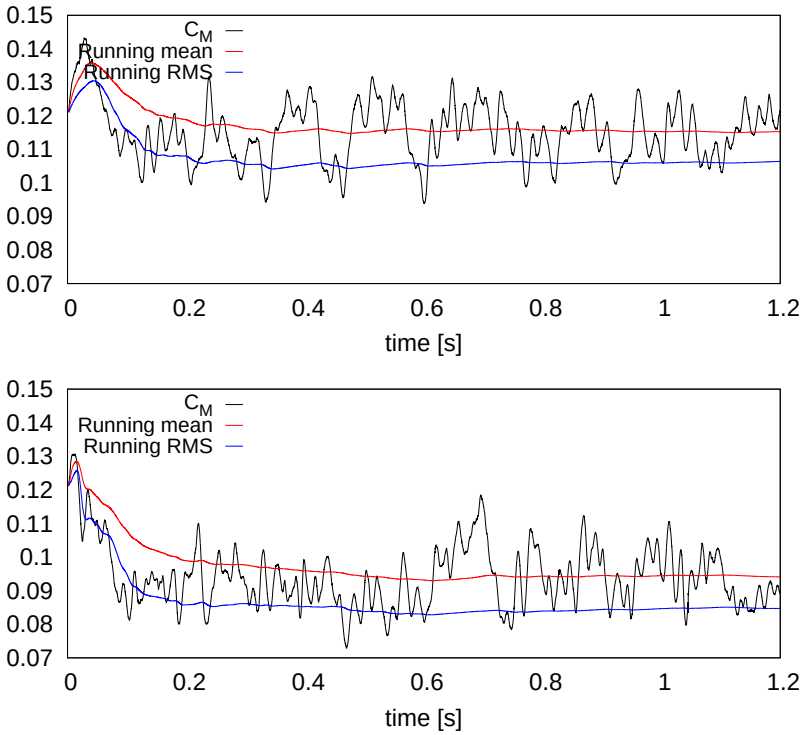

Figure 53: CFD time history of the pitching moment coefficient using RANS (top) and DES (bottom)

Type II geometry

C_L, C_D, and C_M from type II CFD simulation are shown in Figure 54 including EFD data from SS type II. RANS simulation is used for α up to 8 degrees, while DES simulation is used for larger angles. For pre-stall conditions, the agreement is very good for all Re. For post-stall conditions, CFD results at Re = 0.2 and 0.6×10^6 indicate a larger reduction in C_L than shown by EFD data. For Re = 0.2×10^6 the stall angle is under-estimate while it is over-estimated for Re = 0.6×10^6. Errors between CFD and EFD for forces and moment coefficients are reported in Table 9 as percentage of the dynamic range. The average error for pre-stall conditions is 1.08% and is 15.6% for post-stall.

The hydrodynamic efficiency is summarized in Table 10 for all Re and α values. The maximum value given by the EFD and CFD is reached at α equal to 6 degrees for all Re numbers.

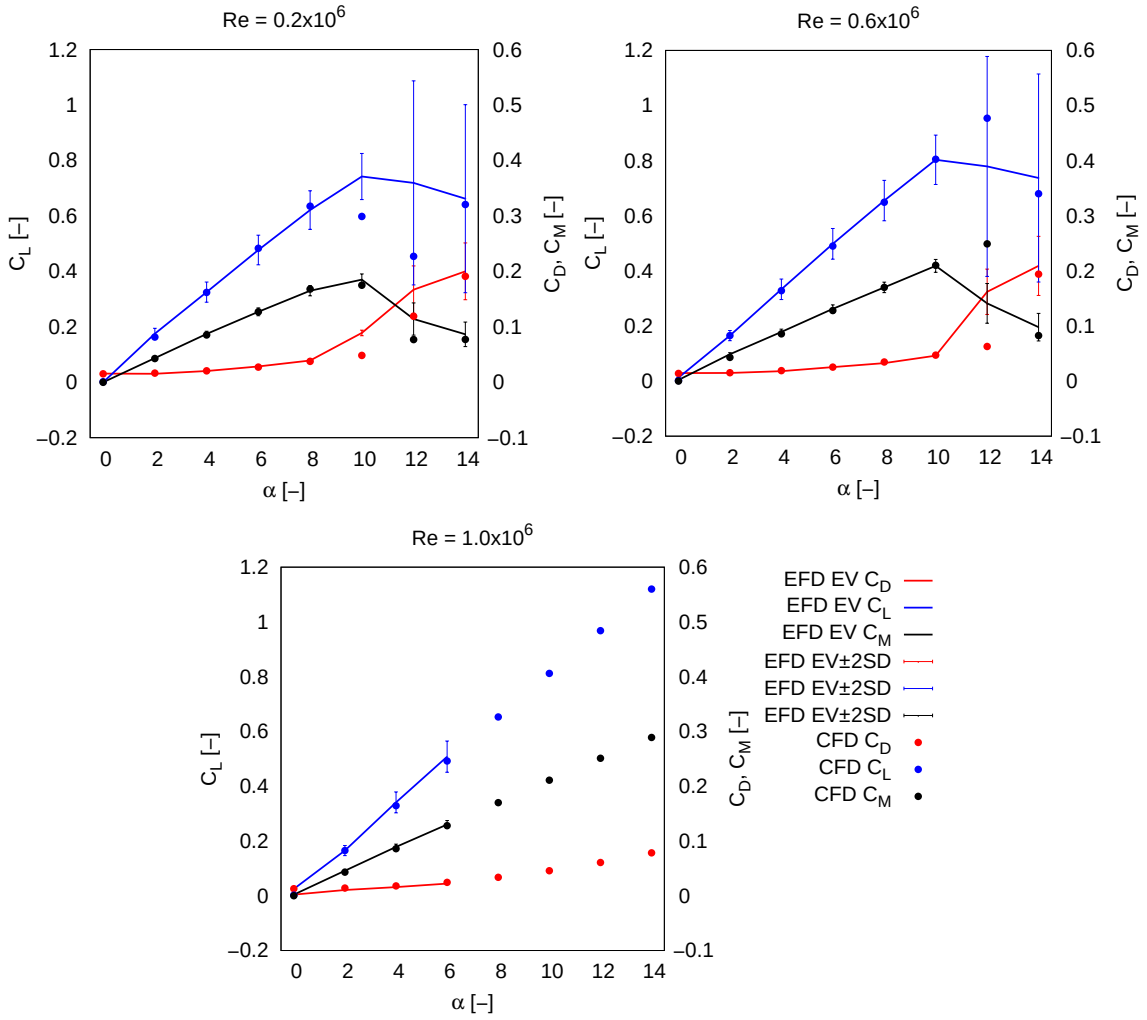

Figure 54: CFD lift, drag, and pitching moment coefficients (type II)

Table 9: CFD lift, drag, and pitching moment coefficient errors with respect to EFD (type II)

α	C_L E%$_{range}$*			C_D E%$_{range}$**			C_M E%$_{range}$***		
	Re = 0.2x10^6	Re = 0.6x10^6	Re = 1.0x10^6	Re = 0.2x10^6	Re = 0.6x10^6	Re = 1.0x10^6	Re = 0.2x10^6	Re = 0.6x10^6	Re = 1.0x10^6
0	0.24	-1.30	-2.87	-0.22	-0.39	5.57	0.00	-1.00	-0.99
2	-1.52	-0.06	0.01	0.61	0.20	1.83	-0.41	-2.84	-1.29
4	-0.15	-0.59	-1.47	0.11	0.52	1.13	-0.88	-1.70	-1.63
6	0.71	-1.01	-2.06	-0.55	0.03	1.15	0.41	-1.27	-0.64
8	1.73	-0.66	-	-0.82	0.84	-	1.62	0.06	-
10	-18.29	0.29	-	-20.85	0.53	-	-4.52	0.86	-
12	-33.49	22.09	-	-24.57	-50.73	-	-17.77	52.42	-
14	-2.71	-7.30	-	-4.56	-7.84	-	-4.48	-7.45	-

*C_L dynamic range = 0.80

**C_D dynamic range = 0.19

***C_M dynamic range = 0.22

Table 10: CFD hydrodynamic efficiency including errors with respect to EFD (type II)

α	Re = 0.2x10^6			Re = 0.6x10^6			Re = 1.0x10^6		
	CFD	EFD	E%D	CFD	EFD	E%D	CFD	EFD	E%D
2	9.90	11.47	-13.67	10.96	11.28	-2.88	11.73	15.70	-25.30
4	15.83	16.05	-1.37	17.35	18.59	-6.69	18.25	21.53	-15.22
6	17.71	16.84	5.16	19.35	19.71	-1.83	20.16	22.93	-12.07
8	16.90	15.86	6.53	18.97	20.08	-5.52	-	-	-
10	12.37	8.34	48.21	17.09	17.42	-1.91	-	-	-
12	3.82	4.31	-11.35	15.21	4.82	215.24	-	-	-
14	3.35	3.31	1.26	3.50	3.52	-0.57	-	-	-

Solution verification

The numerical uncertainty U_{SN} of the steady simulations depend on the grid uncertainty U_g and on the iterative uncertainty U_i. U_{SN} is defined as

$$U_{SN} = \sqrt{U_g^2 + U_i^2} \tag{72}$$

The grid convergence study, aimed at finding U_g, is carried out following Mousaviraad et al. (2013). Three solutions, S1, S2, and S3, characterized by systematic refinement ratio

$$r = \frac{\Delta x_1}{\Delta x_2} = \frac{\Delta x_2}{\Delta x_3} = \sqrt{2} \tag{73}$$

are assessed provided by the coarse, medium, and fine grids (G3, G2, and G1), respectively. The changes in solution are

$$\begin{aligned} \varepsilon_{21} &= \mathrm{S2} - \mathrm{S1} \\ \varepsilon_{32} &= \mathrm{S3} - \mathrm{S2} \end{aligned} \tag{74}$$

and the convergence ratio *R* is defined by

$$R = \frac{\varepsilon_{21}}{\varepsilon_{32}} \tag{75}$$

The convergence is evaluated according to the following criteria:

$$\begin{gathered} \text{Monotonic convergence if } 0 < R < 1 \\ \text{Oscillatory convergence if } -1 < R < 0 \\ \text{Monotonic divergence if } R > 1 \\ \text{Oscillatory divergence if } R < -1 \end{gathered} \tag{76}$$

The change in C_L, C_D, and C_M versus mesh size is given in Table 11 for the simulation of a type II geometry with α = 8 at Re = 0.6x10^6. C_L and C_D show monotonic convergence while C_M shows monotonic divergence.

Table 11: CFD grid study

Parameter	G1	G2	G3	ε_{12}	ε_{23}	R	Result
C_L	0.6497	0.6527	0.6561	0.0030	0.0034	0.8819	monothonic convergence
C_D	0.0343	0.0348	0.0353	0.0005	0.0005	0.9620	monothonic convergence
C_M	0.1703	0.1705	0.1707	0.0003	0.0002	1.3079	monothonic divergence

The Richardson extrapolation (RE) can be used for C_L and C_D to estimate the order of accuracy p_{RE} and the error estimate δ_{RE}

$$p_{RE} = \frac{\ln\left(\frac{1}{R}\right)}{\ln r}$$
$$\delta_{RE} = \frac{\varepsilon_{32}}{r^{p_{RE}} - 1} \tag{77}$$

The distance between the solution and the asymptotic range is measured by the ratio $P = p_{RE}/p$ where p is the theoretical order of accuracy and equal to 2 for the numerical scheme used in CFDShip-Iowa. For solution in the asymptotic range, P should be equal to one. The factor of safety method (Xing and Stern 2010) can be applied for the assessment of the U_g as per

$$U_g = \begin{cases} (2.45 - 0.85P)|\delta_{RE}|, & 0 < P \leq 1 \\ (16.4P - 14.8)|\delta_{RE}|, & P > 1 \end{cases} \tag{78}$$

U_i is evaluated considering the range of variation of the output of interest at simulation convergence. Table 12 provides the uncertainty value. The numerical uncertainty associated to the steady C_L and C_D is 6.3% and 3.1%, respectively.

Table 12: CFD verification

Parameter	G1 result	p_{RE}	δ_{RE}	P	U_g%	U_i%	U_{SN}%
C_L	0.6497	0.4370	0.0180	0.2185	6.2766	0.0551	6.2768
C_D	0.0343	1.4992	0.0006	0.7496	3.0499	0.1493	3.0535

Structural dynamics

The first five natural frequencies in vacuum, air, and water are given in Table 13, Table 14, and Table 15. The first natural frequency predicted with the FE analysis is validated against experimental data in Table 16. The largest error occurs for the AL type II hydrofoil while the smallest for the CFRP00 hydrofoil. The average among all models is 8.2%. Figure 55, Figure 56, and Figure 57 show the mode shapes for the SS, AL, and composite material hydrofoils, respectively.

Table 13: CSD natural frequencies in vacuum

Mode	f_n [Hz]					
	SS	AL	SS	AL	CFRP00	CFRP30
	Type I	Type I	Type II	Type II	Type II	Type II
1	105.30	109.25	105.18	109.12	119.18	77.801
2	441.31	457.85	440.31	456.82	385.59	315.16
3	781.54	810.83	752.14	780.34	457.39	524.80
4	1073.0	1113.2	1072.8	1113.0	834.32	732.91
5	1077.5	1117.9	1111.8	1153.5	996.30	806.84

Table 14: CSD natural frequencies in air

Mode	f_n [Hz]					
	SS	AL	SS	AL	CFRP00	CFRP30
	Type I	Type I	Type II	Type II	Type II	Type II
1	105.27	109.60	105.18	108.97	116.62	76.610
2	441.24	457.19	440.37	456.30	375.70	306.26
3	781.75	810.24	753.28	780.85	432.70	504.18
4	1073.0	1113.2	1073.3	1112.3	799.80	699.59
5	1077.5	1116.6	1111.2	1152.9	917.93	810.79

Table 15: CSD natural frequencies in water

Mode	f_n [Hz]					
	SS	AL	SS	AL	CFRP00	CFRP30
	Type I	Type I	Type II	Type II	Type II	Type II
1	70.626	51.030	71.352	51.804	29.214	19.077
2	303.56	222.16	307.07	226.21	135.37	98.395
3	584.02	451.29	580.91	455.45	156.09	202.68
4	759.33	562.31	769.89	576.64	326.33	259.98
5	1067.9	965.16	1106.2	977.57	361.46	436.79

Table 16: CSD first natural frequencies in air including errors with respect to ESD

Model	f_n [Hz]		
	CSD	ESD	E%D
SS – type I	105.27	100	5.27
AL –type I	109.60	100	9.70
SS – type II	105.18	96	9.79
AL – type II	108.97	96	13.9
CFRP00	116.62	112	4.13
CFRP30	76.610	72	6.40

Mode	Type I		Type II	
	Vacuum/air	Water	Vacuum/air	Water
1	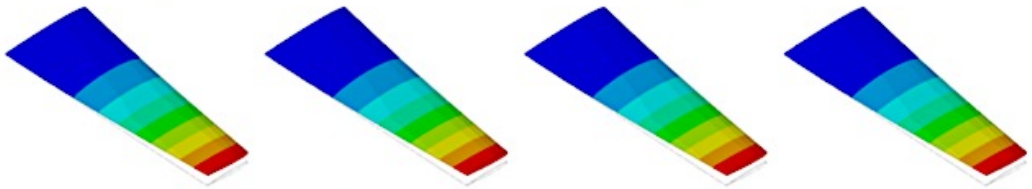			
	y-bending 1	y-bending 1	y-bending 1	y-bending 1
2	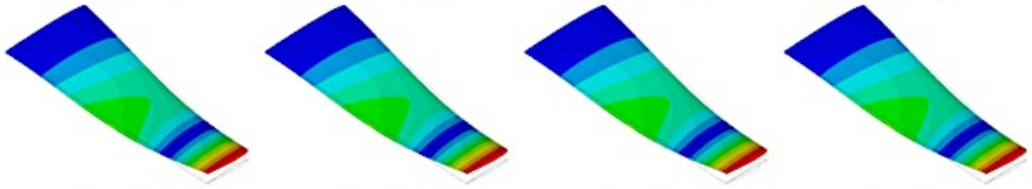			
	y-bending 2	y-bending 2	y-bending 2	y-bending 2
3	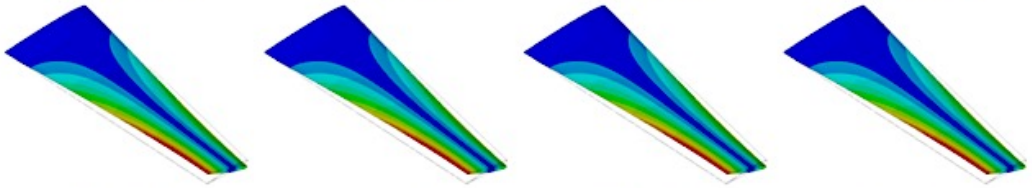			
	Twist 1	Twist 1	Twist 1	Twist 1
4	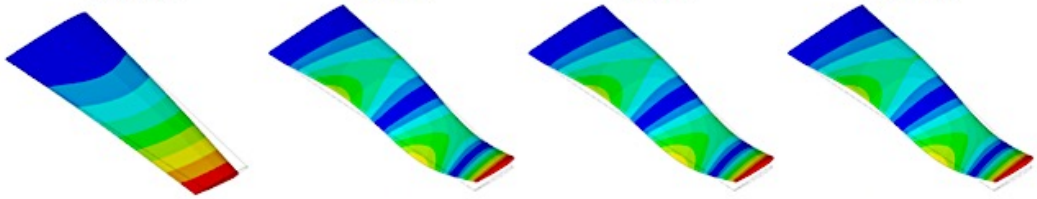			
	x-bending 1	y-bending 3	y-bending 3	y-bending 3
5	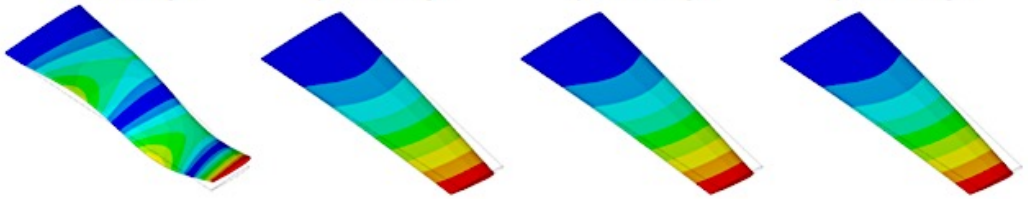			
	y-bending 3	x-bending 1	x-bending 1	x-bending 1

Figure 55: CSD SS hydrofoils mode shapes

Mode	Type I		Type II	
	Vacuum/air	Water	Vacuum/air	Water
1	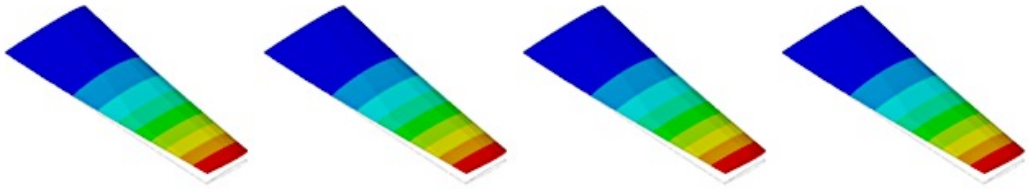			
	y-bending 1	y-bending 1	y-bending 1	y-bending 1
2	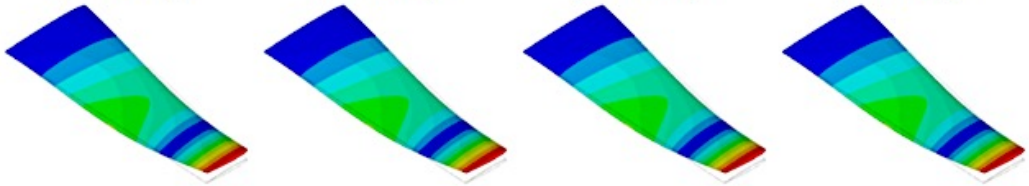			
	y-bending 2	y-bending 2	y-bending 2	y-bending 2
3	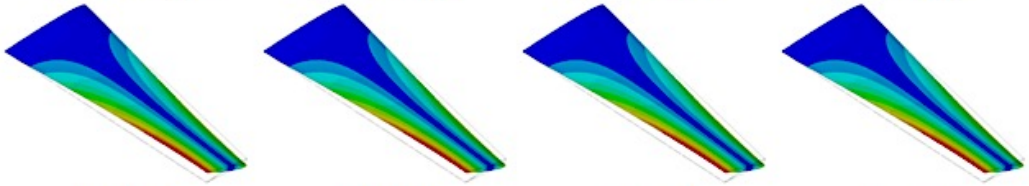			
	Twist 1	Twist 1	Twist 1	Twist 1
4	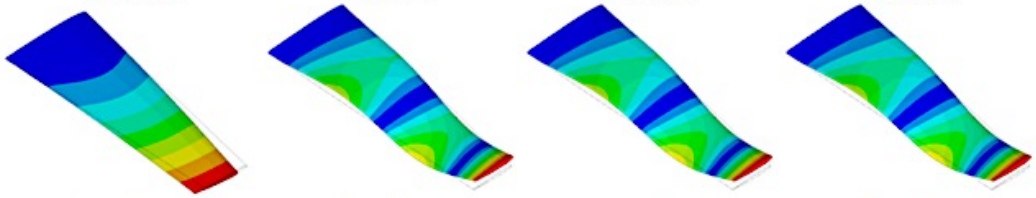			
	x-bending 1	y-bending 3	y-bending 3	y-bending 3
5	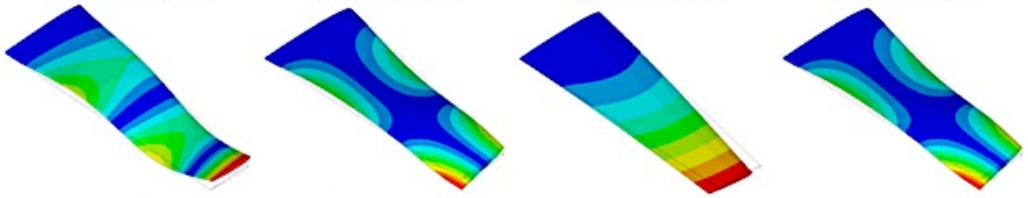			
	y-bending 3	Twist 2	x-bending 1	Twist 2

Figure 56: CSD AL hydrofoils mode shapes

Mode	CFRP00		CFRP30	
	Vacuum/air	Water	Vacuum/air	Water
1	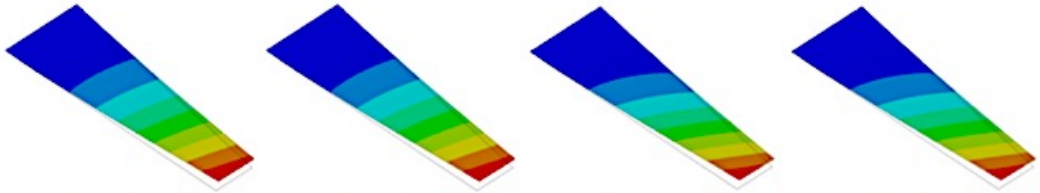			
	y-bending 1	y-bending 1	y-bending 1	y-bending 1
2	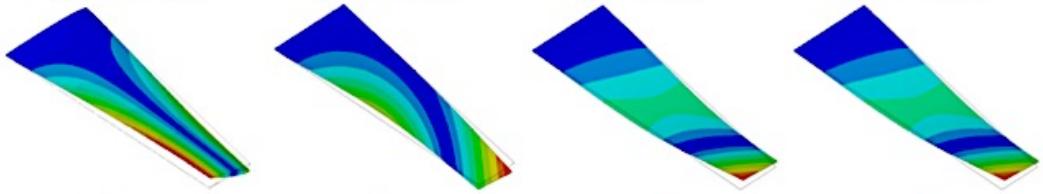			
	Twist 1	Mixed	y-bending 2	y-bending 2
3	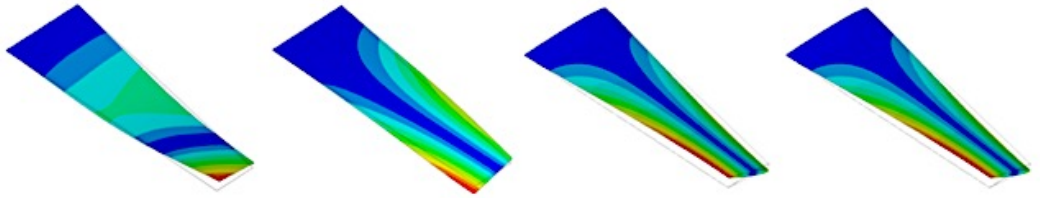			
	y-bending 2	Mixed	Twist 1	Twist 1
4	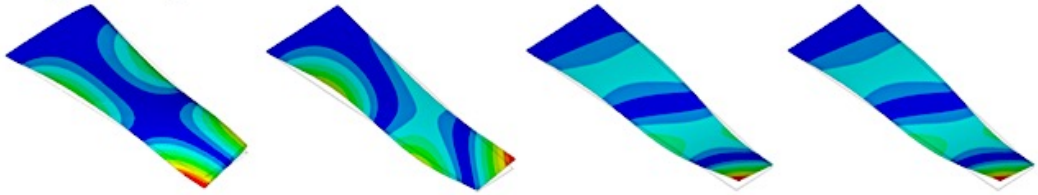			
	Twist 2	Mixed	y-bending 3	y-bending 3
5	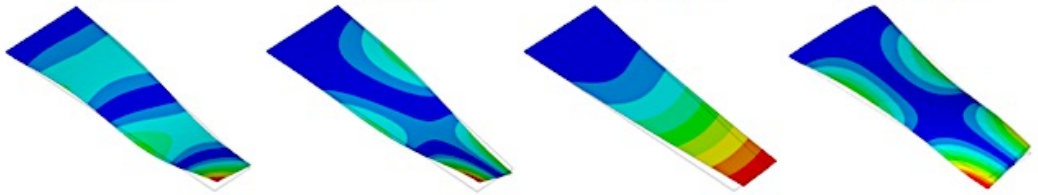			
	y-bending 3	Mixed	x-bending 1	Twist 2

Figure 57: CSD CFRP hydrofoils mode shapes

Grid study

Dry frequency change versus mesh size is given in Table 17 to Table 22 for SS and AL types I and II hydrofoils and CFRP00 and CFRP30 type II hydrofoils. The first five frequencies are evaluated and show monotonic convergence in all cases but the second frequency of the CFRP00 hydrofoil which shows oscillatory convergence. Table 23 gives, as example, the change in wet frequency in water versus acoustic domain size for one model, namely the CFRP00. The G2 body mesh is used for all domains sizes. Monotonic convergence is achieved for all frequencies but the CFRP00 second frequency in vacuum, which shows oscillatory convergence.

Table 17: CSD grid study for dry natural frequencies of the SS type I hydrofoil (vacuum)

Mode	f_n [Hz]			ε_{12}	ε_{23}	R	Result
	G1	G2	G3				
1	105.3	105.35	105.46	0.05	0.11	0.45	monothonic convergence
2	441.31	441.53	442.11	0.22	0.58	0.38	monothonic convergence
3	781.54	782.15	783.92	0.61	1.77	0.34	monothonic convergence
4	1073	1073	1073.1	0.00	0.10	0.00	monothonic convergence
5	1077.5	1078.1	1080	0.60	1.90	0.32	monothonic convergence

Table 18: CSD grid study for dry natural frequencies of the SS type II hydrofoil (vacuum)

Mode	f_n [Hz]			ε_{12}	ε_{23}	R	Result
	G1	G2	G3				
1	109.25	109.3	109.41	0.05	0.11	0.45	monothonic convergence
2	457.85	458.08	458.69	0.23	0.61	0.38	monothonic convergence
3	810.83	811.47	813.31	0.64	1.84	0.35	monothonic convergence
4	1113.2	1113.2	1113.3	0.00	0.10	0.00	monothonic convergence
5	1117.9	1118.5	1120.5	0.60	2.00	0.30	monothonic convergence

Table 19: CSD grid study for dry natural frequencies of the AL type I hydrofoil (vacuum)

Mode	f_n [Hz]			ε_{12}	ε_{23}	R	Result
	G1	G2	G3				
1	105.18	105.25	105.4	0.07	0.15	0.47	monothonic convergence
2	440.31	440.64	441.4	0.33	0.76	0.43	monothonic convergence
3	752.14	753.58	756.53	1.44	2.95	0.49	monothonic convergence
4	1072.8	1073.8	1076.3	1.00	2.50	0.40	monothonic convergence
5	1111.8	1111.2	1110.3	-0.60	-0.90	0.67	monothonic convergence

Table 20: CSD grid study for dry natural frequencies of the AL type II hydrofoil (vacuum)

Mode	f_n [Hz]			ε_{12}	ε_{23}	R	Result
	G1	G2	G3				
1	109.12	109.2	109.36	0.08	0.16	0.50	monothonic convergence
2	456.82	457.16	457.95	0.34	0.79	0.43	monothonic convergence
3	780.34	781.83	784.89	1.49	3.06	0.49	monothonic convergence
4	1113	1114	1116.7	1.00	2.70	0.37	monothonic convergence
5	1153.5	1152.9	1151.9	-0.60	-1.00	0.60	monothonic convergence

Table 21: CSD grid study for dry natural frequencies of the CFRP00 hydrofoil (vacuum)

Mode	f_n [Hz]			ε_{12}	ε_{23}	R	Result
	G1	G2	G3				
1	119.18	119.04	118.75	-0.14	-0.29	0.48	monothonic convergence
2	385.59	385.84	385.55	0.25	-0.29	-0.86	oscillatory convergence
3	457.39	457.04	456.22	-0.35	-0.82	0.43	monothonic convergence
4	834.32	834.31	833.88	-0.01	-0.43	0.02	monothonic convergence
5	996.3	995.71	994.37	-0.59	-1.34	0.44	monothonic convergence

Table 22: CSD grid study for dry natural frequencies of the CFRP30 hydrofoil (vacuum)

Mode	f_n [Hz]			ε_{12}	ε_{23}	R	Result
	G1	G2	G3				
1	77.801	77.771	77.52	-0.03	-0.25	0.12	monothonic convergence
2	315.16	314.87	314.23	-0.29	-0.64	0.45	monothonic convergence
3	524.8	525	525.22	0.20	0.22	0.91	monothonic convergence
4	732.91	732.36	731.1	-0.55	-1.26	0.44	monothonic convergence
5	806.84	804.93	801.71	-1.91	-3.22	0.59	monothonic convergence

Table 23: CSD grid study for wet natural frequencies of the CFRP00 hydrofoil (water)

Mode	f_n [Hz]			ε_{12}	ε_{23}	R	Result
	D1	D2	D3				
1	29.214	29.251	29.65	0.04	0.40	0.09	monothonic convergence
2	135.37	135.72	137.43	0.35	1.71	0.20	monothonic convergence
3	156.09	156.84	158.51	0.75	1.67	0.45	monothonic convergence
4	326.33	327.2	329.99	0.87	2.79	0.31	monothonic convergence
5	361.46	363.03	367.76	1.57	4.73	0.33	monothonic convergence

Fluid-structure interaction

One-way coupling

This section presents the results for the FSI test case 1, for which a one-way coupling is used. Tip displacements at pre-stall conditions are depicted in Figure 58 and Figure 59 for metal and composite material, respectively. The maximum deflection occurs for each hydrofoil for the combination of largest α and largest Re. The SS hydrofoil shows the smallest deformation, with a maximum value equal to 2% of the span. The CFRP30 hydrofoil shows the largest deformation, with a maximum value equal to 16% of the span. EFD/ESM displacements are given for leading edge, mid-chord point, and trailing edge, allowing for evaluating both translation and twist of the tip section. Metal hydrofoils do not show relevant tip twist, whereas composite material hydrofoils present on average a

positive and a negative twist angle for CFRP00 and CFRP30, respectively, which are shown in Figure 60.

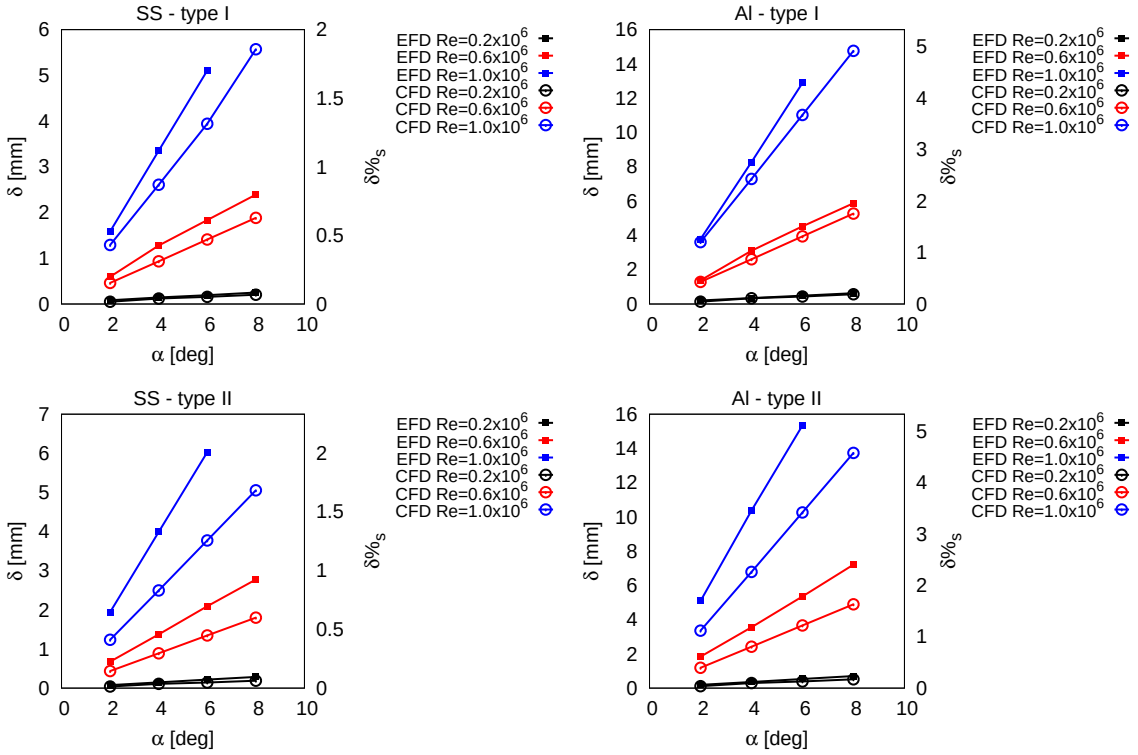

Figure 58: One-way FSI metal hydrofoil tip displacement

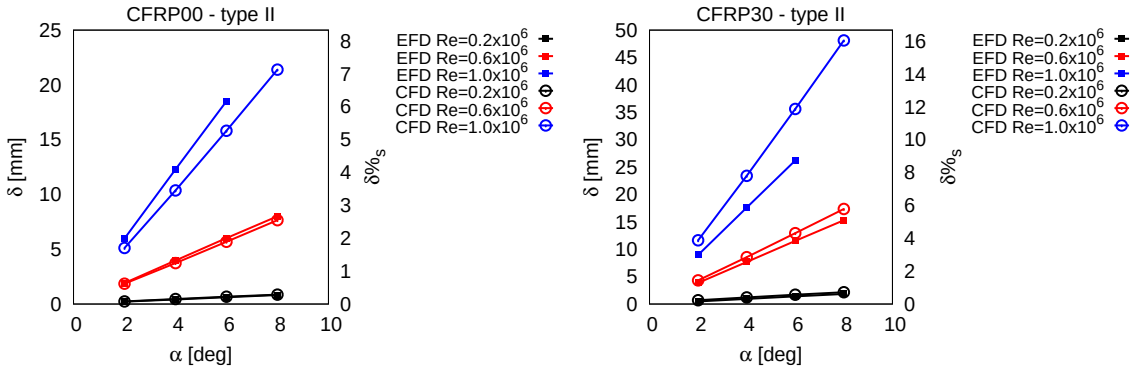

Figure 59: One-way FSI CFRP hydrofoil tip displacement

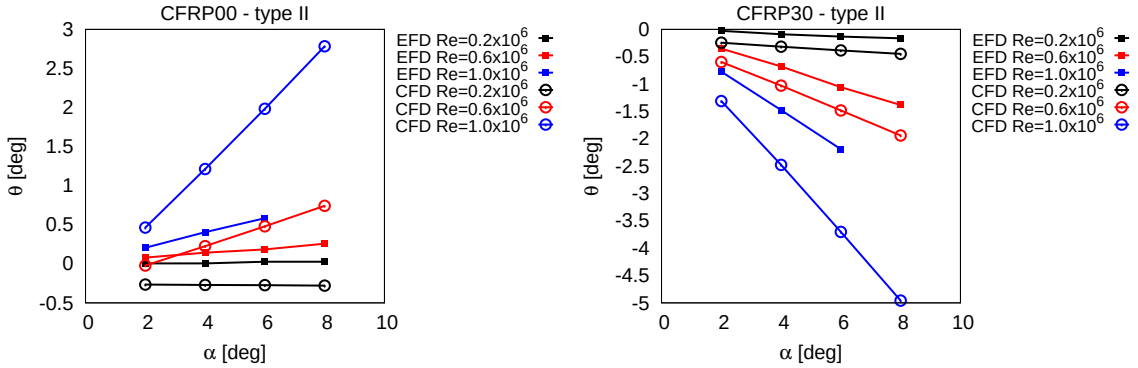

Figure 60: One-way FSI CFRP hydrofoil tip twist

Tip displacement and twist versus angle of attack are given in Table 24 and Table 25, including EFD/ESD data and percentage error. Errors for the displacement, which are expressed as percentage of the dynamic range, indicate good agreement for all hydrofoil models. A larger discrepancy is found between numerical and experimental values of tip twist for the composite materials; the error increases with Re. Nonetheless, the overall behavior of the hydrofoils is well captured.

Table 26 summarizes the errors by computing average over angles of attack and Re numbers. The maximum error for the tip displacement is given by AL type II, the minimum for SS type I. The error increases with Re. Global average error for all materials and conditions is 6.71%. For the tip twist the minimum error is found at Re = 0.6×10^6. The global average error for the twist is 38.7%.

Table 24: One-way FSI validation of tip displacement

Model	α	δ [mm] Re = 0.2x10^6			δ [mm] Re = 0.6x10^6			δ [mm] Re = 1.0x10^6		
		CFD/ CSD	EFD/ ESD	E%δ^*	CFD/ CSD	EFD/ ESD	E%δ^{**}	CFD/ CSD	EFD/ ESD	E%δ^{***}
SS type I	2	0.04	0.08	-2.15	0.41	0.60	-1.29	1.14	1.59	-1.82
	4	0.09	0.14	-2.83	0.83	1.28	-3.08	2.31	3.35	-4.23
	6	0.14	0.19	-2.97	1.26	1.84	-3.95	3.52	5.11	-6.48
	8	0.18	0.25	-3.92	1.66	2.39	-5.03	4.73	-	-
AL type I	2	0.12	0.21	-4.90	1.11	1.38	-1.85	3.10	3.78	-2.80
	4	0.25	0.35	-5.33	2.25	3.11	-5.84	6.29	8.28	-8.11
	6	0.38	0.49	-6.04	3.42	4.53	-7.57	9.56	12.89	-13.59
	8	0.50	0.63	-7.72	4.51	5.88	-9.39	12.86	-	-
SS type II	2	0.04	0.08	-1.93	0.40	0.68	-1.92	1.11	1.94	-3.40
	4	0.09	0.15	-3.16	0.81	1.37	-3.88	2.26	3.99	-7.08
	6	0.14	0.22	-4.71	1.23	2.09	-5.93	3.43	6.03	-10.62
	8	0.18	0.29	-6.19	1.65	2.78	-7.74	4.61	-	-
AL type II	2	0.12	0.19	-4.19	1.08	1.84	-5.19	3.02	5.09	-8.46
	4	0.25	0.36	-6.45	2.20	3.55	-9.30	6.13	10.37	-17.31
	6	0.37	0.53	-9.21	3.33	5.35	-13.84	9.31	15.34	-24.60
	8	0.48	0.70	-12.61	4.47	7.21	-18.77	12.53	-	-
CFRP00	2	0.20	0.22	-1.17	1.59	1.91	-2.20	4.41	5.97	-6.36
	4	0.39	0.41	-1.36	3.22	3.96	-5.05	8.94	12.26	-13.51
	6	0.57	0.62	-2.64	4.88	5.99	-7.60	13.58	18.43	-19.79
	8	0.74	0.81	-4.29	6.54	7.95	-9.69	18.26	-	-
CFRP30	2	0.54	0.47	4.02	3.64	3.85	-1.44	9.90	8.93	3.98
	4	0.98	0.93	3.20	7.28	7.66	-2.60	20.00	17.55	10.01
	6	1.41	1.40	1.02	10.99	11.48	-3.34	30.33	26.09	17.28
	8	1.80	1.83	-1.62	14.69	15.20	-3.50	40.76	-	-

*dynamic range of δ at (Re = 0.2x10^6) = 1.75 mm

**dynamic range of δ at (Re = 0.6x10^6) = 14.60 mm

***dynamic range of δ at (Re = 1.0x10^6) = 24.51 mm

Table 25: One-way FSI validation of tip twist

Model	α	θ [deg] Re = 0.2x10^6			θ [deg] Re = 0.6x10^6			θ [deg] Re = 1.0x10^6		
		CFD/ CSD	EFD/ ESD	E%θ^*	CFD/ CSD	EFD/ ESD	E%θ^{**}	CFD/ CSD	EFD/ ESD	E%θ^{***}
CFRP00	2	-0.15	0.01	-81.25	0.06	0.08	-1.42	0.46	0.20	9.28
	4	-0.15	0.01	-82.85	0.26	0.14	6.91	1.06	0.40	23.75
	6	-0.15	0.03	-94.40	0.46	0.18	16.61	1.67	0.58	39.16
	8	-0.15	0.03	-95.36	0.74	0.26	29.44	2.29	-	-
CFRP30	2	-0.15	-0.03	-67.21	-0.44	-0.35	-5.64	-1.04	-0.77	-9.48
	4	-0.21	-0.09	-65.38	-0.81	-0.68	-8.00	-2.02	-1.48	-19.59
	6	-0.27	-0.13	-73.25	-1.18	-1.06	-7.84	-3.04	-2.19	-30.65
	8	-0.32	-0.16	-84.02	-1.94	-1.38	-34.05	-4.07	-	-

*dynamic range of θ at (Re = 0.2x10^6) = 0.19 deg

**dynamic range of θ at (Re = 0.6x10^6) = 1.64 deg

***dynamic range of θ at (Re = 1.0x10^6) = 2.77 deg

Table 26 One-way FSI deformation average errors with respect to EFD/ESD

Model	Re = 0.2x10^6	Re = 0.6x10^6	Re = 1.0x10^6	Average
	δ |E|%$_{range}$			
SS type I	2.97	3.34	4.18	3.49
AL type I	6.00	6.16	8.17	6.78
SS type II	4.00	4.87	7.03	5.30
AL type II	8.12	11.78	16.79	12.23
CFRP00	2.37	6.14	13.22	7.24
CFRP30	2.47	2.72	10.42	5.20
Ave.	4.32	5.83	9.97	6.71
	θ |E|%$_{range}$			
CFRP00	88.47	13.60	24.06	42.04
CFRP30	72.47	13.88	19.91	35.42
Average	80.47	13.74	21.99	38.73

Two-way coupling

This section presents the results for the FSI test case 2 which is solved using a two-way coupling approach. Figure 61 shows the contour of the *x*-velocity over a cross-section of the hydrofoil at 95% of the span predicted by the CFD simulation. Analogously, the *x*-velocity is shown in Figure 62 to Figure 65 at convergence of the steady FSI using SS, AL, CFRP00 and CFRP30 materials. The behavior of the different materials is well captured: the SS hydrofoil shows the smallest deformation, followed by the AL one, with no significant twist of the tip section; the CFRP00 hydrofoil shows positive twist, while the CFRP30 shows negative twist of the tip.

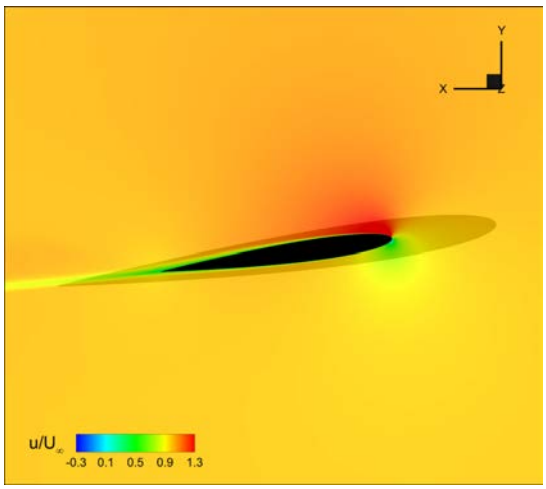

Figure 61: CFD hydrofoil *x*-velocity contour for Re = 0.6×10^6 and α = 8 at 95% of the span (rigid body model)

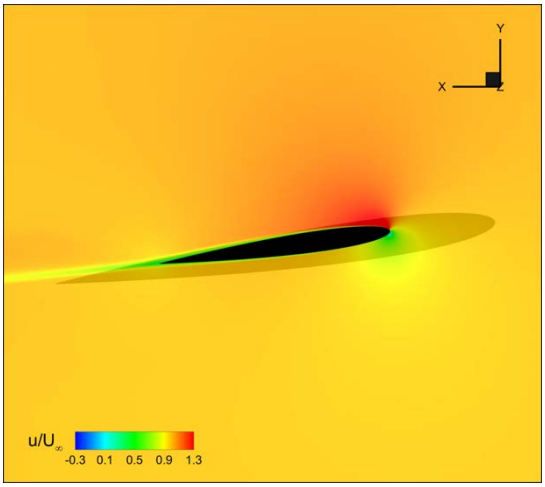

Figure 62: Two-way FSI SS type II hydrofoil displacement and *x*-velocity contour for Re = $0.6x10^6$ and α = 8 at 95% of the span

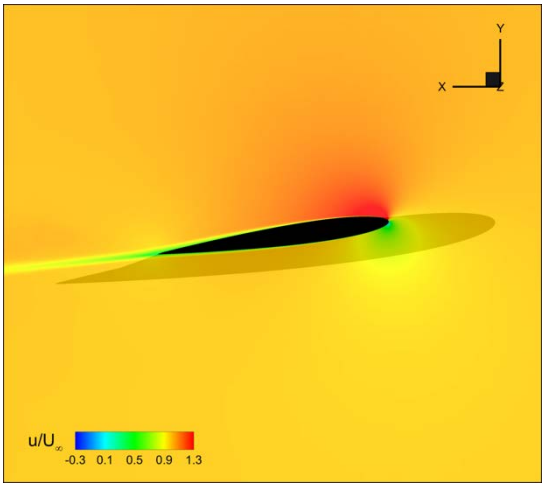

Figure 63: Two-way FSI AL type II hydrofoil displacement and *x*-velocity contour for Re = $0.6x10^6$ and α = 8 at 95% of the span

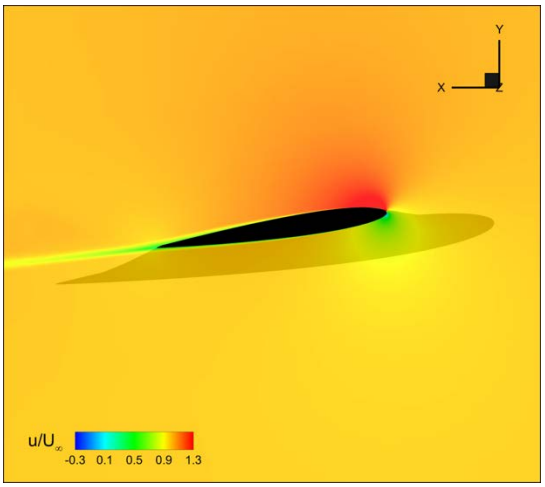

Figure 64: Two-way FSI CFRP00 hydrofoil displacement and *x*-velocity contour for Re = $0.6x10^6$ and α = 8 at 95% of the span

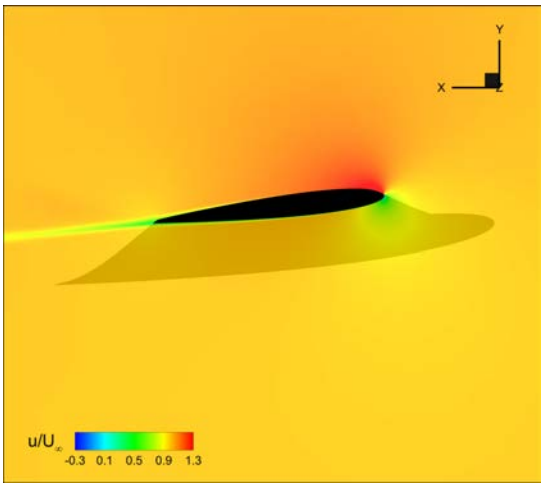

Figure 65: Two-way FSI CFRP30 hydrofoil displacement and *x*-velocity contour for Re = $0.6x10^6$ and α = 8 at 95% of the span

Since a two-way approach is used, the deformation affects the hydrodynamic forces. The tip twist is expected to change the lift according to its sign: a positive twist, as shown by the CFRP00 hydrofoil, by increasing the effective α, increases the lift; on the contrary, a negative twist, as shown by the CFRP30 hydrofoil, decreases the effective α and, consequently, the lift. Table 27 summarizes the effect of the two-way coupling on the force/moment coefficients by comparing the error with respect to the experiment provided

by pure CFD and FSI. The difference between the results is expressed by the variable Δ defined as

$$\Delta = |E\%_{FSI}| - |E\%_{CFD}| \tag{79}$$

For SS, the prediction of C_D improves, while it worsens for C_L and C_D. The AL and CFRP00 hydrofoils show the opposite trend. For CFRP30, all coefficient predictions improve with the application of the two-way FSI. Table 28 gives the error on the hydrodynamic efficiency comparing CFD and FSI. Overall, the hydrodynamic efficiency prediction worsens for SS, AL, and CFRP00 while it improves for CFRP30.

Table 27: Two-way FSI force errors with respect to EFD/ESD

Material	C_L E%range			C_D E%range			C_M E%range		
	CFD	Two-way FSI	Δ	CFD	Two-way FSI	Δ	CFD	Two-way FSI	Δ
SS	-0.66	-0.14	-0.52	0.84	0.97	0.13	0.06	-0.12	0.05
AL	-1.54	-0.45	-1.09	1.71	2.00	0.30	0.61	0.50	-0.11
CFRP00	-2.77	0.75	-2.02	-0.25	0.84	0.60	-0.92	1.45	0.52
CFRP30	7.68	2.40	-5.29	3.37	1.41	-1.96	10.25	0.91	-9.33

Table 28: Two-way FSI hydrodynamic efficiency including errors with respect to EFD/ESD

Material	*Eff*			*Eff* E%D		
	CFD	Two-way FSI	EFD/ESD	CFD	Two-way FSI	Δ
SS	18.97	18.95	20.08	-5.52	-5.61	0.09
AL		18.90	21.4	-11.37	-11.68	0.31
CFRP00		18.62	19.33	-1.89	-3.68	1.78
CFRP30		19.32	21.27	-10.84	-9.18	-1.66

Table 29: Two-way FSI deformation errors with respect to EFD/ESD

Material	δ E%$_{range}$			θ E%$_{range}$		
	CFD/CSD one-way FSI	CFD/CSD two-way FSI	Δ	CFD/CSD one-way FSI	CFD/CSD two-way FSI	Δ
SS	-7.74	-7.55	-0.19	-	-	-
AL	-8.50	-7.98	-0.52	-	-	-
CFRP00	-9.69	-4.77	-4.92	26.12	28.51	2.39
CFRP30	-3.50	-12.66	9.15	-34.05	-16.93	-17.12

The same approach is used to assess the error in the deformations (Table 29). The two-way FSI improves the prediction of tip displacement for all hydrofoil but the CFRP30. Tip twist prediction worsens for the CFRP00 hydrofoil while it significantly improves for the CFRP30. In terms of forces, the effect of the two-way coupling is small for metal hydrofoils, with 1% maximum change in the error, while it is significant for the composite hydrofoils. The CFRP30 is the case that shows a largest sensitivity to the two-way coupling (Figure 66). In terms of deformation, the two-way coupling increases the tip displacement in the hydrofoils that show positive twist, i.e. metals and CFRP00. The effect on the CFRP30 hydrofoil is that of reducing the tip displacement (Figure 67). This behavior agrees to the negative twist of the tip section, whose effect is that of reducing the effective angle of attack. However, since the CFRP30 displacement was under-predicted by the one-way FSI simulation, the error corresponding to the two-way FSI increases.

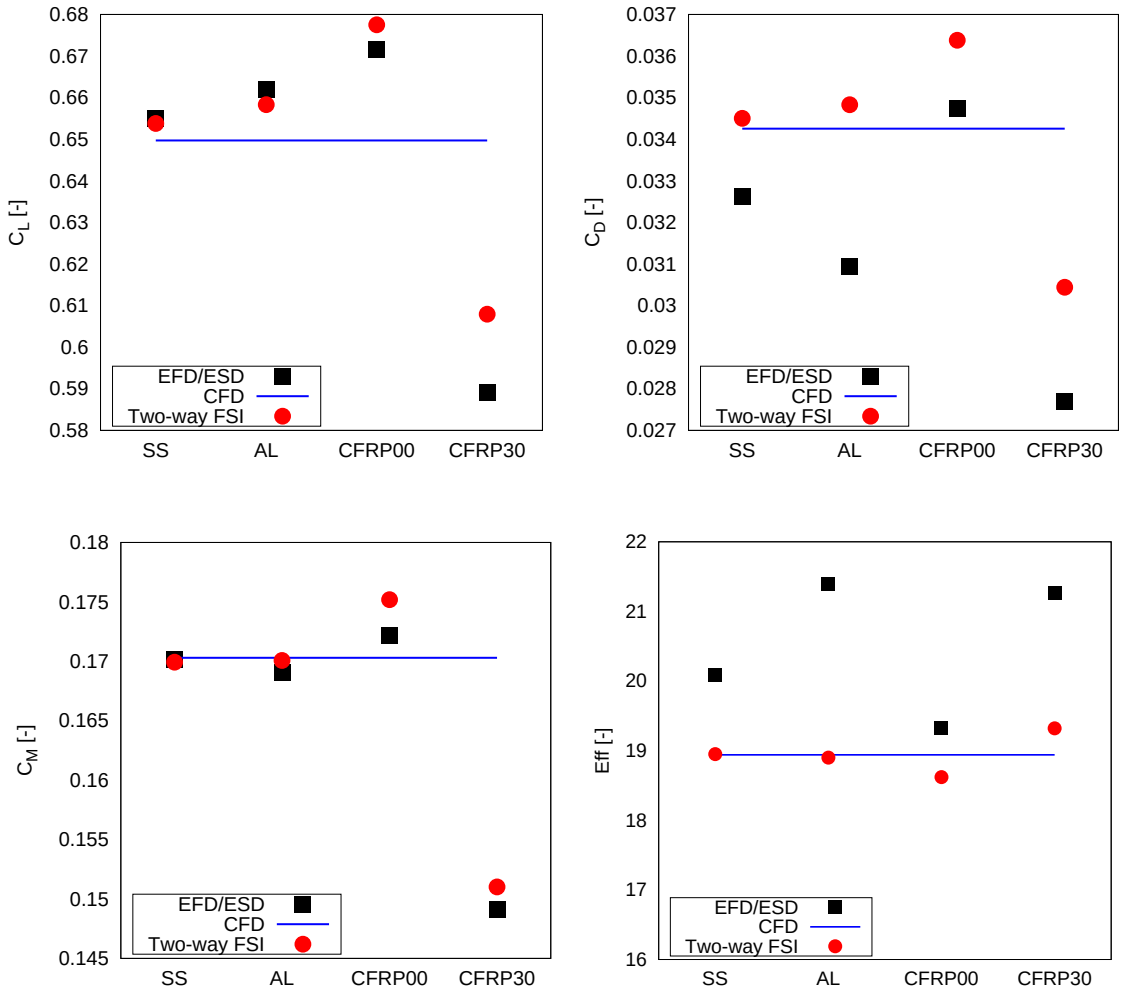

Figure 66: Two-way FSI forces including comparison with one-way FSI and EFD/ESD

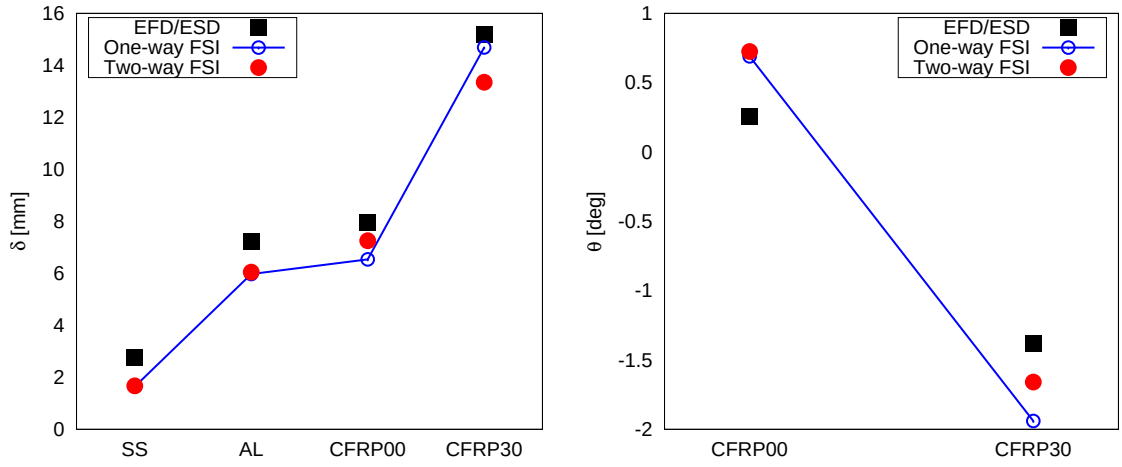

Figure 67: Two-way FSI deformations including comparison with one-way FSI and EFD/ESD

CHAPTER 6: MULTIDISCIPLINARY DESIGN OPTIMIZATION RESULTS

Analytical test problems

The solution of the two-dimensional test problem by MCAS-MDO is achieved with 86 training points and 380 function evaluations. Figure 68 shows the convergence of the optimal objective function and the convergence of the uncertainties versus the number of function evaluations intended as total and equally subdivided between disciplines. As the process advances, the discrepancy between the predicted optimal function value and the true value, evaluated by fully converged MDA for validation purposes, reduces. At each iteration, the prediction falls within the uncertainty band defined by the following overall uncertainty

$$U_{tot} = \sqrt{U_s^2 + U_c^2} \tag{80}$$

U_s, U_c, and U_{tot} reduces significantly in 6 iterations (U_{tot}~0.03%). The optimization converges as U_c reaches the prescribed threshold.

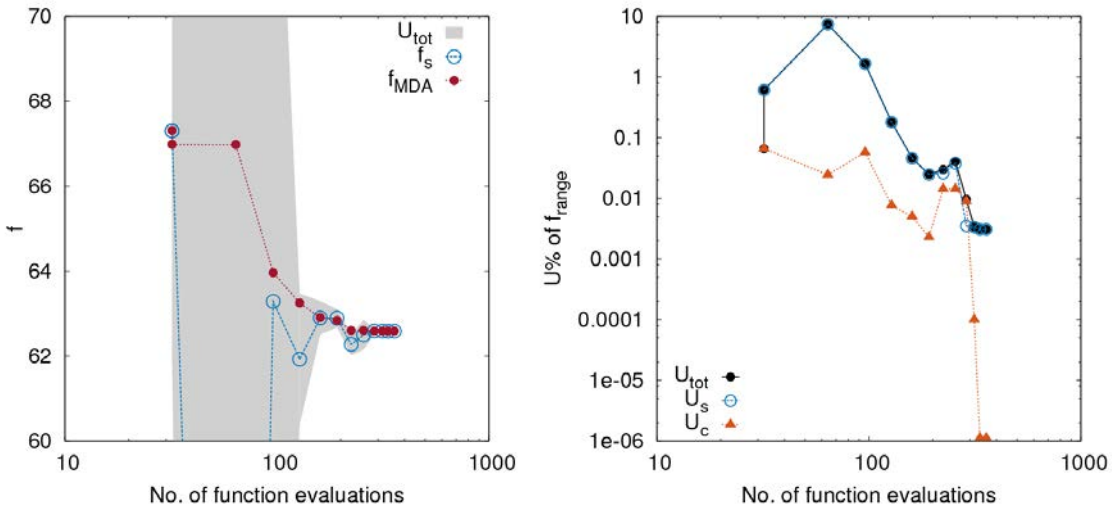

Figure 68: MCAS-MDO convergence of objective function (left) and uncertainties (right) for the two-dimensional test problem

Figure 69 shows the Pareto sets and the sampling selection for one iteration of the MCAS-MDO in order to illustrate the methodology. $\wp_s$ (yellow) and $\wp_c$ (blue) are superposed and the overall non-dominated solutions are in $\wp$ (purple). The samples are shown on the right, where green squares indicate points originally in $\wp_s$ and light blue

squares indicate a point originally in $\wp_c$. The current predicted optimum is represented by a red triangle and it is not included in the set of samples since its uncertainty is below the threshold U_{min}.

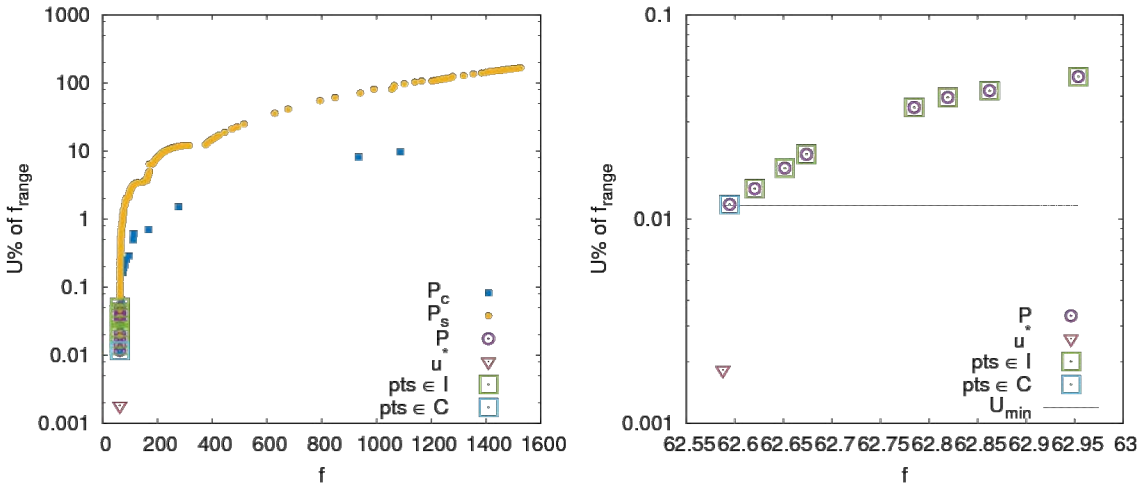

Figure 69: Pareto sets and infill/coupling samples selection

The comparison between MCAS-MDO and MDF is performed using Figure 70 to Figure 72. The acronym G-DF is put to highlight that the methods employ a global derivative-free approach. The solution by MDF is achieved with 288 training points and 2124 function evaluations. Figure 70 shows the convergence of the optimal objective function value. MCAS-MDO outperforms the MDF requiring one order of magnitude fewer function evaluations to achieve the optimum.

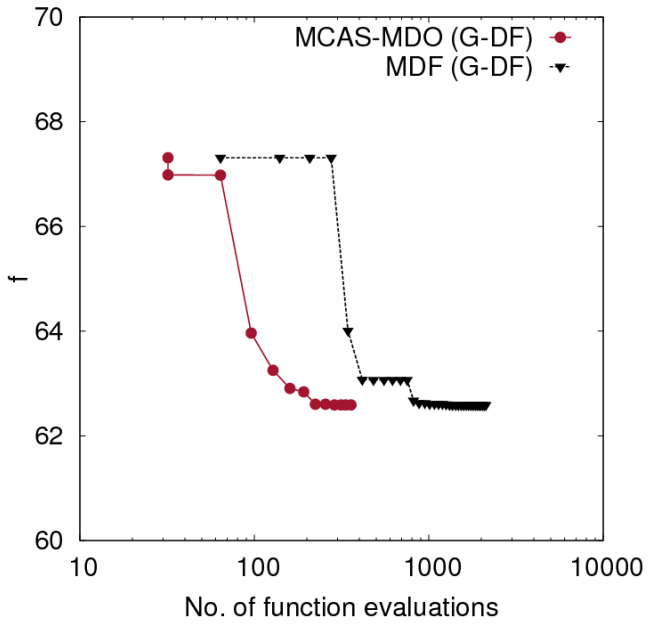

Figure 70: Convergence of objective function given by MCAS-MDO and MDF for the two-dimensional test problem

Figure 71 shows the distribution of training points in the design space. The main difference between MCAS-MDO and MDF is that the samples are more clustered around the optimum and fewer are located in regions with large objective function value. This behavior is confirmed by Figure 72 which displays the training points in the objective function-uncertainty space. MCAS-MDO samples show a correlation between U_c and f: the smaller the value of f, the smaller the associated U_c. This is significant in terms of efficient DoE, since many MDA iterations are performed only at promising locations, i.e. points with a low function value. Since in the MDF the MDA is iterated until reaching a prescribed $U_c^{(tol)}$ over the netire domain, many iterations are spent to achieve $U_c^{(tol)}$ also in regions with a large objective function value.

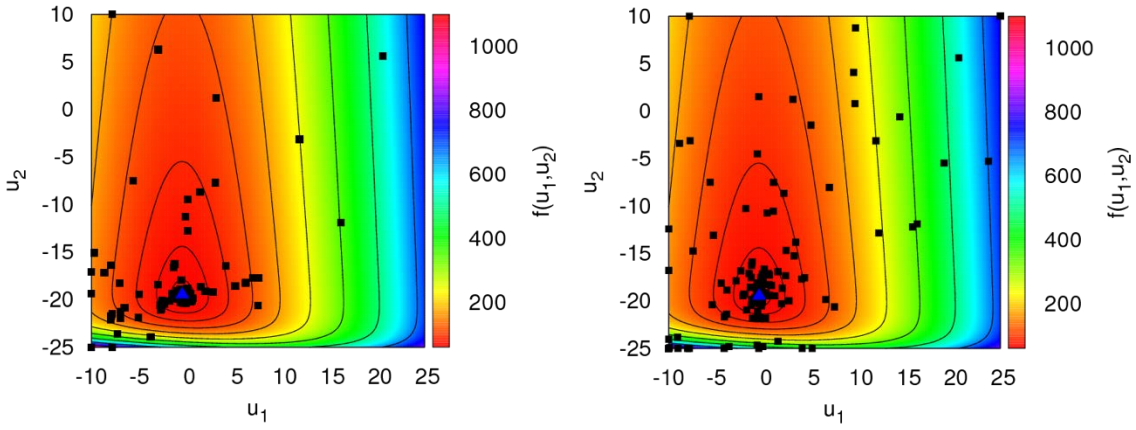

Figure 71: Distribution of training points in the design space given by MCAS-MDO (left) and MDF (right) for the two-dimensional test problem

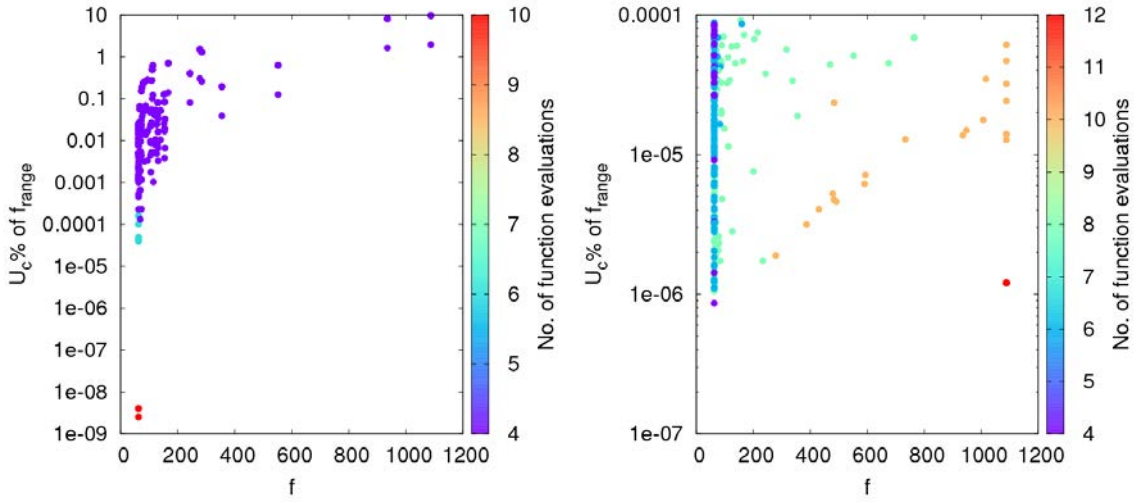

Figure 72: Distribution of training points in the objective function-uncertainty space given by MCAS-MDO (left) and MDF (right) for the two-dimensional test problem

The solution of the three-dimensional test problem by MCAS-MDO is achieved with 229 training points and 1034 function evaluations. Figure 73 shows the convergence of the optimal objective function and the uncertainties. As the process advances, the discrepancy between the predicted optimal function value and the true value, evaluated by fully converged MDA for validation purposes, reduces. The optimization converges as U_c reaches the prescribed threshold. The maximum number of MDA iterations is 10 for the MCAS-MDO and 12 for the MDF.

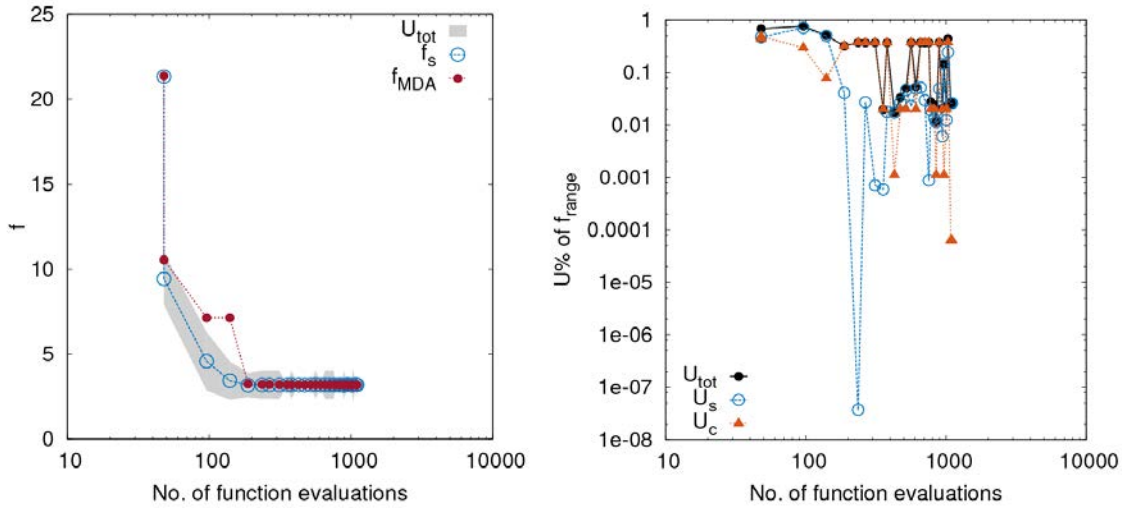

Figure 73: MCAS-MDO convergence of objective function (left) and uncertainties (right) for the three-dimensional test problem

The comparison between MCAS-MDO and the MDF is shown in Figure 74 to Figure 76. The solution by MDF is achieved with 372 training points and 3708 function evaluations. Figure 74 shows the convergence of the optimal objective function value. MCAS-MDO requires fewer function evaluations to achieve the optimum.

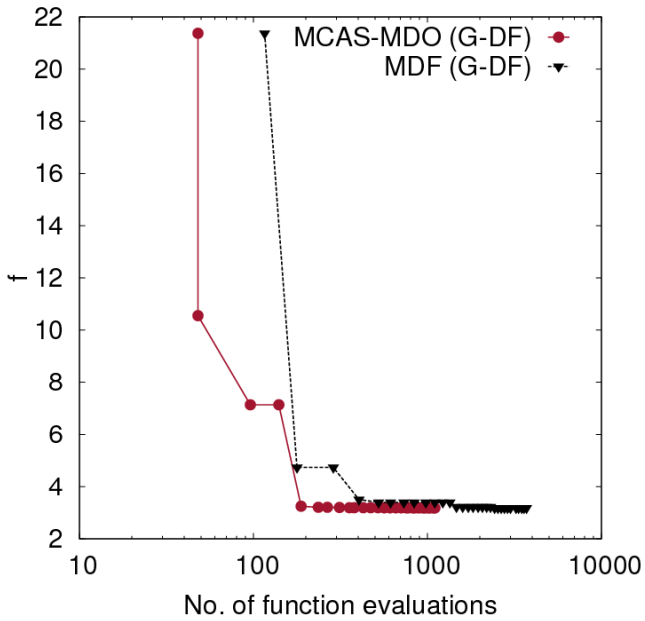

Figure 74: Convergence of objective function given by MCAS-MDO and MDF for the three-dimensional test problem

Figure 75 displays the training points in the objective function-uncertainty space. MCAS-MDO samples show, as found for the two-dimensional test problem, a correlation between U_c and f. Few MDA iterations are performed in regions with large objective function value. MDF samples are more scatter in the space. The maximum number of MDA iterations is16 for the MCAS-MDO and 40 for the MDF.

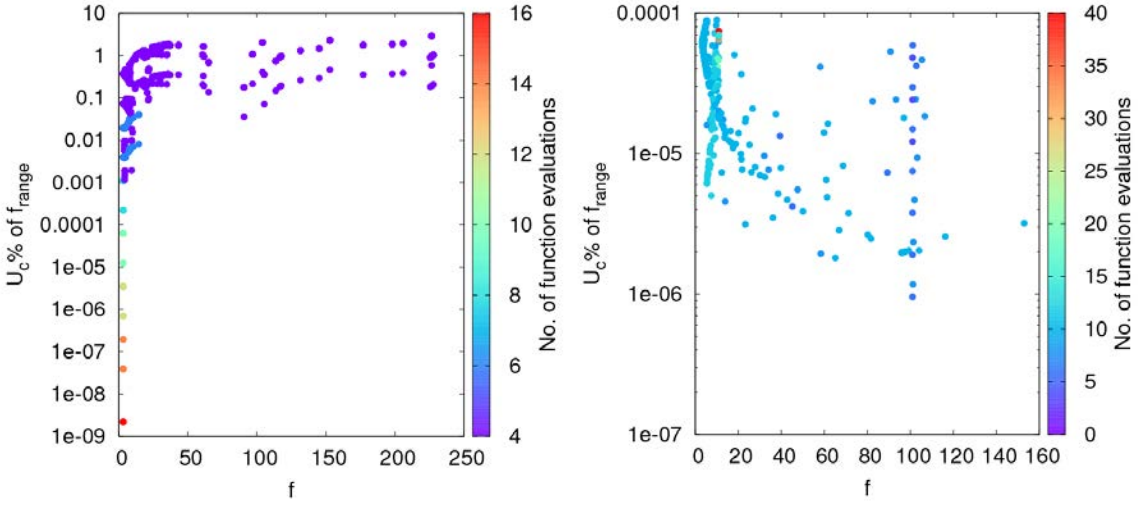

Figure 75: Distribution of training points in the objective function-uncertainty space given by MCAS-MDO (left) and MDF (right) for the two-dimensional test problem

Tedford and Martins (2010) provide a benchmark solution of the problem, which is here used to assess the goodness of the MCAS-MDO and MDF optima. Figure 76 shows the errors with respect to the benchmark location, e_x, and objective function value, e_f, as

$$e_x = \|u - u_{exact}\|_2$$
$$e_f = \left|\frac{f - f_{\text{exact}}}{f_{\text{exact}}}\right| \tag{81}$$

MCAS-MDO shows a faster reduction of e_x than the MDF. However, MCAS-MDO final optimum is further away from the benchmark than the one obtained by the MDF. On the other hand, the optimal function value achieved by MCAS-MDO in closer than the MDF to the benchmark. The efficiency of the methods is assessed by comparison with the gradient-based implementation of IDF, SAND, MDF, CO, and CSSO presented in Tedford and Martins (2010). Note that in the original paper, the convergence of e_f is given versus computational time. Figure 76 is extrapolated using the total number of

function evaluations reported in the paper for each architecture. MCAS-MDO shows an average performance with respect to the benchmark data, while the MDF provides the worst performance. These results are to be expected since gradient-based architecture are usually more efficient than derivative-free approaches. Additionally, the derivative-free methods do not achieve the accuracy of gradient-based architectures.

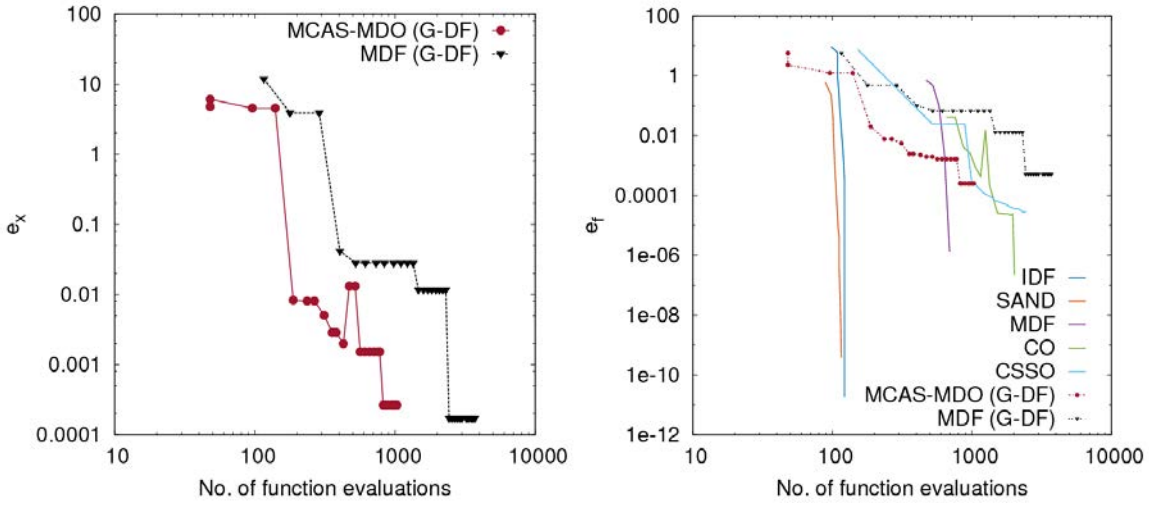

Figure 76: Convergence of optimum location (left) and function value (right) errors for the three-dimensional test problem (gradient-based IDF, SAND, MDF, CO, and CSSO taken from Tedford and Martins 2010)

Design space analysis

Assessment

The total geometric variance σ^2 of the design spaces, evaluated by Eq. 42, is given in Table 30. By comparing design spaces 1 to 4, characterized by the same type of modification, it is possible to assess the effect of the number of FFD control points on the design variability and the number of stochastic samples S of shape modifications needed to perform the KLE. It is found that by increasing the number of control points, σ^2 reduces. The trend is depicted in Figure 77. Table 30 provides the number N of KL modes needed to achieve 50, 75, 90, and 99% of the total σ^2. As the number of variables increases, the number of KL modes needed to retain 50, 75, 90, or 99% of σ^2 with respect to the total number of variables reduces. This is shown in Figure 78 reporting N as percentage of M. For instance, for retaining the 90% of σ^2, 59, 27, 14, and 7% of the initial number of

variables is required by design spaces 1 to 4, respectively. The normalized cumulative sum of the eigenvalues, referred to as KL values, of the design spaces are shown in Figure 79 to Figure 82. Results are found convergent versus S.

Table 30: Design space geometric variance assessment

Case	σ^2	N			
		$50\%\sigma^2$	$75\%\sigma^2$	$90\%\sigma^2$	$99\%\sigma^2$
1	$4.34\text{x}10^{-6}$	3	7	10	14
2	$1.42\text{x}10^{-6}$	8	16	27	54
3	$6.90\text{x}10^{-7}$	16	32	55	116
4	$3.50\text{x}10^{-7}$	27	59	105	226
5	$4.61\text{x}10^{-6}$	3	5	11	38

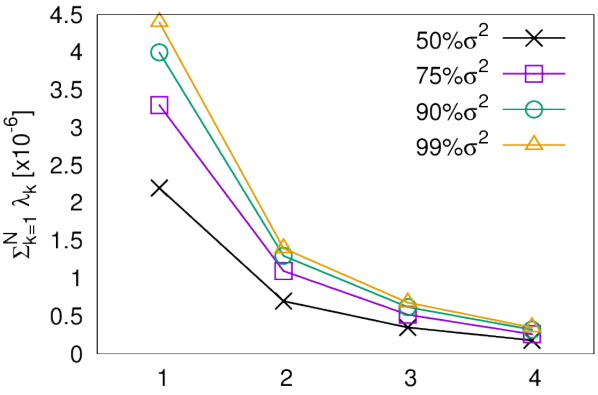

Figure 77: Design space 1 to 4 geometric variances

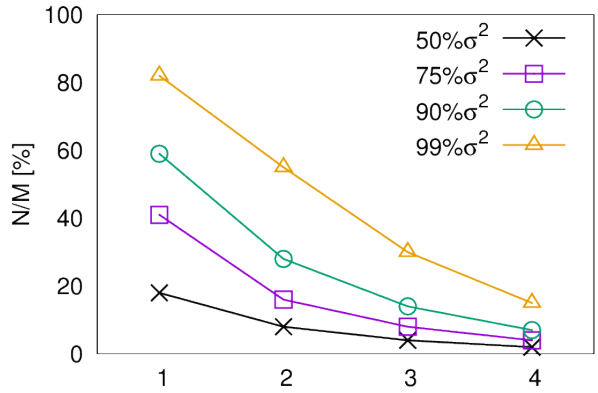

Figure 78: Number of KL modes needed to retain 50, 75, 90, and 99% of the geometric variance

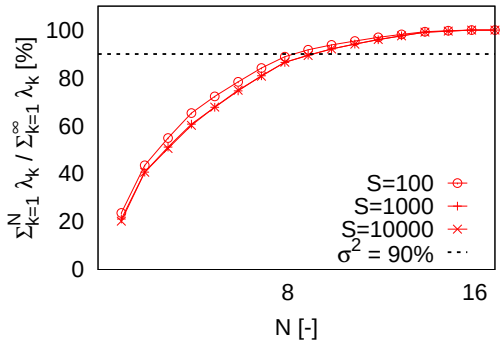

Figure 79: Design space 1 geometric variance convergence

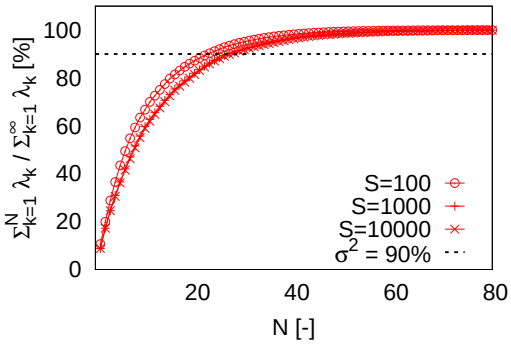

Figure 80: Design space 2 geometric variance convergence

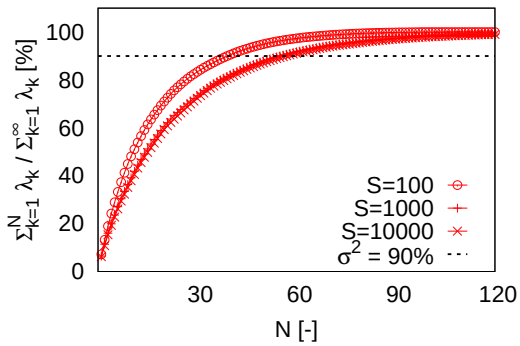

Figure 81: Design space 3 geometric variance convergence

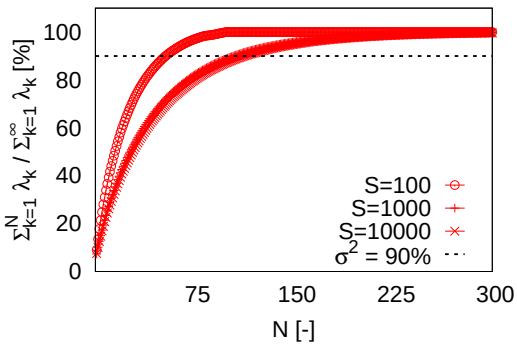

Figure 82: Design space 4 geometric variance convergence

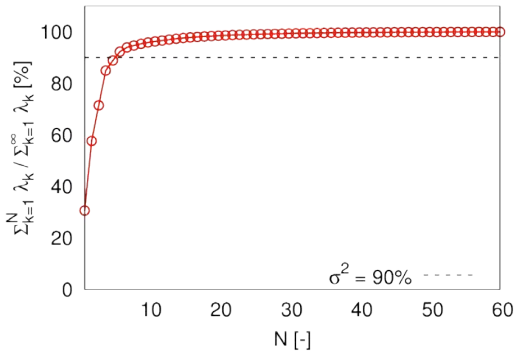

Figure 83: Design space 5 geometric variance convergence

The geometric variance of design space 5 is the largest. The number of eigenvalues N needed to retain the 50, 75, 90, and 99% of the original σ^2 indicate a N/M value similar

to the design space 4. For instance, for retaining the 90% of σ^2, 10% of the initial number of variables is required. The normalized cumulative sum of the KL values is displayed in Figure 83.

Distributed/concentrated parameters KLE

Design space 5 is evaluated by combined distributed/concentrated parameter KLE comparing six sets of relative weights. The number of eigenvalues required to retain the 50, 75, 90, and 99% of σ^2 is summarized in Table 31. The use of even weights among the three parameters leads to the smallest number of modes required to achieve each of the dimensionality reduction confidence levels.

Table 31: Combined distributed/concentrated parameters KLE weights

Displacement weight	Twist weight	Camber weight	N			
			50	75	90	99
1.0	0.0	0.0	3	5	11	38
0.9	0.05	0.05	3	6	13	39
0.8	0.1	0.1	4	6	12	38
0.6	0.2	0.2	4	6	11	35
0.5	0.25	0.25	3	6	10	33
0.333	0.333	0.333	2	5	9	28

A reduced-dimensionality representation for standard and combined distributed/concentrated parameter KLE is built for design space 5. Although the 95% confidence level is generally used, in the current research, the 90% threshold of σ^2 is deemed sufficient and selected to build the reduced-dimensionality representations.

Purely distributed and combined distributed/concentrated parameter KLE bases uses 11 and 9 modes, respectively. The capability of representing a target geometry is evaluated using a hydrofoil design characterized by negative tip twist and positive camber. The geometry is projected onto the KL modes to find α_k. Figure 84 and Figure 85 show the geometry reconstruction by the two models. The combined distributed/concentrated parameter KLE basis is found providing a more efficient and accurate representation than standard KLE for the problem at hand.

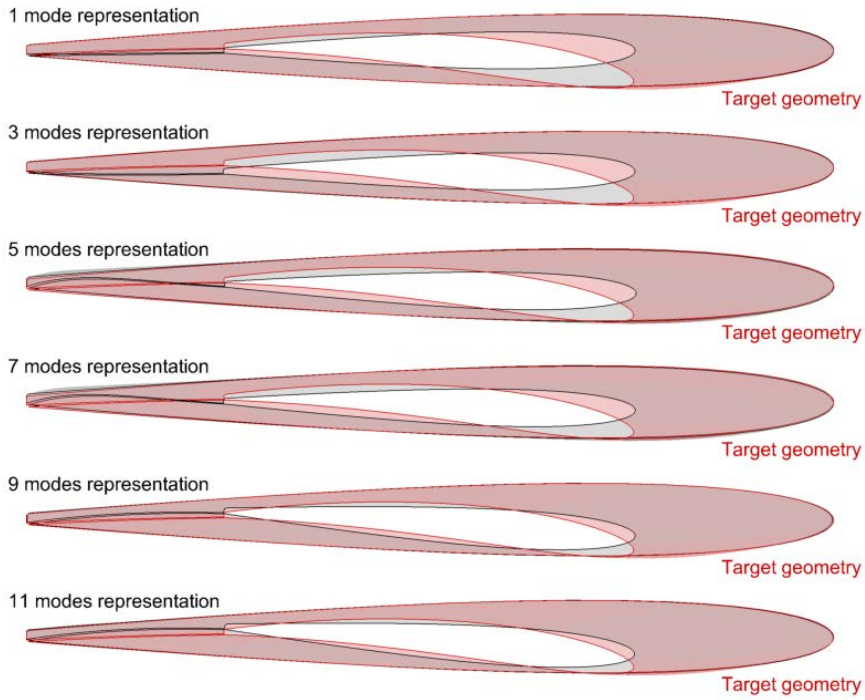

Figure 84: Target geometry reconstruction using standard KLE dimensionality reduction

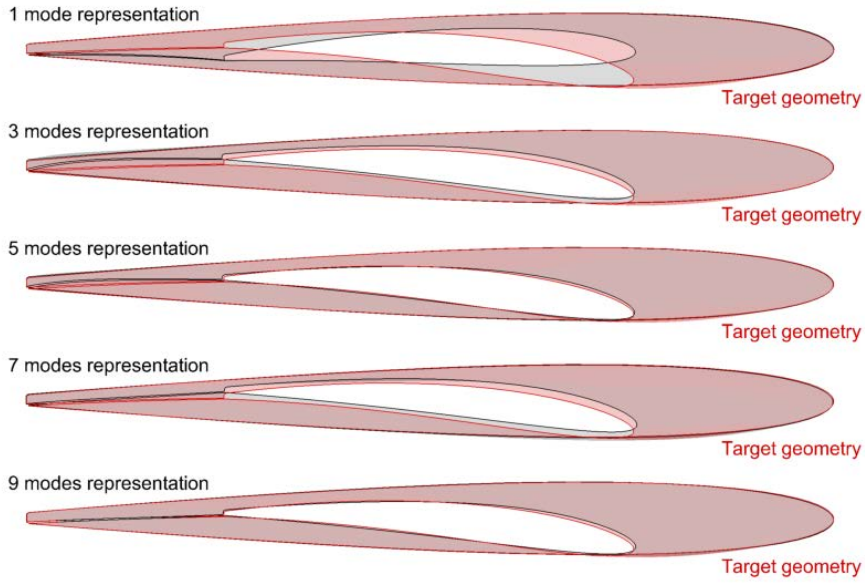

Figure 85: Target geometry reconstruction using combined distributed/concentrated parameters KLE dimensionality reduction

Dimensionality reduction and re-parametrization

The eigenvectors of the design space, also referred to as KL vectors, are the orthogonal basis for the representation of the reduced dimensionality space. As solution of the discrete eigenproblem in Eq. 49, the KL vectors are normalized by

$$\mathbf{z}_k^{\mathrm{T}}\,\mathbf{W}\,\mathbf{z}_k = 1 \tag{82}$$

Any geometry $\mathbf{g}$ is represented using the KL basis (Eq. 50) in discrete form as

$$\mathbf{g}(\boldsymbol{\alpha}) = \mathbf{g}_0 + \langle \mathbf{d} \rangle + \sum_{k=1}^{N} \alpha_k \mathbf{z}_k \tag{83}$$

where $\mathbf{g}_0$ is the original geometry, $\langle \mathbf{d} \rangle$ is the mean geometry modification, which is generally be non-zero, $\mathbf{z}_k$ are the KL vectors representing the geometry modification in the k-direction, and $\boldsymbol{\alpha} = (\alpha_1, \alpha_2, \dots, \alpha_N)^{\mathrm{T}}$ is the vector of the linear combination coefficients. Herein, the mean modification is negligible hence the term $\langle \mathbf{d} \rangle$ is dropped from the formulation.

Eq. 87 allows for substituting the original design variables $\mathbf{u}$ with the reduced space design variables $\boldsymbol{\alpha}$. The original optimization problem in Eq. 24, subject to bound-constraints for the design variables $a_k \leq u_k \leq b_k$ for $k = 1, \dots, M$, is reformulated as

$$\min_{\mathbf{u}} \quad f_p[\boldsymbol{\alpha}, \mathbf{y}(\boldsymbol{\alpha}, \mathbf{y})] \tag{84}$$

$$\text{subject to } c_k \leq \alpha_k \leq d_k,\ k = 1, \dots, N \tag{85}$$

The lower and upper bounds of α_k are determined by projection of the Monte Carlo sampled deviation from the mean of the shape modification on the KL vectors:

$$\begin{aligned} c_k &= \inf\,\{\alpha_k\} = \inf\,\{\mathbf{d}(\mathbf{u}_r)^{\mathrm{T}}\,\mathbf{W}\,\mathbf{z}_k\} \\ d_k &= \sup\,\{\alpha_k\} = \sup\,\{\mathbf{d}(\mathbf{u}_r)^{\mathrm{T}}\,\mathbf{W}\,\mathbf{z}_k\} \end{aligned} \tag{86}$$

Eq. 87 is then written in the form

$$\mathbf{g}(\boldsymbol{\alpha}) = \mathbf{g}_0 + \sum_{k=1}^{N} \hat{\alpha}_k \hat{\mathbf{z}}_k \tag{87}$$

where

$$\hat{\alpha}_k = \alpha_k / d_k \text{ with } c_k / d_k \leq \hat{\alpha}_k \leq 1$$
$$\hat{\mathbf{z}}_k = d_k \mathbf{z}_k \tag{88}$$

Eq. 87 can be interpreted as a linear combination of the original geometry $\mathbf{g}_0$ with the KL basis geometries $\mathbf{g}_k = \mathbf{g}_0 + \hat{\mathbf{z}}_k$ as per

$$\mathbf{g}(\boldsymbol{\alpha}) = \mathbf{g}_0 \left(1 - \sum_{k=1}^{N} \hat{\alpha}_k \right) + \sum_{k=1}^{N} \hat{\alpha}_k \mathbf{g}_k \tag{89}$$

The reduced-dimensionality design space is based on design space 5 and the KL modes obtained via combined distributed/concentrated parameters KLE. Nine modes, retaining 90% of σ^2 form the basis for the re-parametrization. The original geometry is defined by zero-valued $\hat{\alpha}_k$.

Design variables

The shape optimization is performed over the reduced-space design variables $\boldsymbol{\alpha}$ associated with the KL modes, so that $\mathbf{u}_{shape} = \boldsymbol{\alpha}$. The modes in the form of $\mathbf{g}_k$ are shown in Figure 86 to Figure 94 using color mapping according to the magnitude of the shape modification. The range of the variables is approximately $-1 \leq u_{k,shape} \leq 1$.

The geometries $\mathbf{g}_k$ suggests a possible analogy between the KL modes and recognizable shapes, such as the modes of a cantilever beam. In the following, the geometrical quality of each KL modes is listed:

1. Camber
2. 1st order twist (cantilever beam)
3. 2st order twist (cantilever beam)
4. 1st order in-plane bending (cantilever beam)
5. 1st order out-of-plane bending (cantilever beam)
6. 2st order in-plane bending (cantilever beam)
7. 2st order out-of-plane bending (cantilever beam)
8. Membrane
9. 3rd order twist (cantilever beam)

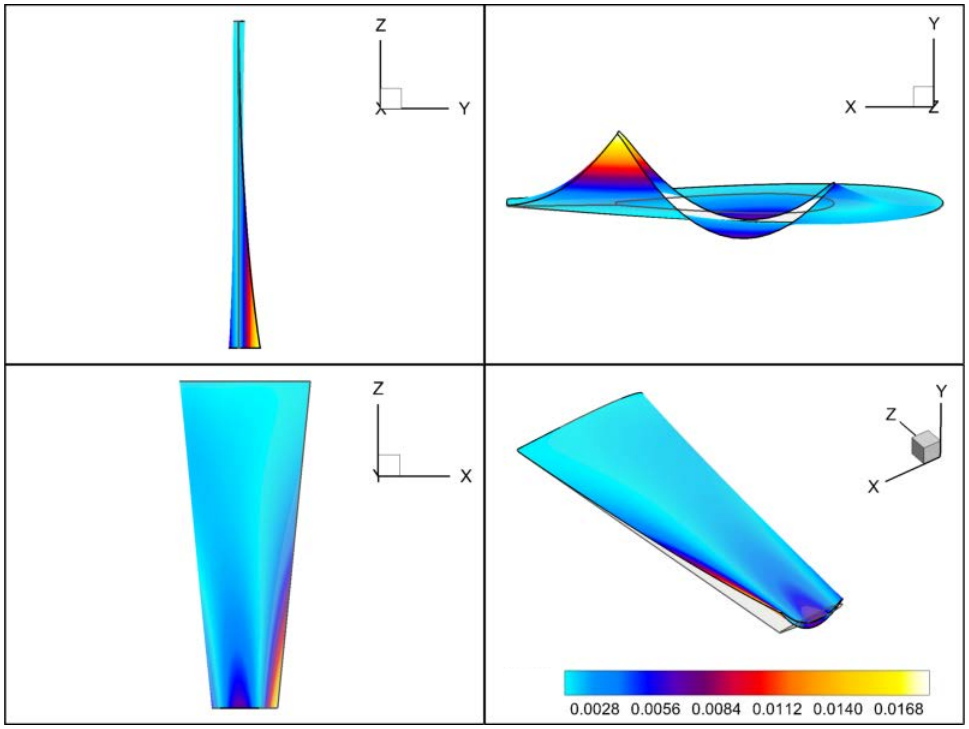

Figure 86: 1st KL mode

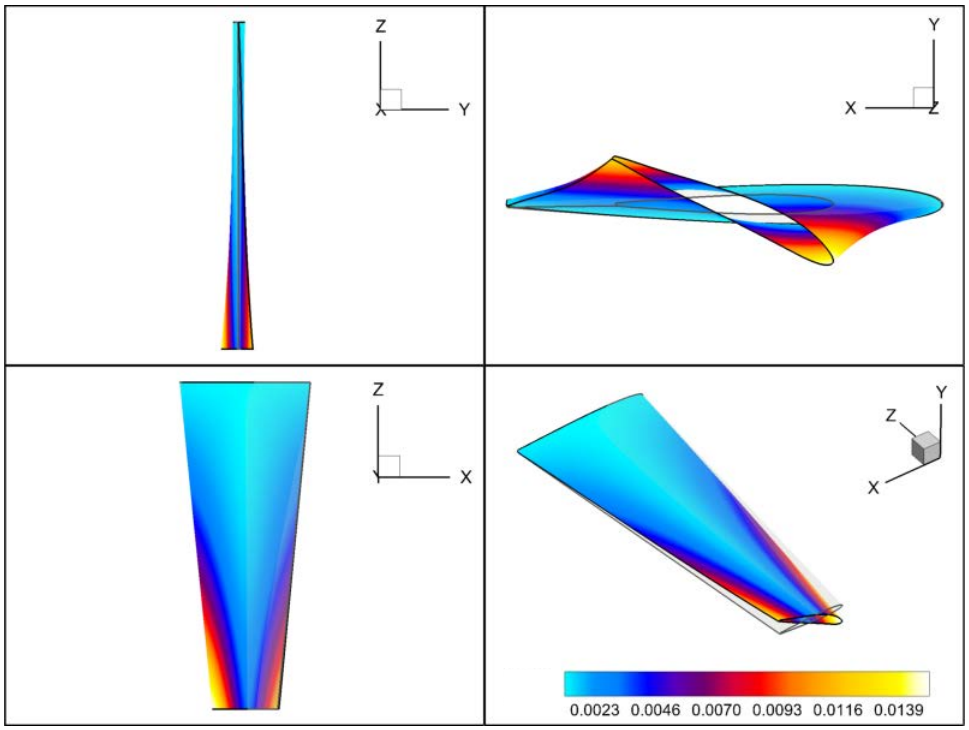

Figure 87: 2nd KL mode

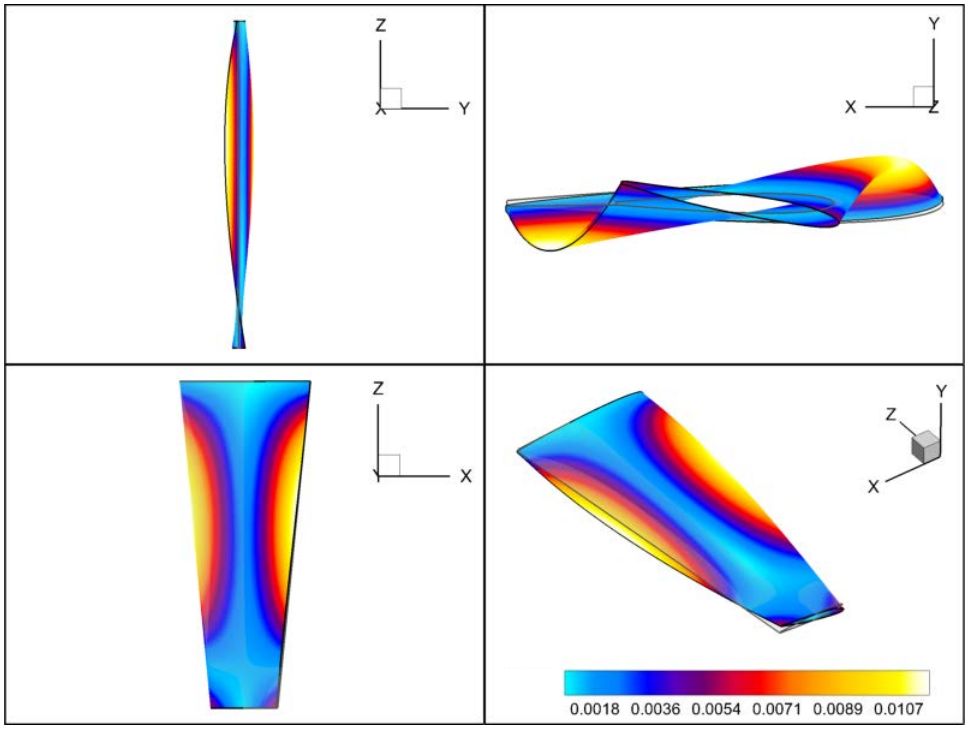

Figure 88: 3rd KL mode

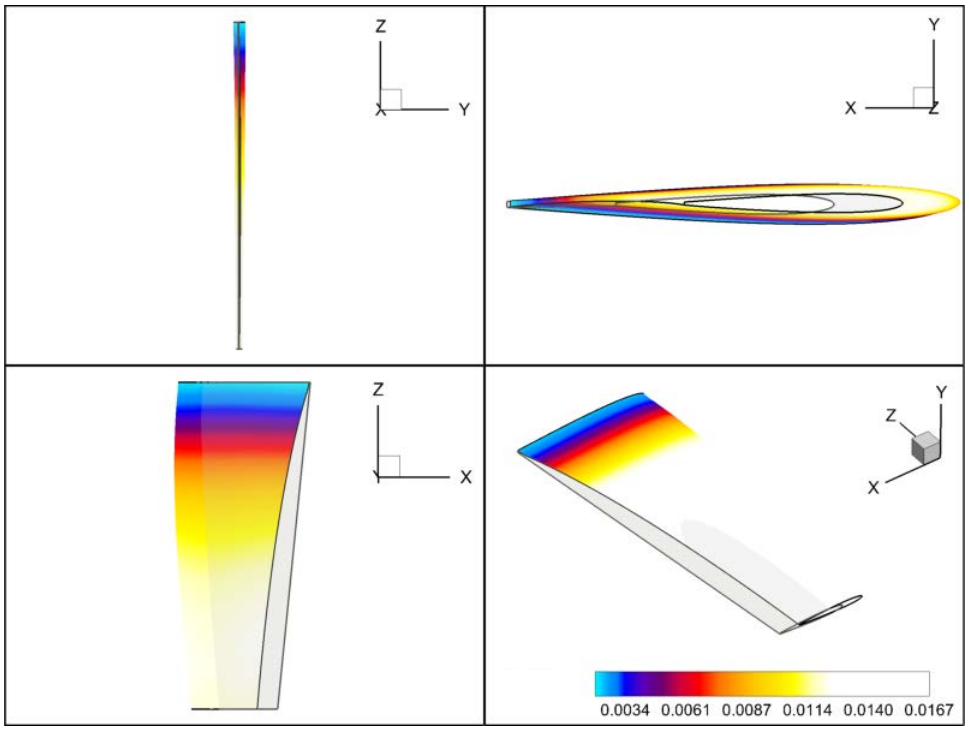

Figure 89: 4th KL mode

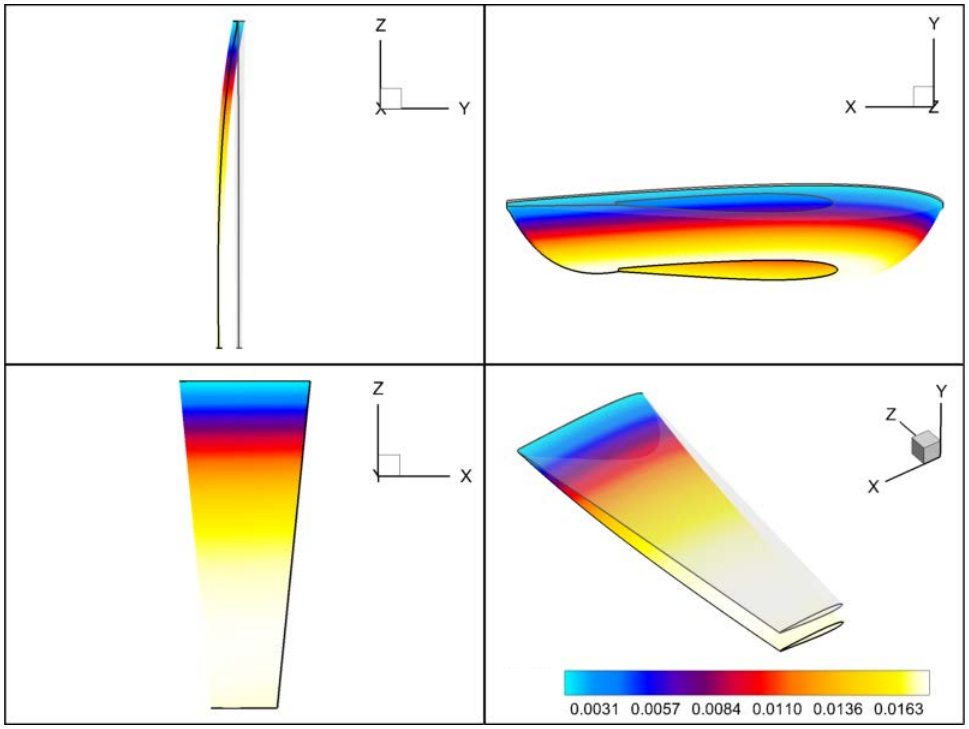

Figure 90: 5th KL mode

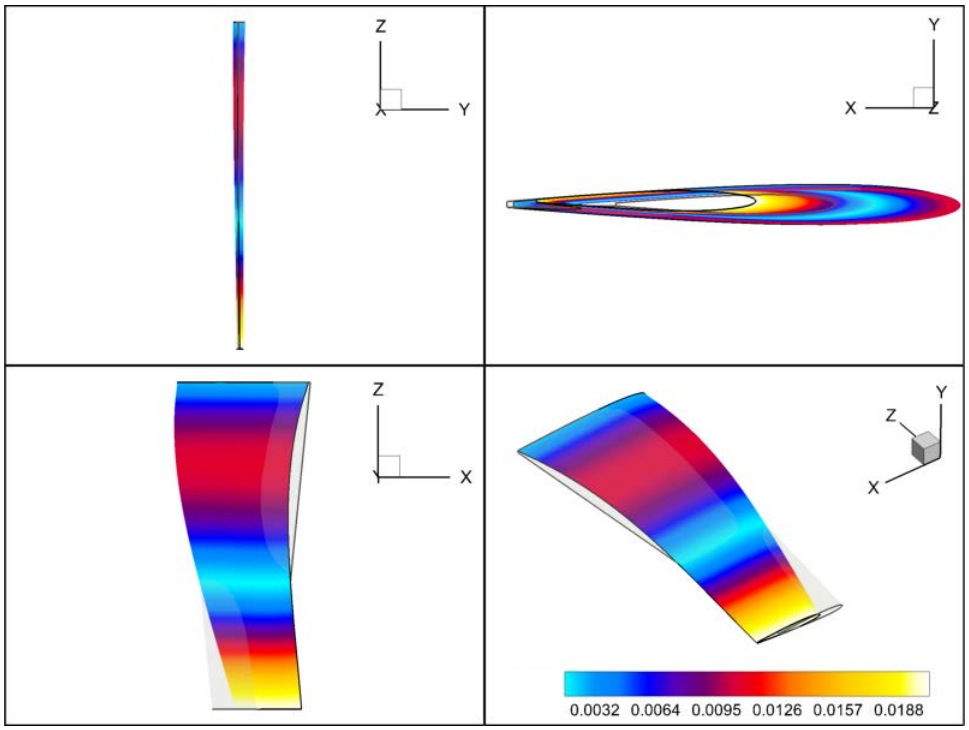

Figure 91: 6th KL mode

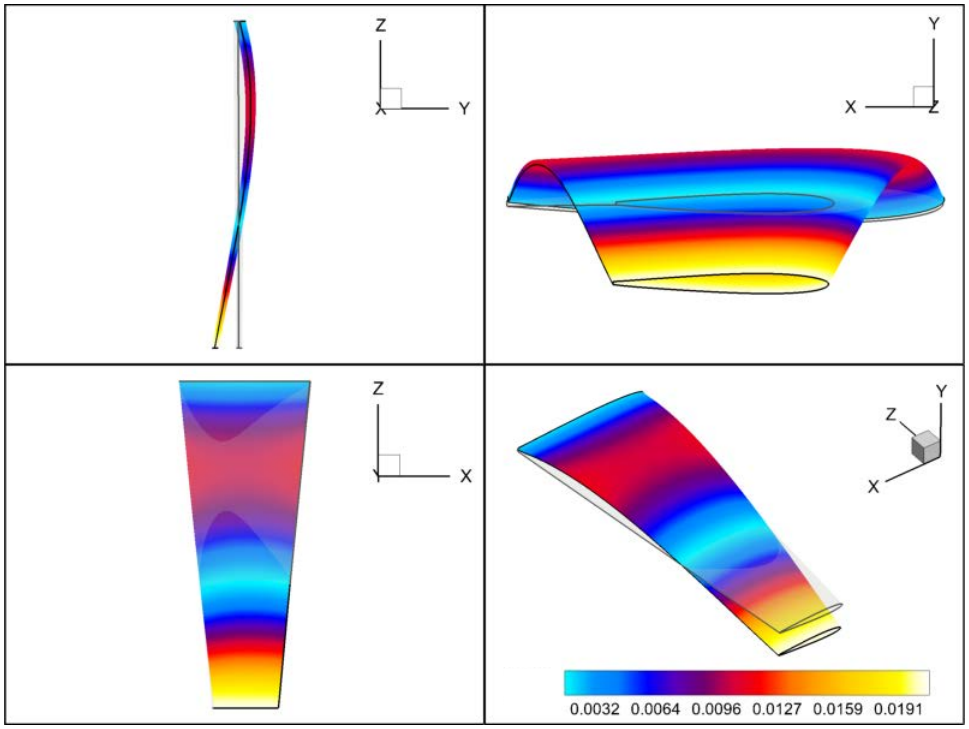

Figure 92: 7th KL mode

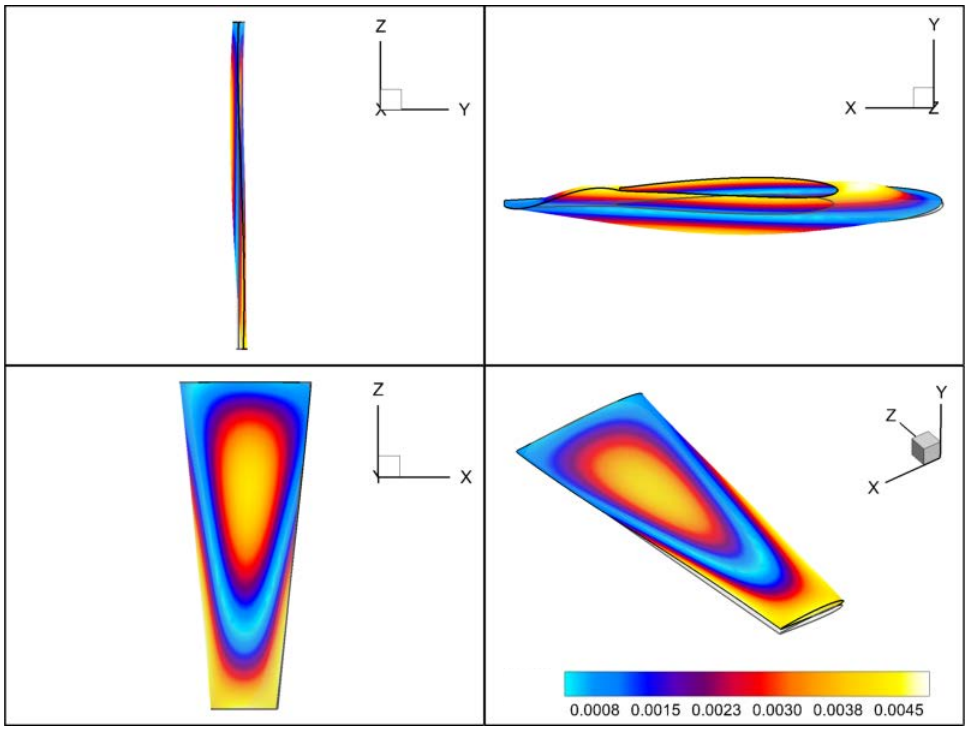

Figure 93: 8th KL mode

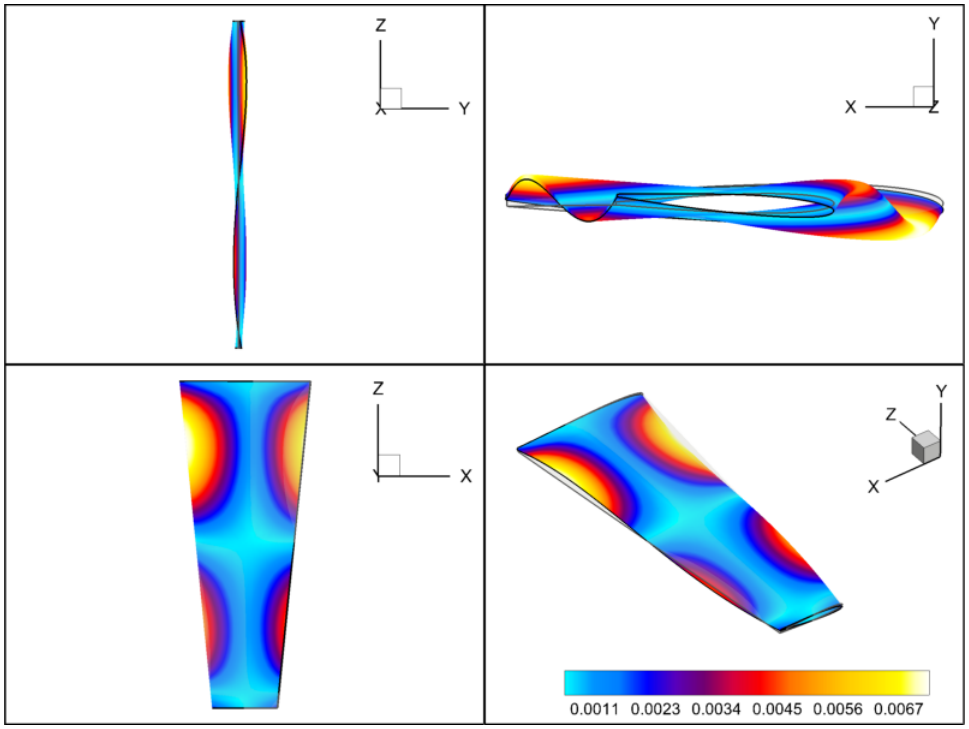

Figure 94: 9th KL mode

The design variable associated with the composite material layout is the fiber orientation $u_{fiber} = \zeta$. The range of the variable is $-90° \leq u_{fiber} \leq 90°$. The original design is assumed having ζ equal to zero, analogously to the CFRP00 model.

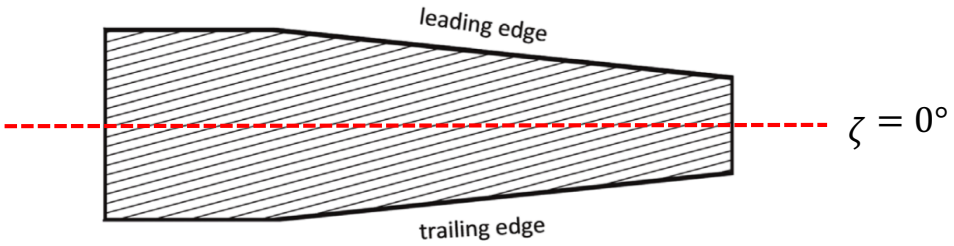

Figure 95: Composite material fiber orientation

In the MDO of the AL hydrofoil, the nine design variables corresponding to the KL modes are used. IN the MDO of the CFRP hydrofoil, ten design variables are used. Design variables from one to nine correspond to the KL modes; the tenth design variable is the fiber orientation.

Sensitivity analysis

Aluminum hydrofoil

The sensitivity analysis for the AL hydrofoil includes 55 FSI simulations, i.e. six simulations for each one of the nine design variables plus the simulation of the original geometry. Due to the lack of convergence of some simulations, the number of numerically feasible designs which are considered in the following analysis is 41. The number of function evaluations is 1466 corresponding to 733 CFD and 733 FE analyses.

Figure 96 to Figure 99 show the sensitivity values for C_L, C_D, C_M and Eff. The C_L of the original geometry is 0.658, while the values obtained by sensitivity range between 0.155 and 1.439. The C_D of the original geometry is 0.0348; the sensitivity results range between 0.019 and 0.394. The C_M of the original geometry is 0.17; the sensitivity results range between 0.051 and 0.291. The Eff of the original geometry is 18.90; the sensitivity results range between 3.65 and 21.68. The range of variation of the hydrodynamic forces for each design variable is given in Table 32. The largest range of variation (375%) corresponds to u_3. Eff shows large fluctuations also for u_2 and u_8.

Figure 100 and Figure 101 show the sensitivity values for the maximum displacement δ_{max} and the failure index ϕ. The δ_{max} of the original geometry is 6.1 mm; the sensitivity results range between 1.5 and 11.1 mm. The ϕ of the original geometry is 0.22; the sensitivity results range between 0.06 and 0.51. The range of variation of the structural parameters for each design variable is given in Table 33. The largest range of variation (175%) corresponds to u_3. δ_{max} shows large fluctuations also for u_1 and u_2.

Figure 102 to Figure 105 show the sensitivity values for the objective and constrain functions. f of the original geometry is 0.0348; the sensitivity results range between 0.019 and 0.394. c_1 of the original geometry is -0.019; the sensitivity results range between -1.23 and 0.76. c_2 of the original geometry is 0; the sensitivity results range between -0.18 and 0.037. The c_3 of the original geometry is -0.66; the sensitivity results range between -0.91 and -0.22. The range of variation of the hydrodynamic forces for each design variable is given in Table 34. The largest range of variation (336%) corresponds to u_3. c_2 shows the largest fluctuations for u_2.

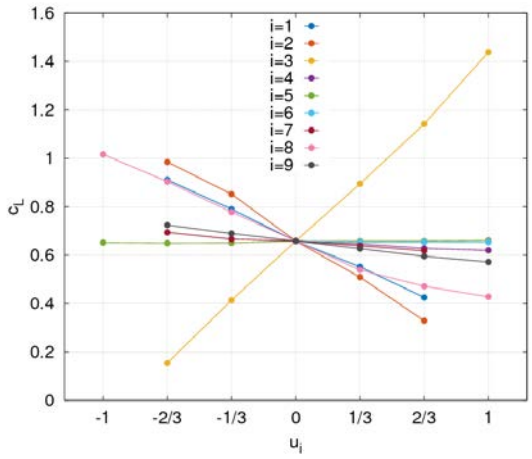

Figure 96: AL lift coefficient sensitivity

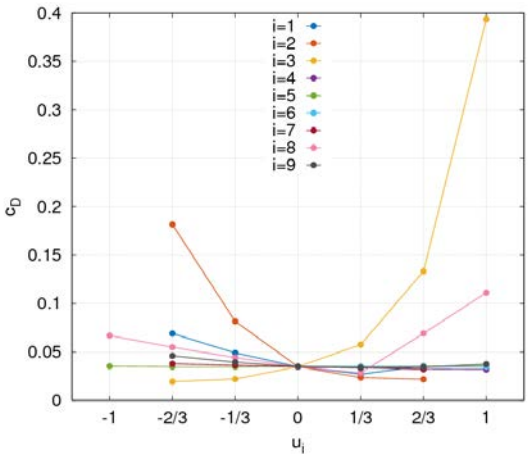

Figure 97: AL drag coefficient sensitivity

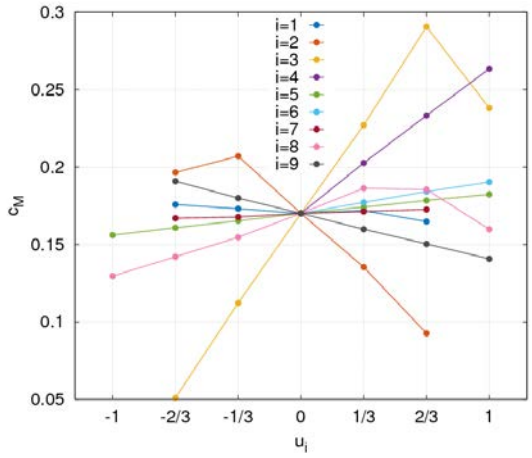

Figure 98: AL pitching moment coefficient sensitivity

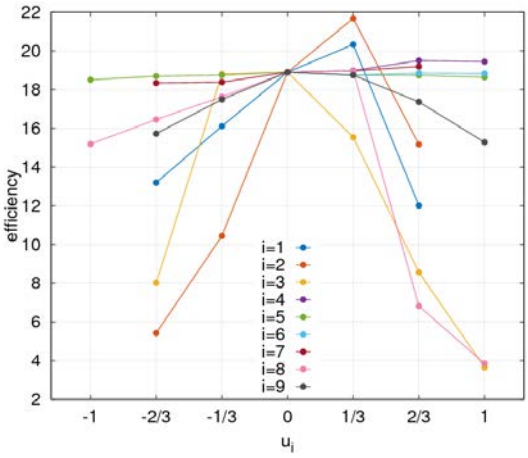

Figure 99: AL hydrodynamic efficiency sensitivity

Table 32: AL hydrodynamic parameter range of variation

%	u_1	u_2	u_3	u_4	u_5	u_6	u_7	u_8	u_9
C_L	73.8	99.6	195.1	5.8	1.8	0.8	11.4	89.4	23.1
C_D	120.4	459.4	1075.6	8.4	2.2	0.4	16.1	238.0	36.2
C_M	6.4	67.3	140.9	54.9	15.5	11.9	3.3	33.4	29.5
Eff	44.0	86.0	80.7	3.2	2.2	0.8	4.5	80.1	19.2
Average	74.0	167.6	374.4	37.4	5.7	3.8	7.9	91.3	42.2

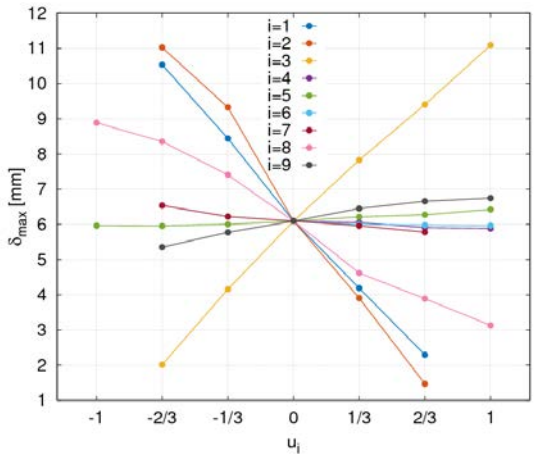

Figure 100: AL displacement sensitivity

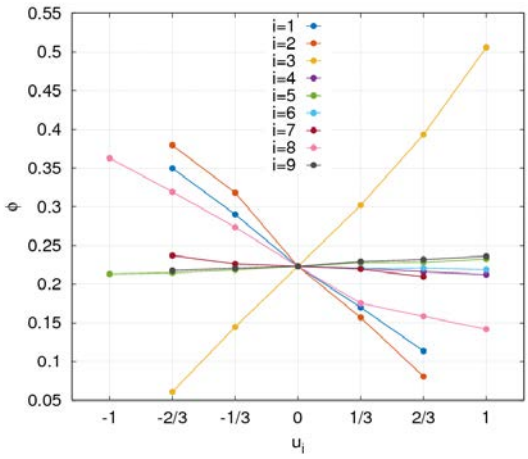

Figure 101: AL failure index sensitivity

Table 33: AL structural parameter range of variation

%	u_1	u_2	u_3	u_4	u_5	u_6	u_7	u_8	u_9
δ_{max}	135.2	156.8	148.9	3.5	7.7	2.2	12.4	94.4	22.9
ϕ	105.8	133.9	199.4	4.8	8.8	1.9	12.3	99.0	8.3
Average	120.5	145.3	174.2	4.1	8.2	2.1	12.3	96.7	15.6

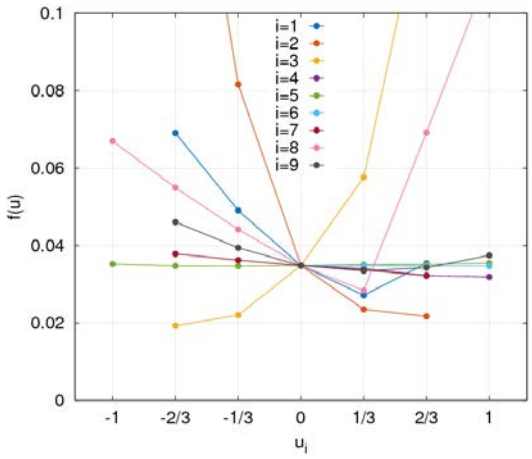

Figure 102: AL f sensitivity

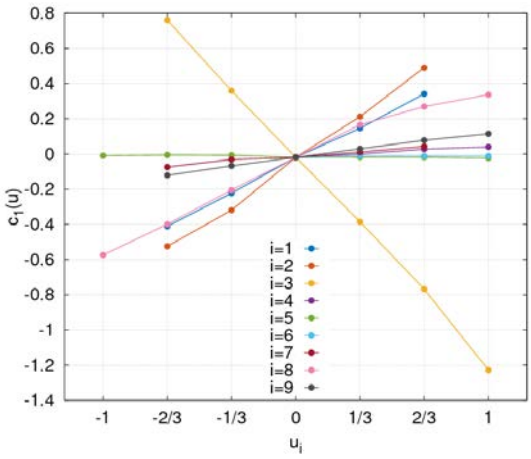

Figure 103: AL c_1 sensitivity

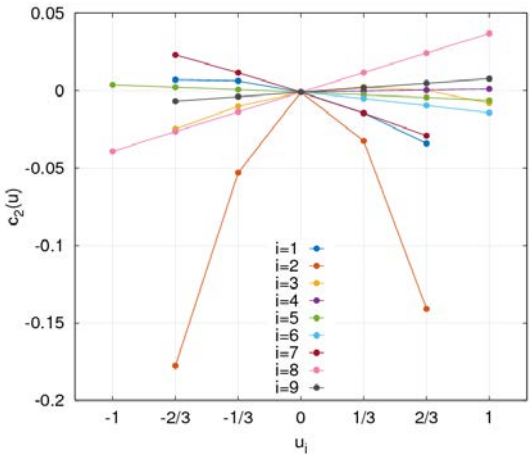

Figure 104: AL c_2 sensitivity

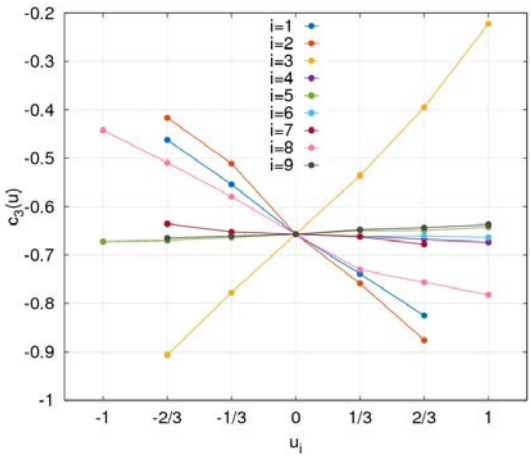

Figure 105: AL c_3 sensitivity

Table 34: AL objective and constraint function range of variation

%	u_1	u_2	u_3	u_4	u_5	u_6	u_7	u_8	u_9
f	120.4	459.4	1075.6	8.4	2.2	0.4	16.1	238.0	36.2
c_1	75.2	101.5	198.9	5.9	1.8	0.8	11.6	91.1	23.6
c_2	4.1	17.7	2.7	0.2	1.0	1.3	5.2	7.6	1.4
c_3	36.3	45.9	68.4	1.6	3.0	0.7	4.2	34.0	2.8
Average	59.0	156.1	336.4	4.0	2.0	0.8	9.3	92.7	16.0

Feasible objective function reductions are achieved along the design variables u_4 and u_6. u_4 = 0.333 provides the largest improvement followed by u_6 = 0.333, 0.667, and 1. A ranking of the design variable sets is given in Table 35 based on the feasible reduction in objective function achieved. Due to the lack of convergence of some CFD simulations, the feasible range of variation associated to each variable is reduced.

Table 35: Ranking of AL sensitivity simulations

Ranking	Variable	Description	Δf%	u_i	Simulation feasible range
1	u_4	1st order in-plane bending	-2.24	0.333	[-0.1;1]
2	u_6	2st order in-plane bending	-0.40	0.333	[-0.1;1]
3	u_1	Camber	0	0	[-0.7;0.7]
	u_2	1st order twist	0	0	[-0.7;0.7]
	u_3	2st order twist	0	0	[-0.7;1]
	u_5	1st order out-of-plane bending	0	0	[-1;1]
	u_7	2st order out-of-plane bending	0	0	[-0.7;0.7]
	u_8	Membrane	0	0	[-1;1]
	u_9	3st order twist	0	0	[-0.7;1]

The best sensitivity analysis simulation, corresponding to the design variable set $\mathbf{u} = [0,0,0,0.333,0,0,0,0,0]^T$, provides 2.24% objective function reduction.

Composite material hydrofoil

The sensitivity analysis for the CFRP hydrofoil includes 61 FSI simulations, i.e. six simulations for each one of the ten design variables plus the simulation of the original geometry. Due to the lack of convergence of some simulations, the number of numerically feasible designs which are considered in the following analysis is 47. The number of function evaluations is 1872 corresponding to 936 CFD and 936 FE analyses.

Figure 106 to Figure 109 show the sensitivity values for C_L, C_D, C_M and Eff. The C_L of the original geometry is 0.678, while the values obtained by sensitivity range between 0.160 and 1.428. The C_D of the original geometry is 0.0364; the sensitivity results range between 0.019 and 0.389. The C_M of the original geometry is 0.18; the sensitivity results range between 0.053 and 0.294. The Eff of the original geometry is 18.62; the sensitivity results range between 3.67 and 20.71. The range of variation of the hydrodynamic forces for each design variable is given in Table 36. The largest range of variation (355%) corresponds to u_3. Eff shows large fluctuations also for u_2 and u_8.

Figure 110 and Figure 111 show the sensitivity values for the maximum displacement δ_{max} and the failure index ϕ. The δ_{max} of the original geometry is 7.7 mm; the sensitivity results range between 1.6 and 28.8 mm. The ϕ of the original geometry is 0.37; the sensitivity results range between 0.11 and 1.01. The range of variation of the structural parameters for each design variable is given in Table 37. The largest range of variation (255%) corresponds to u_{10} showing that the fiber orientation has a strong effect on the deformation.

Figure 112 to Figure 115 show the sensitivity values for the objective and constrain functions. f of the original geometry is 0.0364; the sensitivity results range between 0.019 and 0.389. c_1 of the original geometry is -0.049; the sensitivity results range between -1.21 and 0.75. c_2 of the original geometry is 0; the sensitivity results range between -0.18 and 0.037. The c_3 of the original geometry is -0.43; the sensitivity results range between -0.83 and 0.56. The range of variation of the hydrodynamic forces for each design variable is given in Table 38. The largest range of variation (325%) corresponds to u_3. c_2 shows the largest fluctuations for u_2, while c_2 for u_{10}.

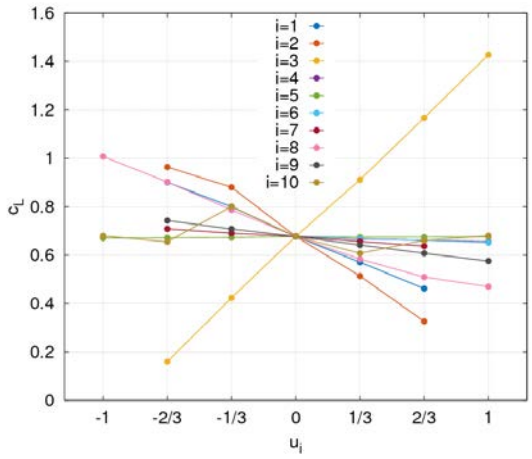

Figure 106: CFRP lift coefficient sensitivity

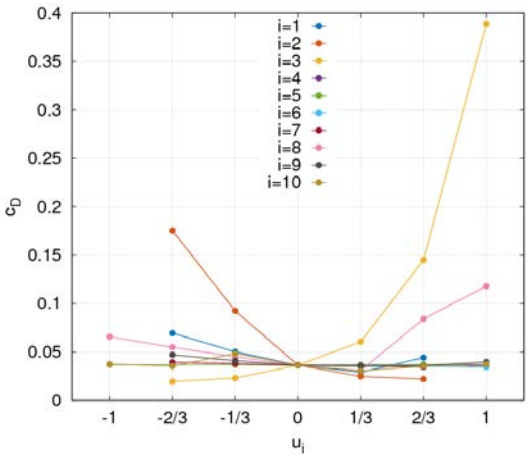

Figure 107: CFRP drag coefficient sensitivity

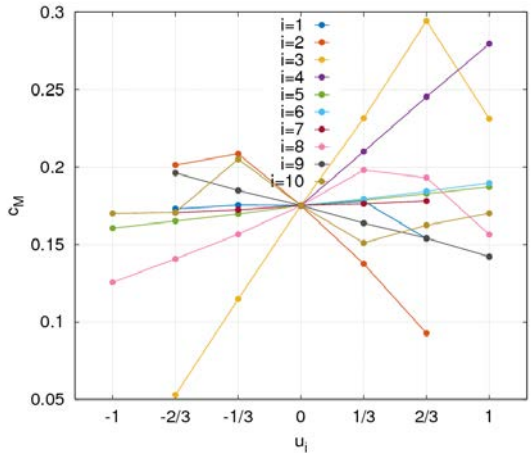

Figure 108: CFRP pitching moment coefficient sensitivity

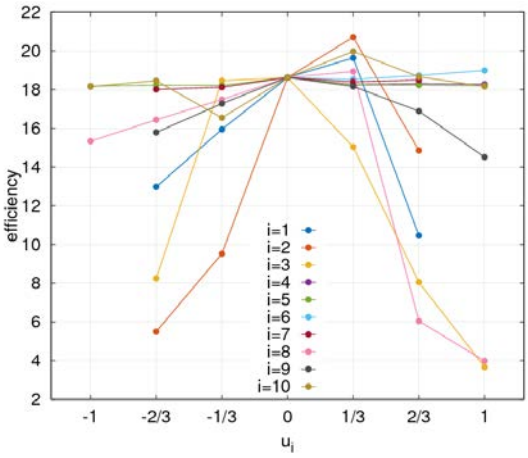

Figure 109: CFRP hydrodynamic efficiency sensitivity

Table 36: CFRP hydrodynamic parameter range of variation

%	u_1	u_2	u_3	u_4	u_5	u_6	u_7	u_8	u_9	u_{10}
C_L	64.8	94.2	187.2	3.3	1.0	3.8	10.5	79.3	24.7	28.5
C_D	111.0	421.9	1015.8	1.8	2.1	5.6	13.3	239.7	32.2	49.4
C_M	13.8	66.2	137.9	59.6	15.1	8.2	4.2	41.4	30.8	30.9
Eff	49.3	81.7	80.3	2.0	2.3	2.5	3.3	80.3	22.0	18.4
Average	59.7	166.0	355.3	16.6	5.1	5.0	7.8	110.2	27.5	31.8

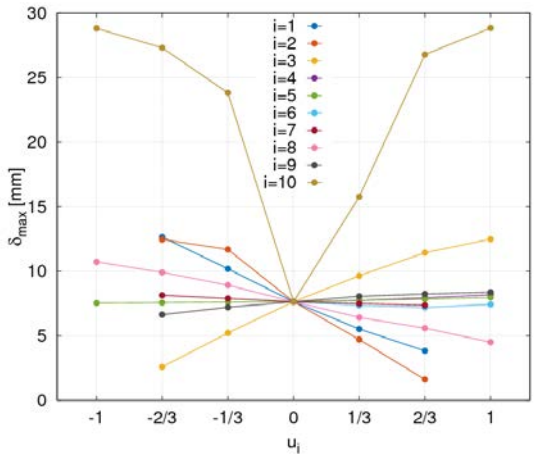

Figure 110: CFRP displacement sensitivity

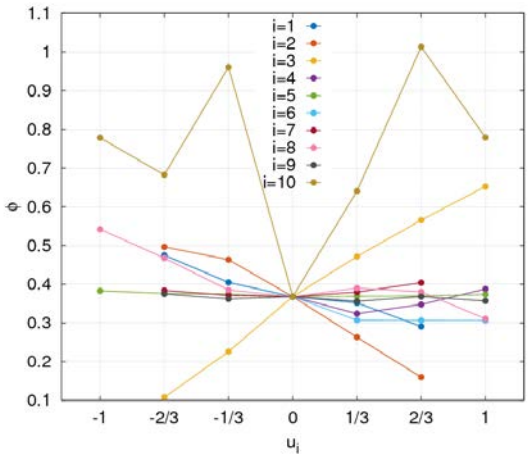

Figure 111: CFRP failure index sensitivity

Table 37: CFRP structural parameter range of variation

%	u_1	u_2	u_3	u_4	u_5	u_6	u_7	u_8	u_9	u_{10}
δ_{max}	115.3	141.7	129.4	7.0	5.7	5.9	10.1	81.4	22.7	277.2
ϕ	50.0	91.4	148.0	17.3	4.1	16.7	9.7	62.8	5.2	175.3
Average	82.7	116.5	138.7	12.2	4.9	11.3	9.9	72.1	13.9	226.3

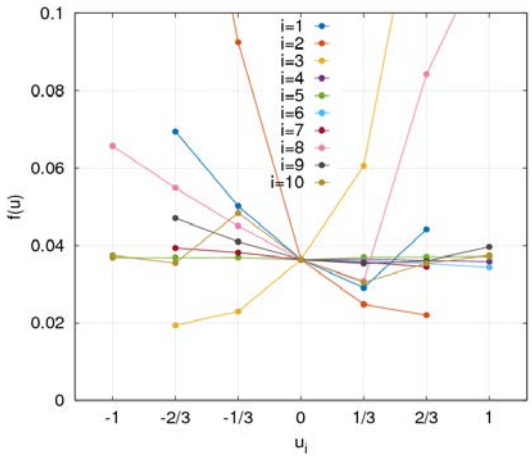

Figure 112: CFRP *f* sensitivity

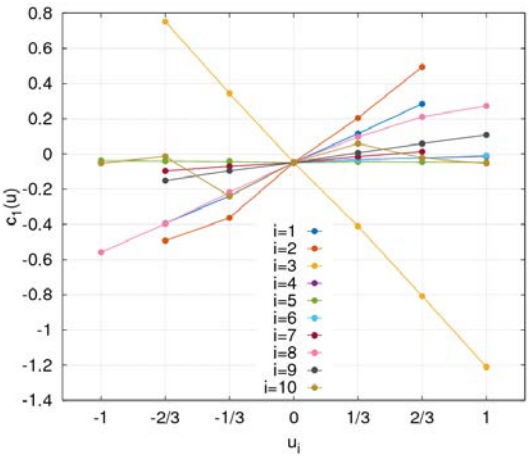

Figure 113: CFRP c_1 sensitivity

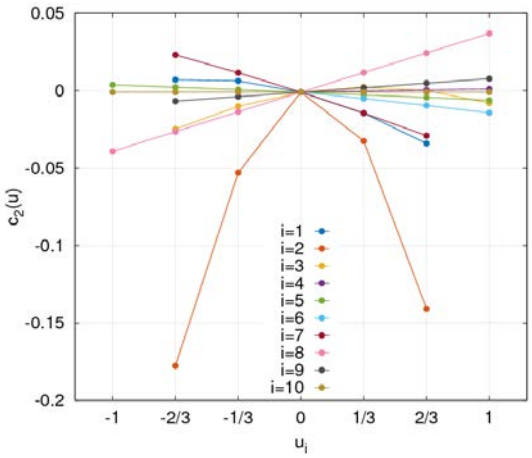

Figure 114: CFRP c_2 sensitivity

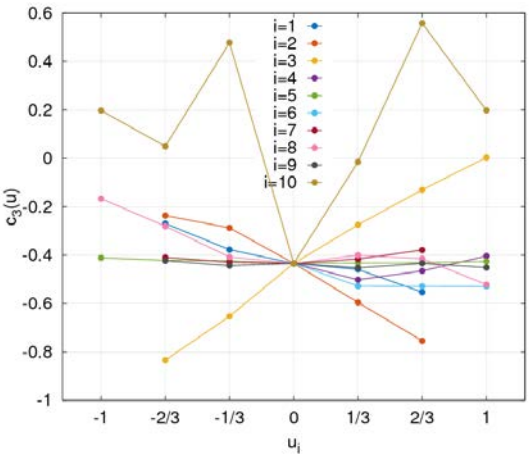

Figure 115: CFRP c_3 sensitivity

Table 38: CFRP objective and constraint function range of variation

%	u_1	u_2	u_3	u_4	u_5	u_6	u_7	u_8	u_9	u_{10}
f	111.0	421.9	1015.8	1.8	2.1	5.6	13.3	239.7	32.2	49.4
c_1	68.0	98.8	196.3	3.4	1.0	4.0	11.0	83.2	25.9	29.9
c_2	4.1	17.7	2.7	0.2	1.0	1.3	5.2	7.6	1.4	0.0
c_3	28.3	51.7	83.8	9.8	2.3	9.5	5.5	35.5	2.9	99.2
Average	52.9	147.5	324.6	3.8	1.6	5.1	8.8	91.5	15.6	44.6

Feasible objective function reductions are achieved along the design variables u_6 and u_7. u_6 = 1 provides the largest improvement followed by u_6 = 0.333, 0.667, and u_7 = 0.333. A ranking of the design variable sets is given in Table 39 based on the feasible reduction in objective function achieved. Due to the lack of convergence of some CFD simulations, the feasible range of variation associated to each variable is reduced.

Table 39: Ranking of CFRP sensitivity simulations

Ranking	Variable	Description	Δf%	u_i	Simulation feasible range
1	u_6	2st order in-plane bending	-5.63	1	[-0.1;1]
2	$u7$	2st order out-of-plane bending	-1.90	0.333	[-0.7;0.7]
3	u_1	Camber	0	0	[-0.7;0.7]
	u_2	1st order twist	0	0	[-0.7;0.7]
	u_3	2st order twist	0	0	[-0.7;1]
	u_4	1st order in-plane bending	0	0	[-0.1;1]
	u_5	1st order out-of-plane bending	0	0	[-1;1]
	u_8	Membrane	0	0	[-1;1]
	u_9	3st order twist	0	0	[-0.7;1]
	u_{10}	Fiber orientation	0	0	[-90;90]

The best sensitivity analysis simulation, corresponding to the design variable set $\mathbf{u} = [0,0,0,0,0,1,0,0,0,0]^T$, provides 5.64% objective function reduction.

Aluminum and composite material hydrofoils comparison

AL and CFRP best sensitivity results are summarized in Table 40. With respect to the original designs, the drag coefficient is reduced by 2.2 and 5.6%, The hydrodynamic efficiency increases by 0.4 and 2.0%, the maximum displacement reduces by 0.7 and 2.7%, for AL and CFRP, respectively.

Table 40: AL and CFRP best sensitivity solutions

Parameter	AL			CFRP		
	Original	Best from sensitivity	Difference %	Original	Best from sensitivity	Difference %
C_L	0.6583	0.6464	-1.8	0.6775	0.6519	-3.8
C_D	0.0348	0.0341	-2.2	0.0364	0.0343	-5.6
C_M	0.1701	0.2026	19.2	0.1752	0.1896	8.2
Eff	18.90	18.98	0.4	18.62	18.99	2.0
δ_{max}	6.10	6.06	-0.7	7.65	7.44	-2.7
ϕ	0.2230	0.2205	-1.1	0.3680	0.3064	-16.7
f	0.0348	0.0341	-2.2	0.0364	0.0343	-5.6
c_1	-0.0191	-0.0006	1.8	-0.0488	-0.0091	4.0
c_2	-0.0010	-0.0002	0.1	-0.0010	-0.0143	-1.3
c_3	-0.6569	-0.6608	-0.4	-0.4339	-0.5286	-9.5

Multidisciplinary design optimization

Aluminum hydrofoil

The solution of the AL hydrofoil problem by MCAS-MDO is achieved using 1666 function evaluations corresponding to 833 calls to the MDA. Given the partitioned approach to the FSI, this corresponds to 833 CFD simulations and 833 FE simulations.

1466 function evaluations, performed to assess the sensitivity of the functions of interest to the design variables, are used to build the initial DoE while the remaining 200 are handled by the MCAS-MDO. The total number of training points used, i.e. the number of designs evaluated, is 100, separated in 41 and 59 from the sensitivity analysis (initial DoE) and the optimization (MCAS), respectively.

Figure 116 depicts the history of the optimal solution including the objective function value corresponding to the original design. The trend is not monotonic due to the refinements of the MDA coupling. Successive iterations of the FSI may either increase or reduce the objective function depending on the specific design at hand. Moreover, the final solution provided by the optimizer may require additional MDA iterations. Unless the associated U_c reaches the prescribed tolerance during the optimization (similarly to what presented in the analytical test problem results), a full convergence of the FSI simulation should be performed to confirm the optimizer solution (achieving U_c < 1%). Accordingly, Figure 116 includes the objective function value corresponding to the optimized design which is larger than the MCAS-MDO indication.

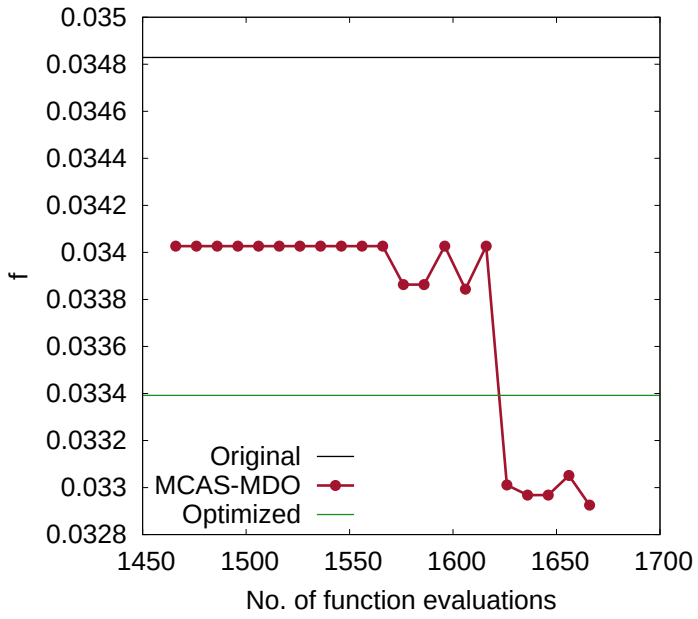

Figure 116: Convergence of the objective function given by MCAS-MDO for the AL hydrofoil problem

Figure 117 depicts the history of U_s, U_c, and U_{tot} (Eq. 80). The surrogate model uncertainty U_s is in the range 10-1000% of the original design objective function value. The coupling uncertainty U_c oscillates between 0.1 and 10000%. U_c fluctuations correspond to the identification of new potential optima. An optimum found after the infill procedure usually has large U_c since determined by loose MDA (one-way). At successive iterations, the MCAS would generally select such point for additional MDA iterations, thus reducing U_c. At the beginning of the optimization, U_c has a small value since the initial DoE is made of fully converged MDA evaluations whose associated coupling uncertainty is lower than 1%. U_{tot} is affected by the fluctuations due to U_c but points to an overall converging trend. U_{tot} at the final iteration is 41.7%, resulting from the combination of U_s = 38.4% and U_c = 16.0%.

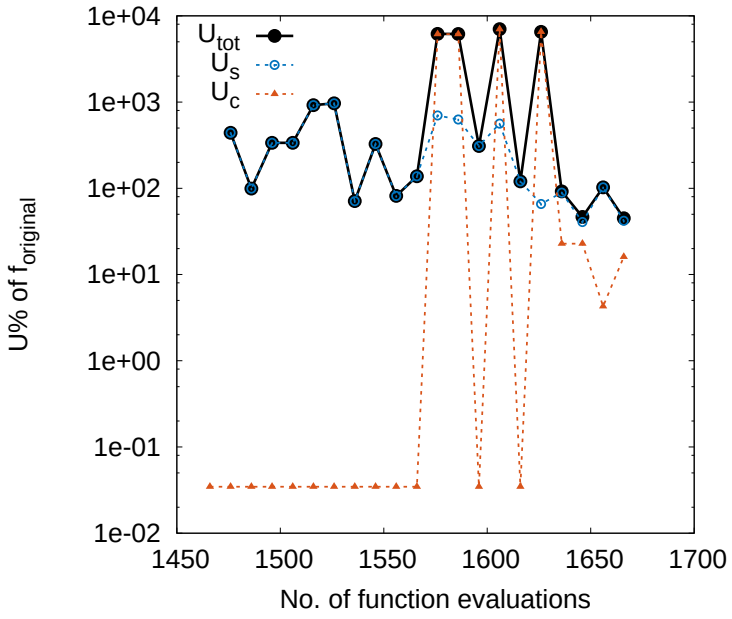

Figure 117: Convergence of the uncertainties given by MCAS-MDO for the AL hydrofoil problem

Figure 118 displays the training points in the objective function-uncertainty space, differently marking initial DoE and MCAS points. Note that some points in the initial DoE do not reach the 1% U_c tolerance within the allowed number of MDA iterations (40). Most of MCAS training points is computed using one MDA iteration. The largest number of MDA iterations is 9 (18 total function evaluations).

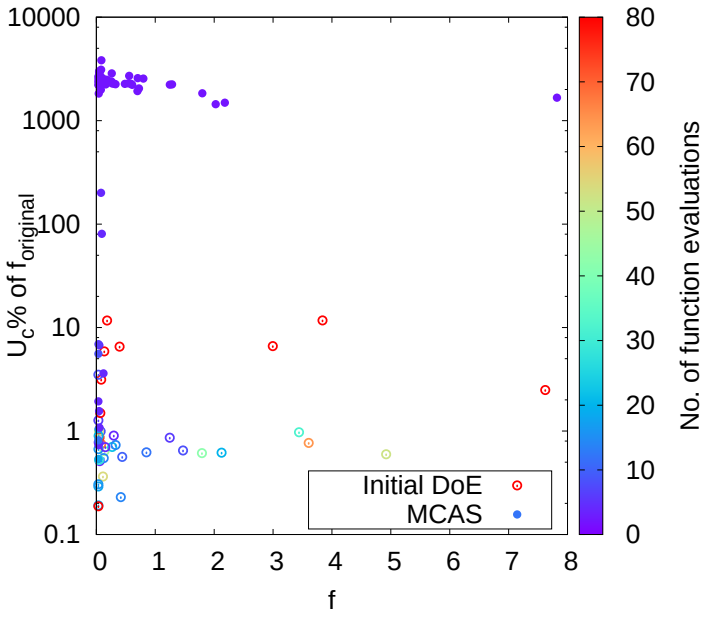

Figure 118: Distribution of training points in the objective function-uncertainty space given by MCAS-MDO for the AL hydrofoil problem

Table 41: AL optimal solution

Parameter	Original	Optimized	Difference %
C_L	0.6583	0.6573	-0.16
C_D	0.0348	0.0334	-4.13
C_M	0.1701	0.1076	-36.76
Eff	18.9011	19.6844	4.14
δ_{max}	6.0967	5.6299	-7.66
ϕ	0.2230	0.2167	-2.85
f	0.0348	0.0334	-4.13
c_1	-0.0191	-0.0191	0.00
c_2	-0.0010	-0.0162	-1.52
c_3	-0.6569	-0.6667	-0.98

The optimal design achieved by MCAS-MDO is defined by

$$\mathbf{u} = [-0.047, 0.201, -0.180, 0.199, -0.539, -0.026, -0.120, -0.540, -0.141]^T \quad (90)$$

Table 41 summarizes the optimal design specifications. The objective function, i.e. C_D, is reduced by 4.1%, which is a meaningful result since larger than the numerical uncertainty U_{SN}=3%. C_L and C_M are also reduced while the hydrodynamic efficiency is increased. Maximum displacement and failure index are smaller than the original, confirming the load-reducing effect of the optimized design. Lift, minimum thickness, and material failure constraints are satisfied and margins are qualitatively similar to the original design.

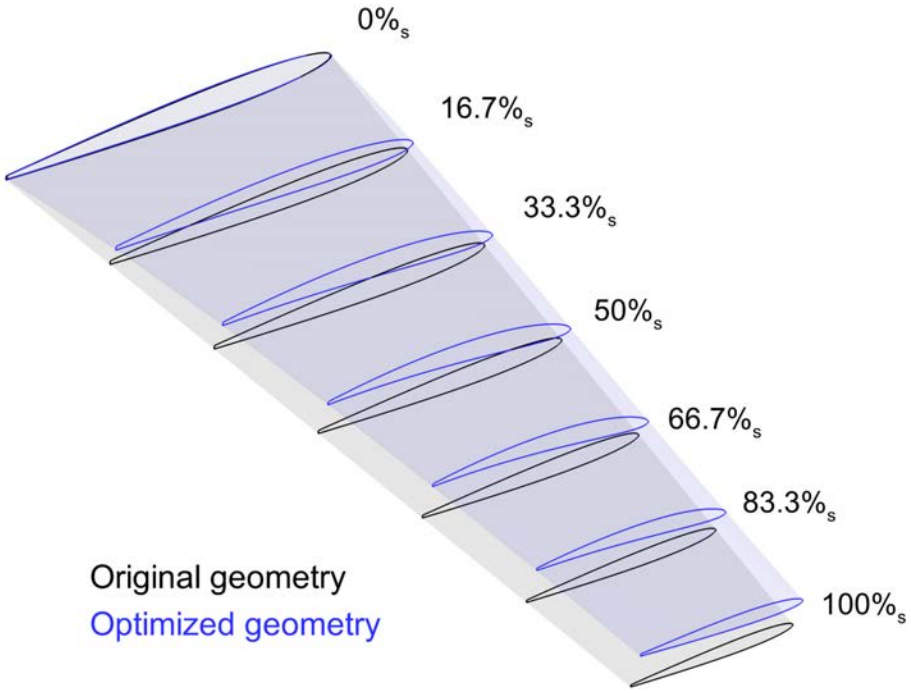

Figure 119: AL optimized geometry

Figure 119 depicts the original and optimized hydrofoil geometries. Several cross-sections along the span help visualize the design differences. The optimized design is slightly bent upward. A negative twist and non-zero camber is shown especially by cross-sections between 33.3 and 83.3% of the span. The tip section instead appears rather

symmetric. Figure 120 shows the planforms indicating a modest curvature of leading and trailing edges toward the incoming flow direction.

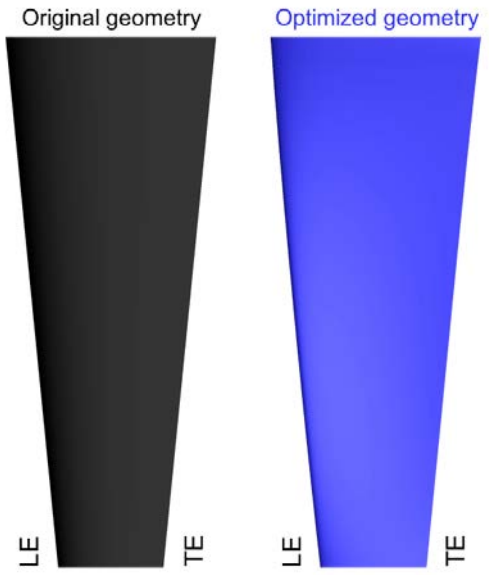

Figure 120: AL optimized planform

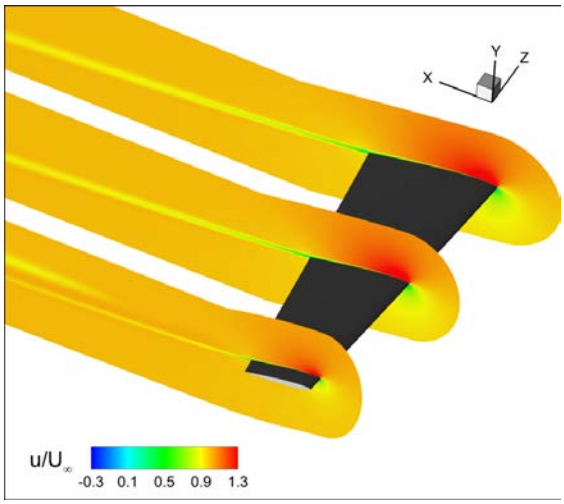

Figure 121: AL original geometry *x*-velocity contours in the *xy* plane

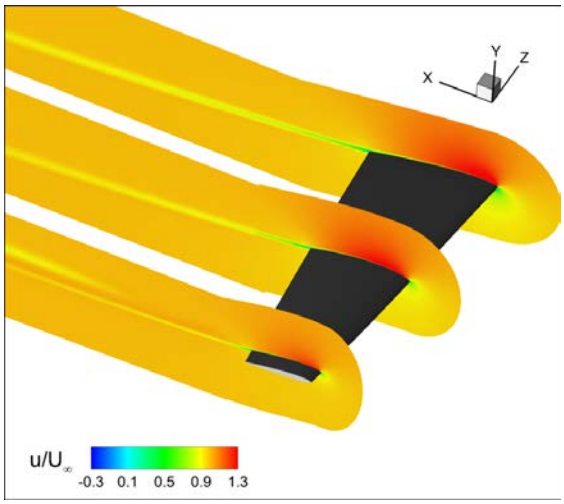

Figure 122: AL optimized geometry *x*-velocity contours in the *xy* plane

Figure 121 to Figure 124 show the contour of the *x*-velocity around the hydrofoil and the wake comparing original and optimized geometries. Figure 121 and Figure 122 use *xy*-planes at 5, 50, and 95% of the span. Figure 123 and Figure 124 use *yz*-planes at several

stream-wise distances, multiples of the mean chord, from the hydrofoil. In both cases, original and optimized designs show a similar behavior characterized by steady flow attached to the body and straight wake subject to comparable dissipation.

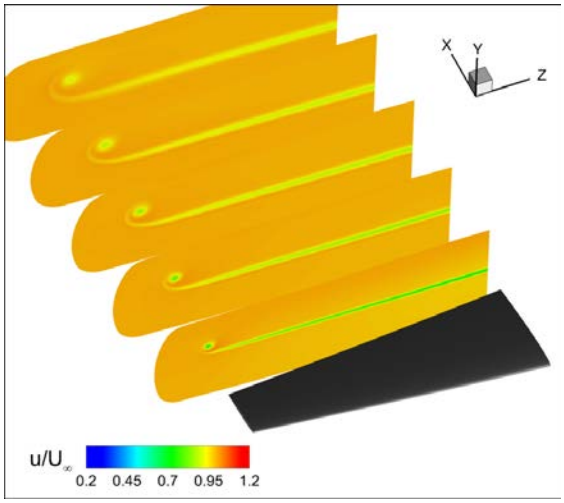

Figure 123: AL original geometry *x*-velocity contours in the *yz* plane

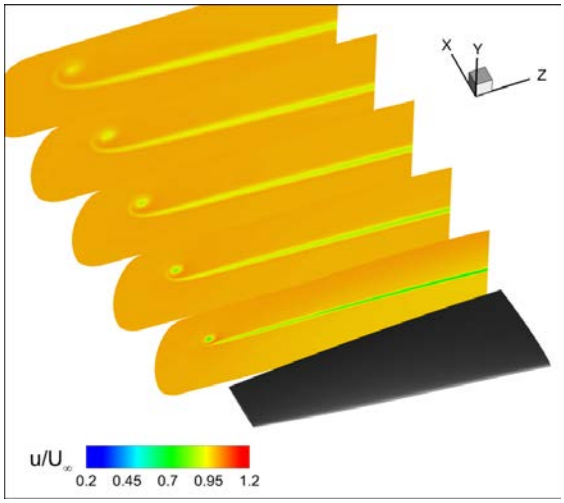

Figure 124: AL optimized geometry *x*-velocity contours in the *yz* plane

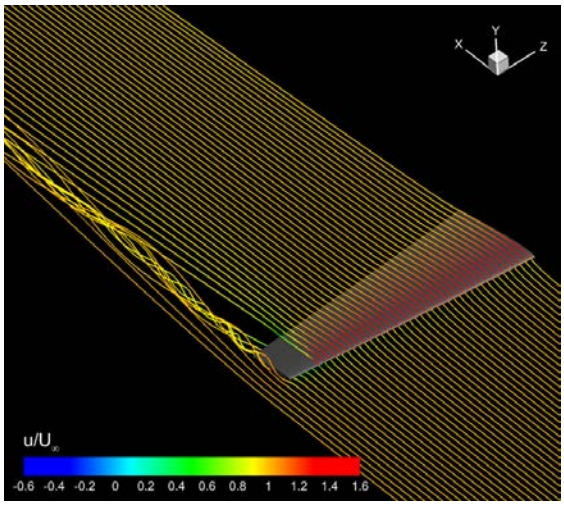

Figure 125: AL original geometry streamlines

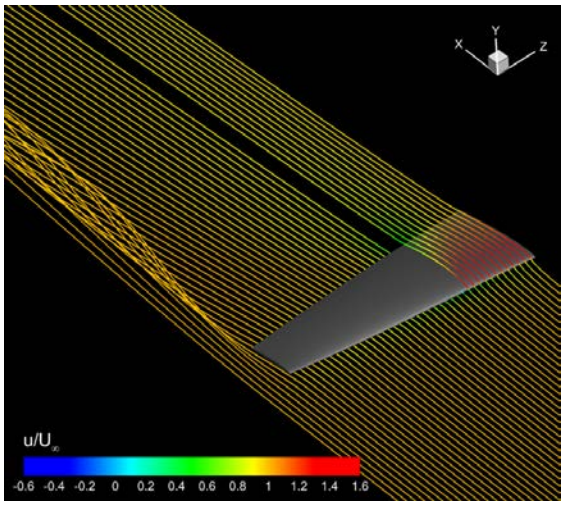

Figure 126: AL optimized geometry streamlines

Figure 125 and Figure 126 show a rake streamlines starting at the same location for the original and optimized designs. In both cases, the flow is attached to the body. The tip vortex, clearly visible in Figure 125, is loosely defined in Figure 126 due to the deflection of the flow given by the optimized geometry.

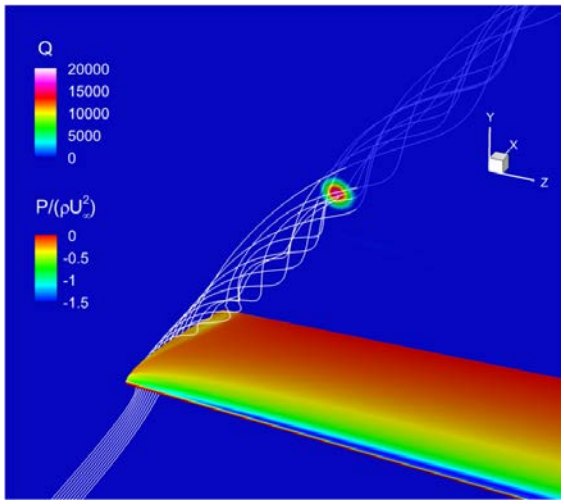

Figure 127: AL original geometry streamlines through the tip vortex and *Q* contours

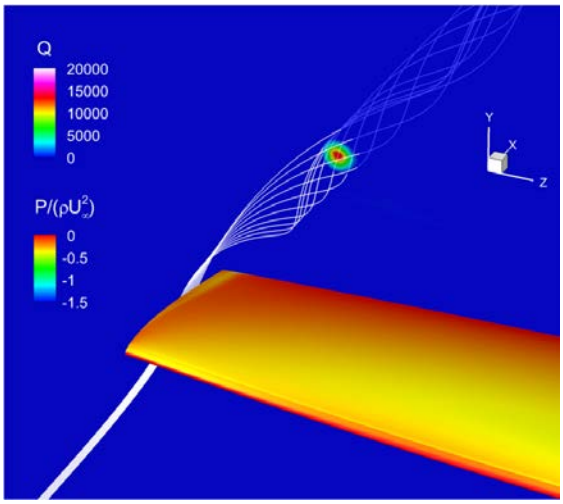

Figure 128: AL optimized geometry streamlines through the tip vortex and *Q* contours

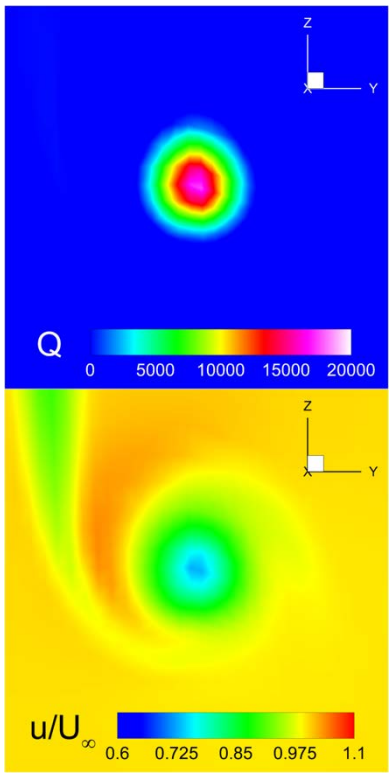

Figure 129: AL original geometry tip vortex detail

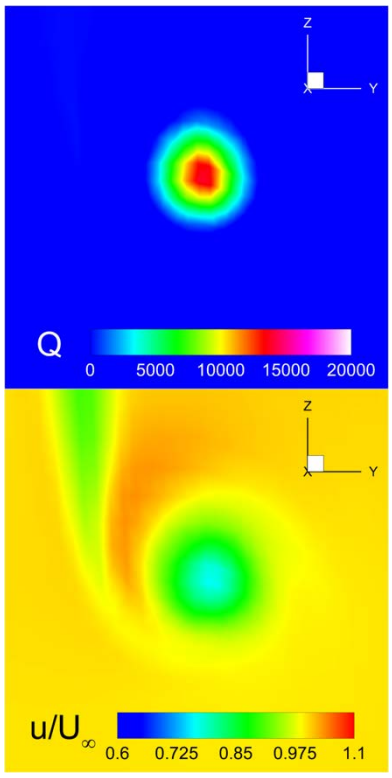

Figure 130: AL optimized geometry tip vortex detail

Figure 127 to Figure 130 show in more detail the tip vortex using the *Q* criterion. Figure 127 and Figure 128 present the streamlines around the vortex while Figure 129 and

Figure 130 show the contour of *x*-velocity and *Q* criterion. The vortex intensity in the optimized design is reduced from approximately *Q* = 17000 to *Q* = 14000.

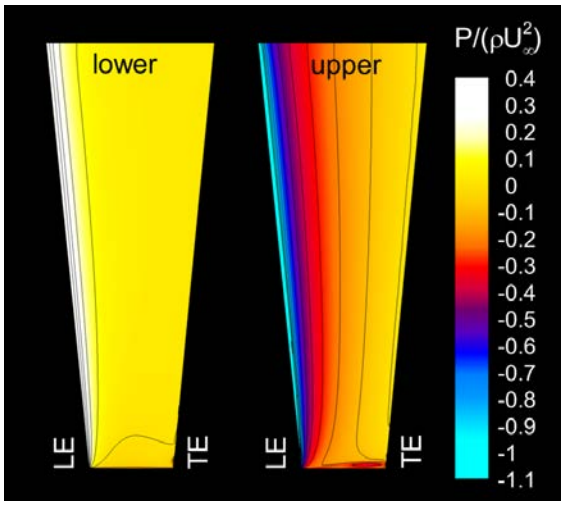

Figure 131: AL original geometry pressure distribution

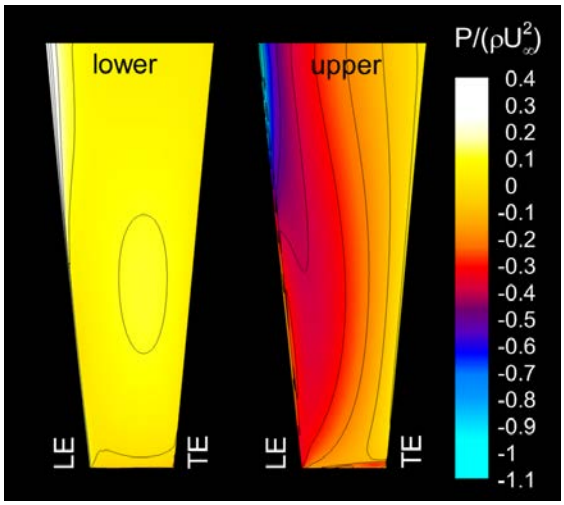

Figure 132: AL optimized geometry pressure distribution

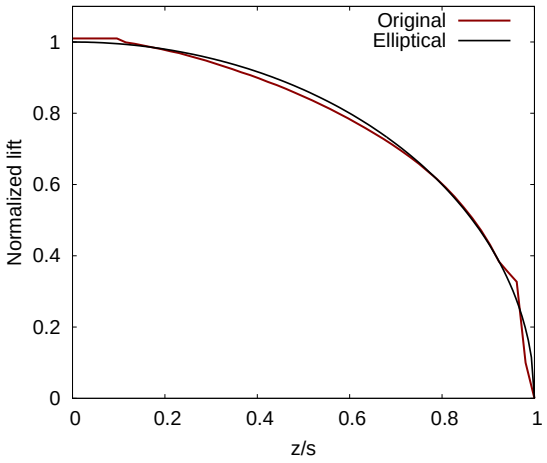

Figure 133: AL original geometry lift distribution

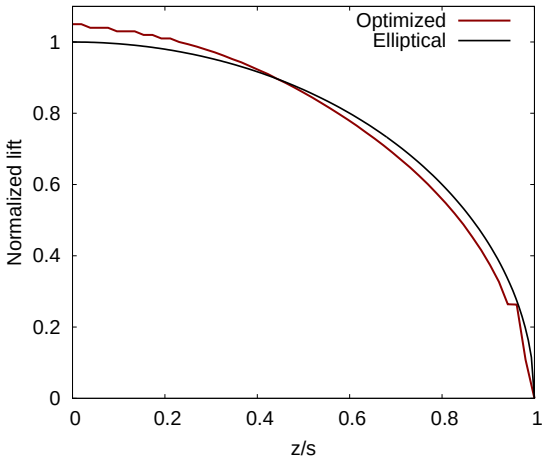

Figure 134: AL optimized geometry lift distribution

Figure 131 and Figure 132 show the pressure distribution over the hydrofoils including lower (pressure) and upper (suction) sides. Smallest and largest pressure values on the optimized geometry are located toward the root. The pressure is overall lower than in the original geometry on a large area around 2/3 of the span. Figure 133 and Figure 134 show the lift distribution along the span, built by normal force integration along the chord,

compared with the ideal elliptical distribution and confirm an increased loading close to the root and reduced loading toward the tip. Figure 135, Figure 136, and Figure 137 depict the pressure distribution around the hydrofoil over three cross-sections at 5, 50, and 85% of the span. Close to the root, the distribution is similar between original and optimized designs. At mid-span and toward the tip, the optimized design shows a significant re-distribution of the pressure drastically reducing the difference toward the leading edge.

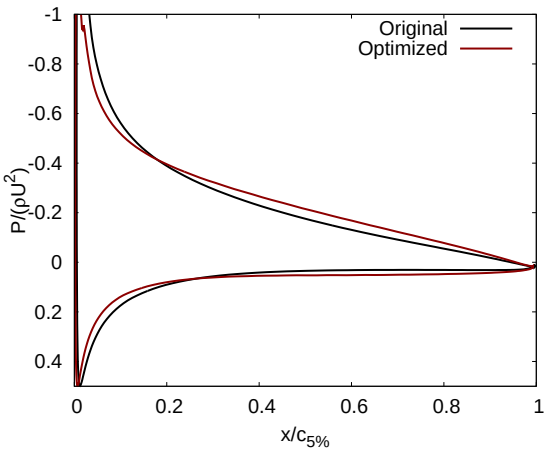

Figure 135: AL sectional pressure distribution at 5% of the span

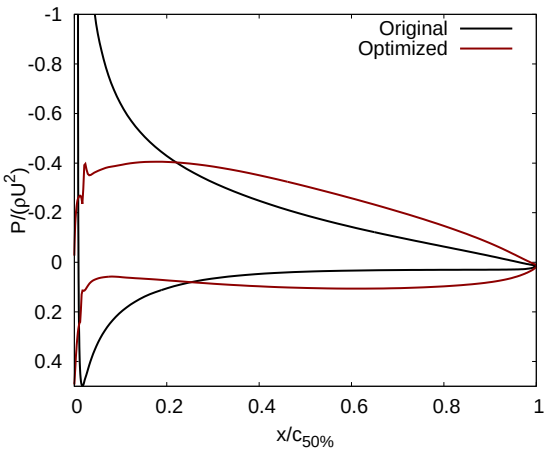

Figure 136: AL sectional pressure distribution at 50% of the span

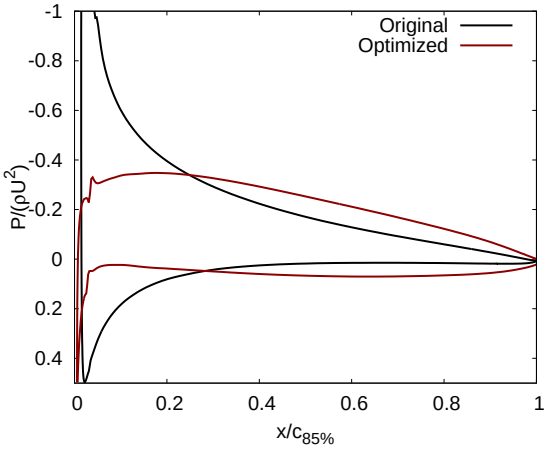

Figure 137: AL sectional pressure distribution at 85% of the span

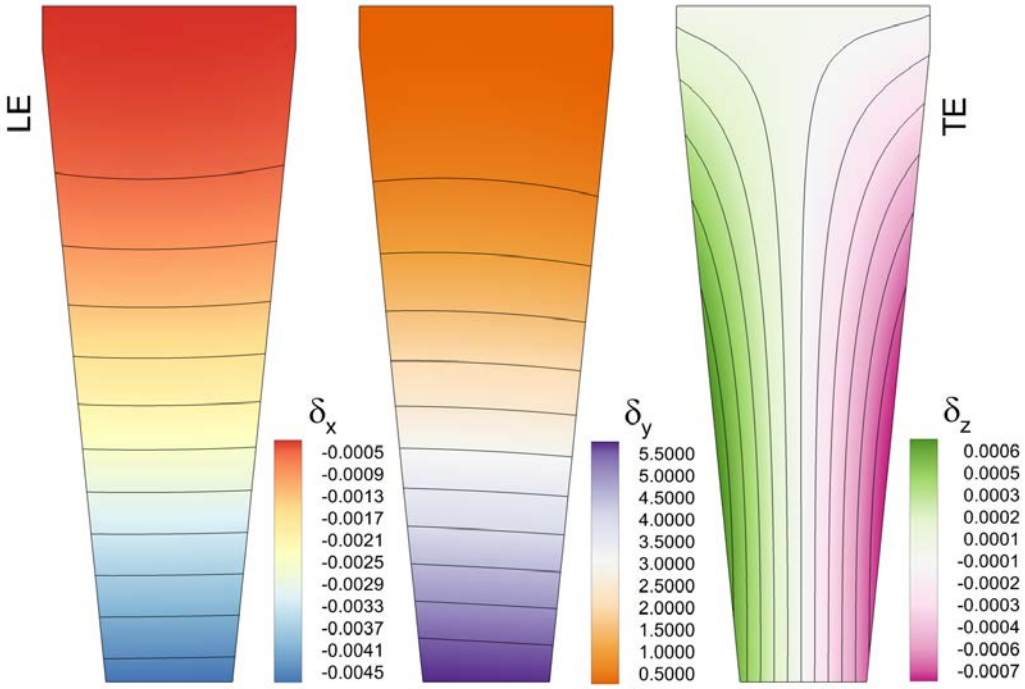

Figure 138: AL original geometry displacement distribution

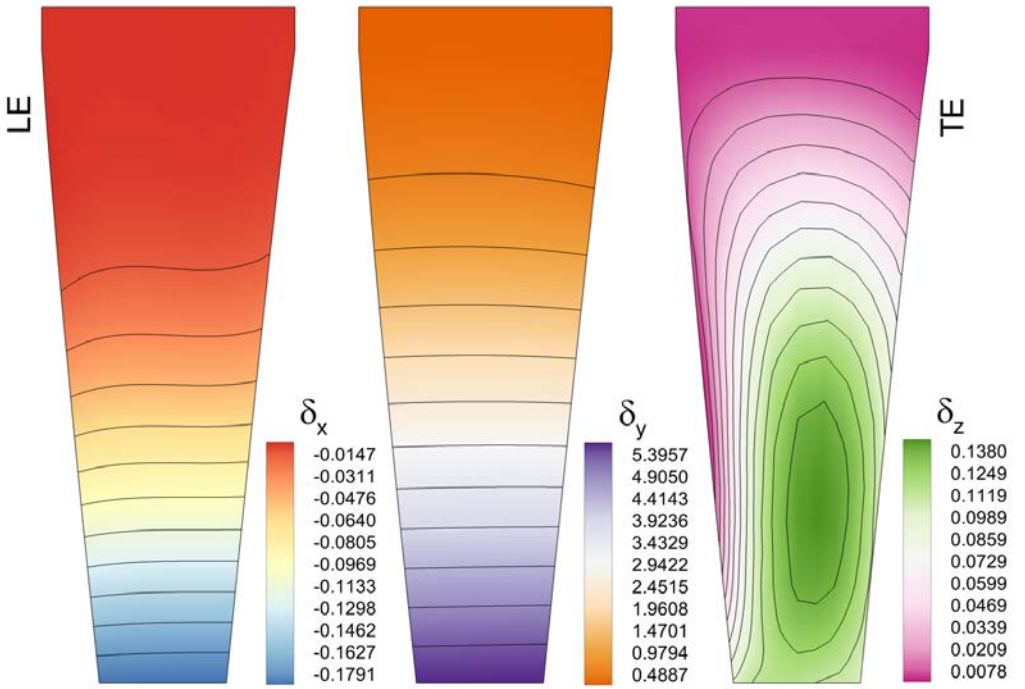

Figure 139: AL optimized geometry displacement distribution

Figure 138 and Figure 139 present the hydrofoil deformation in terms of distribution of displacement ([mm]). Overall, the main displacement component is the out-of-plane δ_y. In the original geometry, a small positive tip twist, revealed by slightly oblique contour lines in the δ_y figure, increases the effective angle of attack while the optimized design reduces the tip twist. δ_x and δ_z are generally larger in the optimized design but they still play a minor role, compared to δ_y. Figure 140 and Figure 141 show the distribution of the failure index over the hydrofoils. In both cases, the largest value is included between upper and lower sides. Overall, the largest stresses are on the suction side. The value of ϕ is comparable between designs and far from the failure limit.

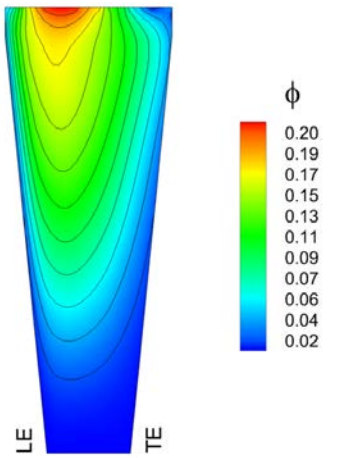

Figure 140: AL original geometry failure index distribution

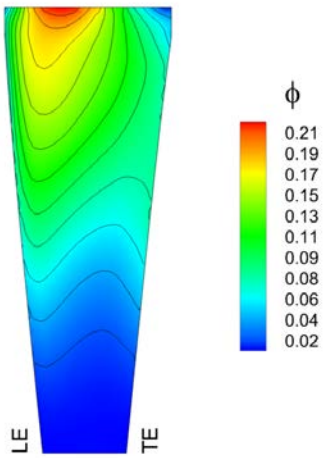

Figure 141: AL optimized geometry failure index distribution

Composite material hydrofoil

The solution of the CFRP hydrofoil problem by MCAS-MDO is achieved using 2072 function evaluations corresponding to 936 calls to the MDA (936 CFD simulations and 936 FE simulations). 1872 function evaluations, performed to assess the sensitivity of the functions of interest to the design variables, are used to build the initial DoE while the remaining 200 are handled by the MCAS-MDO. The total number of training points used, i.e. the number of designs evaluated, is 94, divided in 47 and 53 from the sensitivity analysis (initial DoE) and the optimization (MCAS), respectively.

Figure 142 depicts the history of the optimal solution including the objective function value corresponding to the original design. The trend is not monotonic due to the refinements of the MDA coupling. The final solution provided by the optimizer is iterated till full convergence of the FSI simulation to define the optimized design. The optimal solution is included in the figure and the objective function value is smaller than the MCAS-MDO indication.

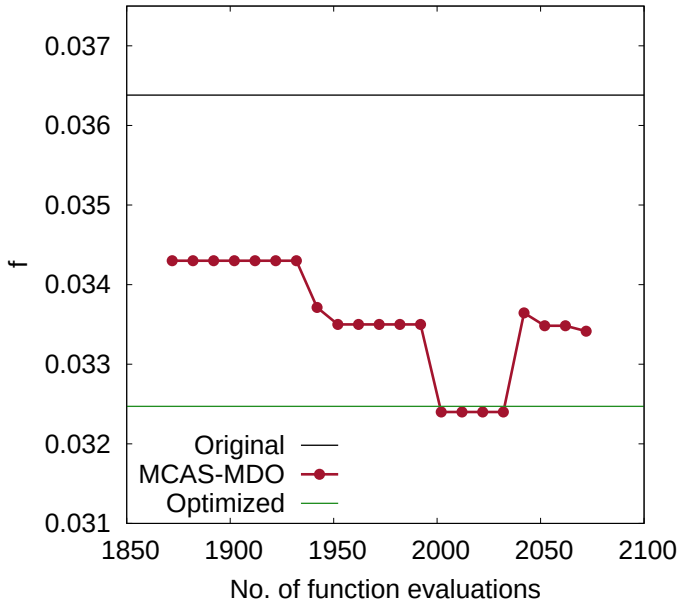

Figure 142: Convergence of the objective function given by MCAS-MDO for the CFRP hydrofoil problem

Figure 143 depicts the history of U_s, U_c, and U_{tot}. The surrogate model uncertainty U_s is in the range 10-1000% of the original design objective function value. The coupling uncertainty U_c oscillates between 0.01 and 10000% according to the identification of new potential optima. U_c has a small value at the beginning of the optimization since the initial DoE is made of fully converged MDA evaluations whose associated coupling uncertainty is lower than 1%. U_{tot} shows the fluctuations due to U_c but points to an overall converging trend. U_{tot} at the final iteration is 40.5%, resulting from the combination of U_s = 40.1.4% and U_c = 5.47%.

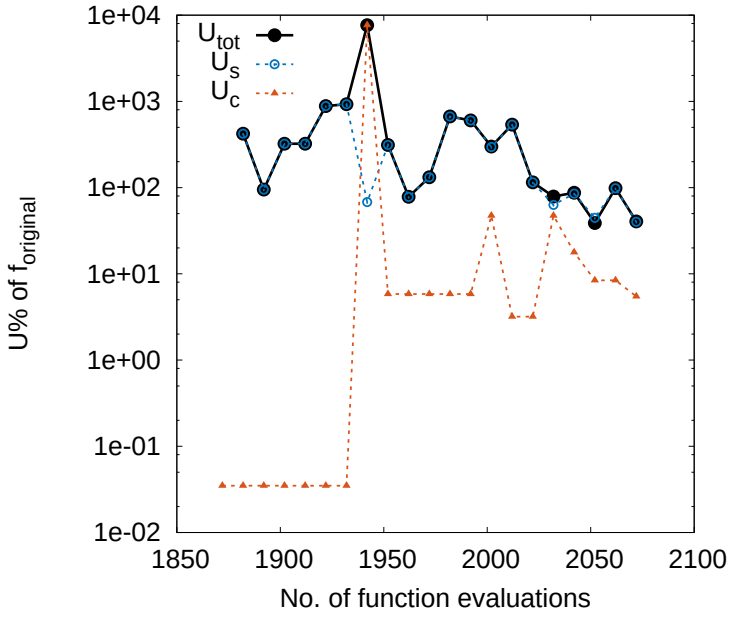

Figure 143: Convergence of the uncertainties given by MCAS-MDO for the CFRP hydrofoil problem

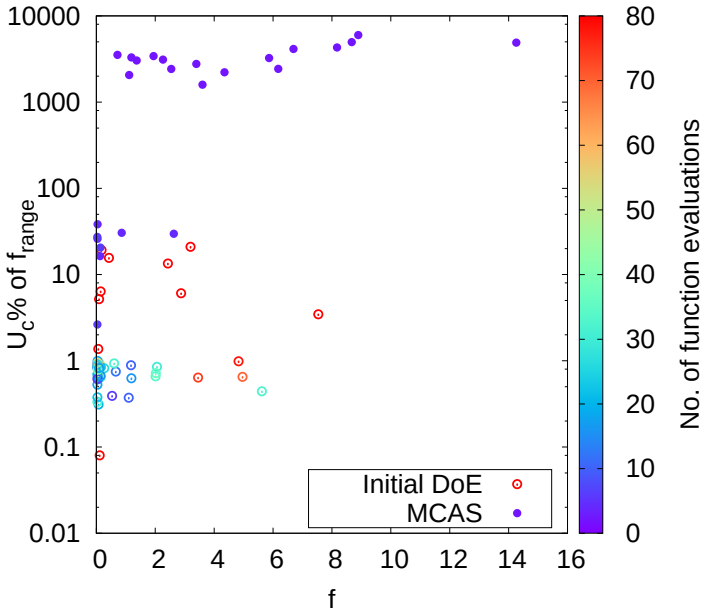

Figure 144: Distribution of training points in the objective function-uncertainty space given by MCAS-MDO for the CFRP hydrofoil problem

Figure 144 displays the training points in the objective function-uncertainty space, differently marking initial DoE and MCAS points. Note that some points in the initial DoE do not reach the 1% U_c tolerance within the allowed number of MDA iterations (40). Most

of MCAS training points is computed using one MDA iteration. The largest number of MDA iterations is 14 (28 total function evaluations).

The optimal design achieved by MCAS-MDO is defined by

$$\mathbf{u} = [-0.123, 0.190, -0.168, 0.062, -0.219, 0.273, 0.439, -0.571, 0.030, 2.763]^T \quad (91)$$

Table 42 summarizes the optimal design specifications. The objective function, i.e. C_D, is reduced by 10.8%, which is a meaningful result since larger than the numerical uncertainty U_{SN}=3%. C_L and C_M are also reduced while the hydrodynamic efficiency is increased indicating a load-reducing effect of the optimized design. Although the maximum displacement is larger than the one showed by the original design, the failure index is smaller. The different behavior of displacement and ratio is due to the change in fiber orientation, which affects the material properties. Lift, minimum thickness, and material failure constraints are satisfied with the C_L being close to the lower bound of the feasible space.

Table 42: CFRP optimal solution

Parameter	Original	Optimized	Difference %
C_L	0.6775	0.6453	-4.76
C_D	0.0364	0.0325	-10.75
C_M	0.1752	0.0959	-45.25
Eff	18.6225	19.8720	6.71
δ_{max}	7.6475	8.4829	10.92
ϕ	0.3680	0.3221	-12.47
f	0.0364	0.0325	-10.75
c_1	-0.0488	-0.0004	4.84
c_2	-0.0010	-0.0353	-3.43
c_3	-0.4339	-0.5045	-7.06

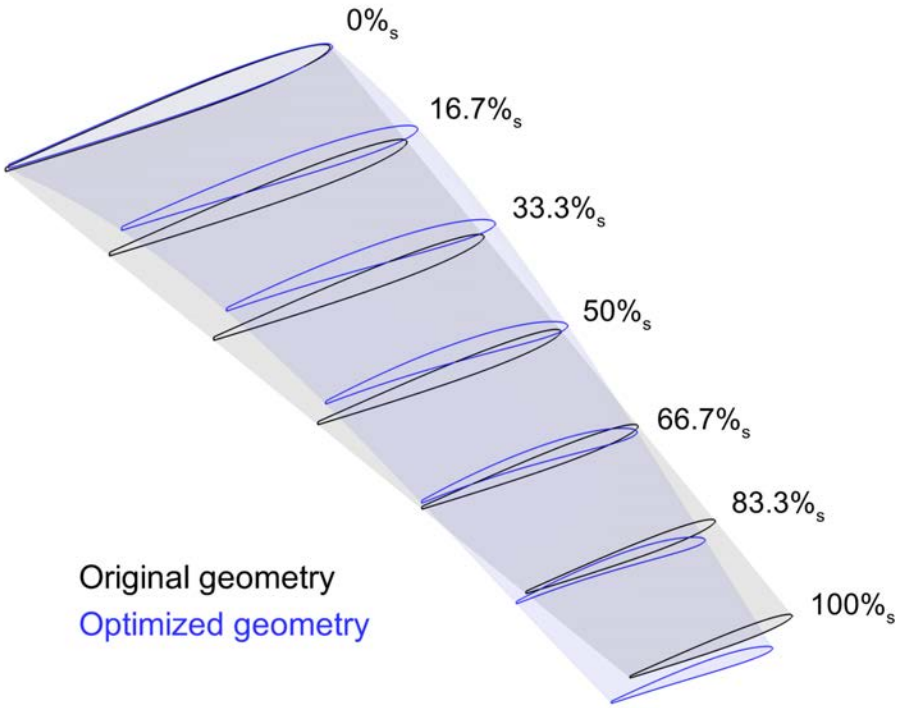

Figure 145: CFRP optimized geometry

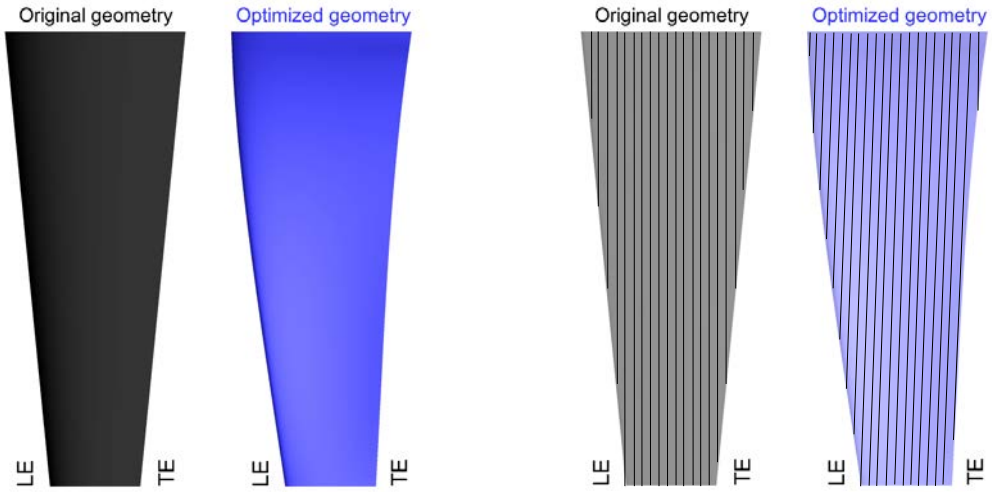

Figure 146: CFRP optimized planform (left) and fiber orientation (right)

Figure 145 depicts the original and optimized hydrofoil geometries. The optimized design is slightly bent upward from the root section till 65% of the span while it is bent downward from 65% to the tip section. A negative twist and non-zero camber is shown by all non-root cross-sections. Figure 146 shows, on the left, the planforms indicating a

significant curvature of leading and trailing edges toward the incoming flow direction and, on the right, the fiber orientation, which is slightly inclined toward the leading edge.

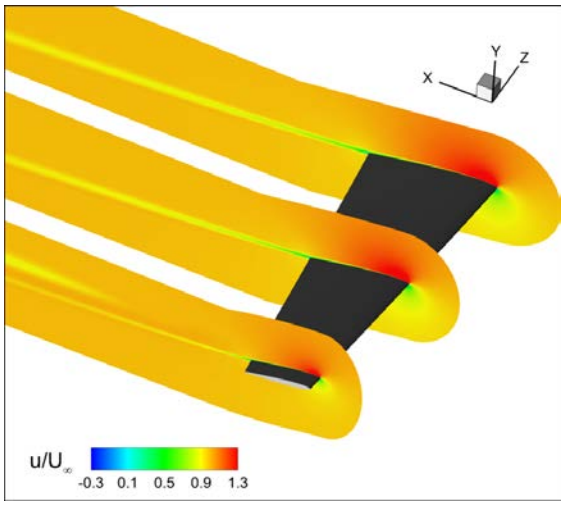

Figure 147: CFRP original geometry *x*-velocity contours in the *xy* plane

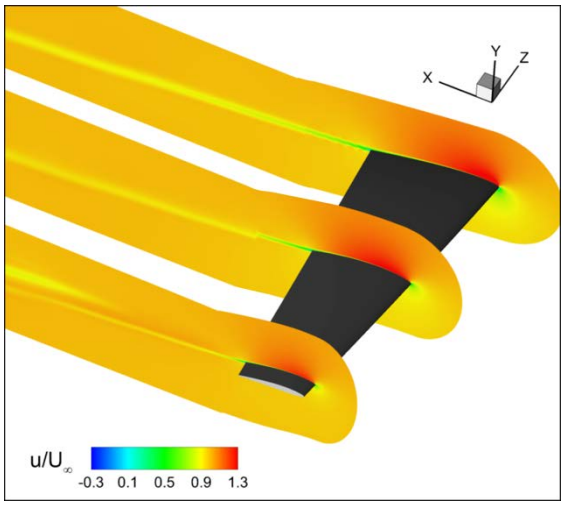

Figure 148: CFRP optimized geometry *x*-velocity contours in the *xy* plane

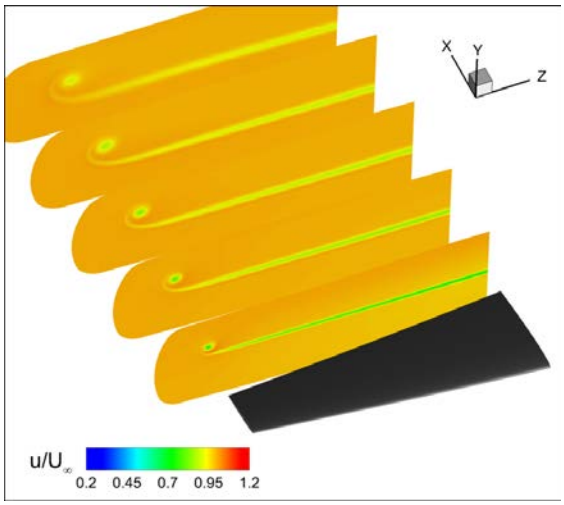

Figure 149: CFRP original geometry *x*-velocity contours in the *yz* plane

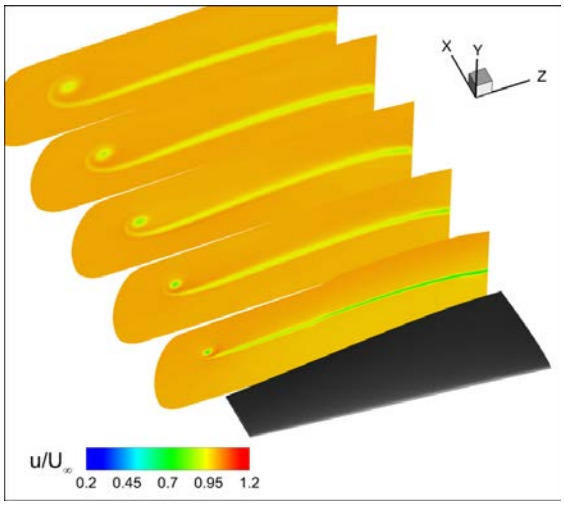

Figure 150: CFRP optimized geometry *x*-velocity contours in the *yz* plane

Figure 147 to Figure 150 show the contour of the *x*-velocity around the hydrofoil and the wake over *xy*- and *yz*-planes. Original and optimized designs show a similar behavior characterized by steady flow attached to the body. The wake of the optimized design appears curved which is consistent with the hydrofoil reshaping.

Figure 151 and Figure 152 show the streamlines around the hydrofoils showing the flow attached to the body. Figure 152 shows the flow deflection due to the optimized shape.

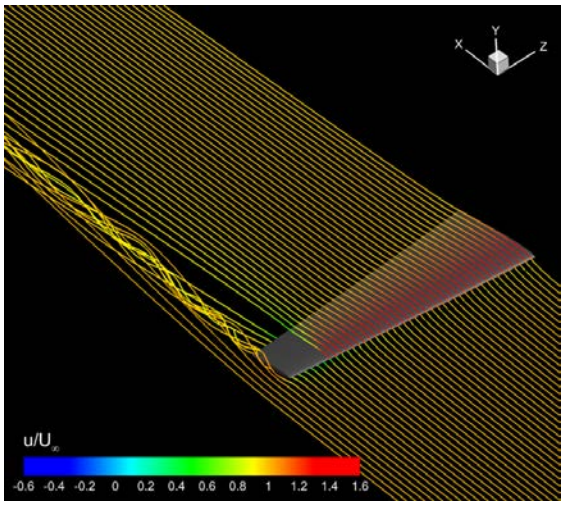

Figure 151: CFRP original geometry streamlines

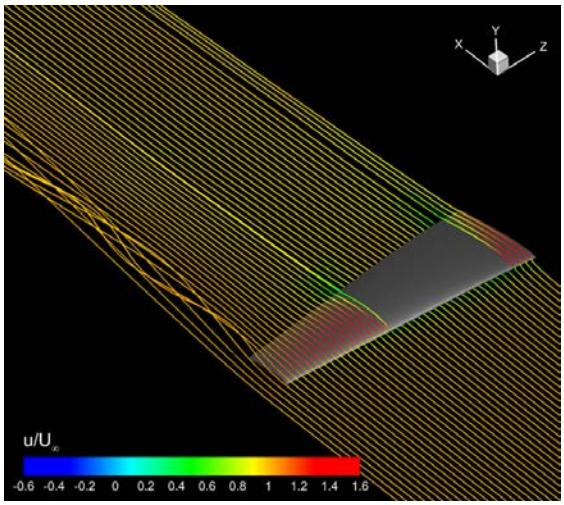

Figure 152: CFRP optimized geometry streamlines

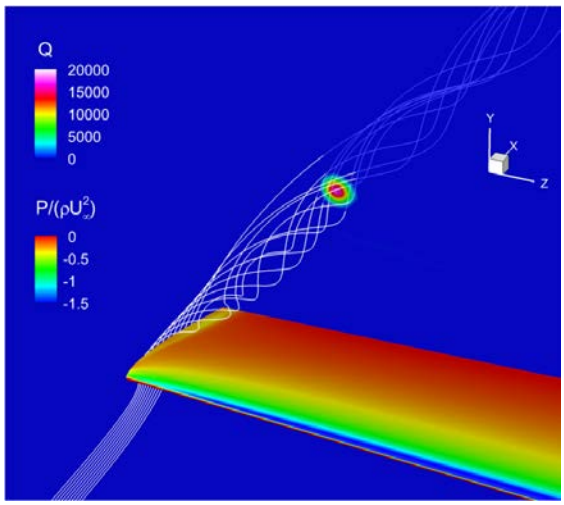

Figure 153: CFRP original geometry streamlines through the tip vortex and *Q* contours

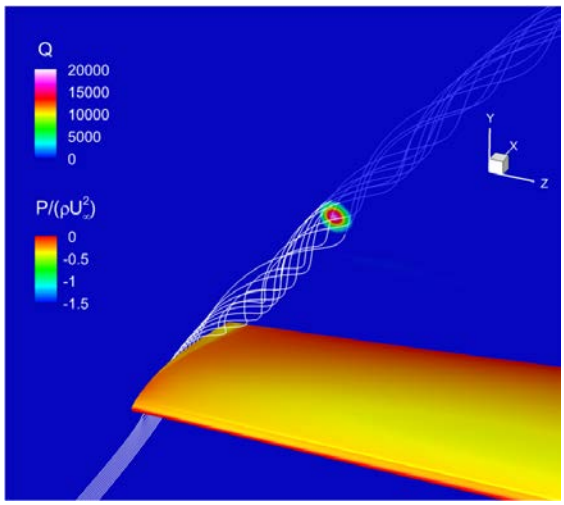

Figure 154: CFRP optimized geometry streamlines through the tip vortex and *Q* contours

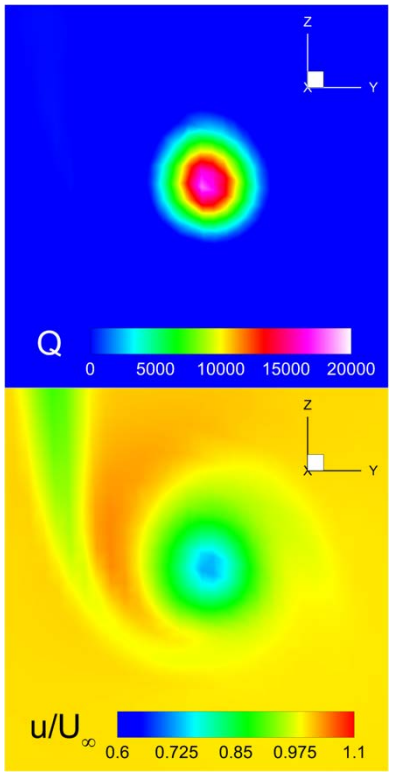

Figure 155: CFRP original geometry tip vortex detail

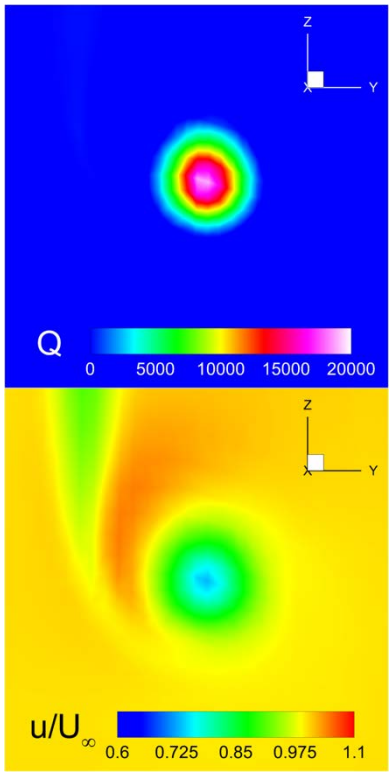

Figure 156: CFRP optimized geometry tip vortex detail

Figure 153 to Figure 156 show in more detail the tip vortex using the *Q* criterion. The vortex intensity in the optimized design is slightly increased from approximately *Q* = 18000 to *Q* = 19000.

Figure 157 and Figure 158 show the pressure distribution over the hydrofoils including lower (pressure) and upper (suction) sides. Smallest and largest pressure values on the optimized geometry are located toward the root. The pressure is overall lower than in the original geometry on a large area around 2/3 of the span. Figure 159 and Figure 160 show the lift distribution along the span compared with the ideal elliptical distribution. The load between root and 50% of the span is reduced while it is increased between 50 and 90%. Figure 161, Figure 162, and Figure 163 depict the pressure distribution around the hydrofoil over three cross-sections at 5, 50, and 85% of the span. Close to the root, the distribution is similar between original and optimized designs with a slight reduction of the upper/lower sides pressure difference at the leading edge. At mid-span and toward the tip,

the optimized design shows a significant re-distribution of the pressure drastically reducing the difference toward the leading edge.

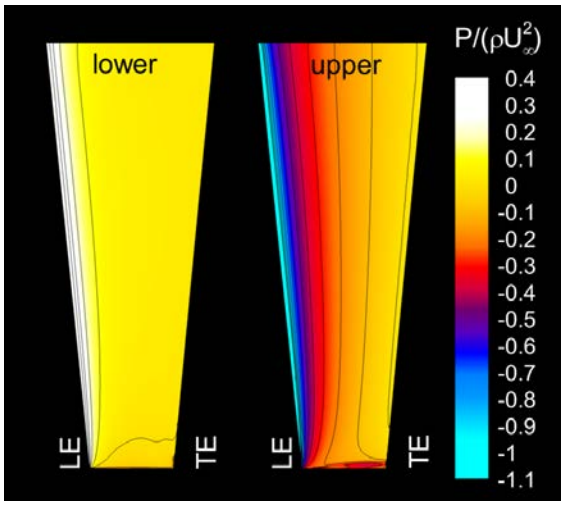

Figure 157: AL original geometry pressure distribution

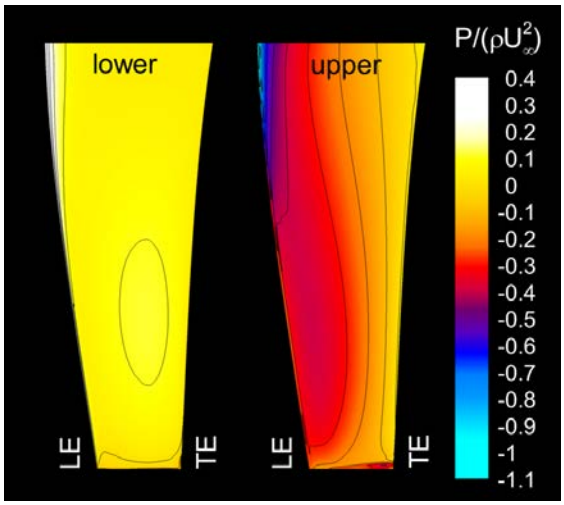

Figure 158: AL optimized geometry pressure distribution

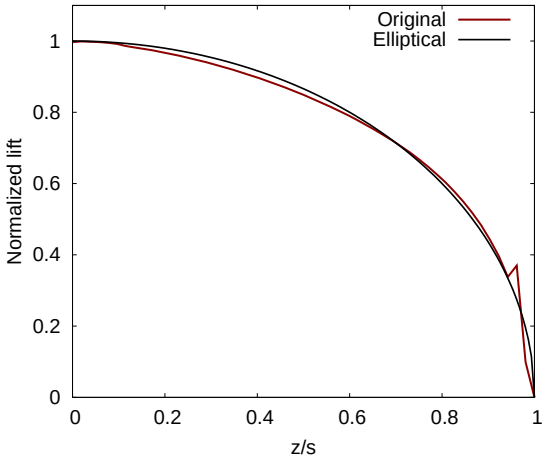

Figure 159: CFRP original geometry lift distribution

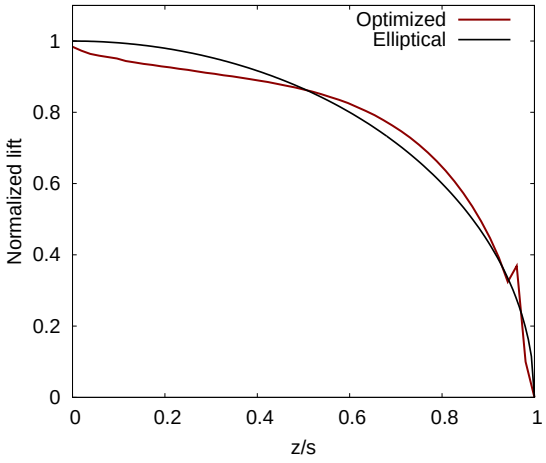

Figure 160: CFRP optimized geometry lift distribution

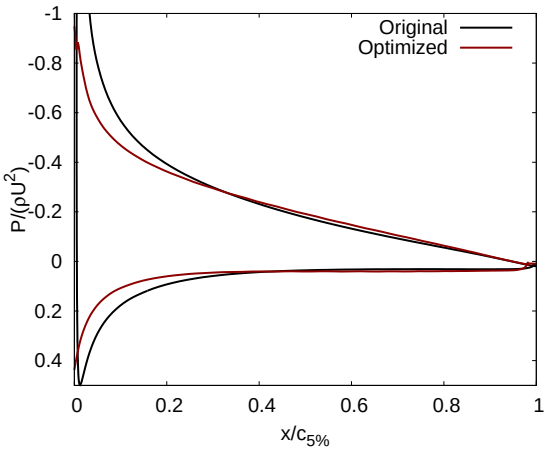

Figure 161: CFRP sectional pressure distribution at 5% of the span

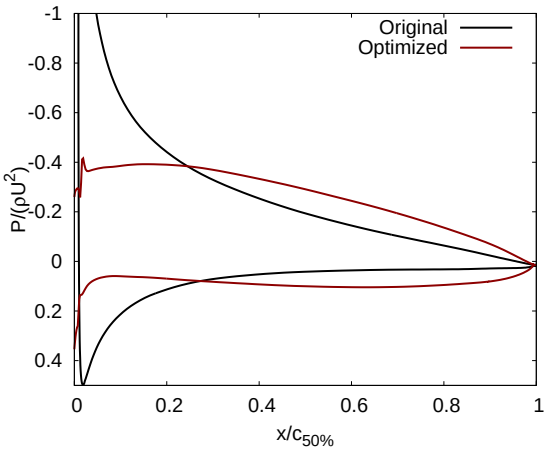

Figure 162: CFRP sectional pressure distribution at 50% of the span

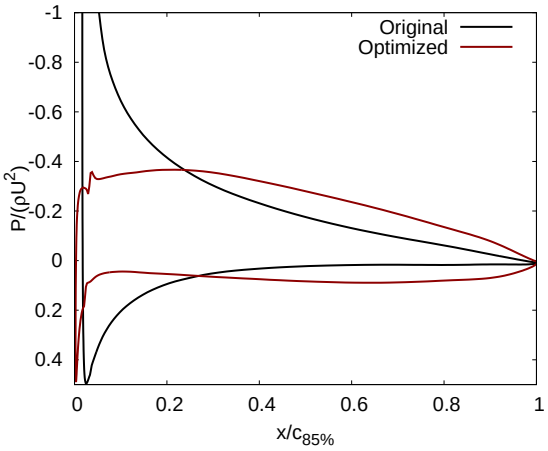

Figure 163: CFRP sectional pressure distribution at 85% of the span

Figure 164 and Figure 165 present the hydrofoil deformation in terms of distribution of displacement ([mm]). The main displacement component is the out-of-plane δ_y. In the original geometry, a significant positive tip twist increases the effective angle of attack while the optimized design shows a significant negative tip twist. δ_x and δ_z are generally larger in the optimized design but they still play a minor role, compared to δ_y. Figure 166 and Figure 167 show the distribution of the failure index over the hydrofoils. In both cases, the largest value among all composite material layers is showed. In the

original design there is a stress concentration at the leading which is absent in the optimized geometry. ϕ is, in both cases, far from the failure limit.

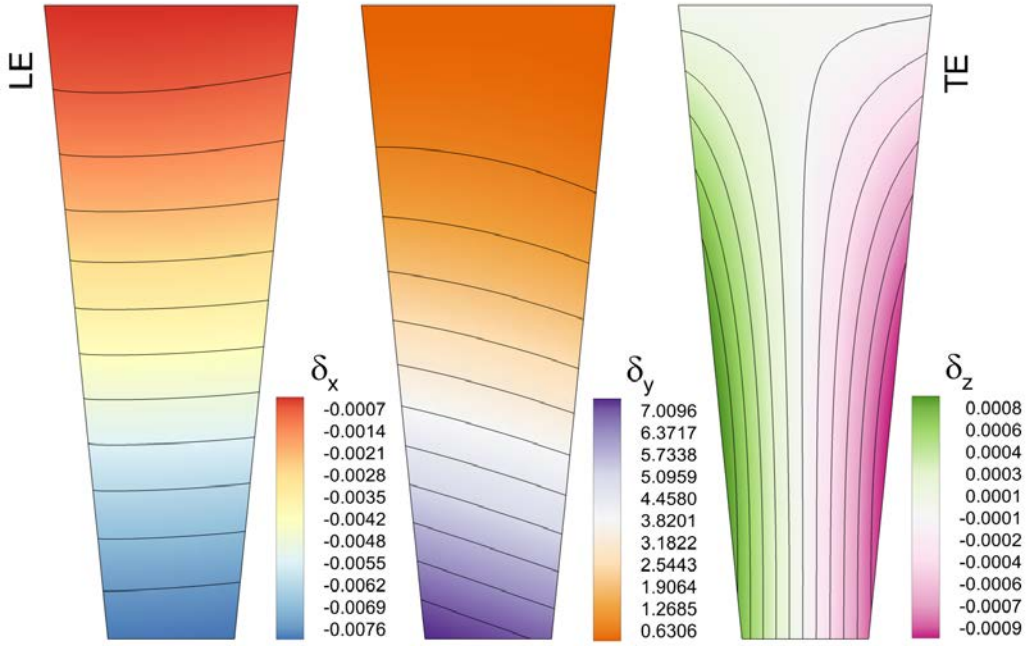

Figure 164: CFRP original geometry displacement distribution

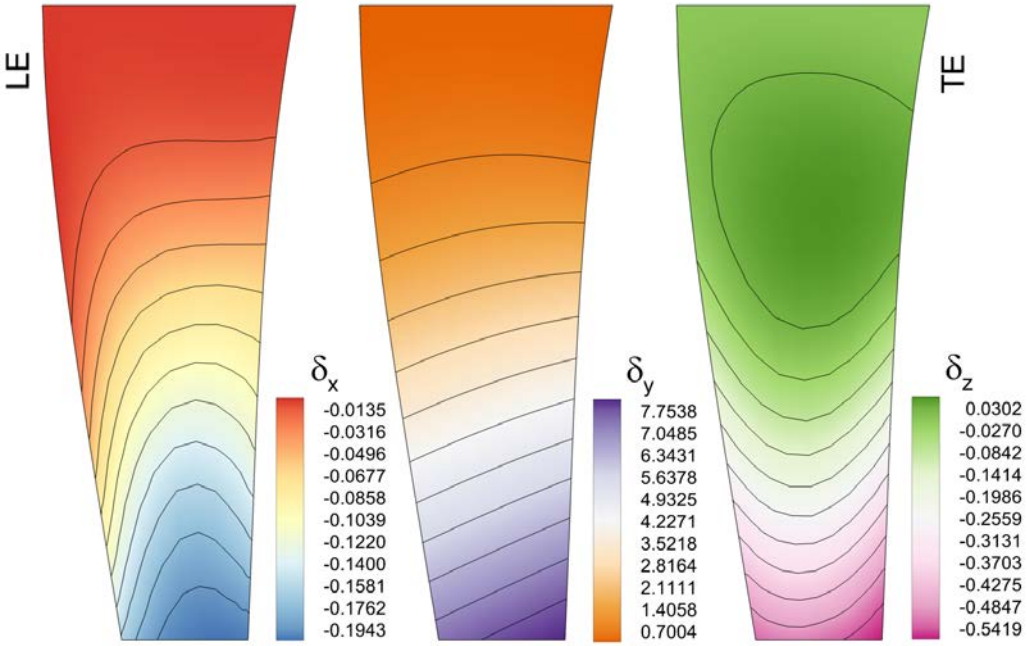

Figure 165: CFRP optimized geometry displacement distribution

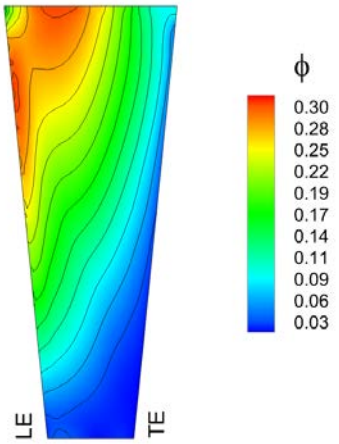

Figure 166: CFRP original geometry pressure distribution

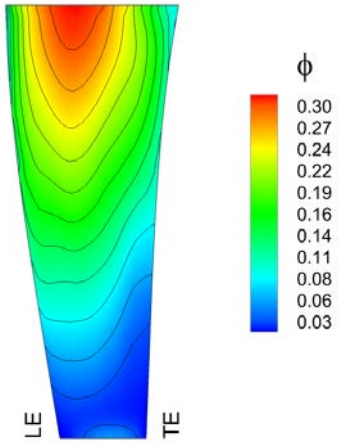

Figure 167: CFRP optimized geometry pressure distribution

Aluminum and composite material hydrofoils comparison

The AL and CFRP optimized designs show added camber, whose effect is that of increasing the load, and negative twist, whose effect is that of reducing the load. Overall, the global loading, as expressed by C_L and C_D, is reduced. With respect to the original designs, C_D reduces by 4.1 and 10.8%, Eff increases by 4.1 and 6.7%, and δ_{max} reduces by 7.7 and increase by 10.9%, for AL and CFRP, respectively. The original AL hydrofoil has lower drag than the original CFRP, indicating that the larger deformation of the CFRP model with positive tip twist is effectively increasing the load. On the contrary, the optimized CFRP hydrofoil has lower drag than the optimized AL, which correlates with the significant load reducing negative tip twist showed by the CFRP model versus the negligible twist of the AL structure.

Table 43: Summary of the optimization results

Parameter	Original AL	Optimized AL	Original CFRP	Optimized CFRP
C_L	0.658	0.657	0.678	0.645
C_D	0.0348	0.0334	0.0364	0.0325
Eff	18.9	19.7	18.6	19.9
δ_{max}	6.10	5.63	7.65	8.48

Table 44 gives the change in the value of the first five natural frequencies in vacuum between the original and the optimized geometry. The frequencies reduce by average 6.6 and 6.9% for AL and CFRP, respectively.

Table 44: Change of natural frequencies in vacuum

Mode	f_n [Hz]					
	AL original	AL optimized	Difference %	CFRP original	CFRP optimized	Difference %
1	109.12	101.76	-6.74	119.18	116.37	-2.36
2	456.82	434.33	-4.92	385.59	356.42	-7.57
3	780.34	711.14	-8.87	457.39	443.02	-3.14
4	1113.0	1027.9	-7.65	834.32	711.33	-14.74
5	1153.5	1097.1	-4.89	996.3	930.25	-6.63

Figure 168 depicts, in the form of a bar chart, the values of the design variables associated with the shape. A similar trend is showed by design variables u_1, u_2, u_3, u_4, u_5, and u_8, which are qualitatively associated with camber, first and second order twist, first in-plane bending, first order out-of-plane bending, and membrane behaviors. u_2, u_3, and u_8 especially have comparable values.

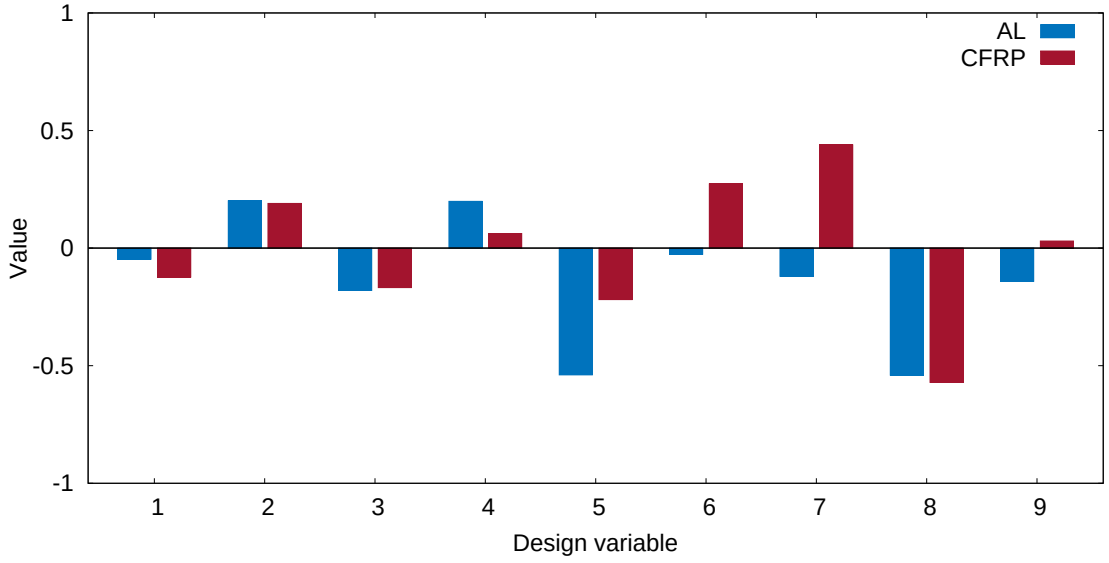

Figure 168: AL and CFRP design variables

CHAPTER 7: CONCLUSIONS

A research study has been presented for the development and validation of a surrogate-based multi-criterion adaptive sampling multidisciplinary design optimization (MCAS-MDO) architecture with application to a complex engineering problem. MCAS-MDO performs global derivative-free optimization using high-fidelity black-box solvers to evaluate the disciplines. MCAS-MDO was firstly validated using analytical test problems and then applied to a complex engineering application. The problem at hand was the design of a composite material marine structure subject to fluid-structure interaction (FSI). Available experimental data for the original design allowed validating the MDA tool. To select the proper design space with the minimum number of design variables, a design space assessment and dimensionality reduction technique was applied ahead of the optimization procedure. The MDO aimed at the minimization of the drag under steady FSI conditions subject to hydrodynamic, structural, and geometric constraints. External shape design and composite material layout were both considered in the optimization.

In the MCAS-MDO, the objective function was determined by multi-disciplinary analysis (MDA) realized through coupling of partitioned black-box solvers for the hydrodynamics and the structural dynamics simulating FSI (related FSI work was published in Volpi et al. 2015b, 2016, and 2017b). The interaction between the disciplines and the optimization procedure were handled by the multi-criterion adaptive sampling (MCAS) which: (1) identifies locations where performing additional MDA and (2) selects available MDA that require additional iterations to improve the multi-disciplinary consistency. MCAS uses a surrogate model (DRBF, published in Volpi et al. 2015a) to approximate the objective function and define the sampling, the latter based on the surrogate model uncertainty and the coupling uncertainty of the MDA. This was carried out by solving a multi-objective optimization problem, including minimizing the objective function and maximizing the uncertainties, and down-sampling the resulting Pareto frontier of non-dominated solutions to the desired number of infill points. MCAS was published for single discipline optimization in Diez et al. (2015b) and extended to MDO in Volpi et al. (2017) and Volpi et al. (2018).

The analytical test problem solution by MCAS-MDO was compared to the solution obtained by a global derivative-free implementation of the multidisciplinary feasible

(MDF) architecture. Results showed that the MCAS-MDO converges faster than the MDF and provides a more effective sampling of the design space. MDA evaluations were concentrated in promising regions; few iterations were spent far away from the optimum while several iterations allowed an accurate description of the objective function around the optimal value.

The marine structure under investigation was a hydrofoil which was experimentally (Zarruk et al. 2014) and numerically (Garg et al. 2015, Garg et al. 2017) studied in earlier research. The hydrofoil was clamped at the root section and free at the tip section. Hydrodynamic, structural dynamic, and FSI analyses, carried out using the RANS solver CFDShip-Iowa and the finite element (FE) solver ANSYS Mechanical APDL, were performed for a stainless steel, aluminum (AL), and two carbon fiber-reinforced plastic (CFRP) models and validated against experimental benchmark.

Hydrodynamic simulation conditions included several Reynolds numbers and angles of attack in both the pre- and post-stall ranges. To capture the frequency content at post-stall conditions, detached eddy simulation was used. Pre-stall forces were found well predicted (E<2%). Post-stall forces were found qualitatively captured (E=15%). CFD verification was carried out for one flow condition to evaluate the numerical uncertainty on the outputs of interest (6% for lift, 3% for drag). The structural simulations aimed at the identification of the modal frequencies of the hydrofoils which agreed with the experiments (E=8%). A FE grid study was performed showing solution convergence. One-way coupling steady FSI simulations were performed at several Reynolds numbers for pre-stall angles of attack indicating satisfactory agreement. The average error in the prediction of the hydrofoil tip displacement was 8%, while E=39% was found for the tip twist. Metal hydrofoils showed a small tip displacement (<5% of span) and no tip twist. CFRP hydrofoils showed larger tip displacement (16% of span) and positive/negative tip twist depending on the orientation of the fibers. Two-way coupling steady FSI was performed for one design condition. Results for different materials indicated that the effects of the two-way coupling were significant when tip displacement and twist were significant, especially in case of negative twist.

The free-form deformation (FFD) was used to generate shape modifications of the hydrofoil. The design space assessment was performed by Karhunen–Loève expansion

(KLE) which allowed for quantifying the associated geometric variability. Several spaces with different types of modification were compared and the one with largest variability was selected. An inverse relationship between the number of FFD control points and the geometric variability was found. A reduced dimensionality representation of the design space was achieved by combination of distributed and concentrated geometrical parameters in the KLE procedure (as published in Volpi et al. 2017). The approach aimed at steering the dimensionality reduction process toward physically meaningful design variables without the need for high-fidelity function evaluations. The design space dimensionality was reduced by 92%. A qualitative analogy was determined between the KLE-defined shape basis functions and the modes of a cantilever beam.

Sensitivity analysis was preliminarily carried out to build the initial design of experiment (DoE). Simulations were performed for the AL and CFRP hydrofoils including the nine design variables defining the shape and a tenth variable for the fiber orientation in the composite material. 41 and 47 designs were evaluated for the AL and CFRP problem, respectively. For the AL hydrofoil, 1466 high-fidelity function evaluations were required to achieve convergence of the MDA corresponding to 733 CFD and 733 FE simulations. For the CFRP hydrofoil, 1872 high-fidelity function evaluations were performed corresponding to 936 CFD and 936 FE simulations. The analysis showed an average change in the objective and constraint functions up to 300%. The fiber orientation strongly affected the deformation providing 230% average change. The best solutions in the sensitivity set yielded 2.2% and 5.6% drag reduction for the AL and CFRP hydrofoils, respectively.

The optimizations were carried out using the DoE provided by the sensitivity analysis and allowing additional 200 high-fidelity function evaluations. For the AL hydrofoil, 59 designs were selected by the MCAS while 41 MDA iterations were spent to refine the coupling at available training points. MCAS-MDO uncertainties were large, indicating the possibility of further objective function improvements. Nonetheless, they showed an overall converging trend. The optimized solution showed a reduction of the drag by 4.1%, an increase of the hydrodynamic efficiency by 4.1%, and a decrease in the maximum displacement by 7.7%. The optimized geometry was characterized by upward span-wise curvature, added camber, and negative twist of the middle cross-sections. The

planform was found similar to the original design. For the CFRP hydrofoil, 47 designs were selected by the MCAS and 47 MDA iterations were spent to refine the coupling at available training points. MCAS-MDO uncertainties were large, indicating the possibility of further objective function improvements, but showed an overall converging trend. The optimized solution showed a reduction of the drag by 10.8%, an increase of the hydrodynamic efficiency by 6.7%, and an increase in the maximum displacement by 10.9%. The optimized geometry was characterized by downward span-wise curvature, added camber, and negative twist; the planform showed a significant leading and trailing edge curvature toward the incoming flow. The optimal fiber orientation was found equal to 2.7 degrees. Overall, both AL and CFRP designs provided a redistribution of the pressure over the hydrofoil, drastically reducing the pressure difference between pressure and suction sides close to the leading edge. The modal frequencies of both the optimized models reduced by approximately 6.8%.

Overall, the application of the MCAS-MDO was found successful in overcoming some of the current limitations of state-of-the-art MDO techniques. The effective off-line dimensionality reduction using the KLE approach with combined distributed/concentrated geometrical parameters provided a 92% dimensionality reduction, alleviating the issue of large dimensionality in shape optimization. Black-box simulation tools were employed requiring no gradient approximation. The effective design space sampling by extension of the MCAS to multidisciplinary problems (clustering of accurate MDA around the optimum) showed the capability in performing optimization using a global approach. The optimization achieved 4-11% drag reduction using global derivative-free optimization over nine- and ten-dimensional design spaces by evaluation of approximately 100 designs. The current methodology and results extended optimization studies available in the literature (Garg et al. 2017) to global MDO including optimization of the composite material layout. The application of the MCAS-MDO architecture proved that the methodology is suitable for complex engineering problems allowing for a computationally feasible high-fidelity analysis using specialized solvers available to the designer.

In order to improve the efficiency of the architecture for hydro-structural MDO, a re-formulation of the problem with separated sub-system structural optimization may be investigated in future research. Furthermore, since the adaptive sampling procedure is

based on balancing uncertainties, the MCAS could be naturally extended to (1) unsteady problems, where the distance from statistical convergence is treated as a source of uncertainty, and to (2) stochastic optimization, by including uncertain design parameters such as operating conditions and manufacturing tolerances. The development of MCAS-MDO is deemed mature for the application to hydro-structural naval problems such as fast planing hull slamming.

APPENDIX

Multidisciplinary design optimization problem

Definitions

Let assume the multidisciplinary optimization problem at hand is single objective that its design variables are continuous, and the objective and constraint functions are differentiable. The optimality is assessed by the Karush-Kuhn-Tucker (KKT) conditions 0 and it is intended in a local sense.

The number of disciplines is N and the index i is used to denote the i^{th} discipline. The set of design variables $\mathbf{u} = [\mathbf{u}_0^T, \mathbf{u}_1^T, \dots, \mathbf{u}_N^T]$ is under the direct control of the optimizer and it includes the variables $\mathbf{u}_0$ shared by disciplines and the variables $\mathbf{u}_i$ that apply to the single i^{th} discipline. The outputs of the disciplines, i.e. the responses of the analyses to the given design, are the coupling variables $\mathbf{y} = [\mathbf{y}_1^T, \dots, \mathbf{y}_N^T]$. Then, state variables $\mathbf{z} = [\mathbf{z}_1^T, \dots, \mathbf{z}_N^T]$ are specific to each discipline and used only within the corresponding discipline analysis.

Each discipline is governed by a set of equations, which can be expressed in the residual form as $\mathbf{R}_i = \mathbf{0}$. Objective and constraint functions can be either specific to a discipline, f_i and $\mathbf{c}_i$, or shared by more than one, f_0 and $\mathbf{c}_0$. The initial guess of design, coupling, and state variables is indicated by $\mathbf{u}^{(0)}$, $\mathbf{y}^{(0)}$, and $\mathbf{z}^{(0)}$, respectively; the optimal values are $\mathbf{u}^*$, $\mathbf{y}^*$, and $\mathbf{z}^*$.

General formulation

The general formulation of the problem is

$$\min_{\mathbf{x},\mathbf{y},\mathbf{z}} f(\mathbf{u},\mathbf{y}) = f_0(\mathbf{u},\mathbf{y}) + \sum_{i=1}^{N} f_i(\mathbf{u}_0,\mathbf{u}_i,\mathbf{y}_i)$$

$$\begin{aligned} \text{subject to } & \mathbf{c}_0(\mathbf{u},\mathbf{y}) \le 0 \\ & \mathbf{c}_i(\mathbf{u}_0,\mathbf{u}_i,\mathbf{y}_i) \le 0 \\ & \mathbf{R}_i(\mathbf{u}_0,\mathbf{u}_i,\mathbf{y}_i,\mathbf{z}_i) = 0 \\ \text{with } & i = 1,\dots,N \end{aligned} \tag{92}$$

The governing equations of the disciplines are treated explicitly as constraint functions. In general, the formulation can be regarded as a constrained nonlinear programming problem.

Monolithic architectures

Monolithic architectures have the same structure of the general formulation in Eq. 92, where disciplines boundaries are not taken into account explicitly. Four monolithic architectures will be presented in the following sections: the all-at-once problem statement (AAO), the simultaneous analysis and design (SAND), the individual discipline feasible architecture (IDF), and the multidisciplinary feasible architecture (MDF).

All-at-once problem

An implementation that treats all the variables explicitly requires creating copies of the coupling variables in order to run different disciplines independently. These variables copies are denoted by $\tilde{\mathbf{y}} = [\tilde{\mathbf{y}}_1^T, \dots, \tilde{\mathbf{y}}_N^T]$. When copies of the same variable have different value, the overall consistency of the framework is compromised. In order to address the issue, consistency constraints $\tilde{\mathbf{c}}_i$ are introduced enforcing $\tilde{\mathbf{y}}_i = \mathbf{y}_i$ at the optimum. The formulation of the AAO includes variables copies and consistency constraints

$$\begin{aligned} \min_{\mathbf{x},\mathbf{y},\mathbf{z},\tilde{\mathbf{y}}} \; & f(\mathbf{u},\mathbf{y}) \\ \text{subject to} \; & \mathbf{c}_0(\mathbf{u},\mathbf{y}) \leq 0 \\ & \mathbf{c}_i(\mathbf{u}_0,\mathbf{u}_i,\mathbf{y}_i) \leq 0 \\ & \tilde{\mathbf{c}}_i = \tilde{\mathbf{y}}_i - \mathbf{y}_i = 0 \\ & \mathbf{R}_i(\mathbf{u}_0,\mathbf{u}_i,\mathbf{y}_i,\tilde{\mathbf{y}}_i,\mathbf{z}_i) = 0 \\ \text{with} \; & i = 1,\dots,N \end{aligned} \tag{93}$$

In the AAO approach, the optimizer runs simultaneously toward the optimization process convergence and the MDA convergence. The MDA converges as the optimizer satisfies the consistency constraints. Figure A. 1 shows the AAO procedure; note that **y** and **c** represent in this case all coupling variables and constraints, including variable copies and consistency constraints.

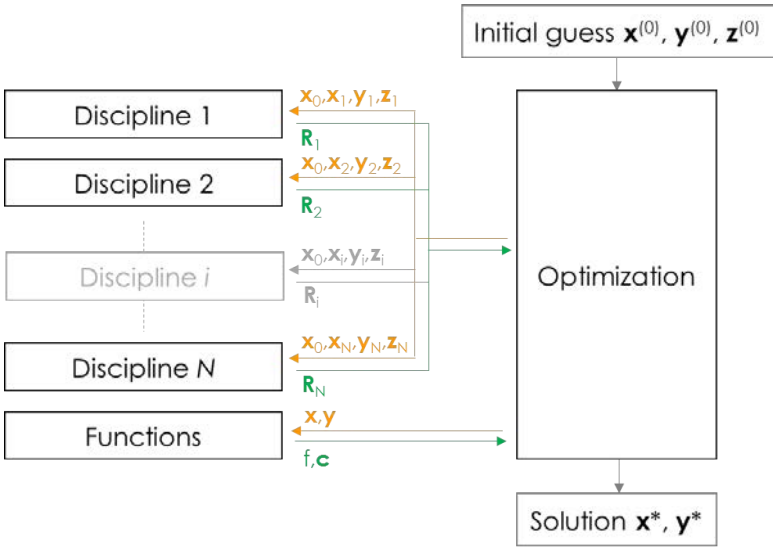

Figure A. 1: AAO architecture

Simultaneous analysis and design

In practice, consistency constraints may be treated implicitly. By avoiding the introduction of $\tilde{\mathbf{y}}$, the constraints $\tilde{\mathbf{c}}$ can be eliminated from the formulation. This allows for using directly Eq. 92, which represents the SAND architecture. Figure A. 1 depicts also the SAND structure, with $\mathbf{y}$ and $\mathbf{c}$ not including variables copies and consistency constraints. As for the AAO architecture, the analysis and the design are performed simultaneously.

In order to lighten the computational effort, a low-fidelity solution of the single discipline (i.e. simulation not completely converged) can be accepted according to the advancement of the optimization process. Such solution is infeasible, since $\mathbf{R}_i = \Delta \neq 0$, and accordingly the corresponding design. However, as the optimization moves toward convergence, a more severe constraint can be use aiming at $\Delta \to 0$ and eventually $\mathbf{R}_i = 0$ at the optimum. This approach may save resources by reducing the computational time spent in obtaining an exact solution from the discipline analysis for suboptimal designs.

Individual discipline feasible

AAO and SAND architectures treats the governing equations of the disciplines explicitly as constraints. However, the single discipline may be described by a black-box tool. A black-box is a software, code, or model that does not make available to the user the residuals of the governing equations or the state variables. The interface between black-

box tools and optimization framework may be limited to the coupling variables. The resulting formulation, where $\mathbf{R}_i$ and $\mathbf{z}_i$ have been eliminated, represents the IDF architecture.

In order to remove analysis constraints and variables, the coupling variables are expressed directly as function of the design variables and the variable copies according to the implicit function theorem

$$\begin{aligned} &\text{If } \mathbf{R}_i = F(\mathbf{u}_0, \mathbf{u}_i, \mathbf{y}_i, \tilde{\mathbf{y}}_i, \mathbf{z}_i) = 0 \\ &\text{then } \mathbf{y}_i = G(\mathbf{u}_0, \mathbf{u}_i, \tilde{\mathbf{y}}_i) \\ &\mathbf{z}_i = H(\mathbf{u}_0, \mathbf{u}_i, \tilde{\mathbf{y}}_i) \end{aligned} \tag{94}$$

Since the disciplines are solved as black-box, the equations for $\mathbf{z}_i$ can be dropped from the optimization problem formulation leading to

$$\begin{aligned} &\min_{\mathbf{x},\mathbf{y},\mathbf{z},\tilde{\mathbf{y}}} f[\mathbf{u}, \mathbf{y}(\mathbf{u}, \tilde{\mathbf{y}})] \\ &\text{subject to } \mathbf{c}_0[\mathbf{u}, \mathbf{y}(\mathbf{u}, \tilde{\mathbf{y}})] \leq 0 \\ &\qquad \mathbf{c}_i\left[\mathbf{u}_0, \mathbf{u}_i, \mathbf{y}_i(\mathbf{u}_0, \mathbf{u}_i, \tilde{\mathbf{y}}_{j\neq i})\right] \leq 0 \\ &\qquad \tilde{\mathbf{c}}_i = \tilde{\mathbf{y}}_i - \mathbf{y}_i(\mathbf{u}_0, \mathbf{u}_i, \tilde{\mathbf{y}}_{j\neq i}) = 0 \\ &\text{with } i = 1, \dots, N \end{aligned} \tag{95}$$

The name of the architecture refers to the assumption that disciplines are solved exactly, providing always feasible solutions in terms of analysis constraints ($\mathbf{R}_i$). Such assumption is required in order to apply the implicit function theorem; it does not imply that the design is feasible at each iteration, since the other constraints may not be satisfied.

The IDF architecture is shown in Figure A. 2. Firstly, disciplines are solved in parallel using the values for $\mathbf{u}$ and $\mathbf{y}$ provided by the optimizer. Then, objective and constraint functions are computed using the analysis response $\mathbf{y}_i$ supplied by each of the discipline, and the design variables $\mathbf{u}$. Advantages of using the IDF formulation versus SAND include reducing the size of the optimization problem, which does no longer include the state variables, and performing discipline analyses exploiting pre-existing software, whose source code may be hidden.

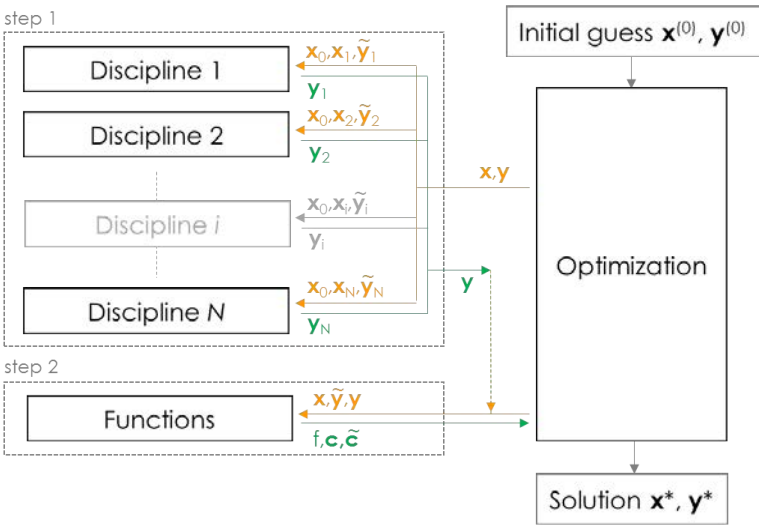

Figure A. 2: IDF architecture

Multidisciplinary feasible

The multidisciplinary feasibility of the MDF refers to the fact that a complete MDA is solved at each iteration of the optimization. Hence, the design is always feasible in terms of discipline interaction. If the analysis equations are treated implicitly as for the IDF method, the design is also individual discipline feasible; again, it does not imply that the design is feasible at each iteration, since the other constraints may not be satisfied. Since the MDA is solved at each iteration, the consistency constraints are automatically satisfied and can be dropped obtaining the MDF formulation

$$\begin{aligned} &\min_{\mathbf{x},\mathbf{y},\mathbf{z},\tilde{\mathbf{y}}} f[\mathbf{u},\mathbf{y}(\mathbf{u},\mathbf{y})] \\ &\text{subject to } \mathbf{c}_0[\mathbf{u},\mathbf{y}(\mathbf{u},\mathbf{y})] \leq 0 \\ &\qquad \mathbf{c}_i\left[\mathbf{u}_0,\mathbf{u}_i,\mathbf{y}_i(\mathbf{u}_0,\mathbf{u}_i,\mathbf{y}_{j\neq i})\right] \leq 0 \\ &\text{with } i = 1,\dots,N \end{aligned} \tag{96}$$

Figure A. 3 shows the structure of the MDF architecture. The MDA box indicates the inner loop in the process needed to achieve convergence of the multidisciplinary system. Several methods are available to solve the MDA. A rather intuitive approach is the Gauss-Seidel method: given N disciplines, let $\mathbf{y}^{(0)}$ being the initial guess for the coupling variables; the discipline analyses are performed sequentially, updating $\mathbf{y}_i$ when the i^{th}

discipline is solved; the *N* sequential steps are then iterated until convergence of the coupling variables.

The advantage of using the MDF architecture versus AAO, SAND, and IDF, is having a feasible design at each iteration, allowing for an improvement over the original design even if the optimization process is not carried out until convergence. Moreover, the size of the optimization problem is further reduced compared to the IDF architecture. The main disadvantage lays in the large computational effort required to solve a complete MDA at each iteration.

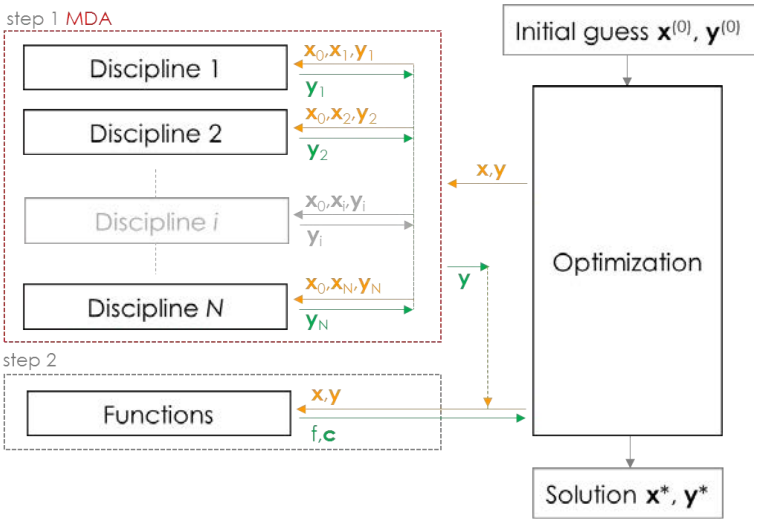

Figure A. 3: MDF architecture

Partitioned architectures

As opposed to monolithic architectures, partitioned approaches (also known as distributed) rely on splitting the optimization problem into a set of sub-problems. The main advantage is the possibility of parallel computing implementations, along with the ability of integrating the architecture into existing organizational structures. Monolithic architecture may use parallel environments; however, all discipline analyses are run the same number of times in a synchronous fashion, exhibiting poor load balancing when analysis times differ significantly. The global computational effort of partitioned architectures may be larger than monolithic architectures; nonetheless, the ability of exploiting efficiently parallel computing resources can provide a significant reduction in wall clock time. Moreover, a partitioned architecture may better suit a design environment

where existing specialized engineering groups work independently on their discipline of competency, sporadically exchanging information with the others. Partitioned architecture are generally built on two levels, namely, the global system level and the discipline level. Consequently, two optimization problems are defined for each architecture and each discipline may perform its own optimization sub-problem in parallel. The concept of decomposing the optimization in sub-problems is based on the idea of taking advantage of discipline independence. Full separability, where there are no shared variables or functions, is unusual and a method for modeling discipline interaction, by means of shared variables and functions, is required.

REFERENCES

ANSYS Mechanical APDL Theory Reference, Release 15.0, November 2013.

Balling, R.J. and Sobieszczanski-Sobieski, J., 1996. Optimization of coupled systems: a critical overview of approaches. *AIAA Journal*, Vol. 34, No. 1, pp.6-17.

Booker, A.J., Dennis, J.E., Frank, P.D., Serafini, D.B., Torczon, V. and Trosset, M.W., 1999. A rigorous framework for optimization of expensive functions by surrogates. *Structural optimization*, Vol. 17, No. 1, pp.1-13.

Borzì, A., Schulz, V., Schillings, C. and Von Winckel, G., 2010. On the treatment of distributed uncertainties in PDE-constrained optimization. *GAMM-Mitteilungen*, Vol. 33, No. 2, pp. 230-246.

Braun, R., Gage, P., Kroo, I. and Sobieski, I., 1996. Implementation and performance issues in collaborative optimization. In *6th Symposium on Multidisciplinary Analysis and Optimization*, pp. 4017.

Campana, E.F., Fasano, G. and Pinto, A., 2010. Dynamic analysis for the selection of parameters and initial population, in particle swarm optimization. *Journal of Global Optimization*, Vol. 48, No. 3, pp. 347-397.

Campana, E.F., Liuzzi, G., Lucidi, S., Peri, D., Piccialli, V. and Pinto, A., 2009. New global optimization methods for ship design problems. *Optimization and Engineering*, Vol. 10, No. 4, pp. 533.

Campana, E.F., Fasano, G. and Peri, D., 2006. Issues on nonlinear programming for Multidisciplinary Design Optimization (MDO), in ship design frameworks. In *III European conference on computational mechanics solids, structures and coupled problems in engineering*. Lisbon, Portugal.

Chen, X., Diez, M., Kandasamy, M., Zhang, Z., Campana, E.F. and Stern, F., 2015. High-fidelity global optimization of shape design by dimensionality reduction, metamodels and deterministic particle swarm. *Engineering Optimization*, Vol. 47, No. 4, pp. 473-494.

Chittick, I.R. and Martins, J.R., 2009. An asymmetric suboptimization approach to aerostructural optimization. *Optimization and Engineering*, Vol. 10, No. 1, pp.133.

Cox, D.D. and John, S., 1992. A statistical method for global optimization. In *Systems, Man and Cybernetics, 1992., IEEE International Conference on*, pp. 1241-1246.

Cramer, E.J., Dennis, Jr, J.E., Frank, P.D., Lewis, R.M., and Shubin, G.R., 1994. Problem formulation for multidisciplinary optimization. *SIAM Journal on Optimization*, Vol. 4, No. 4, pp.754-776.

D'Agostino, D., Serani, A., Campana, E.F. and Diez, M., 2018a. Nonlinear Methods for Design-Space Dimensionality Reduction in Shape Optimization. In *International Workshop on Machine Learning, Optimization, and Big Data*, pp. 121-132. Springer, Cham.

D'Agostino, D., Serani, A., Campana, E.F. and Diez, M., 2018b. Deep Autoencoder for Off-Line Design-Space Dimensionality Reduction in Shape Optimization. In *2018 AIAA/ASCE/AHS/ASC Structures, Structural Dynamics, and Materials Conference*, pp. 1648.

Diez, M., Serani, A., Campana, E.F., Volpi, S., and Stern, F., 2016a. Design Space Dimensionality Reduction for Single- and Multi-Disciplinary Shape Optimization, *17th AIAA/ISSMO Multidisciplinary Analysis and Optimization Conference*, Washington, DC, USA.

Diez, M., Serani, A., Stern, F., and Campana, E.F., 2016b. Combined geometry and physics based method for design-space dimensionality reduction in hydrodynamic shape optimization. *Proceedings of the 31st Symposium on Naval Hydrodynamics*, Monterey, CA, USA.

Diez, M., Campana, E.F., and Stern, F., 2015a. Design-space dimensionality reduction in shape optimization by Karhunen–Loève expansion. *Computer Methods in Applied Mechanics and Engineering*, Vol. 283, pp.1525-1544.

Diez, M., Volpi, S., Serani, A., Stern, F. and Campana, E.F., 2015b. Simulation-based design optimization by sequential multi-criterion adaptive sampling and dynamic radial basis functions. *EUROGEN International Conference on Evolutionary and Deterministic Methods for Design, Optimization and Control with Applications to Industrial and Societal Problems*, Glasgow, UK.

Diez, M., He, W., Campana, E.F. and Stern, F., 2014. Uncertainty quantification of Delft catamaran resistance, sinkage and trim for variable Froude number and geometry using metamodels, quadrature and Karhunen–Loève expansion. *Journal of Marine Science and Technology*, Vol. 19, No. 2, pp. 143-169.

Diez, M., Chen, X., Campana, E.F. and Stern, F., 2013. Reliability-based robust design optimization for ships in real ocean environment. In *12th International Conference on Fast Sea Transportation, FAST2013*, Amsterdam, The Netherlands.

Diez, M. and Iemma, U., 2012. Multidisciplinary conceptual design optimization of aircraft using a sound-matching-based objective function. *Engineering Optimization*, Vol. 44, No. 5, pp. 591-612.

Dorigo, M., Maniezzo, V. and Colorni, A., 1996. Ant system: optimization by a colony of cooperating agents. *IEEE Transactions on Systems, Man, and Cybernetics, Part B (Cybernetics)*, Vol. 26, No.1, pp. 29-41.

Ducoin, A. and Young, Y.L., 2013. Hydroelastic response and stability of a hydrofoil in viscous flow. *Journal of fluids and structures*, Vol. 38, pp. 40-57.

Duvigneau, R., and Visonneau, M., 2004. Hydrodynamic design using a derivative-free method. *Structural and Multidisciplinary Optimization*, Vol. 28, No. 2-3, pp. 195-205.

Farhat, C., Michael, L., and Le Tallec, P., 1998. Load and motion transfer algorithms for fluid/structure interaction problems with non-matching discrete interfaces: Momentum and energy conservation, optimal discretization and application to aeroelasticity. *Computer methods in applied mechanics and engineering*, Vol. 157, No. 1, pp. 95-114.

Forrester, A.I. and Keane, A.J., 2009. Recent advances in surrogate-based optimization. *Progress in Aerospace Sciences*, Vol. 45, No. 1-3, pp. 50-79.

Garg, N., Kenway, G.K., Martins, J.R. and Young, Y.L., 2017. High-fidelity multipoint hydrostructural optimization of a 3-D hydrofoil. *Journal of Fluids and Structures*, *71*, pp. 15-39.

Garg, N., Kenway, G.K., Lyu, Z., Martins, J.R., and Young, Y.L., 2015. High-Fidelity Hydrodynamic Shape Optimization of a 3-D Hydrofoil. *Journal of Ship Research*, Vol. 59, No. 4, pp. 209-226.

Glaz, B., Goel, T., Liu, L., Friedmann, P.P. and Haftka, R.T., 2009. Multiple-surrogate approach to helicopter rotor blade vibration reduction. *AIAA Journal*, Vol. 47, No. 1, pp. 271-282.

Grossman, B., Haftka, R.T., Sobieszczanski-Sobieski, J., Kao, P.J., Polen, D.M. and Rais-Rohani, M., 1990. Integrated aerodynamic-structural design of a transport wing. *Journal of Aircraft*, Vol. 27, No. 12, pp. 1050-1056.

Haftka, R.T., 1985. Simultaneous analysis and design. *AIAA Journal*, Vol. 23, No. 7, pp.1099-1103.

Haftka, R.T., Sobieszczanski-Sobieski, J. and Padula, S.L., 1992. On options for interdisciplinary analysis and design optimization. *Structural optimization*, Vol. 4, No. 2, pp. 65-74.

Hardy, R.L., 1971. Multiquadric equations of topography and other irregular surfaces. *Journal of geophysical research*, Vol. 76, No. 8, pp. 1905-1915.

He, W., Diez, M., Zou, Z., Campana, E. F., and Stern, F., 2013. URANS study of Delft catamaran total/added resistance, motions and slamming loads in head sea including irregular wave and uncertainty quantification for variable regular wave and geometry. *Ocean Engineering*, Vol. 74, pp. 189-217.

Hou, G., Wang, J. and Layton, A., 2012. Numerical methods for fluid-structure interaction: a review. *Communications in Computational Physics*, Vol. 12, No. 2, pp. 337-377.

Hosder, S., Watson, L.T., Grossman, B., Mason, W.H., Kim, H., Haftka, R.T. and Cox, S.E., 2001. Polynomial response surface approximations for the multidisciplinary design optimization of a high speed civil transport. *Optimization and Engineering*, Vol. 2, No. 4, pp. 431-452.

Huang, J., Carrica, P., and Stern, F., 2008. Semi-coupled air/water immersed boundary approach for curvilinear dynamic overset grids with application to ship hydrodynamics. *International Journal for Numerical Methods Fluids*, Vol. 58, No. 6, 2008, pp. 591-624.

Hulme, K. and Bloebaum, C., 1998. A comparison of solution strategies for simulation-based multidisciplinary design optimization. In *7th AIAA/USAF/NASA/ISSMO Symposium on Multidisciplinary Analysis and Optimization*, pp. 4977.

Jin, R., Chen, W. and Simpson, T.W., 2001. Comparative studies of metamodelling techniques under multiple modelling criteria. *Structural and Multidisciplinary Optimization*, Vol. 23, No. 1, pp. 1-13.

Jin, R., Du, X. and Chen, W., 2003. The use of metamodeling techniques for optimization under uncertainty. *Structural and Multidisciplinary Optimization*, Vol. 25, No. 2, pp. 99-116.

Jones, D.R., Schonlau, M. and Welch, W.J., 1998. Efficient global optimization of expensive black-box functions. *Journal of Global optimization*, Vol. 13, No. 4, pp. 455-492.

Kandasamy, M., Peri, D., Tahara, Y., Wilson, W., Miozzi, M., Georgiev, S., Milanov, E., Campana, E.F. and Stern, F., 2013. Simulation based design optimization of waterjet propelled Delft catamaran. *International Shipbuilding Progress*, Vol. 60, No. 1-4, pp. 277-308.

Kennedy, J., Eberhart, R., 1995. Particle swarm optimization, *Proceedings of IEEE International Conference on Neural Networks*, Perth, Australia.

Kleijnen, J.P. and Van Beers, W.C., 2004. Application-driven sequential designs for simulation experiments: Kriging metamodelling. *Journal of the operational research society*,Vol. 55, No. 8, pp. 876-883.

Kroo, I.M., 1997. MDO for large-scale design. Multidisciplinary design optimization: state-of-the-art, *SIAM*, pp. 22-44.

Kumar, J. and Wurm, F.H., 2015. Bi-directional fluid–structure interaction for large deformation of layered composite propeller blades. *Journal of Fluids and Structures*, Vol. 57, pp. 32-48.

Kushner, H.J., 1964. A new method of locating the maximum point of an arbitrary multipeak curve in the presence of noise. *Journal of Basic Engineering*, Vol. 86, No. 1, pp. 97-106.

Leotardi, C., Serani, A., Iemma, U., Campana, E.F. and Diez, M., 2016. A variable-accuracy metamodel-based architecture for global MDO under uncertainty. *Structural and Multidisciplinary Optimization*, pp. 1-21.

Lord, Rayleigh, reissued 1945. *The theory of sound*. Dover Publications, New York.

Lv, J. and Grenestedt, J. L., 2015. Analytical study of the responses of bottom panels to slamming loads. *Ocean Engineering*, Vol. 94, 2015, pp. 116-125.

Martins, J.R. and Lambe, A.B., 2013. Multidisciplinary design optimization: a survey of architectures. *AIAA journal*, Vol. 51, No. 9, pp. 2049-2075.

Matheron, G., 1963. Principles of geostatistics. *Economic geology*, Vol. 58, No. 8, pp. 1246-1266.

Matsumura, T., Haftka, R.T. and Kim, N.H., 2015. Accurate predictions from noisy data: replication versus exploration with applications to structural failure. *Structural and Multidisciplinary Optimization*, Vol. 51, No. 1, pp. 23-40.

Matthies, H.G. and Steindorf, J., 2003. Partitioned strong coupling algorithms for fluid–structure interaction. *Computers & structures*, Vol. 81, No. 8-11, pp. 805-812.

Michler, C., Hulshoff, S.J., Van Brummelen, E.H. and De Borst, R., 2004. A monolithic approach to fluid–structure interaction. *Computers & fluids*, Vol. 33, No. 5-6, pp. 839-848.

Mousaviraad, S.M., He, W., Diez, M. and Stern, F., 2013. Framework for convergence and validation of stochastic uncertainty quantification and relationship to deterministic verification and validation. *International Journal for Uncertainty Quantification*, Vol. 3, No. 5.

Mullur, A.A. and Messac, A., 2006. Metamodeling using extended radial basis functions: a comparative approach. *Engineering with Computers*, Vol. 21, No. 3, pp. 203.

Nocedal, J. and Wright, S., 2006. *Numerical optimization*. Springer Science & Business Media.

Oberhagemann, J., Holtmann, M., el Moctar, O., Schellin, T.E. and Kim, D., 2009. Stern slamming of a LNG carrier. *Journal of Offshore Mechanics and Arctic Engineering*, Vol. 131, No. 3, pp. 031103.

Paik, K.-J., Carrica, P.M., Lee, D., and Maki, K., 2009. Strongly coupled fluid–structure interaction method for structural loads on surface ships. *Ocean Engineering*, Vol. 36, No. 17-18, pp. 1346-1357.

Pellegrini, R., Serani, A., Broglia, R., Diez, M. and Harries, S., 2018. Resistance and Payload Optimization of a Sea Vehicle by Adaptive Multi-Fidelity Metamodeling. In *2018 AIAA/ASCE/AHS/ASC Structures, Structural Dynamics, and Materials Conference*, pp. 1904.

Pellegrini, R., Campana, E.F., Diez, M., Serani, A., Rinaldi, F., Fasano, G., Iemma, U., Liuzzi, G., Lucidi, S. and Stern, F., 2014. Application of derivative-free multi-objective algorithms to reliability-based robust design optimization of a high-speed catamaran in real ocean environment. *Engineering Optimization*, pp.15.

Perez, R., Liu, H. and Behdinan, K., 2004. Evaluation of multidisciplinary optimization approaches for aircraft conceptual design. In *10th AIAA/ISSMO multidisciplinary analysis and optimization conference*, pp. 4537.

Peri, D. and Campana, E.F., 2003. Multidisciplinary design optimization of a naval surface combatant. *Journal of Ship Research*, Vol. 47, No. 1, pp.1-12.

Piro, D.J. and Maki, K.J., 2013. Hydroelastic analysis of bodies that enter and exit water. *Journal of Fluids and Structures*, Vol. 37, pp.134-150.

Queipo, N.V., Haftka, R.T., Shyy, W., Goel, T., Vaidyanathan, R. and Tucker, P.K., 2005. Surrogate-based analysis and optimization. *Progress in aerospace sciences*, Vol. 41, No. 1, pp. 1-28.

Regis, R.G., 2011. Stochastic radial basis function algorithms for large-scale optimization involving expensive black-box objective and constraint functions. *Computers & Operations Research*, Vol. 38, No. 5, pp. 837-853.

Sederberg, T.W. and Parry, S.R., 1986. Free-form deformation of solid geometric models. *ACM SIGGRAPH computer graphics*, Vol. 20, No. 4, pp.151-160.

Sellar, R.S., Batill, S.M. and Renaud, J.E., 1996. Response surface based, concurrent subspace optimization for multidisciplinary system design. *AIAA paper*, Vol. 714.

Serani, A., D'Agostino D., Campana, E.F., and Diez, M., 2018. Assessing the interplay of shape and physical parameters by nonlinear dimensionality reduction methods. In *32nd Symposium on Naval Hydrodynamics*, Hamburg, Germany.

Serani, A., Diez, M., Leotardi, C., Peri, D., Fasano, G., Iemma, U. and Campana, E.F., 2014. On the use of synchronous and asynchronous single-objective deterministic particle swarm optimization in ship design problems, Proceeding of *OPT-i, International Conference on Engineering and Applied Sciences Optimization*, Kos Island, Greece.

Schillings, C., Schmidt, S. and Schulz, V., 2011. Efficient shape optimization for certain and uncertain aerodynamic design. *Computers & Fluids*, Vol. 46, No. 1, pp. 78-87.

Shan, S. and Wang, G.G., 2010. Survey of modeling and optimization strategies to solve high-dimensional design problems with computationally-expensive black-box functions. *Structural and Multidisciplinary Optimization*, Vol. 41, No. 2, pp. 219-241.

Shi, Y. and Eberhart, R., 1998, May. A modified particle swarm optimizer. In *Evolutionary Computation Proceedings, 1998. IEEE World Congress on Computational Intelligence*, The 1998 IEEE International Conference on, pp. 69-73.

Simpson, T.W., Booker, A.J., Ghosh, D., Giunta, A.A., Koch, P.N. and Yang, R.J., 2004. Approximation methods in multidisciplinary analysis and optimization: a panel discussion. *Structural and multidisciplinary optimization*, Vol. 27, No. 5, pp. 302-313.

Simpson, T.W., Mauery, T.M., Korte, J.J. and Mistree, F., 2001a. Kriging models for global approximation in simulation-based multidisciplinary design optimization. *AIAA journal*, Vol.39, No.12, pp. 2233-2241.

Simpson, T.W., Poplinski, J.D., Koch, P.N. and Allen, J.K., 2001b. Metamodels for computer-based engineering design: survey and recommendations. *Engineering with computers*, Vol. 17, No. 2, pp. 129-150.

Sobieszczanski-Sobieski, J., Agte, J.S. and Sandusky, R.R., 2000. Bi-level integrated system synthesis. *AIAA journal*, Vol. 38, No. 1, pp.164-172.

Sobieszczanski-Sobieski, J. and Haftka, R.T., 1997. Multidisciplinary aerospace design optimization: survey of recent developments. *Structural optimization*, Vol. 14, No. 1, pp. 1-23.

Stenius, I., Rosén, A. and Kuttenkeuler, J., 2011. Hydroelastic interaction in panel-water impacts of high-speed craft. *Ocean Engineering*, Vol. 38, No. 2-3, pp. 371-381.

Tahara, Y., Diez, M., Volpi, S., Chen, X., Campana, E.F. and Stern, F., 2012. CFD-based multiobjective stochastic optimization of a waterjet propelled high speed ship. In *29th Symposium on Naval Hydrodynamics, Gothenburg, Sweden*.

Tedford, N.P. and Martins, J.R., 2010. Benchmarking multidisciplinary design optimization algorithms. *Optimization and Engineering*, Vol. 11, No. 1, pp. 159-183.

Thodal R., Grenestedt J.L., and Lv J., 2016. Experimental Study of Structural Responses in High Speed Craft subjected to Atlantic Slamming Loads. In Preparation.

Viana, F.A., Simpson, T.W., Balabanov, V. and Toropov, V., 2014. Special section on multidisciplinary design optimization: metamodeling in multidisciplinary design optimization: how far have we really come?. *AIAA Journal*, Vol. 52, No. 4, pp. 670-690.

Volpi, S., Diez, M., and Stern, F., 2018. Multidisciplinary design optimization of a 3D composite hydrofoil via variable accuracy architecture. To appear in *AIAA/ISSMO Multidisciplinary Analysis and Optimization Conference*, Atlanta, GA, US.

Volpi, S., Diez, M., and Stern, F., 2017a. Towards the high-fidelity multidisciplinary design optimization of a 3D composite material hydrofoil. Proceedings of the *VII International Conference on Computational Methods in Marine Engineering*, Nantes, France.

Volpi, S., Diez, M., Sadat-Hosseini, H., Kim, D.H., Stern, F., Thodal, R.S. and Grenestedt, J.L., 2017b. Composite bottom panel slamming of a fast planing hull via tightly coupled fluid-structure interaction simulations and sea trials. *Ocean Engineering*, Vol. 143, pp. 240-258.

Volpi, S., Diez, M., Sadat-Hosseini, H., Kim, D.-H., Stern, F., Thodal, R.S., and Grenestedt J.L., 2016. Full-scale fluid-structure interaction simulation and experimental validation of high-speed planing-hull slamming with composite panels. Proceedings of the *31st Symposium on Naval Hydrodynamics*, Monterey, CA, USA.

Volpi, S., Diez, M., Gaul, N.J., Song, H., Iemma, U., Choi, K.K., Campana, E.F. and Stern, F., 2015a. Development and validation of a dynamic metamodel based on stochastic radial basis functions and uncertainty quantification, *Structural and Multidisciplinary Optimization*, Vol. 51, No. 2, pp.347-368.

Volpi, S., Sadat-Hosseini, H., Diez, M., Kim, D.-H., Stern, F., Thodal, R.S., and Grenestedt J.L., 2015b. Validation of high fidelity CFD/FE FSI for full-scale high-speed planning hull with composite bottom panels slamming. Proceedings of the *VI Intl. Conf. on Coupled Problems in Science and Engineering*, Venice, Italy.

Wang, G.G. and Shan, S., 2007. Review of metamodeling techniques in support of engineering design optimization. *Journal of Mechanical design*, Vol. 129, No. 4, pp. 370-380.

Weil, C.R., Lee, E.J., Fullerton, A.M., Lien, V.A., Lewis, R.R., Stern, F., and Diez, M., 2018. Experimental and computational fluid-structure interaction studies of a semi-planing hull. In *32st Symposium on Naval Hydrodynamics*, Hamburg, Germany.

Xing, T. and Stern, F., 2010. Factors of safety for Richardson extrapolation. *Journal of Fluids Engineering*, Vol. 132, No. 6, pp. 061403.

Yang, X.S. and Deb, S., 2009. Cuckoo search via Lévy flights. In *Nature & Biologically Inspired Computing, 2009. NaBIC 2009. World Congress on*, pp. 210-214.

Yang, X.S., 2010a. *Nature-inspired metaheuristic algorithms*. Luniver press

Yang, X.S., 2010b. A new metaheuristic bat-inspired algorithm. In *Nature inspired cooperative strategies for optimization (NICSO 2010)*, pp. 65-74. Springer, Berlin, Heidelberg.

Zarruk, G.A., Brandner, P.A., Pearce, B.W. and Phillips, A.W., 2014. Experimental study of the steady fluid–structure interaction of flexible hydrofoils. *Journal of Fluids and Structures*, Vol. 51, pp. 326-343.

Zhao, L., Choi, K.K. and Lee, I., 2011. Metamodeling method using dynamic kriging for design optimization. *AIAA journal*, Vol. 49, No. 9, pp. 2034-2046.